Regional Surface Waveform Inversion for Australian Paths

by

Yoshihisa Hiyoshi

A thesis submitted for the degree of Doctor of Philosophy

of

The Australian National University

January 2001

Author's Declaration

Except as noted throughout the text and in the acknowledgments, the research described in this thesis is solely that of the author.

Yoshihisa HIYOSHI

The Australian National University

January 2001

Author's Declaration

Except as noted throughout the text and in the acknowledgments, the research described in this thesis is solely that of the author.

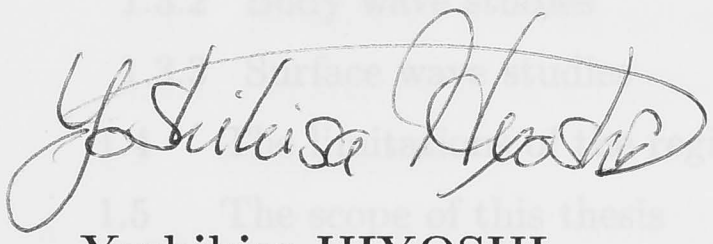

Yoshihisa HIYOSHI

The Australian National University

January 2001

Contents

Acknowledgments

I wish to thank my parents Akira and Keiko HIYOSHI who understood and tolerated me going overseas to undertake my PhD project. I wish also thank my brother, Haruhisa HIYOSHI who has financially supported me.

Prof. Brian Kennett, my supervisor, has been a through and thoughtful guide throughout my candidature. I have appreciated Brian's generosity with his time and energy, and I have benefited enormously from the depth and breath of his understanding.

Dr Eric Debayle, my co-supervisor, provided the inversion program and perfect support to my project. I really appreciate your instruction and kindness.

The opportunity to have been a research student in the fertile environment of RSES is appreciated. I gratefully acknowledge the receipt of the ANU PhD scholarship, which made it financially possible.

Yoshihisa HIYOSHI

Abstract

This thesis seeks to test the assumptions behind current surface wave tomography methods as a basis for improving techniques. The waveform methods are extended to horizontal component data, focuses on the discrepancy between Rayleigh and Love wave dispersion which can be resolved by the introduction of polarisation anisotropy. The earthquake sources in the region lie mostly outside of continental Australia and many paths include an oceanic component. We therefore seek to cross-check tomographic resolution by using purely continental paths by use of all available information such as dispersion and surface wave inversion.

For the above purpose, we first check the ability of the two waveform inversion methods; the PWI method by Nolet (1990) and the CL method by Cara & Lévêque (1987). The series of synthetic recovery tests shows that both PWI and CL waveform inversions have different strengths and weaknesses. The PWI approach is quite robust for the perturbations of β_v in the crust and the uncertainty of the Moho depth. Also a good feature is to separate the portion of the fundamental mode Rayleigh waves from the higher modes and to apply different bandpass filters to the two windows. This will enhance the vertical resolution of the final model. In contrast, the PWI method can provide good results only when an adequate initial model is available. In other words, the PWI technique is quite sensitive to the initial model. Moreover, the separation of the two time windows gives biases on the resulting model, when the higher mode window has enhanced weighting.

The CL approach can recover the + 8 % deviation from the upper mantle initial model in the synthetic test, so that the CL method can be applied for the region of large β_v wavespeed variations in the upper mantle. On the other hand, perturbations of the crustal β_v values give strong impacts on the resulting β_v profile from the CL inversion. In particular, the effect of the estimation error of Moho depth is significant in its amplitude and penetration depth, when the error is more than 10 km.

To improve the results of the PWI method, it is necessary to find a way of obtaining suitable initial models for the inversion. Also special care should be taken for the use of the higher mode time window in the PWI approach. On the other hand, to avoid contamination from the crustal structure, the CL starting model has to have more accurate

crustal structure for each path. The CL approach also needs to invert the β_v profile in the crust and upper mantle, rather than only in the upper mantle.

From the Rayleigh and Love joint and independent inversions for selected Australian paths, we can conclude that the Australian continent has large variations of β_v and β_h values in horizontally and vertically. However, the measurement of polarisation anisotropy ($\xi = (\beta_h/\beta_v)^2$) has rather limited resolution below 200 km depth, so that it is difficult to clarify the structures of β_v and β_h below this depth. Furthermore, the presence of azimuthal anisotropy of Rayleigh waves imposes more complexity of the β_v and β_h profiles for this region. Thus, it is safe to say that the Australian seismological structure could not be represented by one simple seismological model.

In addition, the comparison of the joint inversion results with those of the independent inversions for Australian paths elucidates the difficulty of obtaining stable β_h models for the paths. This is due partly to a strong sensitivity of Love wave inversion to starting model. Also the assumption of a simple TIV (Transverse Isotropy with a Vertical symmetry axis) model for the complex Australian structure makes some of the resulting β_h profiles implausible.

The problem with the waveform inversions for the Australian continent is that we do not have an efficient means of determining acceptable starting models of shear wavespeed for the complex Australian seismological structure.

The FTAN filtering technique can provide a reasonable solution to this problem, in particular, for β_v models, because the FTAN technique plays two important roles for constructing initial models for Australian paths. The first role is that FTAN helps to regionalise the continent into several seismological blocks which are represented by typical FTAN group dispersion curves. Such a classification of the continent can contribute to the construction of closer starting models for the regional inversion. Second, the FTAN approach can generate a good starting model of β_v for each block. However, the FTAN-generated dispersion curves for the T component at stations CAN and PMG display very poor matches to the final results of the CL inversion, so that the FTAN method is inadequate for constructing plausible β_h starting models for paths crossing the complex Australian continental blocks.

Another solution to the difficulty of obtaining adequate starting models of $\beta_{v,h}$ is that inversion should be conducted from multiple base models. Indeed a good approach in an automated scheme would be to adopt a group of 3 base models e.g. PREM, PREM$\pm$6% and carry out the inversion selecting the best fit model with a test for consistency between the different cases.

1

INTRODUCTION:

Australian tectonics and surface wave analysis

1.1 Motivation for surface wave study of the upper mantle

Since the early 1980's, three-component broadband seismometers with digital recording have become a major tool in research in global seismology. The advantage of using such a broadband device is the fidelity of recording ground motion achieved through a wide frequency coverage and high dynamic range. The working frequencies for many observatory instruments span the range from 0.003 Hz to 10 Hz and so the broadband records can contain both the long period surface waves and free oscillations of the Earth as well as the higher frequency body waves. The early attempts to enhance global coverage focussed on vertical component instruments but the current generation of broadband instruments have high quality recording for the horizontal components. The horizontal component of ground motion provides useful additional information. The long period portion includes Love waves and the toroidal free oscillations of the Earth whose expected polarisation is tangential to the great circle path between source and receiver. There is also useful additional information from the component along the path on Rayleigh waves and spheroidal free oscillations. At slightly higher frequencies there is also abundant information on the S body waves which were very poorly recorded using photographic techniques. Although the number of broadband stations around the globe has increased significantly over recent years the station coverage is still limited and the high noise level on the horizontal components at many sites has prevented full use of the information on horizontal broadband seismograms.

In recent years, however, the deployment of portable three-component broadband seismic arrays has paved the way to taking better advantage of the horizontal component data. In such array experiments, enough seismometers are installed to allow investigation of structure on regional scales, and where possible low noise environments are chosen. For

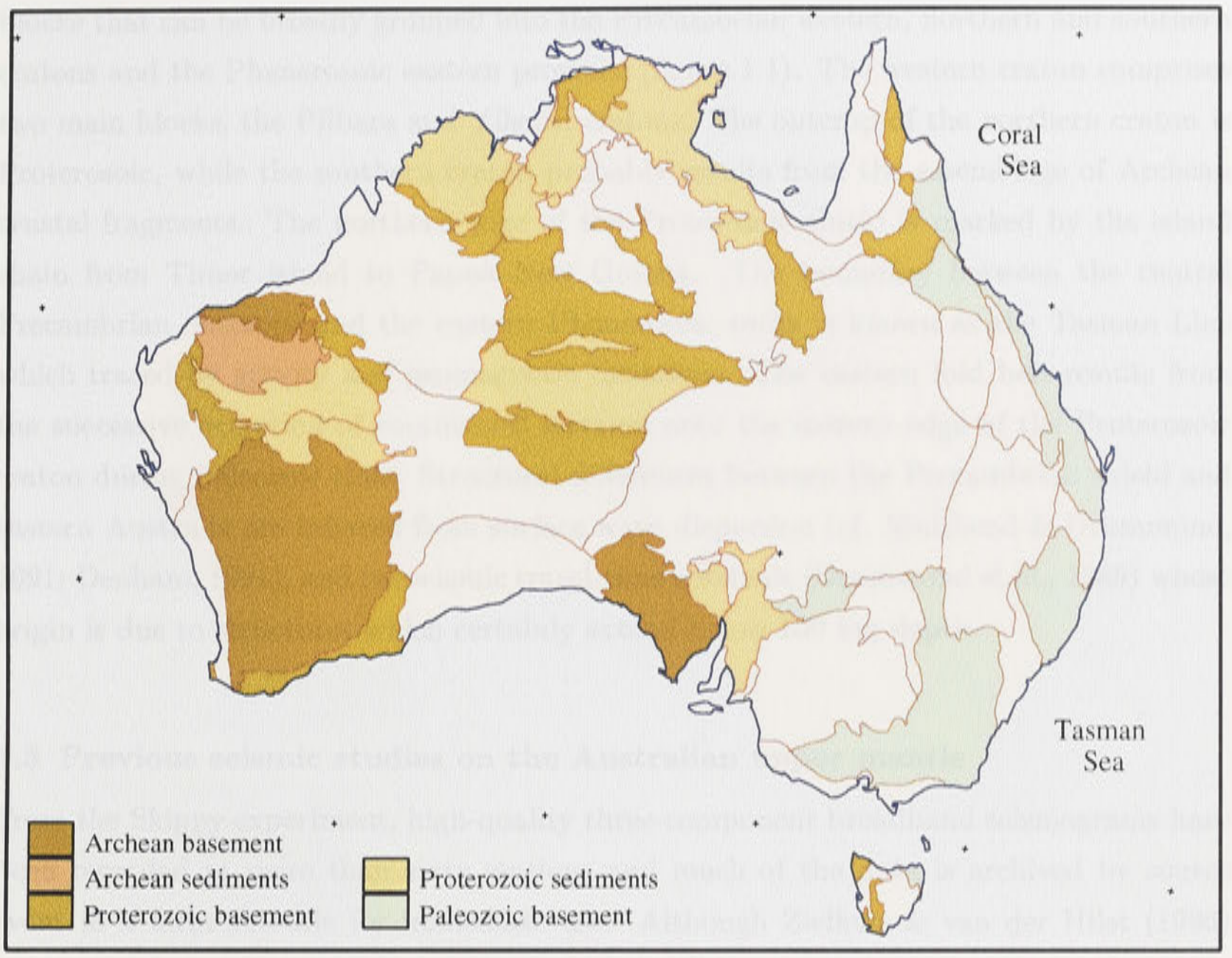

Fig. 1.1. Map of the crustal outcrops and tectonic units of the Australian continent.

the Australian continent, the Skippy experiment (van der Hilst et al., 1994) was conducted from May 1993 to October 1996; this experiment exploited regional seismicity around Australia and more than sixty portable broadband stations covered the whole continent with a spacing of around 400 km. These stations were mainly placed away from urban areas and more than 120 km from the seacoast so that they generally have had relatively low noise.

This accumulation of the high quality broad-band seismograms with a reasonable regional path coverage provides us with opportunities for optimising current regional waveform inversion methods to the Australasian region. In addition, we can obtain the anisotropic structure beneath the Australian continent in exploiting information on the broad-band horizontal component seismograms.

1.2 Tectonics of the Australian region

out crop

The surficial geology of the Australian continent is composed of an assemblage of crustal

blocks that can be broadly grouped into the Precambrian western, northern and southern cratons and the Phanerozoic eastern province (figure 1.1). The western craton comprises two main blocks; the Pilbara and Yilgarn cratons. The outcrop of the northern craton is Proterozoic, while the southern craton probably results from the assemblage of Archean crustal fragments. The northern edge of the Proterozoic shield is marked by the island chain from Timor island to Papua New Guinea. The boundary between the central Precambrian outcrops and the eastern Phanerozoic rocks is known as the Tasman Line which traced by gravity and geomagnetic lineations. The eastern fold belt results from the successive accretion of continental terranes onto the eastern edge of the Proterozoic craton during Paleozoic time. Structural differences between the Precambrian shield and eastern Australia are inferred from surface wave dispersion (cf. Muirhead & Drummond, 1991; Denham, 1991), and teleseismic travel-time residuals (Drummond et al., 1989) whose origin is due to structures which certainly extend below 100 km depth.

1.3 Previous seismic studies on the Australian upper mantle

From the Skippy experiment, high-quality three-component broadband seismograms have been recorded at more than sixty stations and much of the data is archived by source event in a form suitable for immediate use. Although Zielhuis & van der Hilst (1996) have used the vertical component data from the Skippy experiment in eastern Australia for their work on waveform inversion of Rayleigh waves, the horizontal seismograms have only recently been used by Debayle & Kennett (2000b).

The use of the horizontal-component broadband records is needed to investigate the SH wave velocity structure in the study area. The combination of such an investigation with the information on SV velocity structure gives the possibility of mapping anisotropy beneath Australia. The analysis of the horizontal component data, however, requires azimuthal calibration of the instrumental settings, because the seismograms on the horizontal components are quite sensitive to rotation in the horizontal plane.

In this work, the first objective is to improve methods of obtaining SV and SH wavespeed structures beneath Australia. The second objective is to delineate the anisotropic structure beneath the Australian continent based on the SV-SH wavespeed mapping.

1.3.1 Receiver functions

The structure just beneath a seismic station imposes a pattern of reverberations and wavetype conversions on the signals associated with the major seismic phases. The effects are particularly clear following the first arriving P wave and can be isolated and interpreted

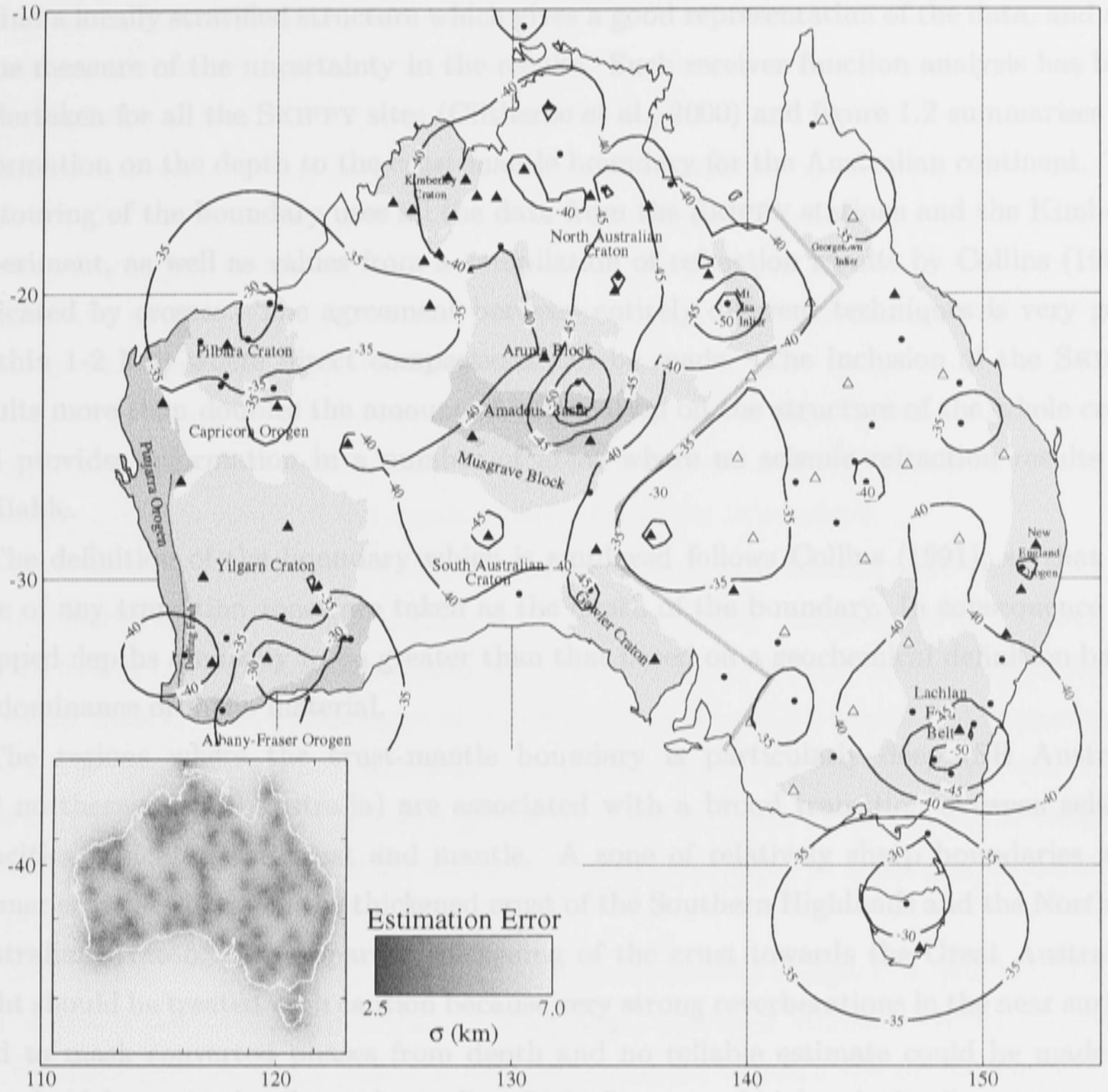

Fig. 1.2. The depth distribution of the crust-mantle boundary beneath the Australian continent.The light shaded areas display the major crustal blocks in figure 1.1. The inset indicates the estimation errors (Clitheroe et al., 2000).

by using the receiver function technique (see e.g. Shibutani et al., 1996), in which the radial component of ground motion is deconvolved using the vertical component. By this means the common effect of the source and path is eliminated and the influence of local structure enhanced. The process of estimating the crustal and uppermost mantle structure then depends on being able to find a close match between the receiver function derived from the data and that calculated from a postulated structure. This approach can be formalised with a systematic inversion scheme and Shibutani et al. (1996) have demonstrated the successful application of genetic algorithm methods.

In order to minimise the influence of local heterogeneity, the receiver functions from many events at different azimuths are stacked before analysis. By this means it is possible

to find a locally stratified structure which gives a good representation of the data, and also some measure of the uncertainty in the results. Such receiver function analysis has been undertaken for all the SKIPPY sites (Clitheroe et al., 2000) and figure 1.2 summarises the information on the depth to the crust-mantle boundary for the Australian continent. The contouring of the boundary uses all the data from the SKIPPY stations and the Kimberly experiment, as well as values from a compilation of refraction results by Collins (1991), indicated by crosses. The agreement between entirely different techniques is very good (within 1-2 km) where direct comparisons can be made. The inclusion of the SKIPPY results more than doubles the amount of information on the structure of the whole crust, and provides information in a number of areas where no seismic refraction results are available.

The definition of the boundary which is employed follows Collins (1991), so that the base of any transition zones are taken as the depth of the boundary. In consequence the mapped depths are likely to be greater than that based on a geochemical definition based on dominance of mafic material.

The regions where the crust-mantle boundary is particularly deep (SE Australia and northern central Australia) are associated with a broad transition between seismic velocities typical of the crust and mantle. A zone of relatively sharp boundaries with thinner crust lies between the thickened crust of the Southern Highlands and the Northern Australian Craton. The apparent thickening of the crust towards the Great Australian Bight should be treated with caution because very strong reverberations in the near surface tend to mask converted phases from depth and no reliable estimate could be made for crustal thickness in the Great Australian Bight because of high velocity limestones close to the surface.

1.3.2 Body wave studies

A number of studies have been done using observations of seismic waves travelling from the seismic belt to the north of Australia to delineate the major features of the upper mantle structures beneath the Australian continent. Simpson (1973) uses traveltime and slowness observation at the Warramunga array (WRA) in the Northern Territory and displays differences in upper mantle structure between different azimuthal windows. Hales et al. (1980) use records from Indonesian earthquakes at a variety of depths at a number of portable stations in a traveltime analysis. The resulting P-wave model has rather complex features with many small discontinuities and low velocity zones, which may well reflect the mapping of 3-D structure into a 1-D model. However, to interpret the observed data they model a clear velocity discontinuity at around 200 km depth with the uncertainty of

5 to 10 km in the northern Australia. Leven (1985) reinterprets the data with comparison between empirical and synthetic seismograms. The new profile has a somewhat simplified structure but a profound velocity contrast remains around 210 km depth.

Extensive use of portable short-period vertical seismometers opens opportunities for the more detailed studies beneath northern Australia. Bowman & Kennett (1990) introduce stacking techniques to the seismograms from the Flores arc to produce composite record sections and develop a detailed seismic profile for depths from 150 km and 600 km. They demonstrate significant variation in P wave velocity structure in the upper mantle, in particular, the clear P-velocity contrast near 210 km depth with the base of the seismic lithosphere. Based on a broader set of observation Dey et al. (1993) confirm the need for a velocity contrast near 210 km depth as the base of the lithosphere.

Taking advantage of broad-band instruments, several new studies have been done for getting more detailed images beneath northern Australia. Kennett et al. (1994) use records from a broad-band seismometer at WRA and depict S and P wavespeed profiles in the upper mantle. Gudmundsson et al. (1994) also use the WRA broad-band records and show the presence of a high-Q lithosphere to depths of about 210 km and a relatively low-Q asthenosphere beneath. From investigation of the shear wave splittings of the refracted waves in the radial and tangential components at WRA, Tong et al. (1994) demonstrate the presence of anisotropy in the lithosphere.

These studies of the upper mantle structures draw detailed images in a relatively limited area beneath the northern margins of Australia. Kaiho & Kennett (2000) propose a 3-D representation of the P and S wavespeed structure beneath the entire Australasian region using more than 2700 SKIPPY seismograms sampling the upper mantle structure. The SKIPPY project provides a good coverage of refracted wave paths originating from the seismic belt extending from Indonesia through Papua New Guinea, Vanuatu to Tonga-Kermadec. However, the interstation spacing of 400 km for the project causes limited resolution for a single event. Thus they introduce stacking techniques of the seismograms and combine event station pairs along a common band of azimuths in order to produce composite record sections for P and S arrivals. Applying traveltime and synthetic seismogram analyses to the composite records, they construct 1-D seismic models for a set of azimuthal corridors across the Australasian region. Based on the suite of 1-D models, an indication of an appropriate 3-D wavespeed model in the upper mantle is also generated.

In the upper most mantle, Kaiho & Kennett (2000) find the presence of substantial variation of seismic wavespeed which was suggested by Dey et al.(1993) and by the traveltime study of Bowman & Kennett (1993). The western half of the continent has very fast but varying S-wave speed beneath the Precambrian cratons with a lithospheric

thickness of about 200 km and significant low velocity layer beneath the lithosphere. In the eastern part, the lithospheric thickness becomes much thinner. They also observe high seismic wavespeed towards the base of the transition zone with high S wavespeed beneath the continent and high P wavespeed beneath the ocean.

1.3.3 Surface wave studies

To draw the upper mantle shear wavespeed structure beneath the Australasian region, two styles of regional surface waveform inversion schemes are introduced. One approach is developed by Nolet (1990) and the other is by Cara & Lévêque (1987). Both schemes have two distinct steps; first obtaining shear wavespeed models for individual paths by waveform fittings and second inverting all the models into a 3-D wave speed structure over the path coverage area.

The first approach is called as 'Partitioned Waveform Inversion' (Nolet, 1990) based on the theoretical work on waveform inversion by Nolet et al. (1986). This approach at first directly inverts the differences between empirical waveforms and comparable portion of theoretical seismograms into the perturbations of the 1-D shear wavespeed structures beneath individual paths. Second the compilation of the perturbations of the 1-D models for all the paths is linearly inverted into a 3-D shear wavespeed model having discrete 2-D horizontal grids and vertical nodes.

Zielhuis & van der Hilst (1996) and van der Hilst et al. (1998) apply this style of inversion method to the SKIPPY data and construct the 3-D shear wavespeed model beneath the Australian continent (figure 1.3). They achieve a horizontal resolution of about 300 km in the eastern two thirds of the continent, while in the western third the horizontal resolution rapidly decreases corresponding to the poor path coverage. The most pronounced characteristic of the upper mantle structure in the figure is the strong contrast of the shear wavespeed between the part of Australia east of $140E$ and the rest of the continent. The wavespeed gradient in the east-west direction is predominant and its peak-to-peak amplitude variations reach up to 10 percent relative to the reference model used for the display. This pattern of the shear wavespeed contrast roughly matches geological settings of the two major regions, that is, the Phanerozoic eastern fold belt is marked by the lower shear wavespeed and the Precambrian shield regions are characterised by the faster shear wavespeed. The 140 km depth slice in the figure clearly indicates this wavespeed contrast.

The second approach to regional waveform inversion introduced by Cara & Lévêque (1987) has also two distinct steps: the first step is to perform a non-linear waveform inversion in order to obtain a 1-D shear wavespeed structure for each path; and the second

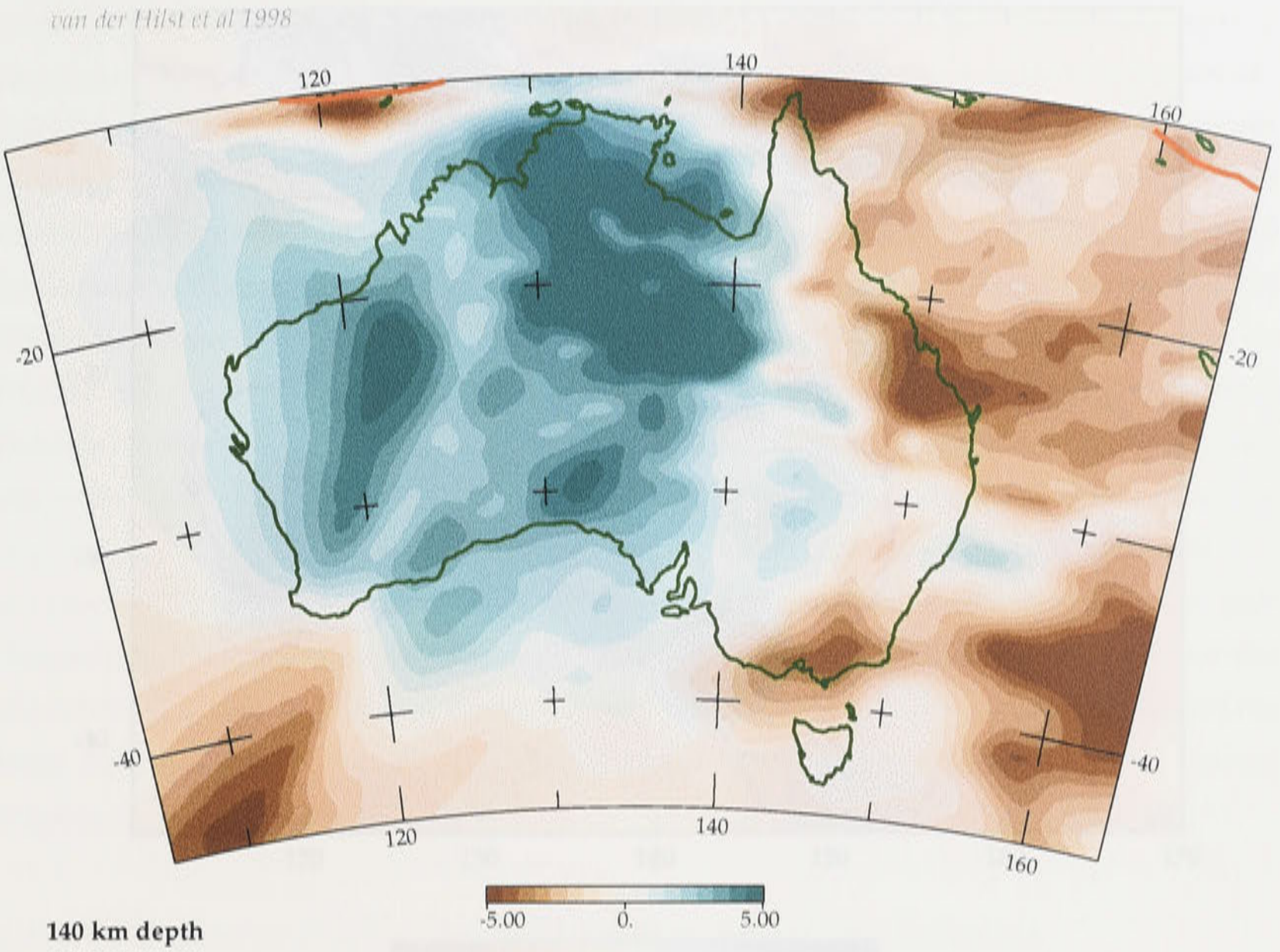

Fig. 1.3. Map view of shear wavespeed at 140 km depth. [After van der Hilst et al., 1998]

step is to regard all the 1-D models as linear constraints on the average properties of the 3-D shear wavespeed model and to perform a linear inversion for the 3-D structure. However, the Cara & Lévêque (1987) approach is clearly different from the Nolet (1990) approach in the following two aspects. The first difference is that the Cara & Lévêque (1987) method introduces 'secondary observables' and inverts the differences of the empirical and synthetic secondary observables into the perturbations of the shear wavespeed from the reference model, whilst the Nolet-style approach derives the perturbations of the shear wavespeed directly from the difference of the observed and synthetic seismograms. These secondary observables are extracted by cross-correlation between a seismogram and the synthetic seismograms corresponding to a single mode. The introduction of the secondary observables makes the dependence of the waveform on the elastic parameters close to weakly nonlinear, so that the Cara & Lévêque (1987) approach is generally less sensitive to the starting model than the Nolet-style approach. The second difference from the Nolet-style approach is that the resulting 3-D model obtained in the second stage is continuous rather than a discrete 3-D block style expression. Because it uses the continuous regionalisation procedure developed by Montagner (1986), the Cara & Lévêque

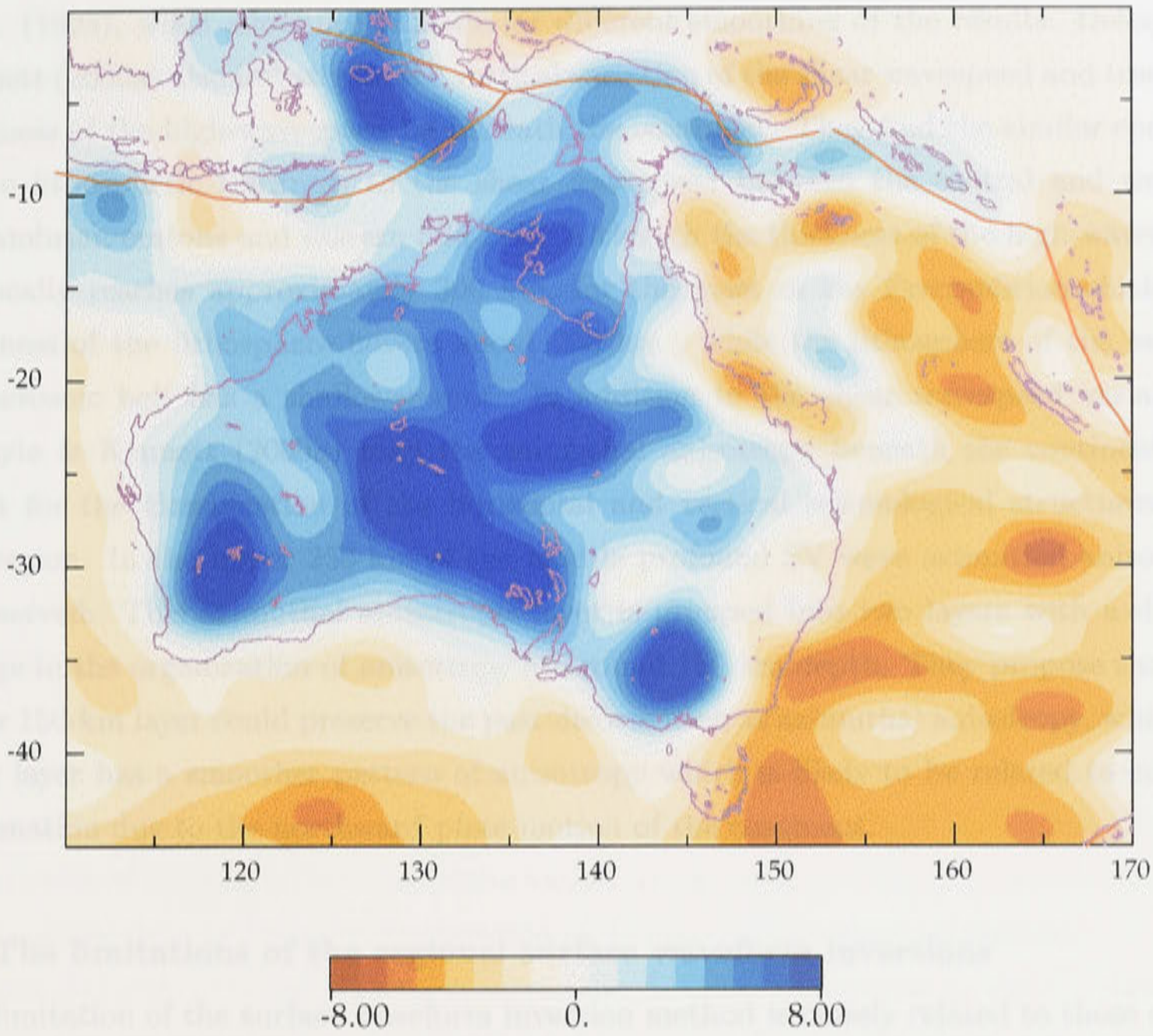

Fig. 1.4. Map view of shear wavespeed at 150 km depth. [After Debayle & Kennett (2000a)]

(1987) approach can depict shear wavespeed heterogeneity and the pattern of azimuthal anisotropy. Lévêque et al. (1998) demonstrate the distribution of the azimuthal anisotropy as well as the variation of the shear wavespeed beneath the Indian ocean.

From the practical application of this 'secondary observable' method to the Australian continent, Debayle (1999) and Debayle & Kennett (2000a) illustrate images of the lateral variation of SV wavespeed and azimuthal anisotropy in the upper mantle of the Australasian region. Using more than 2000 of the latest Rayleigh wave recordings with a denser crossing ray path coverage, Debayle & Kennett (2000a) achieve a lateral resolution of the order of a few hundred kilometers. Including several higher mode Rayleigh waveforms enhances a vertical resolution of the shear wavespeed model down to depths of at least 400 km. The resulting model of the shear wavespeed heterogeneity in the upper 200 km (figure 1.4) depicts the shear wavespeed pattern of the slower Phanerozoic fold belt and the faster Precambrian central and western cratons. The lateral variation of the SV wavespeed is in good agreement with the 3-D structure obtained by van der Hilst

et al. (1998), when allowance is made for different smoothing of the results. Debayle & Kennett (2000a) also investigate the vertical variation of the shear wavespeed and trace the thickness of the high-wavespeed lid beneath the continent. They find the similar contrast of the lithospheric thickness to the shear wavespeed between the central and western Precambrian cratons and eastern fold belt. Although the thickness of the high-wavespeed lid locally reaches approximately 300 km, for the most of the Precambrian shield the thickness of the lithosphere hovers about 200 km , while the lithosphere of the eastern Phanerozoic belt has a shallower root. In addition to the shear wavespeed variations, Debayle & Kennett (2000a) map the azimuthal anisotropy beneath the continent and use it for the classification of the horizontal and vertical seismological structures over this region. In the upper 250 km of the mantle profound SV wave azimuthal anisotropy is observed. This azimuthal anisotropic layer is grouped into two layers with a drastic change in the organization of anisotropy at around 150 km depth. They propose that the upper 150-km layer could preserve the past deformation as azimuthal anisotropy, while the lower layer has a smoother pattern of anisotropy which is likely to be related to current deformation due to the northward plate motion of the continent.

1.4 The limitations of the regional surface waveform inversions

The limitation of the surface waveform inversion method is closely related to those of the assumptions it takes. The 'partitioned waveform inversion' method and the 'secondary observable' method are based on the common assumption that the actual structure between epicentre and station is expected to be represented by a path-average 1-D structure along the great circle path between epicentre and station and the average 1-D structure should not go very far from the reference 1-D model. In other words, both inversions are taken to carry out in laterally smoothly varying media. Under the condition that this assumption could become invalid, we carefully consider whether our inversion method goes beyond its limitation or not.

Two characteristics of the Australian seismological setting potentially make the assumption invalid. The first factor is the strong contrast in shear wavespeed between the central-western Precambrian cratons and the eastern Phanerozoic margins. The second factor is the rapid changes of the crustal thickness at the ocean-continent boundaries around the Australian continent. In the case that the ray path between epicentre and station comes across the inner continental or ocean-continent boundary, the actual surface waves could neither follow the great circle path nor would the propagation be characterised by the averaged wavespeed along the great circle path.

However, the path average assumption can be still valid if we chose an adequate

frequency range and epicentral distance, because the deviation of the path average structure along the great circle path from the real structure depends on the frequency and travel distance ranges we employ. For example, the higher frequency we use, the larger wavespeed deviation we expected, because the higher-frequency waves are more sensitive to the sudden changes of the crustal structure at the ocean-continent or crustal block boundaries. Moreover, the longer distance of the surface waves propagation, the larger is the expected deviation between the path averaged and actual wavespeed models, because the path averaged structure is strongly influenced by the conditions encountered along the path. In consequence, we should seek suitable ranges of the frequency and travel distance in order to perform the waveform inversion in regions with laterally smoothly varying media.

In addition, we need to pay attention to the fact that the two waveform inversion methods take the different approaches to the linearisation of the non-linearity between the perturbations of waveform characteristics and of the shear wavespeed structure. The partitioned waveform inversion method linearises the relation between the waveform (wavenumber) perturbations and those of the shear wavespeed, whilst the Cara & Lévêque (1987) method linearly relates the perturbations of the cross-correlation function between the empirical data and synthetic seismograms to those of the shear wavespeed.

These different linearisation styles reflect the different robustness to the non-linearity between the perturbations of waveform characteristics and of the shear wavespeed. In the Australian continent, however, the relation between the perturbations of waveform characteristics and of the shear wavespeed structure could be highly non-linear, in particular, if surface waves propagate through the structural boundaries such as the ocean-continent boundary. Under such condition, both styles of linearisations become invalid in different ways, although the Cara & Lévêque (1987) method would be expected to be more robust to the nonlinearity than the Nolet-style approach. It is therefore worth while comparing the two inversion methods and examining under which conditions the two methods face their limitations.

The investigation of the anisotropy based on the SV and SH waveform inversions should be conducted taking into account the limitations of the waveform inversion methodologies.

1.5 The scope of this thesis

The two main objectives of this thesis are first to establish procedure of the regional waveform inversion method for obtaining the SH and SV wavespeed structures and second to delineate the anisotropic structure beneath the Australian continent based on the information on the SV and SH structure.

However, surface waves recorded at Australian seismic stations have experienced significant modification in its waveforms, firstly because strong lateral heterogeneity of seismic wave speed occurs at the boundaries of oceanic and continental lithospheres and of different crustal blocks within the Australian continent. The waveform modification recorded at Australian stations is secondly due to the event distribution in the Australasian region. The earthquake sources in the region lie mostly outside of continental Australia and many paths include an oceanic component. Thus the ocean-continent mixed paths enhance the boundary effects on the surface wave signals at the boundaries of the major crustal blocks and the margin of the continent. In particular, the effect of the rapid crustal thickness changes appears more in SH waveforms than in SV waveforms.

We thus have to establish the most appropriate conditions for regional surface waveform inversion methods using the Australian 3-component waveform data. Indeed to lessen the boundary effects on the signals and optimise the inversion techniques to the Australian data, we seek to test the major assumptions behind current surface wave tomography methods. In particular, we focus on the assumption of a linear or weakly nonlinear relation between waveform changes and those of the shear wavespeeds $\beta_{v,h}$. For the purpose, a series of comprehensive synthetic tests are designed for purely continental paths.

The waveform inversion methods are then extended to three-component data, emphasizing the discrepancy between Rayleigh and Love wave dispersion. This discrepancy is explained by introducing polarisation anisotropy. In the inversion using vertical and tangential component data, the TIV assumption (Transverse Isotropy with a Vertical symmetry axis) is examined.

We finally seek to cross-check tomographic resolutions by using purely continental paths by use of all available information such as dispersion and surface wave inversion.

2

REPRESENTATION OF SURFACE-WAVE TRAINS BY MODAL SUMMATION

In this chapter, we explore the representation of the surface wave portion of the seismic wavefield, especially looking at the contributions of the source, the receiver, and the propagation path. We begin by considering a stratified medium for which the theoretical structure is well developed and then look at the way in which the modal representation can be adapted to laterally varying media.

2.1 Nature of surface waves

The longer period ground motions of surface waves for a stratified structure can be represented as a sum over contributions from a number of modes with a sum over angular order components generated by the nature of the source mechanism, when the surface waves can be assumed to propagate along a great-circle and over a one-dimensional path averaged structure. In addition, when the receiver is far enough from the source for an asymptotic representation of the horizontal phase functions to be used, the surface wave part of the wave field can be represented in a form which displays the dependence of the source depth, propagation paths, and receiver depth.

We build on the development of Kennett (1983; Chapter 11) to explore the representation of the surface-wave synthetic seismograms, and particularly examine the influences from the source, receiver and propagation path on the phase changes in the surface wave field.

In section 2.2, it is shown that the surface-wave displacements can be expressed as a vector surface-harmonic expansion in cylindrical coordinates. The modal weights are determined by the solution of a set of coupled first-order differential equations in the depth coordinate, subject to the boundary conditions of vanishing traction at the free-surface and decay of the surface-wave field at depth. In the far-field the harmonic expansion

provides a simple representation of the surface wave portion of the seismogram. However, the horizontal harmonic vectors ($\mathbf{S}_m$ and $\mathbf{T}_m$) have near-field terms which couple the radial and tangential components. Therefore, we have no clear separation by components of SV and SH motion at small epicentral distances (r) or low frequencies (ω).

We show how the boundary and source conditions can be combined to provide representations of the displacement vectors for Rayleigh and Love waves as a function of horizontal slowness p and frequency ω which lead to pole singularities of the displacement representation in the (ω, p) domain. The dispersion of each individual mode is associated with the locus of a pole in frequency and slowness.

Section 2.3 is concerned with the excitation of surface waves. The spectral method is introduced which first performs the slowness integral in the double-integral expressions of the displacement field. In this approach, the contributions from surface waves to the displacement field separate from the body wave contributions through modification of the integral path.

The representations of the surface-wave field are combined with the source term, the receiver term, and the horizontal propagation term; so that we are able to provide expressions of the synthetic far-field seismograms for surface waves including the source radiation with the moment tensor elements and the presence of attenuation through the quality factor.

Finally in *section 2.4* we consider the extension of the surface wave representation into laterally varying media.

2.2 Surface vector harmonics and coupled equations for seismic waves

Takeuchi & Saito (1972) introduced the expressions for the three components of displacement (U, V, and W) as a vector surface-harmonic expansion in terms of frequency ω and horizontal wavenumber k. It is convenient to introduce the horizontal slowness p such that $k = \omega p$ and then the vector surface harmonic representation takes the form:

$$\begin{aligned}\mathbf{u}(r,\phi,t) &= \frac{1}{2\pi}\int_{-\infty}^{\infty} \mathrm{d}\omega \mathrm{e}^{-\mathrm{i}\omega t} \int_0^{\infty} \mathrm{d}k\; k \sum_m \\ &\quad [U(p,m,\omega)\mathbf{R}_m(\omega p r) + V(p,m,\omega)\mathbf{S}_m(\omega p r) + W(p,m,\omega)\mathbf{T}_m(\omega p r)]\,, \quad (2.1)\end{aligned}$$

where the orthogonal vector harmonics ($\mathbf{R}_m, \mathbf{S}_m, \mathbf{T}_m$) are explicitly expressed in terms of Bessel function entries as

$$\begin{aligned}\mathbf{R}_m(\omega p r) &= [\mathbf{e_z} J_m(\omega p r)]\ \mathrm{e}^{\mathrm{i}m\phi}\,, \\ \mathbf{S}_m(\omega p r) &= [\mathbf{e_r} J_{m-1}(\omega p r) - (\mathbf{e_r} - \mathrm{i}\mathbf{e}_\phi) m J_m(\omega p r)/\omega p r]\ \mathrm{e}^{\mathrm{i}m\phi}\,, \quad (2.2) \\ \mathbf{T}_m(\omega p r) &= [-\mathbf{e}_\phi J_{m-1}(\omega p r) + (\mathbf{e}_\phi + \mathrm{i}\mathbf{e}_r) m J_m(\omega p r)/\omega p r]\ \mathrm{e}^{\mathrm{i}m\phi}.\end{aligned}$$

The horizontal terms ($\mathbf{S}_m$ and $\mathbf{T}_m$) have 'near-field' (or 'low-frequency') components depending on $mJ_m(\omega pr)/\omega pr$ which vanish more quickly than the terms directed along the three unit vectors ($\mathbf{e}_r$, $\mathbf{e}_\phi$, and $\mathbf{e}_z$). However, the near-field terms couple the radial and tangential components. Thus, there is no clear separation by component of SV and SH motion at small epicentral distances (r) or low frequencies (ω).

Following Kennett (1983), we introduce the tensor field

$$\mathbf{T}(\omega pr) = [\mathbf{R}(\omega pr), \mathbf{S}(\omega pr), \mathbf{T}(\omega pr)]^{\mathrm{T}}. \tag{2.3}$$

Also we define the displacement vector for the P-SV wave field at the surface (z=0)

$$\boldsymbol{w}_0 = [U,\ V,\ 0]^{\mathrm{T}}, \tag{2.4}$$

where $^{\mathrm{T}}$ denotes the transpose of the row vector. The SH waves at the free surface are similarly expressed as in terms of the transverse element $\boldsymbol{w}_{H0}$. We may rewrite the double integral (2.1) with respect to the slowness p and the surface displacement vector w_0^{T}, therefore the P-SV response may be recast as

$$\mathbf{u}_S(r,\phi,t) \;=\; \frac{1}{2\pi}\int_{-\infty}^{\infty} \mathrm{d}\omega \mathrm{e}^{-\mathrm{i}\omega t}\,\omega^2 \int_0^{\infty} \mathrm{d}p\; p \sum_m \boldsymbol{w}_0^{\mathrm{T}}(p,m,\omega)\mathbf{T}_m(\omega pr), \tag{2.5}$$

where

$$\boldsymbol{w}_0^{\mathrm{T}}(p,m,\omega)\mathbf{T}(\omega pr) = U(p,m,\omega)\mathbf{R}(\omega pr) + V(p,m,\omega)\mathbf{S}(\omega pr). \tag{2.6}$$

The SH wave field has a similar expression:

$$\mathbf{u}_H(r,\phi,t) \;=\; \frac{1}{2\pi}\int_{-\infty}^{\infty} \mathrm{d}\omega \mathrm{e}^{-\mathrm{i}\omega t}\,\omega^2 \int_0^{\infty} \mathrm{d}p\; p \sum_m w_{H0}^{\mathrm{T}}(p,m,\omega)\mathbf{T}_m(\omega pr), \tag{2.7}$$

where

$$\boldsymbol{w}_{H0}^{\mathrm{T}}(p,m,\omega)\mathbf{T}(\omega pr) = W(p,m,\omega)\mathbf{T}(\omega pr). \tag{2.8}$$

2.2.1 Coupled equations for seismic waves

As a result of the vector harmonic decomposition we have a representation of the displacement field for each azimuthal order m in terms of the variables

$$\mathbf{w} = [U,\ V,\ W]^{\mathrm{T}}$$

There is a corresponding decomposition of the z-component of the traction $\mathbf{t}_z$ as

$$\mathbf{t}_z = \omega[\,P,\ S,\ T]^{\mathrm{T}}$$

The displacement and stress quantities for isotropic media are related by

$$\begin{aligned}
\omega P &= \rho\alpha^2\partial_z U - \omega p\rho(\alpha^2 - 2\beta^2)V, \\
\omega S &= \rho\beta^2(\partial_z V + \omega p U), \\
\omega T &= \rho\beta^2\partial_z W,
\end{aligned} \tag{2.9}$$

in terms of the P and S wavespeeds α , β .

In terms of the displacement and stress quantities $U(p, m, z, \omega)$, $P(p, m, z, \omega)$ etc, the equation of motion and the stress-strain relations can be combined to give coupled sets of ordinary differential equations with respect to depth z. These transformed equations take a very convenient form if we work in terms of the horizontal slowness $p = k/\omega$, with units of reciprocal wavespeed, rather than the horizontal wavenumber k. Thus for P-SV waves we have

$$\frac{\partial}{\partial z}\begin{pmatrix} U \\ V \\ P \\ S \end{pmatrix} = \omega \begin{pmatrix} 0 & p[1-2(\beta^2/\alpha^2)] & [\rho\alpha^2]^{-1} & 0 \\ -p & 0 & 0 & [\rho\beta^2]^{-1} \\ -\rho & 0 & 0 & p \\ 0 & \rho[\nu p^2 - 1] & -p[1-2(\beta^2/\alpha^2)] & 0 \end{pmatrix} \begin{pmatrix} U \\ V \\ P \\ S \end{pmatrix}. \tag{2.10}$$

where $\nu = 4\beta^2[1 - (\beta^2/\alpha^2)]$.

and for SH waves

$$\frac{\partial}{\partial z}\begin{pmatrix} W \\ T \end{pmatrix} = \omega \begin{pmatrix} 0 & [\rho\beta^2]^{-1} \\ \rho[\beta^2 p^2 - 1] & 0 \end{pmatrix} \begin{pmatrix} W \\ T \end{pmatrix} \tag{2.11}$$

For an isotropic medium, or transverse isotropy with a vertical symmetry axis, the coefficients appearing in (2.10), (2.11) are independent of the azimuthal order m and the azimuthal dependence of $U(p, m, z, \omega)$ etc. will arise solely from the nature of any source. The elements of the coupling matrices involve only the elastic parameters at the depth z and not their vertical derivatives. Each of the sets of coupled equations (2.10) and (2.11) can be written in the form

$$\partial_z \mathbf{b}(p, m, z, \omega) = \omega \mathbf{A}(p, z)\mathbf{b}(p, m, z, \omega), \tag{2.12}$$

in terms of a column vector $\mathbf{b}$ whose entries are the displacement and stress quantities. For P-SV waves

$$\mathbf{b}_P(p, m, z, \omega) = [\,U,\, V,\, P,\, S\,]^T, \tag{2.13}$$

where ^{T} denotes the transpose of the row vector. For SH waves

$$\mathbf{b}_H(p, m, z, \omega) = [\,W,\, T\,]^T. \tag{2.14}$$

It is convenient to express a general displacement-traction vector $\mathbf{b}$ in the form

$$\mathbf{b}(p, m, z, \omega) = [\,\boldsymbol{w},\, \boldsymbol{t}\,]^T, \tag{2.15}$$

and then specialise, when appropriate, to the *P-SV* and *SH* systems.

The displacement $\mathbf{u}$ and traction $\mathbf{t}_z$ across any horizontal plane are required to be continuous, and the vector harmonic representation preserves these continuity properties, and thus the displacement-traction vector $\mathbf{b}$ will be continuous across any plane of discontinuity in material properties as well as all other planes $z = const.$

In the depth intervals where the elastic properties are continuous we may solve (2.12) to construct the displacement-traction vector $\mathbf{b}$, and then we are able to use the continuity of $\mathbf{b}$ to carry the solution across the level of any jump in the elastic parameters. The effect of a source can be introduced by a discontinuity in the displacement-traction vector.

2.2.2 Theory of surface waves

The displacement vectors (w and w_H) should satisfy the condition at the free surface, the radiation condition at some depth ($z \to \infty$) and the discontinuity at the source level (z_s).

We introduce sets of displacement-traction fields which satisfy just one of these boundary conditions and then we combine them at the source level to include a representation of the source. We introduce displacement-traction fields ($\boldsymbol{W}_{1s}, \boldsymbol{T}_{1s}$ and $\boldsymbol{W}_{2s}, \boldsymbol{T}_{2s}$) for the zones above and below the source level. These matrix displacement fields satisfy one of the free-surface and bottom boundary conditions.

(1) $\boldsymbol{W}_{1s}(z)$ - traction vanishes at the free surface,

(2) $\boldsymbol{W}_{2s}(z)$ - the radiation condition of only downward propagating or decaying evanescent waves in the underlying uniform medium.

For the zone above the source ($z < z_s$),

$$\begin{aligned} \boldsymbol{w}(z) &= \boldsymbol{W}_{1s}(z)\nu_1, \\ t(z) &= \boldsymbol{T}_{1s}(z)\nu_1, \end{aligned} \tag{2.16}$$

and the zone below the source ($z > z_s$)

$$\begin{aligned} \boldsymbol{w}(z) &= \boldsymbol{W}_{2s}(z)\nu_2, \\ t(z) &= \boldsymbol{T}_{2s}(z)\nu_2, \end{aligned} \tag{2.17}$$

where $\nu_{1,2}$ are constant vectors.

The effect of the source can be represented by discontinuities in the displacement (w) and traction (t) across the source plane ($z = z_s$)

$$\boldsymbol{S}_W^m(z_s) = \boldsymbol{w}(z_s+) - \boldsymbol{w}(z_s-), \tag{2.18}$$

$$\boldsymbol{S}_T^m(z_s) = t(z_s+) - t(z_s-). \tag{2.19}$$

These 'source jump' terms ($\boldsymbol{S}_W^m(z_s)$ and $\boldsymbol{S}_T^m(z_s)$) link the displacement (w) and traction (t) above and below the source and also relate them to the source itself, so that the two terms depend on the azimuthal order m.

Using the equations (2.16 - 2.19) and the invariant (Kennett 1983, chapter 2)

$$<\boldsymbol{W}_{1s}, \boldsymbol{W}_{1s}> = <\boldsymbol{W}_{2s}, \boldsymbol{W}_{2s}> = 0, \tag{2.20}$$

we can rewrite the displacements above and below the source level:

For the zone above the source ($z < z_s$)

$$\boldsymbol{w}(z) = \boldsymbol{W}_{1s}(z)<\boldsymbol{W}_{1s}, \boldsymbol{W}_{2s}>^{-\mathrm{T}}\{\boldsymbol{T}_{2s}^{\mathrm{T}}(z_s)\boldsymbol{S}_W^m - \boldsymbol{W}_{2s}^{\mathrm{T}}(z_s)\boldsymbol{S}_T^m\}, \tag{2.21}$$

and below the source level ($z > z_s$),

$$\boldsymbol{w}(z) = \boldsymbol{W}_{2s}(z)<\boldsymbol{W}_{1s}, \boldsymbol{W}_{2s}>^{-\mathrm{T}}\{\boldsymbol{T}_{1s}^{\mathrm{T}}(z_s)\boldsymbol{S}_W^m - \boldsymbol{W}_{1s}^{\mathrm{T}}(z_s)\boldsymbol{S}_T^m\}. \tag{2.22}$$

where $^{-\mathrm{T}}$ refers to the inverse of the transpose of the matrix. At the free surface (z=0), the displacement can be represented as

$$\boldsymbol{w}_0(p, m, \omega) = \boldsymbol{W}_{1s}(0)<\boldsymbol{W}_{1s}, \boldsymbol{W}_{2s}>^{-\mathrm{T}}\{\boldsymbol{T}_{2s}^{\mathrm{T}}(z_s)\boldsymbol{S}_W^m - \boldsymbol{W}_{2s}^{\mathrm{T}}(z_s)\boldsymbol{S}_T^m\}. \tag{2.23}$$

To include the influence of the free surface (z=0) and radiation conditions below the source level into the displacement (w_0), we introduce the displacement fields for the up-going and down-going waves ($\boldsymbol{W}_{US}$ and $\boldsymbol{W}_{DS}$) and the reflection responses ($\mathbf{R}_{\mathrm{U}}^{\mathrm{f}S}$ and $\mathbf{R}_{\mathrm{D}}^{SL}$). $\mathbf{R}_{\mathrm{U}}^{\mathrm{f}S}$ denotes the reflection response for the zone above the source including the influence of the surface and $\mathbf{R}_{\mathrm{D}}^{SL}$ represents the reflection response for down-going waves incident on the entire zone below the source.

The displacement-traction fields above the source level ($z < z_s$) can be expressed in the form

$$\begin{aligned} \boldsymbol{W}_{1s}(z) &= \boldsymbol{W}_{US}(z) + \boldsymbol{W}_{DS}(z)\mathbf{R}_{\mathrm{U}}^{\mathrm{f}S} \\ \boldsymbol{T}_{1s}(z) &= \boldsymbol{T}_{US}(z) + \boldsymbol{T}_{DS}(z)\mathbf{R}_{\mathrm{U}}^{\mathrm{f}S}. \end{aligned} \tag{2.24}$$

and the displacement-traction fields below the source level ($z > z_s$) can be written as

$$\begin{aligned} \boldsymbol{W}_{2s}(z) &= \boldsymbol{W}_{DS}(z) + \boldsymbol{W}_{US}(z)\mathbf{R}_{\mathrm{D}}^{SL} \\ \boldsymbol{T}_{2s}(z) &= \boldsymbol{T}_{DS}(z) + \boldsymbol{T}_{US}(z)\mathbf{R}_{\mathrm{D}}^{SL}. \end{aligned} \tag{2.25}$$

The displacement vector (w) satisfies (1) the free surface condition at z=0, (2) the discontinuities across the source level (z=z_s), and (3) the radiation condition ($z \to \infty$).

From the equations (2.24) and (2.25), the relation between the invariant $<\boldsymbol{W}_{1s}, \boldsymbol{W}_{2s}>$ and the reflection matrices takes the form

$$<\boldsymbol{W}_{1s}, \boldsymbol{W}_{2s}>^{-\mathrm{T}} = \mathrm{i}[\mathbf{I} - \mathbf{R}_{\mathrm{D}}^{SL}\mathbf{R}_{\mathrm{U}}^{\mathrm{f}S}]^{-1}, \tag{2.26}$$

so that we further rewrite the displacement at the free surface as

$$\boldsymbol{w}_0(p,m,\omega) = \mathrm{i}\boldsymbol{W}_{1s}(0)\,[\mathbf{I} - \mathbf{R}_{\mathrm{D}}^{SL}\mathbf{R}_{\mathrm{U}}^{\mathrm{f}S}]^{-1}\{\boldsymbol{T}_{2s}^{\mathrm{T}}(z_s)\boldsymbol{S}_W^m - \boldsymbol{W}_{2s}^{\mathrm{T}}(z_s)\boldsymbol{S}_T^m\}. \tag{2.27}$$

In order to have surface waves which can exist independent of a source, it is necessary for the displacement-traction fields to simultaneously satisfy the free surface and radiation conditions.

Therefore $\boldsymbol{W}_{1s}(z)$ satisfies

$$\begin{aligned} \boldsymbol{W}_{1s}(z) &= \boldsymbol{W}_{US}(z) + \boldsymbol{W}_{DS}(z)\mathbf{R}_{\mathrm{U}}^{\mathrm{f}S}\,, \\ \boldsymbol{T}_{1s}(0) &= \boldsymbol{T}_{US}(0) + \boldsymbol{T}_{DS}(0)\mathbf{R}_{\mathrm{U}}^{\mathrm{f}S} = 0\,. \end{aligned} \tag{2.28}$$

The radiation condition that requires no up-going wave is present below the source level, so that $\boldsymbol{W}_{2s}$ fulfills

$$\begin{aligned} \boldsymbol{W}_{2s}(z) &= \boldsymbol{W}_{DS}(z) + \boldsymbol{W}_{US}(z)\mathbf{R}_{\mathrm{D}}^{\mathrm{S}L}\,, \\ \boldsymbol{W}_{US}(z)\mathbf{R}_{\mathrm{D}}^{\mathrm{S}L} &= 0\,. \end{aligned} \tag{2.29}$$

Under the conditions of (2.28) and (2.29), the reflection matrices ($\mathbf{R}_{\mathrm{U}}^{\mathrm{f}S}$ and $\mathbf{R}_{\mathrm{D}}^{\mathrm{S}L}$) satisfy the relation

$$\det[\mathbf{I} - \mathbf{R}_{\mathrm{D}}^{SL}\mathbf{R}_{\mathrm{U}}^{\mathrm{f}S}] = 0\,. \tag{2.30}$$

Since w_0 contains $[\mathbf{I} - \mathbf{R}_{\mathrm{D}}^{SL}\mathbf{R}_{\mathrm{U}}^{\mathrm{f}S}]^{-1}$ in the equation (2.27), the displacement (w_0) has singularities in the form of poles in the complex ω - p plane at the combinations of slowness p_j and frequency ω such that both boundary conditions are satisfied.

2.2.3 Surface wave dispersion

Each individual surface wave mode is associated with a pole trajectory in the ω - p domain. The implicit relationship $p(\omega)$ describing the trajectory of this pole path describes the phase dispersion associated with the mode.

The various modes are indexed by a mode number which would represent their order in ω at fixed slowness p and for Love waves is also the number of zero-crossings in the eigen-displacement as a function of depth. For Rayleigh waves the mode number is usually the number of zero-crossings in the vertical component of the eigenfunction but the coupling between P-SV waves means that this association can be distorted, depending on the specific structure.

Because of the frequency dispersion of the slowness $p(\omega)$, the slowness at which energy propagates $g(\omega)$ differs from the phase slowness $p(\omega)$. A wave packet for a particular mode will travel with group slowness

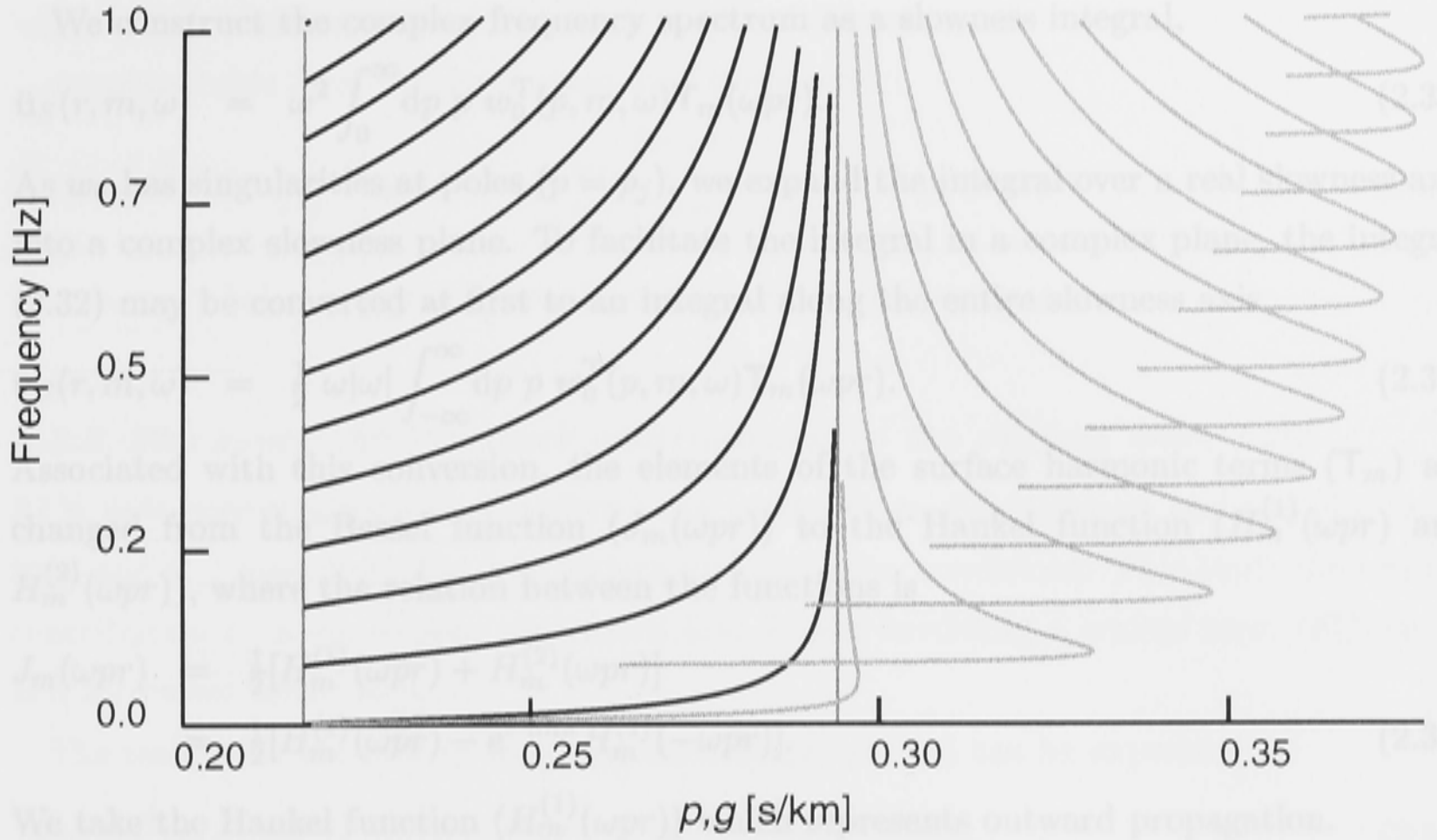

Fig. 2.1. Dispersion curves for phase slowness p and group slowness g (grey tone) for Love waves in a layer over a halfspace

$$g(\omega) = \frac{\partial}{\partial\omega}(\omega p) = p(\omega) + \omega\frac{\partial}{\partial\omega}p(\omega) \ . \tag{2.31}$$

The behaviour of the group and phase slownesses as a function of frequency for the first 12 modes of Love waves for a layer over a halfspace is illustrated in figure 2.1. At high frequencies group and phase slownesses both asymptote to the surface shear slowness β_0^{-1}. However the group slowness is usually greater than the slowness in the upper layer and the guided wave energy will therefore travel slower than the surface shear velocity. The main contribution from each mode will come from the frequency at which the group slowness is a maximum and this is known as the Airy phase for the mode.

2.3 The excitation of surface wave

2.3.1 The spectral method

In calculating the double integral (2.5), we can choose the order of integration over the frequency and the slowness. If we first integrate it in terms of slowness, the intermediate product is the complex frequency spectrum $\bar{\mathbf{u}}_S(r, m, \omega)$ at a particular location. This approach is called as the *spectral method*. On the other hand, when the frequency integral is performed first, the intermediate result is a time response for each slowness p. This approach is designated the *slowness method*. In this section, we employ the *spectral method* which is suitable for smoothly stratified media.

We construct the complex frequency spectrum as a slowness integral,

$$\bar{\mathbf{u}}_S(r,m,\omega) = \omega^2 \int_0^\infty \mathrm{d}p\; p\; \boldsymbol{w}_0^{\mathrm{T}}(p,m,\omega)\mathbf{T}_m(\omega p r). \tag{2.32}$$

As $\boldsymbol{w}_0$ has singularities at poles ($p = p_j$), we expand the integral over a real slowness axis into a complex slowness plane. To facilitate the integral in a complex plane, the integral (2.32) may be converted at first to an integral along the entire slowness axis

$$\bar{\mathbf{u}}_S(r,m,\omega) = \tfrac{1}{2}\,\omega|\omega| \int_{-\infty}^\infty \mathrm{d}p\; p\; \boldsymbol{w}_0^{\mathrm{T}}(p,m,\omega)\mathbf{T}_m(\omega p r). \tag{2.33}$$

Associated with this conversion, the elements of the surface harmonic terms ($\mathbf{T}_m$) are changed from the Bessel function ($J_m(\omega p r)$) to the Hankel function ($H_m^{(1)}(\omega p r)$ and $H_m^{(2)}(\omega p r)$), where the relation between the functions is

$$\begin{aligned} J_m(\omega p r) &= \tfrac{1}{2}[H_m^{(1)}(\omega p r) + H_m^{(2)}(\omega p r)] \\ &= \tfrac{1}{2}[H_m^{(1)}(\omega p r) - \mathrm{e}^{-\mathrm{i}m\pi} H_m^{(1)}(-\omega p r)]. \end{aligned} \tag{2.34}$$

We take the Hankel function ($H_m^{(1)}(\omega p r)$) which represents outward propagation.

Now the integration along the real slowness axis becomes

$$\bar{\mathbf{u}}_S(r,m,\omega) = \tfrac{1}{2}\,\omega|\omega| \int_{-\infty}^\infty \mathrm{d}p\; p\; \boldsymbol{w}_0^{\mathrm{T}}(p,m,\omega)\mathbf{T}_m^{(1)}(\omega p r). \tag{2.35}$$

The relation between the two functions (2.34) shows that (2.32) represents standing waves and (2.35) indicates the surface waves propagating outward.

The presence of poles on the real p axis is a major obstacle to the direct integration (2.35) along the slowness axis, so that we expand the integration into a complex slowness plane. If we modify the contour of integration in (2.35) into the upper half plane to D, the displacement spectrum consists of a sum of a contour integral and residue series

$$\begin{aligned} \bar{\mathbf{u}}_S(r,m,\omega) = {} & \tfrac{1}{2}\,\omega|\omega| \int_D \mathrm{d}p\; p\; \boldsymbol{w}_0^{\mathrm{T}}(p,m,\omega)\mathbf{T}_m^{(1)}(\omega p r) \\ & + \pi \mathrm{i}\omega^2 \left[\sum_{j=0}^{N(\omega)} p_j\, \mathrm{Res_j}[\boldsymbol{w}_0^{\mathrm{T}}(p,m,\omega)]\mathbf{T}_m^{(1)}(\omega p_j r) \right]. \end{aligned} \tag{2.36}$$

The contour integral in (2.36) comprises an integration along the real slowness axis from -∞ to β_L^{-1} and that along a line segment off into the first quadrant. This contour integral represents the frequency spectrum of body waves which do not satisfy the free-surface and bottom boundary conditions. Therefore we can neglect this contour integral in the surface wave expressions.

Consequently, the modal contribution to the surface displacement for Rayleigh waves can be represented as

$$\mathbf{u}_S(r,\phi,t) = \tfrac{1}{2} \int_{-\infty}^\infty \mathrm{d}\omega \mathrm{e}^{-\mathrm{i}\omega t}\; \mathrm{i}\omega^2 \sum_m \left[\sum_{j=0}^{N(\omega)} p_j \operatorname*{Res}_{\omega, p=p_j} [\boldsymbol{w}_0^{\mathrm{T}}(p,m,\omega)]\mathbf{T}_m^{(1)}(\omega p_j r) \right]. \tag{2.37}$$

where $N(\omega)$ is the number of Rayleigh modes at frequency ω.

A comparable form can be derived for Love waves

$$\mathbf{u}_H(r,\phi,t) \;=\; \tfrac{1}{2}\int_{-\infty}^{\infty} \mathrm{d}\omega \mathrm{e}^{-\mathrm{i}\omega t}\, \mathrm{i}\omega^2 \sum_m \left[\sum_{l=0}^{M(\omega)} p_l \operatorname*{Res}_{\omega,p=p_l} [W_0(p,m,\omega)] \mathbf{T}_m^{(1)}(\omega p_l r) \right], \tag{2.38}$$

where, now, $M(\omega)$ is the number of Love modes at frequency ω.

2.3.2 The source and receiver contributions to the surface wave field

At a pole corresponding to a surface-wave mode, eigen-displacement and traction fields (w_{ej} and t_{ej}) meet both the free surface and radiation conditions. This leads the residue contribution to a convenient separation into a part involving a source term ($\mathcal{S}^m_{\mathrm{R,L}}(p_j)$), and a receiver term ($\boldsymbol{\mathcal{R}}(p_j)$).

The residue at the pole ($p = p_j$), at fixed frequency (ω) can be expressed as

$$\operatorname*{Res}_{\omega,p=p_j} [\boldsymbol{w}_0^{\mathrm{T}}(p,m,\omega)] = \frac{g_j}{2\omega I_j} \boldsymbol{w}_{ej}(0) [\boldsymbol{t}_{ej}^{\mathrm{T}}(z_s) \boldsymbol{S}_W^m \;-\; \boldsymbol{w}_{ej}^{\mathrm{T}}(z_s) \boldsymbol{S}_T^m] \;, \tag{2.39}$$

where g_j is the group slowness for the particular mode, and I_j is related to the kinetic energy content in the eigen-field

$$I_j = \int_0^{\infty} \mathrm{d}z\, \rho\, \boldsymbol{w}_{ej}^{\mathrm{T}} \boldsymbol{w}_{ej} \;. \tag{2.40}$$

Similarly the residue for SH waves is

$$\operatorname*{Res}_{\omega,p=p_l} [\boldsymbol{w}_{H0}^{\mathrm{T}}(p,m,\omega)] = \frac{g_l}{2\omega I_l} \boldsymbol{W}_{el}(0) [\boldsymbol{T}_{el}^{\mathrm{T}}(z_s) \boldsymbol{S}_W^m \;-\; \boldsymbol{W}_{el}^{\mathrm{T}}(z_s) \boldsymbol{S}_T^m] \;, \tag{2.41}$$

where

$$I_l = \int_0^{\infty} \mathrm{d}z\, \rho\, \boldsymbol{W}_{el}^{\mathrm{T}} \boldsymbol{W}_{el} \;. \tag{2.42}$$

The expressions for the residues [(2.39) and (2.41)] are convenient for linking the excitation of the azimuthal order m to moment tensor components through the source jumps.

It is also apparent that the source contribution ($[\boldsymbol{t}_{ej}^{\mathrm{T}}(z_s) \boldsymbol{S}_W^m \;-\; \boldsymbol{w}_{ej}^{\mathrm{T}}(z_s) \boldsymbol{S}_T^m]$) depends on the eigenfunction at the source depth. Furthermore, the source contribution for the P-SV waves is

$$\boldsymbol{\mathcal{S}}^m_{\mathrm{R}}(p_j) = [\boldsymbol{t}_{ej}^{\mathrm{T}}(z_s) \boldsymbol{S}_W^m \;-\; \boldsymbol{w}_{ej}^{\mathrm{T}}(z_s) \boldsymbol{S}_T^m] = -\mathrm{i}[\boldsymbol{\Sigma}^m_{\mathrm{U}}(z_s) + \mathbf{R}^{SL}_{\mathrm{D}} \boldsymbol{\Sigma}^m_{\mathrm{D}}(z_s)] \;, \tag{2.43}$$

where $\boldsymbol{\Sigma}^m_{\mathrm{U}}(z_s)$ is the up-going wave vectors from the source in angular order m and $\boldsymbol{\Sigma}^m_{\mathrm{D}}(z_s)$ is the corresponding down-going radiation. Since (2.43) includes $\mathbf{R}^{SL}_{\mathrm{D}}$ which indicates the processes of reflection from beneath the source level, the source contribution is not localized at the source itself, but will involve the full propagation path. The receiver contribution can be expressed as the eigenfunction at the receiver depth ($\boldsymbol{w}_{ej}(0)$). The

receiver contribution for the P-SV waves includes the processes of transmission from the source level to the surface

$$\boldsymbol{\mathcal{R}}(p_j) = \boldsymbol{w}_{ej}(0) = w^{\mathrm{f}}[\mathbf{I} - \mathbf{R}_{\mathrm{D}}^{0S}\mathbf{R}^{\mathrm{f}}]^{-1}\mathbf{T}_{\mathrm{U}}^{0S} \ , \tag{2.44}$$

where w^{f} is the amplification of displacement due to interaction with the free surface and the instrument response. $\mathbf{R}^{\mathrm{f}}$ is the free-surface reflection matrix. The reflection and transmission terms $\mathbf{R}_{\mathrm{D}}^{0S}$, $\mathbf{T}_{\mathrm{U}}^{0S}$ involve the region between the source and the surface.

Because of (2.37) and (2.39), the surface displacement for P-SV waves is described as

$$\mathbf{u}_S(r,\phi,t) = \int_{-\infty}^{\infty} \mathrm{d}\omega \mathrm{e}^{-\mathrm{i}\omega t} \mathrm{i}\omega \sum_m \left[\sum_{j=0}^{N(\omega)} \frac{p_j g_j}{4I_j} [t_{ej}^{\mathrm{T}}(z_s)\boldsymbol{S}_W^m - \boldsymbol{w}_{ej}^{\mathrm{T}}(z_s)\boldsymbol{S}_T^m]\boldsymbol{w}_{ej}(0)\mathbf{T}_m^{(1)}(\omega p_j r) \right] . \tag{2.45}$$

Also the displacement for the SH waves is

$$\mathbf{u}_H(r,\phi,t) = \int_{-\infty}^{\infty} \mathrm{d}\omega \mathrm{e}^{-\mathrm{i}\omega t} \mathrm{i}\omega \sum_m \left[\sum_{l=0}^{M(\omega)} \frac{p_l g_l}{4I_l} [\boldsymbol{T}_{el}^{\mathrm{T}}(z_s)\boldsymbol{S}_W^m - \boldsymbol{W}_{el}^{\mathrm{T}}(z_s)\boldsymbol{S}_T^m]\boldsymbol{W}_{el}(0)\mathbf{T}_m^{(1)}(\omega p_l r) \right] . \tag{2.46}$$

For large epicentral distances or high frequencies, we may replace the Hankel function $(H_m^{(1)}(\omega pr))$ in $\mathbf{T}_m^{(1)}$ with its asymptotic form

$$H_m^{(1)}(\omega pr) \sim \left(\frac{2}{\pi\omega p_j r} \right)^{1/2} \exp[\,\mathrm{i}\omega p_j r - \mathrm{i}(2m+1)\pi/4] \ . \tag{2.47}$$

Kennett (1983) suggests that if the frequency band and the propagation path are such that $\omega_{min}\ p\ r_{min} > 6$, the asymptotic form is applicable to the tensor field $\mathbf{T}_m^{(1)}$. This lower limit for values of ωpr results from the nature of the Hankel function. Fine sampling in frequency (large ω) is required to accurately represent the rapidly oscillating Hankel function at large distance (large values of r).

The tensor field for Rayleigh (P-SV) waves becomes

$$\mathbf{T}_m^{(1)}(\omega p_j r) \sim [\mathbf{e}_z, \mathrm{i}\mathbf{e}_r]^{\mathrm{T}} \left(\frac{2}{\pi\omega p_j r} \right)^{1/2} \exp[\,\mathrm{i}\omega p_j r - \mathrm{i}(2m+1)\pi/4]. \tag{2.48}$$

The comparable form for Love (SH) waves is

$$\mathbf{T}_m^{(1)}(\omega p_l r) \sim -\mathrm{i}\mathbf{e}_\phi \left(\frac{2}{\pi\omega p_l r} \right)^{1/2} \exp[\,\mathrm{i}\omega p_l r - \mathrm{i}(2m+1)\pi/4]. \tag{2.49}$$

In this approximation, the near-field terms depending on ωpr disappear, so the tensor field for Love waves lies on the local transverse direction to the path.

Consequently under the condition of $(\omega_{min}\ p\ r_{min} > 6)$, we can use the asymptotic approximations (2.48) and (2.49) to the representations of the surface-wave fields.

For Rayleigh waves,

$$\mathbf{u}_S(r,\phi,t) = \begin{pmatrix} \mathbf{e}_z \\ \mathrm{i}\mathbf{e}_r \end{pmatrix} \sum_m \int_{-\infty}^{\infty} \mathrm{d}\omega \; \mathrm{i} \sum_{j=0}^{N(\omega)} \sqrt{\frac{2\omega p_j}{\pi r}} \frac{g_j}{4I_{\mathrm{R}j}} \mathcal{S}_{\mathrm{R}}^m(p_j)\, \mathcal{R}_{\mathrm{R}}(p_j)\, \mathrm{e}^{[\,\mathrm{i}\omega(p_j r - t) - \mathrm{i}(2m+1)\pi/4]}. \tag{2.50}$$

The equivalent representation for Love waves is

$$\mathbf{u}_H(r,\phi,t) = \mathbf{e}_\phi \sum_m \int_{-\infty}^{\infty} \mathrm{d}\omega \sum_{l=0}^{M(\omega)} \sqrt{\frac{2\omega p_l}{\pi r}} \frac{g_l}{4I_{\mathrm{L}l}} \mathcal{S}_{\mathrm{L}}^m(p_l)\, \mathcal{R}_{\mathrm{L}}(p_l)\, \mathrm{e}^{[\,\mathrm{i}\omega(p_l r - t) - \mathrm{i}(2m+1)\pi/4]}. \tag{2.51}$$

In a completely homogeneous medium, the source term can be represented by the combination of the displacement and traction eigen vectors at the source depth ($w_{ej}(z_s)$ and $t_{ej}(z_s)$) and the source jumps ($S_W^m(z_s)$ and $S_T^m(z_s)$). The source excitation is taken in the surface-wave field as the form of moment tensor elements through the source jump terms. Because it includes the reflection matrix ($\mathbf{R}_{\mathrm{D}}^{SL}$), the source term is influenced from the full propagation path.

The receiver term comes from the displacement eigen vectors at the receiver depth ($w_{ej}(0)$). This term has non-localized property because it involves the reflection and transmission terms which include the region between the source and the receiver. The instrumental response is involved through this term.

The horizontal propagation term plays a major role in the phase changes of the surface-wave field. However, the source and receiver terms have some influence on to the phase contribution through their reflection matrices.

2.3.3 Calculation of far-field seismograms

Nolet (1987) has provided explicit expressions for synthetic far-field seismograms of surface waves for use with the Partitioned Waveform Inversion method including the radiation characteristics of the source. In spherical coordinates (r,θ,ϕ) including the quality factor Q we can write the frequency domain representation of a Rayleigh wave seismogram as :

$$\mathbf{u}_S(\mathbf{p},\mathbf{r},\omega) = -\frac{1}{(2\sqrt{\sin\theta})} \begin{pmatrix} \mathbf{e}_r \\ \mathrm{i}\mathbf{e}_\theta \end{pmatrix} \sum_j \begin{pmatrix} U_j(r) \\ \omega p_j V_j(r) \end{pmatrix} g_j(\omega) A_j^R(\phi)\, \mathrm{e}^{[\,\mathrm{i}\omega p_j \theta - \omega\theta/(2Q_j g_j(\omega))]}, \tag{2.52}$$

where j is the mode index, and ωp_j is the wave number. U is the vertical and V the radial eigenfunction at the receiver. The amplitude factor A^R depends on the source mechanism.

For Love waves,

$$\mathbf{u}_H(\mathbf{p},\mathbf{r},\omega) \;=\; \frac{1}{(2\sqrt{\sin\theta})}\,\mathrm{i}\mathbf{e}_\phi \sum_l \omega p_l W_l(r) g_l(\omega)\, A_l^L(\phi)\, \mathrm{e}^{[\,\mathrm{i}\omega p_l\theta - \omega\theta/(2Q_l g_l(\omega))]}, \tag{2.53}$$

with mode index l and transverse eigenfunction W. The amplitude factor A^L again depends on the source mechanism. In the above equations, the receiver terms $\mathcal{R}$ involve of the eigenfunctions (U, V, W) and the source terms $\mathcal{S}$ are included in the amplitude factors $A^{R,L}(\phi)$.

The amplitude of the surface waves is linearly related to the components M_i of the moment tensor; and so we can write

$$\begin{aligned} A_j^R(\phi) &= (\omega p_j/2\pi)^{1/2} \sum_{k=0}^{6} B_{kj}^R M_k, \\ A_l^L(\phi) &= (\omega p_j/2\pi)^{1/2} \sum_{k=0}^{6} B_{kl}^L M_k, \end{aligned} \tag{2.54}$$

with the convention :

$$\begin{aligned} &M_1 = M_{rr}, \quad M_2 = M_{r\theta}, \quad M_3 = M_{r\phi}, \\ &M_4 = M_{\theta\theta}, \quad M_5 = M_{\phi\phi}, \quad M_6 = M_{\theta\phi}. \end{aligned} \tag{2.55}$$

The azimuthal terms take the form, for Rayleigh waves,

$$\begin{aligned} B_1^R &= \partial_r U_s \cdot \mathrm{e}^{-\mathrm{i}\pi/4} \\ B_2^R &= -\omega p_j[\partial_r V_s + r_s^{-1}(U_s - V_s)]\cos\zeta_s \cdot \mathrm{e}^{-\mathrm{i}\pi/4} \\ B_3^R &= -\omega p_j[\partial_r V_s + r_s^{-1}(U_s - V_s)]\sin\zeta_s \cdot \mathrm{e}^{-\mathrm{i}\pi/4} \\ B_4^R &= \frac{1}{2}\cdot r_s^{-1}[2U_s - (\omega p_j)^2 V_s]\cdot \mathrm{e}^{-\mathrm{i}\pi/4} - \frac{1}{2}\cdot(\omega p_j)^2 r_s^{-1} V_s \cos 2\zeta_s \cdot \mathrm{e}^{-\mathrm{i}\pi/4} \\ B_5^R &= \frac{1}{2}\cdot r_s^{-1}[2U_s - (\omega p_j)^2 V_s]\cdot \mathrm{e}^{-\mathrm{i}\pi/4} + \frac{1}{2}\cdot(\omega p_j)^2 r_s^{-1} V_s \cos 2\zeta_s \cdot \mathrm{e}^{-\mathrm{i}\pi/4} \\ B_6^R &= -(\omega p_j)^2 r_s^{-1} V_s \sin 2\zeta_s \cdot \mathrm{e}^{-\mathrm{i}\pi/4}, \end{aligned} \tag{2.56}$$

and for Love waves

$$\begin{aligned} B_1^L &= 0 \\ B_2^L &= -\omega p_j[\partial_r W_s + r_s^{-1} W_s]\sin\zeta_s \cdot \mathrm{e}^{-\mathrm{i}\pi/4} \\ B_3^L &= -\omega p_j[\partial_r W_s + r_s^{-1} W_s]\cos\zeta_s \cdot \mathrm{e}^{-\mathrm{i}\pi/4} \\ B_4^L &= -\frac{1}{2}\cdot(\omega p_j)^2 r_s^{-1} W_s \sin 2\zeta_s \cdot \mathrm{e}^{-\mathrm{i}\pi/4} \\ B_5^L &= -B_4^L \\ B_6^L &= (\omega p_j)^2 r_s^{-1} W_s \cos 2\zeta_s \cdot \mathrm{e}^{-\mathrm{i}\pi/4}, \end{aligned} \tag{2.57}$$

where the subscript s denotes the source and ζ_s denotes the source-to-station azimuth.

Through the coefficients $(B_{kj}^{R,L})$, the two equations can express the surface wave radiation from a point source for which angular order is restricted to less than the second degree.

2.4 Extension to a laterally heterogeneous medium

For a stratified medium there is no horizontal variation in seismic properties and the propagation path will automatically lie along the great-circle between source and receiver. For a more realistic medium we have to account for the presence of three-dimensional variations in seismic properties and therefore need to know to what extent we can rely on the results of calculations for stratified media for interpretation and waveform inversion.

Woodhouse (1974) has considered the case of surface wave propagation with a smoothly varying medium where the seismic parameters depend weakly on the horizontal coordinates. He demonstrated that the propagation characteristics are governed by the vertical structure beneath each point on the propagation path. The path followed by a particular mode is governed by the variations in phase slowness for that mode and the incremental phase $\phi_j(\omega)$ along the path is simply the integral of the phase slowness

$$\phi_j(\omega) = \omega \int_{path} \mathbf{p}_j . \mathrm{d}\mathbf{r}, \tag{2.58}$$

where $\mathbf{p}_j$ is the horizontal slowness vector for the mode and $\mathrm{d}\mathbf{r}$ is an element along the path. This style of phase representation is dependent on a far-field approximation and so for a propagation range r, we require the combination $\omega p_j r \gg 1$.

When the structure changes slowly horizontally the expressions for a stratified medium can be adapted to the laterally varying case by making a three stage approximation. The modal field is considered to be established in a stratified structure with the properties at the source. The modes are then assumed to propagate independently from source to receiver. Finally the modal fields at the receiver are used to construct the displacement using the receiver structure.

When the propagation paths for all the significant modes do not deviate significantly from a great circle, the phase terms can be simplified by working in terms of the averaged structure which produces the same incremental phase. At range r, we define the phase slowness for the averaged structure p_j^{av} from

$$\omega p_j^{av} r = \phi_j(\omega) = \omega \int_{path} \mathbf{p}_j . \mathrm{d}\mathbf{r}. \tag{2.59}$$

We can then generate an approximation to the surface wave part of the wavefield which is a close analogue to the forms for a stratified medium (2.50).

Thus, for Rayleigh waves (Kennett, 1995)

$$\mathbf{u}_S(r,\phi,t) = \begin{pmatrix} \mathrm{i}\mathbf{e}_z \\ -\mathbf{e}_r \end{pmatrix} \sum_m \mathrm{e}^{\mathrm{i}m\phi} \int_{-\infty}^{\infty} \mathrm{d}\omega \sum_{j=0}^{N(\omega)} \sqrt{\frac{2\omega p_j^{av}}{\pi r}} \frac{g_j^{av}}{4I_{\mathrm{R}j}} \mathcal{S}_{\mathrm{R}}^m(p_j^s)\, \mathcal{R}_{\mathrm{R}}(p_j^r)\, \mathrm{e}^{[\,\mathrm{i}\omega(p_j^{av}r - t) - \mathrm{i}(2m+1)\pi/4]}. \quad (2.60)$$

where the source, receiver and path contributions are evaluated in different structures, as indicated by the superscripts for the relevant slownesses. A comparable expansion holds for Love waves.

This representation of the wavefield is based on a model of non-interacting normal modes, and as pointed out by Kennett (1995) some care needs to be taken if different stratified structures are employed for the source, path and receiver components. This difficulty arises because the "source" and "receiver" terms are not in fact just local in their action. Too large a difference between the structures will invalidate the approximation (2.60).

As the level of heterogeneity in the medium becomes larger the assumption of independent propagation of the modal components from source to receiver will no longer be valid. The full representation of propagation through heterogeneous media has been made by Kennett (1984) for the 2-D case with a subsequent extension to 3-D media (Kennett, 1998). The effects of the heterogeneity are introduced by introducing spatial varying coupling between the weighting coefficients of the modal branches (and for 3-D the directions of propagation). The strength of the coupling depends on both the wavelength of the surface waves and the nature of the structure. Kennett & Nolet (1990) have looked at the influence of 2-D heterogeneity in the mantle and demonstrated that the coupling effects of heterogeneity are not too severe for frequencies less than 0.05 Hz. Approximations such as (2.60) can therefore be used to about 0.03 Hz provided that there no abrupt changes in the character of heterogeneity.

3

SURFACE WAVE INVERSION

3.1 Introduction

Since the early part of the 20th century, the study of surface waves has been developed to understand the structure of the Earth. From an early stage, research into surface wave dispersion has contributed to understanding the 3-D structure of the Earth with limited lateral and vertical resolutions. In the past 20 years, the exploitation of surface waveform information has provided another contribution to delineating Earth structure, and has been reviewed by Snieder (1993) and Nolet (1987).

Recent developments in surface wave observations and computer-related technologies have further improved 3-D images of the Earth. The world-wide deployment of digital long-period and broadband seismometers, such as IDA, GDSN, and GEOSCOPE, provides an accessible source of high quality surface waveform data. These waveform data have been exploited by many authors who have proposed different inversion methods and generated different global Earth models (see eg. Dziewonski and Steim 1982; Woodhouse & Dziewonski, 1984; Tanimoto, 1990; Su & Dziewonski, 1991; Su et al., 1994). The improvements in world-wide broadband observations have also contributed to the construction of several reference Earth models such as *PREM* (Dziewonski & Anderson, 1981), *iasp91* (Kennett & Engdahl, 1991) and *ak135* (Kennett et al., 1995). These improved spherical reference models help to further the progress of improved resolution in 3-D Earth models. Also improvements in supercomputers and related technologies such as parallel computing techniques have provided major support to constructing 3-D images of the Earth. In surface wave analysis, it is crucial to develop accurate and efficient methods for calculating synthetic seismograms (Hara et al., 1993; Kennett, 1995). Moreover we have to be able to evaluate the accuracy and efficiency of surface waveform inversion methods (Snieder et al., 1991; Um et al., 1992; Li & Tanimoto, 1993; Li & Romanowicz 1995;

Geller & Takeuchi, 1995). The development of the appropriate synthetic methods and the consequent detailed evaluations of 3-D structure requires intensive use of computing power and efficient computing algorithms.

Due to the improvements in surface wave measurements and analysis techniques, two major approaches have been developed to extract the 3-D structure of the Earth. The first approach exploits information on surface wave dispersion which represents the frequency dependence of the group or phase velocity; the second approach extracts information from surface waveforms which are primarily controlled by the phase velocity distribution.

3.1.1 Dispersion information

The traveltime analysis of surface waves provides two sources of information on the wavespeed structure beneath travelling paths. One is group velocity dispersion which represents the relation between the velocity of energy transportation and its frequency content (Ritzwoller & Levshin, 1998). The other source is phase velocity dispersion which relates the phase changes to its frequencies (Nataf et al., 1986). Although two different sources of dispersion information exist, the ways of constructing a 3-D shear wavespeed structure from the two different sources are quite similar. Both ways have two distinct stages. The first stage is to produce 2-D phase or group velocity maps at each wave period and the second stage is to invert the perturbations of phase or group wavespeeds from the reference model into a 3-D model using phase or group sensitivity kernels for each wave period. For example, Nataf et al. (1986) investigate lateral heterogeneity in the upper mantle over the globe by inverting phase dispersion curves of long-period surface waves (100 - 330 seconds), while Ritzwoller & Levshin (1998) use a similar inversion scheme but apply it to the group dispersion curves for 20 - 200 second surface waves. Ritzwoller & Levshin (1998) retrieve the group dispersion maps over Eurasia with significantly high resolution, which later leads to the construction of a 3-D shear wavespeed model over the Eurasian region.

Ritzwoller & Levshin (1998) summarise three major differences between study of phase velocity dispersion and that of group velocity dispersion. First, the use of group velocity dispersion enables one to analyse seismic signals from small events for which no moment tensor has been estimated, because measurements of group velocities are much less sensitive to source mechanism than those of phase velocities. This is because group velocities are estimated in measuring the arrival times of the maximum wave packet amplitudes rather than the constituent phases. Second, studies of group velocity dispersion should provide a better way to resolve crustal structure from uppermost mantle structure, because group velocity sensitivity kernels, which are later used in constructing a 3-D model,

are compressed closer to the surface than the corresponding phase velocity kernels. Third, their study of the group velocity dispersion displays maps of polarisation anisotropy, while recent phase velocity studies demonstrate shear velocity maps with azimuthal anisotropy.

There are several benefits of dispersion studies compared with waveform inversion. First, measurements of phase or group arrival times is technically simpler than any waveform inversion with the calculation of synthetic seismograms at each iteration. Second, we do not have to use moment tensor information for determining group dispersion curves, therefore, we can use more events for dispersion analyses than waveform studies. Third, the increased number of usable events enhances the spatial resolution of the 2-D dispersion maps. Ritzwoller & Levshin (1998) achieve average resolutions across Eurasia from 5 to 7.5 degrees.

We also have to point out one major shortcoming of dispersion studies. That is, dispersion studies can normally exploit only fundamental mode information, because it is quite difficult to identify the group and/or phase arrival times of higher mode waves. However, higher mode waves carry information on both finer and deeper structures of the shear wavespeed, so that dispersion studies could not achieve the resolution of the crust and upper mantle that can be attained with full-mode waveform inversion method can obtain.

3.1.2 Waveform information

The use of phase or group arrival time information exploits only a small part of the rich information content of a seismogram. The matching of observed seismic waveforms with computations for a three-dimensional model gives the potential for gaining more information abut the Earth, particularly for S velocity. Such waveform inversion has become increasingly important in recent years.

The approach to waveform inversion generally takes the following stages (Hara et al., 1993):

(1) Choose a suitable reference model;
(2) Compute synthetic seismograms from the reference model;
(3) Compare synthetics with observed seismograms, and obtain residuals;
(4) Invert the residuals to determine perturbations to the initial model;
(5) Update the model with the perturbations;
(6) Repeat (2) - (5) until the residuals converge.

The difference between the variants of waveform inversion lies mainly in the way the synthetic seismograms are generated and compared with observations in steps (2) and (3).

Also the discretization of the three dimensional velocity structure varies between different groups of waveform inversions.

We can recognize three principal advantages of waveform inversion. First, we can extract information on phases and amplitudes of both body waves and surface waves, although only few researchers (Woodhouse & Wong, 1986; Hara et al., 1993) have currently exploited amplitude information. Second, we have better resolution in the upper mantle, in particular above 300 km depth, than from delaytime tomography, because we can exploit surface wave data whose energy is concentrated near the surface. Third, we can analyse phases (eg. SS and SSS) whose arrivals are difficult to pick as well as higher order S multiples which interfere to produce a complex wave train. Zielhuis & van der Hilst (1996) made use of multiple S phases to delineate the transition zone beneath the Australasian region.

Waveform inversion offers considerable promise for understanding the internal structure of the earth but at present does suffer from some disadvantages. First, waveform inversion has not yet achieved better lateral resolution than the most successful delaytime tomography. The reason is that we require high-quality and complete waveform data for a large number of paths crossing the region of interest; however, there are far fewer digital long-period and broadband seismometers to cover the Earth surface than short-period sensors. One of the highest resolution studies of a region using waveform inversion (Zielhuis & van der Hilst, 1996) reached about 200 km lateral resolution, while Widiyantoro & van der Hilst (1996) are able to resolve the velocity anomalies of one-degree (111 km) size for parts of Indonesia using delaytime tomography. Second, the synthesis of seismograms for complex structures requires intensive computer power. Although efficient calculation schemes are being developed, there are still only a few fully three-dimensional synthetic methods available (eg. Hara et al., 1993; Cummins et al 1996). Third, almost all work on waveform inversion assumes that seismic waves propagate in laterally smoothly varying media. Therefore, the effects of the off-great-circle propagation and of multi-path propagation are ignored. Few authors have considered possible effects of focusing-defocusing (Hara et al., 1993). Mode coupling appears in strong lateral heterogeneity (Kennett, 1984; Marquering & Snieder, 1995) but also not usually considered in synthesizing seismograms. In fact, the normal assumption used in waveform inversion for surface waves is that the scale of heterogeneity is such that for the frequency range of interest, modes propagate independently. Coupling between modes is to be expected for strong heterogeneity (Kennett, 1984) and is particularly important for synthesizing S body wave pulses from higher modes (Marquering & Snieder, 1995). The

computational cost of including mode-coupling is large and Marquering & Snieder (1995) resort to simplified approximations in their implementation.

3.1.3 3-D model construction

Depending on which information we choose out of the above two sources, namely, dispersion or waveform, we have two different ways of constructing a regional 3-D shear wavespeed model. One way is based on the dispersion information. We first retrieve a phase or group dispersion curve for each station-epicentre pair and combine all the curves to obtain 2-D phase or group velocity maps for each wave period. Next, we invert the perturbations of phase or group wavespeed into those of the shear wavespeed at a geographical point using a given sensitivity kernel at each wave period (e.g. Nataf et al. (1986) and Ritzwoller & Levshin (1998)). Finally all the vertical profiles of the shear wavespeed are merged into a 3-D model.

Another way is based on the waveform information. Both partitioned waveform inversion method (Nolet,1990) and waveform inversion with cross-correlations (Cara & Lévêque, 1987) have two stages for deriving a regional 3-D structure from the waveform information. The first stage is to gain a path dependent 1-D model of the shear wavespeed beneath each ray path with non-linear inversion schemes. Second the suite of all the 1-D models are inverted into a 3-D model over the path coveraged area.

3.2 Frequency-time analysis (FTAN)

Frequency-time analysis (FTAN) method is based on both moving window analysis (Dziewonski et al.,1969) and phase-matched filtering techniques (Dziewonski et al.,1972; Herrin & Goforth, 1977). Its theoretical basis and applications to digital seismograms are described by Levshin et al. (1972) and Levshin et al. (1992). This method aims to produce a group velocity dispersion curve by applying time-variable and phase matched floating filters to broad-band digital recording seismograms. The procedure of FTAN method is first to produce amplitude energy diagram in time-frequency plane from an observed seismogram and trace the highest ridges in the diagram as preliminary estimation of the group velocity arrivals of the fundamental mode surface waves (figure 3.1). Second, the floating filters are designed with phase equalisation technique and then applied over the ridges in the diagram to enhance the signal-to-noise ratio of the fundamental mode group arrivals. Third, the interpolation of the enhanced highest peaks in the energy diagram draws the filtered group velocity dispersion curve.

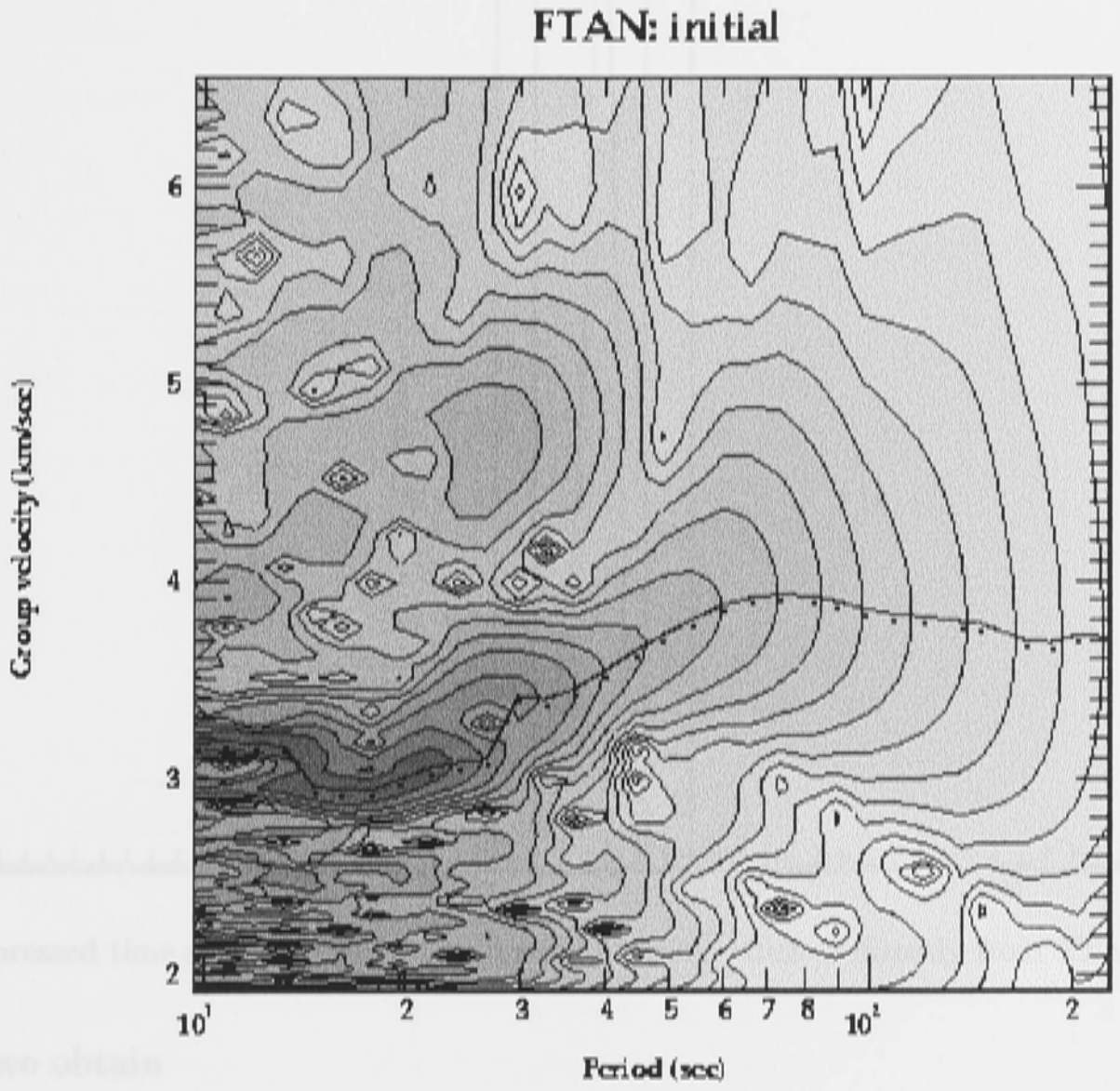

Fig. 3.1. FTAN diagram for the original signal which is directly from FTAN output.

3.2.1 The amplitude energy diagram in the frequency-time domain

We define the seismogram $f(t)$ and its Hilbert transform $g(t)$ after removing the instrument response from the observed seismogram. Fourier Transform $F(\omega)$ is given by

$$F(\omega) = \int_{-\infty}^{\infty} f(t)e^{i\omega t}dt \ . \tag{3.1}$$

Next, a set of multiple narrow-band Gaussian filters $(H(\omega, \omega_n))$,

$$H(\omega, \omega_n) = \exp\left[-\alpha_n \cdot \left(\frac{\omega - \omega_n}{\omega_n}\right)^2\right] , \tag{3.2}$$

is applied to the spectrum $F(\omega)$, where ω_n and α_n govern the central frequency and relative width of the n-th Gaussian filter. We then make the inverse Fourier transform to the filtered spectrum $F_n(\omega) = H(\omega, \omega_n) \cdot F(\omega)$ and obtain the filtered time signal $f_n(t)$ as

$$f_n(t) = \frac{1}{2\pi}\int_{-\infty}^{\infty} F_n(\omega)e^{-i\omega t}d\omega \ . \tag{3.3}$$

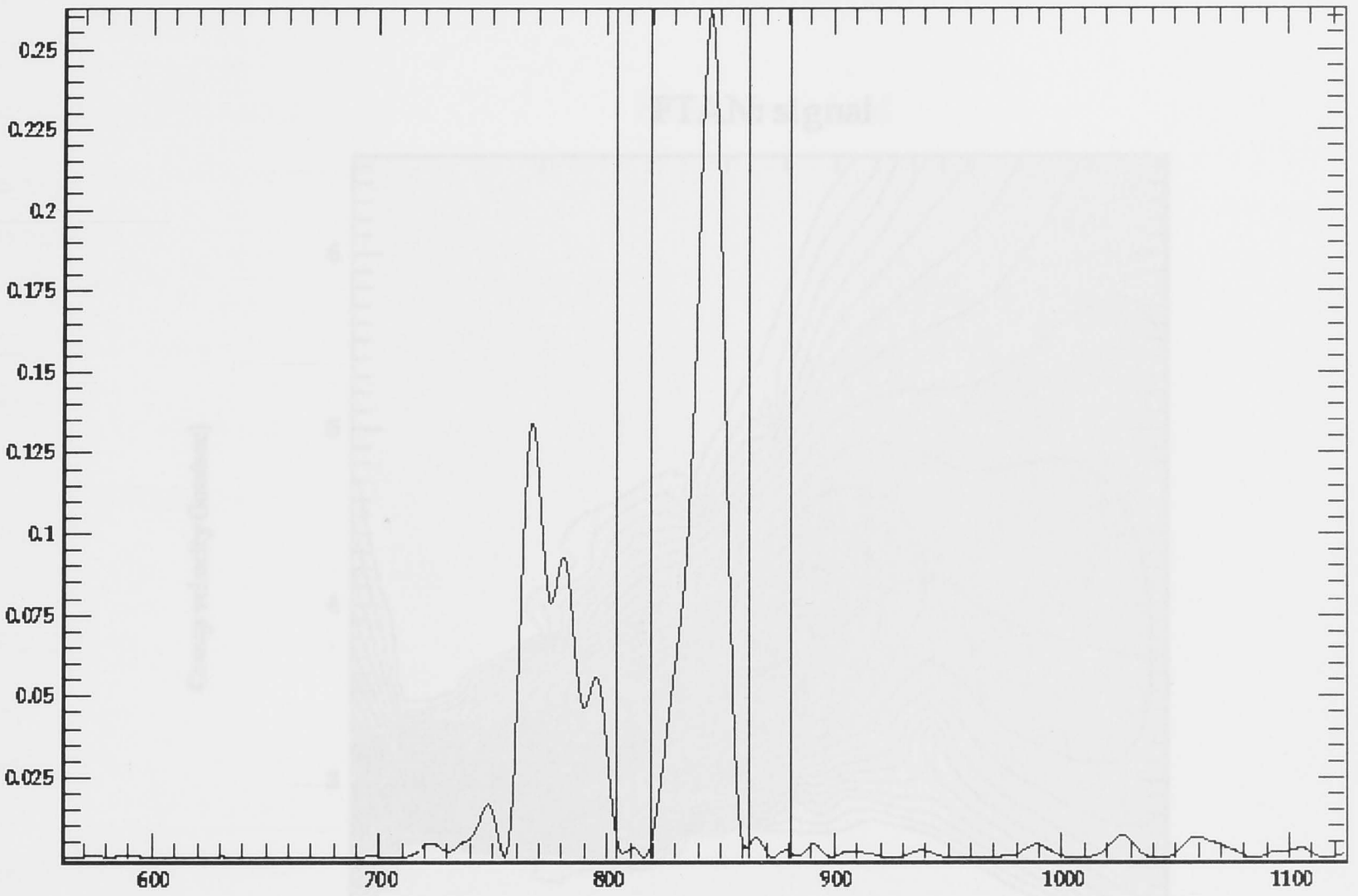

Fig. 3.2. Compressed time signals with cosine-tapered filtering which is directly from FTAN output.

Similarly we obtain

$$g_n(t) = \frac{1}{2\pi}\int_{-\infty}^{\infty} G_n(\omega)e^{-i\omega t}d\omega \ , \tag{3.4}$$

where $G_n(\omega)$ is the Hilbert transform of $F_n(\omega)$.

The envelope of the n-th filtered seismogram $f_n(t)$ is written as

$$A(\omega_n, t) = \left[f_n(t)^2 + g_n(t)^2\right]^{\frac{1}{2}} \ . \tag{3.5}$$

In practice, we apply a set of multiple filters ($n = 1, \cdots, N$) to the data and use a range of discrete time samplings $t_m (m = 1, \cdots, M)$, so that we can draw the N-by-M energy diagram $A(\omega_n, t_m)$ in the frequency-time plane. To obtain a group velocity curve of the signal $f(t)$, we first find discrete arrival times (t_{gr}: group velocity arrival) of the strongest energy in the energy diagram for discrete frequencies (ω_n). The group arrival time curve $t_{gr}(\Omega_i)$ is found in the energy diagram where Ω_i is an apparent frequency of the signal defined as

$$\Omega_i = \frac{\partial}{\partial t}\left[argA(\omega_i, t)\right]_{t=t_{gr}(\omega_i)} \ . \tag{3.6}$$

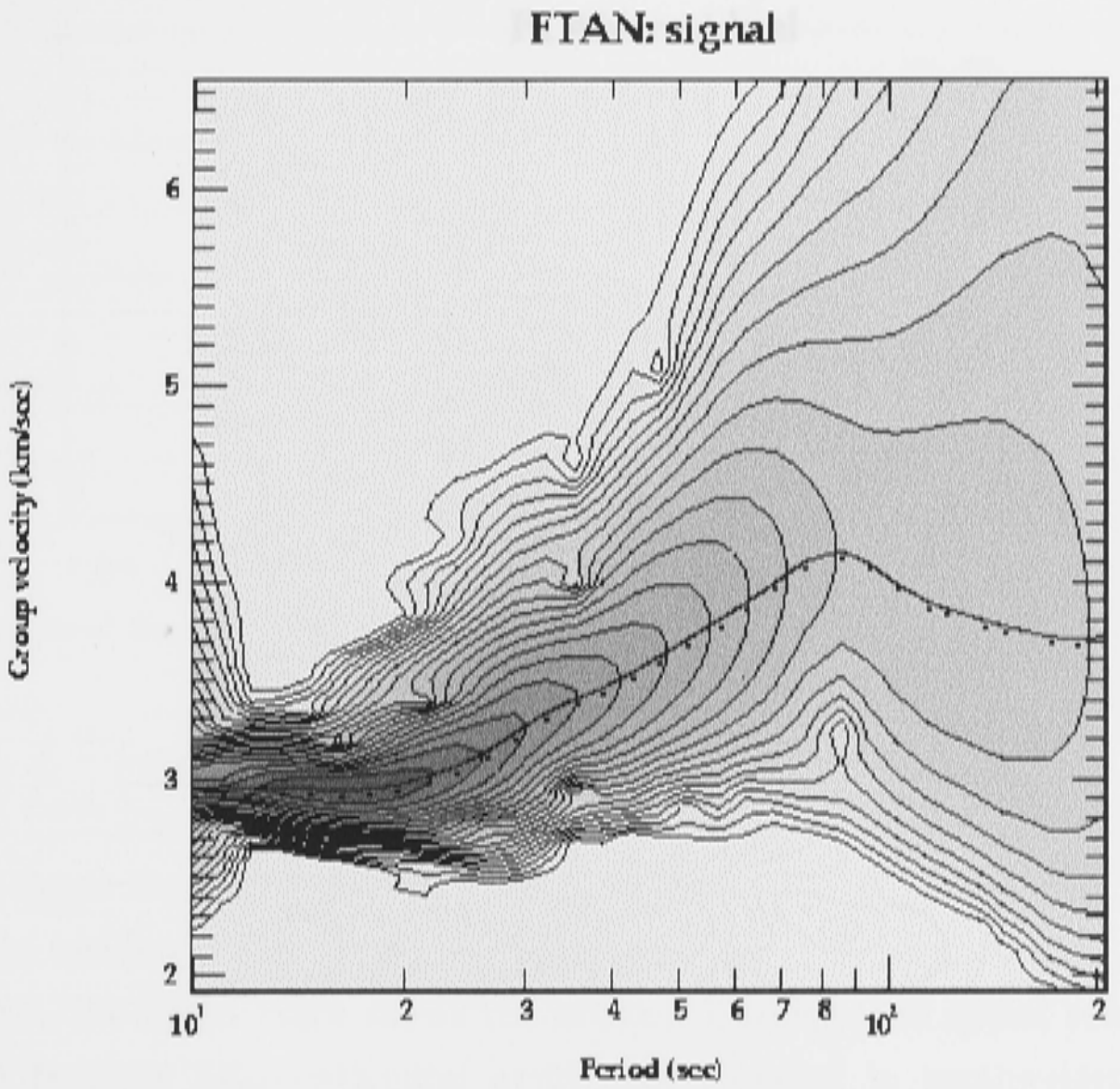

Fig. 3.3. Energy diagram of the filtered signals which is directly from FTAN output.

The preliminary group velocity curve $U(\omega) = r/t_{gr}(\omega)$ is given by interpolation of $t_{gr}(\Omega_i)$ into $t_{gr}(\omega)$, where r is an epicentral distance.

3.2.2 Time-variable and phase matched filters

To derive a more signal-enhanced group velocity curve from the preliminary group velocity curve in the energy diagram, we try to eliminate unnecessary signals such as random noise, overtones, and surface wave coda, around desired signals. First, we pick some points on the preliminary group velocity curve connecting the amplitude ridges of the signal in the energy diagram. For each point, where $\omega_i < \omega < \omega_{i+1}$ and $t = t_{gr}(\omega)$, the phase correction term c_i is introduced to try to equalise all the different phase values at each ω and $t = t_{gr}$ to one particular phase value $\phi(\omega)$:

$$\phi(\omega) = \int_{\omega_i}^{\omega_{i+1}} t_{gr}(\omega)d\omega + \omega c_i \,, \tag{3.7}$$

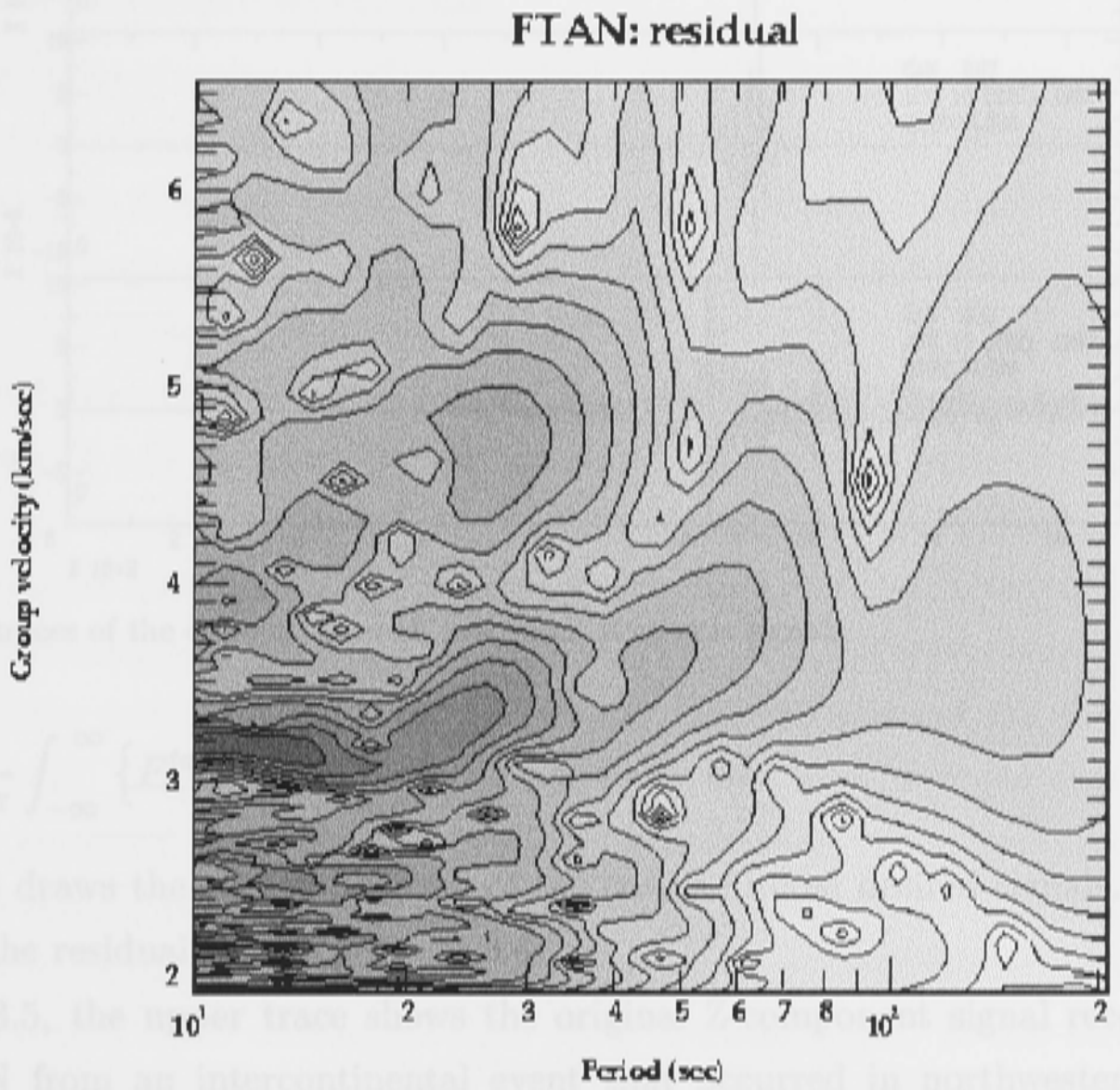

Fig. 3.4. Energy diagram of the residual signals which is directly from FTAN output.

for enhancing the desired signal along the preliminary group velocity curve. After the phase correction, the signal should have a single phase value $\phi(\omega)$ at each frequency ω. In the time domain, this phase correction enables to compress the seismogram in time and therefore leads to enhancing the signal-to-noise ratio. Applying the inverse Fourier transform to the phase corrected spectra, the compressed time signal $f_n^{cm}(t)$ is

$$f_n^{cm}(t) = \frac{1}{2\pi} \int_{-\infty}^{\infty} \{F_n(\omega) \exp[+i\phi(\omega)]\} \cdot \exp[i\omega t] \cdot d\omega \; . \tag{3.8}$$

We further apply a cosine-tapered filter to the envelope of $f_n^{cm}(t)$ around the clear impulsive part of the desired signal (figure 3.2). The resulting tapered signal $f_n^{tap}(t)$ is signal-enhanced because of the elimination of other signals and random noise. $f_n^{tap}(t)$ is Fourier transformed to $F_n^{tap}(\omega)$ in the frequency domain, then we expand the compressed and tapered signal to restore the initial phase spectrum by multiplying $F_n^{tap}(\omega)$ with $\exp[-i\phi(\omega)]$. Finally, we have a floating filtered signal:

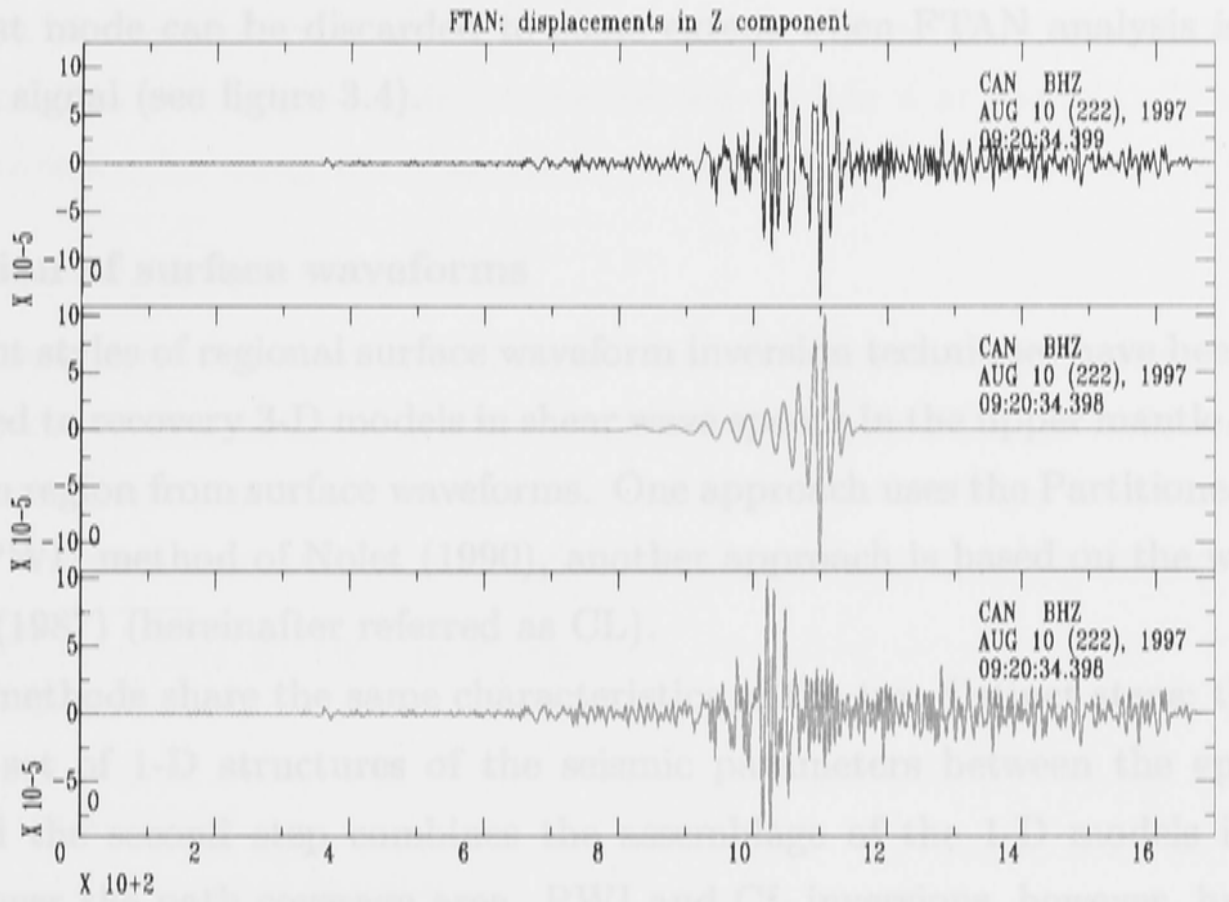

Fig. 3.5. The traces of the original, filtered, and residual seismic signals

$$f_n^{flo}(t) = \frac{1}{2\pi}\int_{-\infty}^{\infty}\left\{F_n^{tap}(\omega)\exp[-i\phi(\omega)]\right\}\cdot\exp[i\omega t]\cdot d\omega\ . \tag{3.9}$$

Figure 3.3 draws the energy diagram of the cosine-filtered desired signals. The energy diagram of the residual signals is figure 3.4.

In figure 3.5, the upper trace shows the original Z-component signal recorded at the station CAN from an intercontinental event that occurred in northwestern Australia. The second seismogram is the FTAN-filtered fundamental Rayleigh-mode signal and the lowest record is the residual signal after subtraction of the filtered signal from the original seismogram.

We consider the seismograms at the station CAN from intercontinental event in northwestern Australia at an epicentral distance of 3251.78 km. The seismogram is shown in figure 3.5(a). The course of the FTAN procedure for this event can be followed in figures 3.1-3.4. The FTAN filtering aims at isolating the fundamental Rayleigh mode from the observed seismogram. After applying the FTAN filtering to the Z component seismogram in figure 3.5, the energy diagram is obtained with the locus of the maximum fundamental-mode energy marked. The energy diagram for the filtered signals is shown in figure 3.3. The trajectory of the group velocity dispersion curve is then picked from the marked locus of the maximum energy at each frequency. The fundamental mode seismogram after filtering is illustrated in figure 3.5(b). After subtracting the filtered fundamental mode signal from the original one , we can observe significant residual signals (figure 3.5(c)). This indicates the presence of higher Rayleigh modes. The dispersion of

the strongest mode can be discarded to some extent when FTAN analysis is applied to the residual signal (see figure 3.4).

3.3 Inversion of surface waveforms

Two different styles of regional surface waveform inversion techniques have been developed and employed to recovery 3-D models in shear wave speeds in the upper mantle beneath the Australasian region from surface waveforms. One approach uses the Partitioned Waveform Inversion (PWI) method of Nolet (1990), another approach is based on the work of Cara & Lévêque (1987) (hereinafter referred as CL).

The two methods share the same characteristics of the two distinct steps; the first step produces a set of 1-D structures of the seismic parameters between the epicentre and station; and the second step combines the assemblage of the 1-D models into a quasi 3-D model over the path coverage area. PWI and CL inversions, however, have different approaches in dealing with surface waveforms in the first step. On one hand, PWI directly inverts the phase perturbation of the surface waveform into that of the shear wavespeed beneath the path. On the other hand, the CL method relates cross-correlation functions between the empirical data and the synthetic seismogram to the perturbations of the model of the seismic parameters. In the second step, PWI produces a shear wavespeed model in a 3-D (horizontal grid and vertical node) discrete representation while the CL inversion constructs a 3-D continuous shear wave slowness model. In this section, we thus introduce the theoretical aspects of the two methods for shedding light on the different and common features of the two inversions.

3.3.1 Partitioned Waveform Inversion

Nolet et al., (1986) formalise a nonlinear optimisation method to efficiently obtain reasonable surface waveform fitting. Nolet (1990) further develops this formalisation and introduced it as the Partitioned Waveform Inversion (PWI) method. Since then, the approach has been implemented and extended by a number of authors (Nolet 1993; Das & Nolet, 1995; Marquering & Snieder, 1996; Marquering et al., 1996; Marquering & Snieder, 1995; Zielhuis, 1993; Zielhuis & Nolet, 1994; Zielhuis & van der Hilst, 1996; van der Lee & Nolet, 1997).

We will mainly follow the development by Nolet (1990) and clarify the theory of the PWI method as follows: (1) definition of the penalty function $F(\mathbf{p})$; (2) construction of synthetic seismograms; (3) introduction of a phase integral approximation; (4) linearisation of the relation between $\delta k_n(\omega)$ and $\delta\beta(\mathbf{r})$ and (5) minimisation of a new penalty function $F(\boldsymbol{\gamma})$.

Although it is beyond the scope of this thesis to recover a three-dimensional structure from a suite of one-dimensional path specific models, we explain it at the end of this section as a natural extension for using the compilation of one-dimensional structures.

3.3.1.1 The penalty function $F(\mathbf{p})$

The goal of waveform inversion is to extract the velocity structure in the study area by matching observed and calculated waveforms. We will describe the velocity structures by a set of parameters $\mathbf{p}$ and introduce the penalty function $F(\mathbf{p})$ as a measure of the discrepancy between observations and synthetics for a model specified by $\mathbf{p}$:

$$F(\mathbf{p}) = \int [Rd(t) - Rs(t, \mathbf{p})]^2 dt + \mathbf{p}^T C_p^{-1} \mathbf{p} \,, \tag{3.10}$$

where

$\mathbf{p}$: model parameter

R : time and frequency window

$d(t)$: observed seismogram

$s(t, \mathbf{p})$: synthetic seismogram

C : a priori covariance matrix for the parameter $\mathbf{p}$.

The object of the inversion procedure is to find the parameter $\mathbf{p}$ which minimises the penalty function $F(\mathbf{p})$. In other words, the parameter set $\mathbf{p}$ simultaneously minimises the difference between the calculated and observed waveforms and the length of $\mathbf{p}$ itself. The term $\mathbf{p}^T C_p^{-1} \mathbf{p}$ prevents any elements of the $\mathbf{p}$ (wavespeeds in the 1-D depth layers) from having arbitrary values. Some elements of $\mathbf{p}$ make almost no contribution to the value of the F when sensitivity kernels of surface waves have very small values at the depths of those layers. Moreover, we allow for correlations between the elements of the $\mathbf{p}$ vector. It is quite possible that velocity changes for one parameter correlate with those for neighbouring parameters. The closer the separation between the parameters, the stronger is the likelihood of correlation which we express through the covariance matrix C_p. The introduction of the correlation terms prevents any $\mathbf{p}$ elements from acquiring arbitrary large values.

3.3.1.2 Construction of synthetic seismograms

We construct synthetic seismograms $S_j(\omega)$ in the frequency domain:

$$S_j(\omega) = \sum_{n=0}^{\infty} A_{nj}^0(\omega) \exp[i(k_n^0(\omega) + \delta k_n(\omega))\Delta_j] \,, \tag{3.11}$$

where

j : raypath index

n : mode number

0 : laterally homogeneous reference model

ω : angular frequency

Δ : epicentral distance

A : excitation coefficient

k : wave number

δk : perturbations of wave number from the reference model

We adopt a great-circle-path approximation to the synthetic seismograms $S_j(\omega)$, so that the equation 3.11 gives only synthetic waveforms traveling along the great circle path. In addition, we assume that the S wavespeed perturbation $\delta\beta(\mathbf{r}) = \beta(\mathbf{r}) - \beta^0(\mathbf{r})$ is not large and affects only the wave number (k_n) of the nth mode, and not the amplitude factor (A^0_{nj}). The consequent phase changes $\delta k_n(\omega) = k_n(\omega) - k^0_n(\omega)$ modify the waveforms. The relation between the synthetic seismogram $S_j(\omega)$ and the wave numbers k_n is closely linearised in the equation 3.11; however, the non-linear effects $\delta k_n(\omega)\Delta_j$ become noticeable at the large epicentral distance Δ_j.

3.3.1.3 A phase integral approximation

The first step of the Partitioned Waveform Inversion scheme is to perform waveform matches and obtain a 1-D path average model ($\beta^0(\mathbf{r}) + \delta\beta(\mathbf{r})$) which minimises the penalty function F($\mathbf{p}$) for each path. We determine the wavespeed perturbation ($\delta\beta(\mathbf{r})$) to obtain the closest synthetic seismogram to the empirical waveforms using the equation 3.11. Thus it is necessary to assume a relation between the wavespeed perturbation $\delta\beta(\mathbf{r})$ and that of the wave number $\delta k_n(\omega)$.

Under the great-circle-path approximation, we represent the perturbed phase factor using a phase integral approximation.

$$(k^0_n(\omega) + \delta k_n(\omega))\Delta_j \approx \int_{P_j} k_n[\theta(\Delta), \Phi(\Delta); \omega] d\Delta \,, \tag{3.12}$$

where

θ : the colatitude along a ray path

Φ : the longitude along a ray path

P_j : integration along the path j

$k_n(\theta, \Phi; \omega)$: the local wave number

After replacing the phase factor in (3.11) with the phase integral (3.12) we have

$$S_j(\omega) = \sum_{P_j} A^0_{nj}(\omega) \exp\left\{ i \int_0^{\Delta_j} k_n[\theta(\Delta), \Phi(\Delta); \omega] d\Delta \right\} . \tag{3.13}$$

Note that our initial synthetic seismograms of the reference model do not contain effects of lateral heterogeneity on the amplitude factor $A^0_{nj}(\omega)$. Zielhuis & van der Hilst (1996) have used an approximation which employs different crustal thickness at the source, along the raypath, and near the receiver in the seismogram calculations. Kennett (1995) has examined some of the theoretical consequences of such an approach.

3.3.1.4 Linearisation of the relation between $\delta k_n(\omega)$ and $\delta\beta(\mathbf{r})$

In the relation between $\delta k_n(\omega)$ and $\delta\beta(\mathbf{r})$, we can approximate that $\delta k_n(\omega)$ is linearly related to $\delta\beta(\mathbf{r})$ through the Frechet derivatives $(\partial k_n(\omega)/\partial\beta(r))$ (see eg. Takeuchi & Saito (1972)). We then apply the first-order Taylor expansion to the phase integral with respect to$\beta(\mathbf{r})$. We have

$$\begin{aligned} \int_{P_j} k_n[\theta(\Delta), \Phi(\Delta); \omega] d\Delta &= k^0_n(\omega)\Delta_j + \delta k_n(\omega)\Delta_j \\ &= k^0_n(\omega)\Delta_j + \int_{P_j} \int_0^a \left[\frac{\partial k_n(\omega)}{\partial\beta(r)}\right] \delta\beta(\mathbf{r}) dr d\Delta \\ &= k^0_n(\omega)\Delta_j + \int_0^a \left[\frac{\partial k_n(\omega)}{\partial\beta(r)}\right] \int_{P_j} \delta\beta(\mathbf{r}) d\Delta dr. \end{aligned} \tag{3.14}$$

After averaging the velocity perturbation with depth $\delta\beta(\mathbf{r})$ along the ray path, we expand it in terms of a set of basis function $h_i(r)$ with coefficients γ^j_i,

$$\frac{1}{\Delta_j} \int_{P_j} \delta\beta(\mathbf{r}) d\Delta = \sum_{i=1}^{N} \gamma^j_i h_i(r) , \tag{3.15}$$

where N is the total number of modal parameters.

We use basis functions $(h_i(r))$ which have boxcar or triangular shapes. On substituting (3.15) into (3.14), we change the second term of (3.14) to:

$$\begin{aligned} \int_0^a \left[\frac{\partial k_n(\omega)}{\partial\beta(r)}\right] \int_{P_j} \delta\beta(\mathbf{r}) d\Delta dr &= \sum_{i=1}^{N} \gamma^j_i \int_{P_j} \int_0^a \left[\frac{\partial k_n(\omega)}{\partial\beta(r)}\right] h_i(r) dr d\Delta \\ &= \Delta_j \sum_i \gamma^j_i \mathcal{H}_i(\omega) , \end{aligned} \tag{3.16}$$

where

$$\mathcal{H}_i(\omega) = \int_0^a \left[\frac{\partial k_n(\omega)}{\partial\beta(r)}\right] h_i(r) dr. \tag{3.17}$$

Consequently, we obtain the spectral representation:

$$S_j(\omega) = \sum_{n=0}^{\infty} A_{nj}^0(\omega) \exp\left[i\Delta_j[k_n^0(\omega) + \sum_i \gamma_i^j \mathcal{H}_i(\omega)]\right]. \tag{3.18}$$

$S_j(\omega)$ is also a non-linear function of γ_i^j, through $\delta k_n(\omega) = \sum \gamma_i^j \mathcal{H}_i(\omega)$. As a result, the synthetic seismogram (s_j), which is the Fourier-transform of $S_j(\omega)$, is a non-linear function of γ_i^j or $s_j = s_j(t, \boldsymbol{\gamma})$.

3.3.1.5 Minimisation of a new penalty function $F(\boldsymbol{\gamma})$

The penalty function (1) is now written as a non-linear function of the path integrals $\boldsymbol{\gamma}$,

$$F(\boldsymbol{\gamma}) = \int [Rd_j(t) - Rs_j(t, \boldsymbol{\gamma})]^2 dt + \boldsymbol{\gamma}^T C_\gamma^{-1} \boldsymbol{\gamma}\,. \tag{3.19}$$

The first step of the PWI is therefore to determine $\boldsymbol{\gamma}_{opt}$ which minimizes the penalty function $F(\boldsymbol{\gamma})$. Using a non-linear optimisation method such as a conjugate gradient method (Press et al., 1986), we iteratively search for the global minimum value of $F(\boldsymbol{\gamma})$. In this procedure, the operator R has two functions. First, it filters the data which reduces the chance of ending up in a local minimum of F. In the first iteration, we find the minimum with the strongest low-pass filter in R. Then we add higher frequency signals to the previous case and find an new minimum value at every iteration. Second, the operator R isolates the two portions of the seismograms as the higher mode and the fundamental mode waves. This time-window separation enables to simultaneously conduct higher mode and fundamental mode waveform inversions.

Next, we examine the relation between the model misfit $\Delta\boldsymbol{\gamma} = \boldsymbol{\gamma} - \boldsymbol{\gamma}_{opt}$ and an acceptable small difference (ε) between the two waveform misfits ($F(\boldsymbol{\gamma})$ and $F(\boldsymbol{\gamma}_{opt})$). The condition of convergence is written as

$$F(\boldsymbol{\gamma}) - F(\boldsymbol{\gamma}_{opt}) < \varepsilon\,. \tag{3.20}$$

We apply a second-order Taylor expansion to the penalty function F around $\boldsymbol{\gamma}_{opt}$. Then we take $\partial F/\partial\gamma|_{\gamma_{opt}} = 0$ assuming that we have indeed reached a minimum of F at the optimum value $\boldsymbol{\gamma}_{opt}$,

$$F(\boldsymbol{\gamma}) \approx F(\boldsymbol{\gamma}_{opt}) + \frac{1}{2}(\boldsymbol{\gamma} - \boldsymbol{\gamma}_{opt})^T \mathbf{H} (\boldsymbol{\gamma} - \boldsymbol{\gamma}_{opt})\,, \tag{3.21}$$

where the Hessian matrix

$$H_{ij} = \frac{\partial^2 F}{\partial\gamma_i \partial\gamma_j}\,. \tag{3.22}$$

Therefore (3.20) can now be written as

$$\frac{1}{2}\Delta\boldsymbol{\gamma}^T \mathbf{H} \Delta\boldsymbol{\gamma} < \varepsilon\,. \tag{3.23}$$

In our case, the number of the parameters for each source-receiver pair is twenty ; therefore the Hessian matrix is readily solvable numerically. The parameters $\boldsymbol{\gamma}$, however, are generally correlated with each other. Thus, we transform the correlated parameters $\boldsymbol{\gamma}$ into an independent set of parameters $\boldsymbol{\eta}$. Then we relate $\boldsymbol{\eta}$ to the condition of convergence ε. Applying eigenvalue decomposition to the symmetric Hessian matrix $\mathbf{H}$ leads to

$$\mathbf{H} = \mathbf{S}\boldsymbol{\Lambda}\mathbf{S}^T \ , \tag{3.24}$$

where

$\mathbf{S}$: the eigenmatrix with the eigenvectors of $\mathbf{H}$

$\boldsymbol{\Lambda}$: the diagonal matrix with the real eigenvalues of $\mathbf{H}$.

$\mathbf{S}$ is comprised of the eigenvectors $\mathbf{e}$ of $\mathbf{H}$ as column vectors. Using $\mathbf{S}$, we introduce the new model parameter$\boldsymbol{\eta}$ through:

$$\boldsymbol{\gamma} = \mathbf{S}\boldsymbol{\eta}$$

or equivalently,

$$\boldsymbol{\eta} = \mathbf{S}^T\boldsymbol{\gamma} \tag{3.25}$$

$\boldsymbol{\eta}$ is the projection of the original set of parameters $\boldsymbol{\gamma}$ on the orthonormal eigenvectors $\mathbf{e}$. Thus, all the elements of $\boldsymbol{\eta}$ have no correlation with each other, so that the deviation, $\Delta\boldsymbol{\eta} = \boldsymbol{\eta} - \boldsymbol{\eta}_{opt}$, is also independent. We rewrite the acceptable misfit criterion for our waveform matching as

$$\frac{1}{2}\Delta\boldsymbol{\eta}^T\boldsymbol{\Lambda}\Delta\boldsymbol{\eta} < \varepsilon$$

or

$$|\Delta\eta_i| \leq \sqrt{\frac{2\varepsilon}{\lambda_i}} \ . \tag{3.26}$$

3.3.1.6 Construction of a 3-D models from path averages

The approach adapted for the second stage of the partitioned waveform inversion is to recognize that the individual path averaged structures represent a set of linear constraints on the properties of the 3-D model and so a linear inverse problem can be posed for the 3-D velocity structure. Because the estimates of path averaged structure include the effect of noise and misfit, the results for different paths may be inconsistent. This needs to be taken into account in the inversion.

By this non-linear inversion procedure we produce a 'path-averaged' shear wavespeed structure as a function of depth. We regard this set of models as a linear constraint on

the 3-D structure $\boldsymbol{\gamma}$ for each of the receiver-epicentre pairs. The $\boldsymbol{\gamma}$ then were transformed to the independent parameter vector $\boldsymbol{\eta}$ by the equation (3.25).

With the relations (3.15 and 3.25), we expand the horizontally averaged velocity structure in terms of η_j and the new basis function $g_j(r)$

$$\frac{1}{\Delta_j}\int\limits_{P_j}\delta\beta(\mathbf{r})d\Delta = \sum_{i=1}^{N}\sum_{j=1}^{N}\mathcal{S}_{ij}\eta_j h_i(r) = \sum_{j=1}^{N}\eta_j g_j(r)\ , \tag{3.27}$$

where we have defined

$$g_j(r) = \sum_{j=1}^{N}\mathcal{S}_{ij}h_i(r)\ , \tag{3.28}$$

and $\mathcal{S}_{ij}$ is equal to the eigenmatrix $\mathbf{S}$ in (3.24).

With a continuous depth variable r, (3.27) expresses an infinite set of equations. To transform them to a finite set of independent equations, we introduce a dual sampling function $\tilde{g}_j(r)$, which satisfies the orthogonality condition

$$\int\limits_0^a \tilde{g}_j(r)\cdot g_i(r) = \delta_{ij}\ . \tag{3.29}$$

Multiplication of (3.27) with the dual function leads to the linear relation

$$\frac{1}{\Delta_k}\int\limits_{P_j}\int\limits_0^a \delta\beta(\mathbf{r})\cdot\tilde{g}_k(r)drd\Delta = \eta_k \pm \Delta\eta_k. \tag{3.30}$$

where we have used the path index k. From each waveform fitting procedure, we have a set of new linear constraints η_k with an uncertainty $\Delta\eta_k$. Using the deviation $\delta\beta(\mathbf{r})$ from a symmetrical reference model $\delta\beta^0(r)$, (3.30) becomes

$$\frac{1}{\Delta_k}\int\limits_{P_j}\int\limits_0^a \beta(\mathbf{r})\cdot\tilde{g}_k(r)drd\Delta = \frac{1}{\Delta_k}\int\limits_{P_j}\int\limits_0^a \beta^0(r)\cdot\tilde{g}_k(r)drd\Delta + \eta_k \pm \Delta\eta_k\ . \tag{3.31}$$

To generalise (3.31) to any three-dimensional reference Earth model ($\beta^R(\mathbf{r}) = \beta(\mathbf{r}) - \delta\beta^R(\mathbf{r})$), we add the path integral of $\beta^0(\mathbf{r})$ and subtract that of $\beta^R(\mathbf{r})$ from both sides of (3.31),

$$\frac{1}{\Delta_k}\int\limits_{P_k}\int\limits_0^a \delta\beta^R(\mathbf{r})\cdot\tilde{g}_k(r)drd\Delta = \eta_k - \frac{1}{\Delta_k}\int\limits_{P_k}\int\limits_0^a \beta^R(\mathbf{r})\cdot\tilde{g}_k(r)drd\Delta \pm \Delta\eta_k\ . \tag{3.32}$$

To scale all the data to unit variance, we divide (3.32) by $\Delta\eta_k$. (3.32) satisfies

$$\frac{1}{\Delta_k}\int\limits_{P_k}\int\limits_0^a G_k(r)\delta\beta^R(\mathbf{r})drd\Delta = q_k, \tag{3.33}$$

where the scaled kernel $G_k(r)$;

$$G_k(r) = \tilde{g}_k(r)/\Delta\eta_k,$$

and the shifted and scaled parameter q_k;

$$q_k = [\eta_k - \frac{1}{\Delta_k}\int\limits_{P_k}\int\limits_{0}^{a} \beta^R(r)\cdot\tilde{g}_k(r)drd\Delta]/\Delta\eta_k \pm 1.$$

The three-dimensional velocity perturbation $\delta\beta(\mathbf{r})$ now is expanded in a set of three-dimensional basis function $s_i(\theta,\phi,r) = l_i(\theta,\phi)h_i(r)$,

$$\delta\beta(\mathbf{r}) = \sum_{i=1}^{M} b_i s_i(\theta,\phi,r) = \sum_{i=1}^{M} b_i l_i(\theta,\phi)h_i(r)\ , \tag{3.34}$$

where $\mathbf{M}$ represents the total number of cells.

We divide the region of interest into cells which have horizontally uniform but vertically different sizes. To obtain the velocity perturbation in each cell, we set the three-dimensional basis functionss_i as the multiplication of the horizontal function $l_i(\theta,\phi)$ by the radial function $h_i(r)$. If a particular point (θ,ϕ) at which we conduct inversion is within the cell, $l_i(\theta,\phi) = 1$, otherwise $l_i(\theta,\phi) = 0$. Substituting (3.34) into (3.33), we have

$$\sum_i A_{ki}b_i = q_k\ , \tag{3.35}$$

where

$$A_{ki} = \frac{1}{\Delta_k}\int\limits_{P_k}\int\limits_{0}^{a} l_i(\theta,\phi)h_i(r)G_k(r)drd\Delta = \frac{L_{ik}}{\Delta_k}\int\limits_{0}^{a} h_i(r)G_k(r)dr\ , \tag{3.36}$$

where L_{ik} is the length of the segment of path k in cell i.

Our goal is to obtain the model or the coefficient $b_i(i = 1\cdots N$; where N is the total number of ray paths) in the equation (3.35). With the data $q_k(k = 1\cdots M$; where M is the total number of cells), we write the linear equations as

$$\mathbf{Ab} = \mathbf{q}\ . \tag{3.37}$$

In addition to minimising the data misfit $(\mathbf{Ab}-\mathbf{q})$, we impose a minimum norm and a minimum gradient constraint on the solution.

$$\min[(\mathbf{Ab}-\mathbf{q})^{\mathbf{T}}(\mathbf{Ab}-\mathbf{q}) + \alpha\mathbf{b}^{\mathbf{T}}\mathbf{b} + \gamma(\mathbf{Gb})^{\mathbf{T}}(\mathbf{Gb})]\ . \tag{3.38}$$

The operator $\mathbf{G}$ is the gradient of the model $\mathbf{b}$, so that it smoothes away the solution. α and γ weight the trade off between data misfit, model norm, and gradient norm. Nolet(1987) formulated this minimisation as a the linear system:

$$\begin{bmatrix} \mathbf{A} \\ \alpha\mathbf{I} \\ \gamma\mathbf{G} \end{bmatrix} \mathbf{b} = \begin{bmatrix} \mathbf{q} \\ \mathbf{0} \\ \mathbf{0} \end{bmatrix}, \tag{3.39}$$

I is the identity matrix. **G** comprises the first order derivatives in the r, θ , and ϕ directions:

$$[\mathbf{G}] = \begin{bmatrix} \gamma_v \mathbf{G}_r \\ \gamma_h \mathbf{G}_\theta \\ \gamma_h \mathbf{G}_\phi \end{bmatrix}, \tag{3.40}$$

γ_v and γ_h are weights imposed on the vertical and horizontal gradients. The weights therefore apply different smoothnesses of the solution in the vertical and horizontal direction.

$$\begin{bmatrix} \mathbf{A} \\ \alpha\mathbf{I} \\ \gamma_v\mathbf{G}_r \\ \gamma_h\mathbf{G}_\theta \\ \gamma_h\mathbf{G}_\phi \end{bmatrix} \mathbf{b} = \begin{bmatrix} \mathbf{q} \\ \mathbf{0} \\ \mathbf{0} \\ \mathbf{0} \\ \mathbf{0} \end{bmatrix}. \tag{3.41}$$

Finally we solve the equation (3.41) with the LSQR algorithm (Paige & Saunders, 1982).

The LSQR inversion provides the expansion coefficients(**b**) of the three-dimensional velocity perturbation($\delta\beta(\mathbf{r})$). The equation (3.34) gives the perturbation($\delta\beta(\mathbf{r})$) in each cell. Combining $\delta\beta(\mathbf{r})$ with the reference model, we construct a new three-dimensional velocity model.

3.3.2 Inversion of Secondary Observables

To clarify distinct differences and common features between PWI and the CL methods, we further introduce the theoretical framework for the CL method developed by Cara & Lévêque (1987). Both PWI and the CL method share the two-stage inversion scheme with the same end of gaining a 3-D shear wavespeed structure over the path coverage area. The first stage is a non-linear waveform fitting for each epicentre-station pair, while in the second stage all the vertical models for individual paths are combined into a globally linear inversion for a 3-D shear wavespeed model. However, the two methods are different styles of inversion and make use of different algorithms.

In the first stage, as we discuss in the previous section, PWI directly inverts the waveform differences between the observed and synthetic seismograms into the perturbation of the shear wavespeeds from a reference model beneath the epicentre-station path. In contrast, the CL method first computes the envelopes and phases of the bandpassed cross-correlogram between the full-mode synthetic and a few single-mode synthetic

seismograms. Next the algorithm calculates the envelopes and phases between the empirical data and a few single-mode synthetic seismograms. Thirdly, subtracting the synthetic-synthetic envelopes and phases from those of the observed-synthetic cross-correlograms, the CL algorithm obtains the perturbations of the envelopes and phases between synthetic-synthetic and observed-synthetic pairs. The method then inverts the perturbations of the envelopes and phases into those of the elastic parameters and the quality factors in the 1-D structure along the great circle path between the source and epicentre. The advantages of taking cross-correlation are to (1) reinforce the multi-mode synthetic seismogram close to the real seismogram; (2) leave the noise dispersed; and (3) avoid strong non-linearity in the direct dependence of the waveform on the elastic parameters

In the second stage, the CL inversion constructs a 3-D upper mantle shear wave slowness model using the continuous regionalisation algorithm of Montagner (1986), while PWI produces an upper mantle shear wavespeed model with a 3-D horizontal-cell and vertical-node structure.

In the following sections, we present (1) discrete expressions of the full mode and single-mode (p) synthetic seismograms for a angular frequency (ω) and a mode rank (n); (2) the bandpassed cross-correlogram (g_p) between the full-mode synthetic and a single-mode synthetic; (3) the partial derivatives of g_p with respect to the elastic parameters(m) and the inverse of the quality factor (Q^{-1}); (4) secondary observables such as the envelope (E_p) and phase (Φ_p) of g_p; (5) the partial derivatives of E_p and Φ_p with respect to m and Q^{-1}; (6) the formulation of the CL inversion scheme for deriving the perturbations of the elastic parameters and the loss factors from those of the envelope and phase of g_p; and (7) the derivation of a continuous quasi-3D model from the assemblage of the 1-D structures.

3.3.2.1 Construction of synthetic seismograms

A discrete expression of the multi-mode synthetic seismogram for a circular frequency ω in a spherical reference earth model can be written as a modal summation in the frequency domain:

$$S_j(\omega) \;=\; \sum_n \{A^0_{nj}(\omega)\cdot \exp\left[ik^0_n(\omega)\Delta_j - a^0_n(\omega)\Delta_j\right]\;, \tag{3.42}$$

where

j : path index

n : mode index

0 : laterally homogeneous reference model

Δ : epicentral distance

a_n : apparent attenuation factor

k_n : wave number

A_n : coefficient of source excitation and instrumental response

Thus a single-mode(p) synthetic seismogram for a reference model is written as

$$S_{pj}(\omega) \quad = \quad A^0_{pj}(\omega) \exp\left[ik^0_p(\omega)\Delta_j - a^0_p(\omega)\Delta_j\right] \ . \tag{3.43}$$

The observed seismogram is expected to be represented by a similar spectral form of (3.42), but replacing $k^0_n(\omega)$ and $a^0_n(\omega)$ with the perturbations $[k^0_n(\omega) + \delta k_n(\omega)]$ and $[a^0_n(\omega) + \delta a_n(\omega)]$. This is due to the assumption that the deviations $\delta k_n(\omega)$ and $\delta a_n(\omega)$ should be much smaller than the magnitudes of $k^0_n(\omega)$ and $a^0_n(\omega)$ themselves. In other words, this replacement could be allowed only if a 1-D path dependent model beneath the epicentre-station path could not differ very much from the reference model.

3.3.2.2 The band-passed cross-correlogram $g_p(\omega_q, t)$

We introduce $g_p(\omega_q, t)$ as the band-passed cross-correlation function between the full multi-mode synthetic seismogram($s(t)$) and the synthetic seismogram for a single mode p ($s_p(t)$):

$$g_p(\omega_q, t) = h(\omega_q, t) * \overline{s_p}(-t) * s(t) \tag{3.44}$$

where $*$ indicates a convolution, $h(\omega_p, t)$ is the impulse response of a band-pass filter centered on the circular frequency ω_q; $\overline{s_p(t)}$ represents the complex conjugate of the signal $s_p(t)$. Similarly, $g_p(\omega_q, t)$ for the observed seismogram is obtained. Furthermore, we rewrite $g_p(\omega_q, t)$ using the modal expressions for the spectra $S(\omega)$ and $S_p(\omega)$ as

$$g_p(\omega_q, t) = \int \left[H(\omega - \omega_q) \cdot \sum_n \overline{A_p} A_n exp\{i(k_n - k_p)x - (a_n + a_p)x - i\omega t\} \right] d\omega \ , \tag{3.45}$$

where $H(\omega - \omega_q)$ is the representation of $h(\omega_p, t)$ in the frequency domain.

3.3.2.3 Calculation of partial derivatives of $g_p(\omega_q, t)$

The CL inversion algorithm tries to match the synthetic seismogram to the observed seismogram by matching the behaviour of the cross-correlation function $g_p(\omega_q, t)$. As we have seen in the previous section, the perturbations of $\delta k_n(\omega)$ and $\delta a_n(\omega)$ could give rise to variations in $g_p(\omega_q, t)$. Thus the cross-correlogram is expected to be a nonlinear function of the elastic parameters and the quality factor through $\delta k_n(\omega)$ and $\delta a_n(\omega)$. Therefore it is worthwhile to obtain in advance the partial derivatives of the cross-correlogram($g_p(\omega_q, t)$) with respect to the elastic parameters m_i(i is the layer index) and the inverse of the quality factor Q_{β_i}.

Taking the partial derivative of (3.45) with respect to m_i, gives

$$\frac{\partial g_p(\omega_q,t)}{\partial m_i} = ix \cdot \int H(\omega-\omega_q) \cdot \sum_n (\frac{\partial k_n}{\partial m_i})\overline{A_p}A_n exp\{i(k_n-k_p)x-(a_n+a_p)x-i\omega t\}\, d\omega\,, \tag{3.46}$$

where the wave number

$$k_n(\omega) = \frac{\omega}{C_n} \tag{3.47}$$

in terms of the phase velocity C_n for mode rank n; therefore,

$$\frac{\partial k_n}{\partial m_i} = \frac{\partial k_n}{\partial C_n}\cdot\frac{\partial C_n}{\partial m_i} = -\frac{\omega}{C_n^2}\cdot\frac{\partial C_n}{\partial m_i}\,. \tag{3.48}$$

Similarly, we can write the partial derivative of $g_p(\omega_q,t)$ with respect to the inverse of the quality factor for shear waves $Q_{\beta_i}^{-1}$:

$$\frac{\partial g_p(\omega_q,t)}{\partial Q_{\beta_i}^{-1}} = -x \cdot \int H(\omega-\omega_q) \cdot \sum_n (\frac{\partial a_n}{\partial Q_{\beta_i}^{-1}})\overline{A_p}A_n exp\{i(k_n-k_p)x-(a_n+a_p)x-i\omega t\}\, d\omega, \tag{3.49}$$

By analogy to the relation between (3.46) and (3.48), we would like to obtain the partial derivative of the attenuation factor a_n with respect to $Q_{\beta_i}^{-1}$ for the equation (3.49). In the presence of small attenuation, we may introduce imaginary perturbations into the compressional velocity(α), the shear velocity(β), and the phase velocity(C) as $\alpha + i\alpha^{'}$, $\beta + i\beta^{'}$, and $C + iC^{'}$.

The resulting perturbation of the phase velocity can be represented as

$$C^{'} = \int \left\{ \left[\frac{\partial C}{\partial \alpha}\right] \alpha^{'}(z) + \left[\frac{\partial C}{\partial \beta}\right] \beta^{'}(z) \right\} dz. \tag{3.50}$$

With the inverse of the quality factors of the compressional and shear waves

$$Q_\alpha^{-1} = \frac{2\alpha^{'}}{\alpha} \qquad Q_\beta^{-1} = \frac{2\beta^{'}}{\beta}, \tag{3.51}$$

(3.50) can be rewritten in forms of the loss factor Q^{-1} for surface waves as

$$Q^{-1} = \frac{2C^{'}}{C} = \int \left\{ \frac{\alpha}{C}\left[\frac{\partial C}{\partial \alpha}\right]_\omega Q_\alpha^{-1}(z) + \frac{\beta}{C}\left[\frac{\partial C}{\partial \beta}\right]_\omega Q_\beta^{-1}(z) \right\} dz. \tag{3.52}$$

If the dilatational loss is much smaller than that in shear, Q_α^{-1} and Q_β^{-1} are related by(Anderson et al., 1965)

$$Q_\alpha^{-1} \approx \frac{4\beta^2}{3\alpha^2}\cdot Q_\beta^{-1} \tag{3.53}$$

Given the above relation, we may transform the depth integral (3.52) into a discrete expression for mode n in terms of the individual layers(i)

$$\begin{aligned} Q_n^{-1} &= \sum_i \left[\frac{\alpha_i}{C_n} \cdot \left. \frac{\partial C_n}{\partial \alpha_i} \right|_\omega \cdot Q_{\alpha_i}^{-1} + \frac{\beta_i}{C_n} \cdot \left. \frac{\partial C_n}{\partial \beta_i} \right|_\omega \cdot Q_{\beta_i}^{-1} \right] \\ &= \sum_i \left[\left(\frac{4\beta_i^2}{3\alpha_i^2} \cdot \frac{\alpha_i}{C_n} \cdot \left. \frac{\partial C_n}{\partial \alpha_i} \right|_\omega + \frac{\beta_i}{C_n} \cdot \left. \frac{\partial C_n}{\partial \beta_i} \right|_\omega \right) \cdot Q_{\beta_i}^{-1} \right]. \end{aligned} \tag{3.54}$$

The apparent attenuation factor(a_n) is written as

$$a_n(\omega) = \frac{\omega}{2C_n Q_n}, \tag{3.55}$$

we therefore find the partial derivative of a_n with respect to $Q_{\beta_i}^{-1}$ at a layer i as:

$$\frac{\partial a_n}{\partial Q_{\beta_i}^{-1}} = \frac{\omega}{2C_n} \cdot \left[\frac{4\beta_i^2}{3\alpha_i^2} \cdot \frac{\alpha_i}{C_n} \cdot \left. \frac{\partial C_n}{\partial \alpha_i} \right|_\omega + \frac{\beta_i}{C_n} \cdot \left. \frac{\partial C_n}{\partial \beta_i} \right|_\omega \right]. \tag{3.56}$$

For the bandpassed cross-correlogram between the observed seismogram and the single mode seismogram, the terms of the wave number ($k_n(\omega)$) and the apparent attenuation factor($a_n(\omega)$) could be replaced with $k_n(\omega) + \delta k_n(\omega)$ and $a_n(\omega) + \delta a_n(\omega)$ in the equations (3.46) and (3.49).

3.3.2.4 Definitions of secondary observables $E_p(\omega_q, t)$ and $\Phi_p(\omega_q, t)$

To facilitate a further reduction of the nonlinearity between $g_p(\omega_q, t)$ and the elastic parameters (m_i) and the inverse of the quality factor ($Q_{\beta_i}^{-1}$), new data ('secondary observables') are introduced, instead of directly using waveforms. The first data is defined as the envelope of $g_p(\omega_q, t)$:

$$E_p(\omega_q, t) = \| g_p(\omega_q, t) \|, \tag{3.57}$$

and the second data is the phase of $g_p(\omega_q, t)$:

$$\Phi_p(\omega_q, t) = tan^{-1} \left[\frac{\Im(g_p(\omega_q, t))}{\Re(g_p(\omega_q, t))} \right], \tag{3.58}$$

where $\Im(g_p)$ and $\Re(g_p)$ designate the imaginary and real part of the cross-correlogram g_p.

Cara & Lévêque (1987) demonstrate a quasi-linear relation between the central value of the envelope $E_p(\omega_q, t)$ and S velocity perturbations with three percent deviation for modes up to the third higher mode Rayleigh waves at 50 second period. They therefore assume a linearity between the secondary observables (E_p and Φ_p) and the elastic parameters within the limited magnitudes of δE_p and $\delta \Phi_p$. The CL method then inverts the differences of the envelope and the phase between the observed and synthetic values, namely $\delta E_p(\omega_q, t)$ and $\delta \Phi_p(\omega_q, t)$ into the perturbations of the elastic parameters (m_i) and the inverse of the quality factor ($Q_{\beta_i}^{-1}$) beneath the great circle path between the epicentre and the station.

Thus it is necessary to obtain the partial derivatives of $E_p(\omega_q, t)$ and $\Phi_p(\omega_q, t)$ with respect to m_i and $Q_{\beta_i}^{-1}$ for the later inversion procedure.

From the relation

$$[E_p(\omega_q, t)]^2 = \|g_p(\omega_q, t)\|^2 = g_p \cdot \overline{g}_p \,, \tag{3.59}$$

we take the partial derivative of the envelope $E_p(\omega_q, t)$

$$\frac{\partial}{\partial m_i} [E_p(\omega_q, t)]^2 = \frac{\partial \left(g_p \cdot \overline{g}_p \right)}{\partial m_i} = \frac{\partial g_p}{\partial m_i} \cdot \overline{g}_p + g_p \cdot \frac{\partial \overline{g}_p}{\partial m_i} \,, \tag{3.60}$$

At the same time, we can write

$$\frac{\partial}{\partial m_i} [E_p(\omega_q, t)]^2 = 2E_p(\omega_q, t) \cdot \frac{\partial}{\partial m_i} E_p(\omega_q, t) \tag{3.61}$$

Therefore we obtain

$$\frac{\partial}{\partial m_i} E_p(\omega_q, t) \;=\; \frac{1}{2\,[E_p(\omega_q, t)]} \cdot \left(\frac{\partial g_p}{\partial m_i} \cdot \overline{g}_p + g_p \cdot \frac{\partial \overline{g}_p}{\partial m_i} \right) \,. \tag{3.62}$$

For the phase $(\Phi_p(\omega_q, t))$ of the bandpassed cross-correlogram $g_p(\omega_q, t)$, we first use the relation

$$\frac{\partial \tan \Phi_p}{\partial m_i} = \frac{\partial \tan \Phi_p}{\partial \phi_p} \cdot \frac{\partial \Phi_p}{\partial m_i}. \tag{3.63}$$

With (3.58), this relation can be rewritten as

$$\begin{aligned} \frac{\partial}{\partial m_i} \Phi_p(\omega_q, t) \;&=\; \frac{1}{1 + \tan^2 \Phi_p} \cdot \frac{\partial \tan \Phi_p}{\partial \phi_p} \\ &=\; \frac{1}{[E_p(\omega_q, t)]^2} \cdot \left[\Re[g_p] \frac{\partial \Im[g_p]}{\partial m_i} - \Im[g_p] \frac{\partial \Re[g_p]}{\partial m_i} \right] \,. \end{aligned} \tag{3.64}$$

The partial derivatives of $E_p(\omega_q, t)$ and $\Phi_p(\omega_q, t)$ with respect to Q_β^{-1} are similarly expressed as

$$\frac{\partial}{\partial Q_{\beta_i}^{-1}} E_p(\omega_q, t) \;=\; \frac{1}{2\,[E_p(\omega_q, t)]} \cdot \left(\frac{\partial g_p}{\partial Q_{\beta_i}^{-1}} \cdot \overline{g}_p + g_p \cdot \frac{\partial \overline{g}_p}{\partial Q_{\beta_i}^{-1}} \right) , \tag{3.65}$$

and

$$\frac{\partial}{\partial Q_{\beta_i}^{-1}} \Phi_p(\omega_q, t) = \frac{1}{[E_p(\omega_q, t)]^2} \cdot \left[\Re[g_p] \frac{\partial \Im[g_p]}{\partial Q_{\beta_i}^{-1}} - \Im[g_p] \frac{\partial \Re[g_p]}{\partial Q_{\beta_i}^{-1}} \right] \,. \tag{3.66}$$

Consequently, we obtain the partial derivatives of $E_p(\omega_q, t)$ and $\Phi_p(\omega_q, t)$ with respect to m_i and $Q_{\beta_i}^{-1}$ as the forms of (3.62), (3.64), (3.65), and (3.66). We then proceed with the non-linear inversion for obtaining combinations of the elastic parameters and the loss factors which minimise the differences between the observed and synthetic $E_p(\omega_q, t)$ and $\Phi_p(\omega_q, t)$.

3.3.2.5 formulation of the inversion procedure

The non-linear inversion scheme of Tarantola & Valette (1982) is suitable to minimise the difference between sets of secondary observables (E_p and Φ_p) based on the empirical data and those on the predicted model. It formulates the model vector $\mathbf{m}$ at iteration k+1 as

$$\widehat{\mathbf{m}}_{k+1} = \mathbf{m}_0 + C_{\mathbf{m}_0} G_k^t \left(C_{\mathbf{d}_0} + G_k C_{\mathbf{m}_0} G_k^t \right)^{-1} [\mathbf{d}_0 - \mathbf{d}(\widehat{\mathbf{m}}_k) + G_k(\widehat{\mathbf{m}}_k - \mathbf{m}_0)] , \qquad (3.67)$$

where $\mathbf{m}_0$ is the *a priori* model, $\mathbf{m}_1$ is the starting model, and $\widehat{\mathbf{m}}_k$ designates the predicted model at iteration k. The data vector $\mathbf{d}_0$ comprises the envelope $E_p(w_q, t)$ and the phase $\Phi_p(w_q, t)$ of the cross-correlogram $g_p(w_q, t)$ between the observed seismogram and the synthetics based on the *a priori* model $\mathbf{m}_0$. $\mathbf{d}(\widehat{\mathbf{m}}_k)$ means the predicted envelope and phase from the model $\widehat{\mathbf{m}}_k$. $C_{\mathbf{d}_0}$ and $C_{\mathbf{m}_0}$ represent the *a priori* covariance matrices of the data $\mathbf{d}_0$ and the model parameters $\mathbf{m}_0$. The matrix G_k denotes the partial derivatives of the data with respect to the model parameters at iteration k:

$$(G_{ij})_k = \left(\frac{\partial \widehat{d}_p^j}{\partial m_i} \right)_{\widehat{m}_k} \qquad (3.68)$$

where $\widehat{d}_p^j$ consists of the predicted secondary observables for the single mode p and the j-th frequency window. m_i indicates the i-th depth layer value of the model $\widehat{\mathbf{m}}_k$.

When a weak nonlinearity between the secondary observables and the elastic parameters is expected, the equation (3.67) should yield the best fit model $\mathbf{m}_{k+1}$ in a few iterations.

3.3.2.6 Construction of a 3-D model from 1-D structures along the paths

The second step of the CL inversion is to combine all the path specific 1-D wavespeed structures into a quasi 3-D model with lateral heterogeneity in shear wavespeed. In this step, we assume a linearity between a local slowness structure and a 1-D slowness structure between the epicentre and station. Thus we first present the basic idea of the linear inversion scheme for obtaining a quasi-3D model from the compilation of the 1-D structures. Based on Montagner (1986) we then introduce the transformation from a horizontal 2-D grid inversion to a continuous non-grid inversion.

Montagner (1986) elucidates the discrete form of the relation between the local phase slowness ($1/C^{loc}$) at a point along the ray path and the observed phase slowness ($1/C^{es}$) between the epicentre and station as

$$\frac{1}{C^{es}(T)} = \frac{1}{\Delta} \int_{path} \frac{1}{C^{loc}(T)} \, d\Delta \, , \qquad (3.69)$$

where T is the period of the observed surface waves and Δ indicates the path length between the epicentre and station. Assuming a weak nonlinearity between perturbations of the phase velocity (C) and of the SV wavespeed (β), Debayle & Kennett (2000a)

demonstrate that for weak heterogeneity the equation (3.69) can be transformed to the representation of the shear wavespeed β:

$$\frac{1}{\beta^{es}(z)} = \frac{1}{\Delta}\int_{path}\frac{1}{\beta^{loc}(z)}\,d\Delta\,, \tag{3.70}$$

where $\beta^{es}(z)$ means the shear wavespeed along the great circle path between the epicentre and the station and $\beta^{loc}(z)$ indicates the local shear wavespeed at a point r on the ray path at a depth z.

We extend (3.70) to a horizontal 2-D grid system (with index i and a total number of the grid n) with continuous vertical values (z). Assuming that the contribution of the local slowness (p^{loc}) to the slowness (p^{es}) between the epicentre and station is proportional to the ratio of the local path length (l) to the total path length (Δ), we can reformulate the relation (3.70) as

$$p_j^{es}(z) = \sum_{i=1}^{n}\frac{l_{ij}}{\Delta_j}\cdot p_i^{loc}(z)\,, \tag{3.71}$$

i : horizontal grid index
j : path index
l_{ij} : length of the local path crossing the i-th grid
Δ_j : total path length for a path j .

Thus we aim to invert the compilation of the slownesses (p^{es}) between all the epicentre-station pairs along the great circle paths into unknown local slownesses (p^{loc}) over the path coveraged region, with solving a general least-squares problem.

Solving the general non-linear least-squares problem means searching the pair of the empirical data vector($\mathbf{d}$) and the model parameter vector ($\mathbf{p}$) which simultaneously satisfies the following two conditions: (1) all the pairs obey the forward equation $\mathbf{d} = g(\mathbf{p})$; and (2) the pairs are the closest to the pair $(\mathbf{d}_0, \mathbf{p}_0)$ in the least-squares sense, where the subscript $_0$ represents the reference model. The above conditions are restated that the pair $(\mathbf{d}, \mathbf{p})$ we are seeking should fulfill the condition

$$minimum\left[(\mathbf{d}_0-\mathbf{d})C_{d_0d_0}^{-1}(\mathbf{d}_0-\mathbf{d}) + (\mathbf{p}_0-\mathbf{p})C_{p_0p_0}^{-1}(\mathbf{p}_0-\mathbf{p})\right]\,, \tag{3.72}$$

where

$$\mathbf{d} = g(\mathbf{p})\,. \tag{3.73}$$

$C_{d_0d_0}$, the covariance matrix of $\mathbf{d}_0$, becomes a diagonal matrix for independent data. Any error in the forward problem appears in the non-diagonal terms. $C_{p_0p_0}$, the covariance matrix of $\mathbf{p}_0$, represents the confidence in the model $\mathbf{p}_0(\mathbf{r})$. In addition, $C_{p_0p_0}$

provides additional *a priori* information on the model parameter $\mathbf{p}_0$ through correlating neighbouring points, if our inversion problem is highly underdetermined.

Tarantola & Valette (1982) demonstrate that the solution of the problem (3.72) meets the condition:

$$\hat{\mathbf{p}} = \mathbf{p}_0 + C_{p_0p_0}G^* \left(C_{d_0d_0} + GC_{p_0p_0}G^*\right)^{-1} \left\{\mathbf{d}_0 - g(\mathbf{p}) + G(\mathbf{p} - \mathbf{p}_0)\right\} , \tag{3.74}$$

where the linear operator G is the Frechet derivative at the point $\mathbf{p}$ of the non-linear operator g and G^* means the adjoint of G.

Solving the equation(3.74), Tarantola & Valette (1982) use an iterative locally linearised inversion scheme at a fixed point ($\mathbf{p}_k$; a model at the iteration k) :

$$\hat{\mathbf{p}}_{k+1} = \mathbf{p}_0 + C_{p_0p_0}G_k^* \left(C_{d_0d_0} + G_kC_{p_0p_0}G_k^*\right)^{-1} \left\{\mathbf{d}_0 - g(\mathbf{p}_k) - G(\mathbf{p}_k - \mathbf{p}_0)\right\} , \tag{3.75}$$

where the matrix G_k designates the derivative of g at the iteration k. This algorithm is exactly the same as the equation (3.67) used for obtaining the seismic parameters $\mathbf{m}$ for individual paths.

Based on the form of the equation (3.71), we can globally linearise the relation between the data ($\mathbf{d}$) and the model ($\mathbf{p}$) as

$$\mathbf{d}^{(j)} = g(\mathbf{p}) = \sum_{i=1}^{n} \frac{l_{ij}}{\Delta_j} \cdot p_i = G \cdot \mathbf{p} . \tag{3.76}$$

We are now seeking the solution of a globally linear problem, in stead of the nonlinear problem (3.74). Substituting the relation (3.76) into (3.75), we reach a converged solution after one iteration;

$$\hat{\mathbf{p}}_1 = \mathbf{p}_0 + C_{p_0p_0}G^* \left(C_{d_0d_0} + GC_{p_0p_0}G^*\right)^{-1} \left(\mathbf{d}_0 - G \cdot \mathbf{p}_0\right) , \tag{3.77}$$

Uncertainties in a linear solution for (3.77) are represented by the *a posteriori* covariance operator

$$C_{\hat{p}\hat{p}} = C_{p_0p_0} - C_{p_0p_0}G^* \left(C_{d_0d_0} + GC_{p_0p_0}G^*\right)^{-1} GC_{p_0p_0} . \tag{3.78}$$

To obtain a continuous model $\mathbf{p}(r)$ rather than a discrete model p_i at each grid i, we introduce a continuous vector (r) into the equation (3.71), instead of the i-th discrete horizontal grids. The formula of the globally linearised forward problem (3.76) can be rewritten as a continuous form;

$$\begin{aligned} d^j &= \int_{pathj} dr_j \cdot G^j(r_j) \cdot p(r_j) \\ &= \int_{pathj} \frac{dr_j}{\Delta j} \cdot p(r_j) , \end{aligned} \tag{3.79}$$

d^j is the path dependent model structure for a path j and $p(r)$ indicates a local model structure at a position r. We assume the integral is simply taken along the ray path.

Therefore the solution (3.77) takes a continuous form

$$\begin{aligned}\widehat{p}(r) &= p_0(r) + \sum_i \sum_j \int_{path i} \frac{dr_i}{\Delta i} \cdot C_{p_0 p_0}(r, r_i) \cdot (S^{-1})^{ij} \\ &\quad \cdot \left\{ d_0^j - \int_{path j} \frac{dr_j}{\Delta j} \cdot p_0(r_j) \right\} ,\end{aligned} \tag{3.80}$$

where

$$S^{ij} = (C_{d_0 d_0})^{ij} + \int_{path i} \frac{dr_i}{\Delta i} \int_{path j} \frac{dr_j}{\Delta j} \cdot C_{p_0 p_0}(r_i, r_j) \ . \tag{3.81}$$

The estimated error of the data measurement is represented by

$$C^{ij}_{d_0 d_0}(r_i, r_j) = \sigma_{d_0}(r_i) \cdot \sigma_{d_0}(r_j) \cdot \delta_{ij} \ , \tag{3.82}$$

where the *a priori* standard deviation $\sigma_{d_0}(\mathbf{r})$ denotes the uncertainty of the date measurement at a point r, when all the errors are independent and are within the order of σ_{d_0}.

The *a priori* information on the model p_0 is defined as the covariance function using a scale factor σ and a scale length L:

$$C_{p_0 p_0}(\mathbf{r}, \mathbf{r}') = \sigma_{p_0}(\mathbf{r}) \cdot \sigma_{p_0}(\mathbf{r}') \cdot \exp\left\{ -\frac{1}{2} \frac{\|\mathbf{r} - \mathbf{r}'\|^2}{L_{cor}^2} \right\} \ , \tag{3.83}$$

where the standard deviation σ_{p_0} is the uncertainty of the model p_0 at a point r which controls the amplitude of the perturbation, while L_{cor} is the correlation length between the two neighbouring points $(\mathbf{r}, \mathbf{r}')$ which decides the lateral smoothness of the model . This *a priori* Gaussian function therefore makes the *a priori* model smoothed in amplitude and lateral extension.

The estimation errors of the solutions $(\hat{p})$ to our linear problem can be represented by the *a posteriori* covariance matrix:

$$C_{\hat{p}\hat{p}}(r, r') = C_{p_0 p_0}(r, r') - A(r, r') \ , \tag{3.84}$$

where

$$A(\mathbf{r}, \mathbf{r}') = \sum_i^m \sum_j^m \int_{path\ i} C_{p_0 p_0}(r, r_i) \frac{dr_i}{\Delta_i} \cdot \int_{path\ j} (S^{-1})^{ij} \cdot C_{p_0 p_0}(r_j, r') \frac{dr_j}{\Delta_j} \ . \tag{3.85}$$

This *a posteriori* covariance matrix reveals how the errors of a new model are changed from *a priori* errors $(C_{p_0 p_0})$ of the parameters p_0.

4

COMPARISON OF SURFACE WAVE INVERSIONS

4.1 Introduction

In this chapter, we compare the two regional waveform inversion methods proposed by Nolet (1990) and Cara & Lévêque (1987) and attempt to find appropriate conditions under which the two classes of methods can be applied. To clarify the differences between the two methods, two kinds of synthetic tests are conducted. The first test is to examine the sensitivity of the two types of methods to different starting models. Waveform inversion is non-linear, because the dependence of the waveform on the seismic parameters is not simple. The Nolet-style method is a linearised iterative waveform inversion, so that its linearisation between the waveform and seismic parameters could lead to a stronger sensitivity to the starting model. On the other hand, Cara & Lévêque (1987) find an alternative representation involving secondary variables with the object of reducing the non-linearity. Thus, the CL method should be less sensitive to the starting model. If this speculation is appropriate, the differences in the sensitivity to the starting model could provide different classes of applications for the two methods. Thus, the PWI method by Nolet (1990) requires more prior information on the path coverage area than is needed for the CL method, while the CL method could be applied to regions where prior information has not been well accumulated.

The second test is to check how the two methods respond to the differences in crustal structures. We perform this kind of test by changing the shear wavespeed in the crust and also the Moho depth. The two waveform inversion methods make different assumptions about the treatment of crustal structure, so that they are likely to have different types of effects in crustal contamination of the upper mantle shear speed structure. Nolet (1990) includes the crustal structure into his inversion. In contrast, Cara & Lévêque (1987) exclude the crustal inversion and set the inversion region from just below the Moho depth

to the bottom of the transition zone. Consequently these different treatments of the crusts could affect the inversion results differently. However, no systematic evaluation of the differences has been done. Although Zielhuis & van der Hilst (1996) try to avoid the crustal contamination and only use their results below 80 km depth, they do not quantify how much the contamination might have occurred and to what depth it could have penetrated. Based on synthetic tests using several models of the thinner oceanic crust (5 - 11 km thick) Lévêque et al. (1991) point out that their method is sensitive to small variations in the near-surface crustal structures. They conclude that crustal contamination can reach up to 150 km depth.

For the Australian continent we have thicker continental crust and variations of the Moho over depths from 35 - 55 km are expected. Also, at the boundary between different crustal blocks and at the ocean-continent boundary where the crustal thickness is not constant but rapidly changes, strong lateral heterogeneities of the crustal shear wavespeeds can be expected. Because the two waveform inversion methods assume a 1-D crustal model which averages the shear wavespeed variations along the path, it is possible that the penetration depth of the crustal effect could be deeper and its amplitude could be larger than in the oceanic environment. In addition, the station-epicentre distribution of our surface wave data may tend to magnify crustal effects, because the majority of the surface waves we use in the inversion travel across the ocean-continent boundary or the boundaries between different crustal blocks.

4.2 Implementation of the two waveform inversion techniques

Each of the methods has different limitations and strengths, but the two techniques are based on a common set of assumptions related to the interpretation of the velocity model from the inversion as the path average of the shear wavespeed along the source receiver path. We describe the way in which the two waveform inversions are implemented here using a common data example.

4.2.1 Common assumptions used in surface waveform inversion techniques

The main assumptions employed are based on knowledge of the source mechanism and source-time function and a level of heterogeneity such that the propagation along the source-receiver path lies close to the great-circle path with independent propagation of the different modes (Kennett 1983, Chapter 6).

Although the two methods of waveform inversion described in the previous chapter have

many common assumptions, there are also significant differences in the way the inversion is carried out.

In each case the core of the scheme involves the comparison of observed and synthetic seismograms for a given source mechanism, either directly by Nolet (1990) or via secondary observables by Cara & Lévêque (1987). The synthetics in both cases are computed from a 1-D structure for the path, with known source character and an assumed crustal structure on the basis of three key assumptions:

(a) modes can be treated independently,

(b) propagation occurs along the great-circle between source and receiver,

(c) the receiver lies in the far-field of the source.

The source mechanism is taken from either the Harvard Centroid Moment Tensor catalogue or, for shallow events, from the body wave moment tensors calculated by the US National Earthquake Information Center (NEIC). The source excitation is included by using a point moment tensor following the point double couple source used by Cara (1979). The computation of the source excitation uses the eigenfunctions for both displacement and traction for each of the modes evaluated at the focal depth.

The frequency filtering applied to data and synthetics is designed to be such that the two sets of information should correspond as closely as possible. Kennett (1995) has given a discussion of the circumstances in which the assumptions (a) - (c) are likely to be reasonable and for propagation over distances of more than 1500 km suggests the frequency windows:

(1) 0.01 Hz - 0.020 Hz for fundamental mode,

(2) 0.01 Hz - 0.035 Hz for higher modes.

The treatment of the observed data at the receiver is somewhat different in the two methods. In the PWI approach the response of seismometers is deconvolved from all three-components to try to recover ground displacements. Whereas in the CL method, the instrumental effects are retained or the data is reshaped to match an alternative common instrument response e.g. to enhance low frequencies somewhat. Usually the application of the CL method keeps the vertical component response of the seismometer with the vertical component data, while the radial and tangential seismograms are reconvolved with the north-south component response to give a common dependence before rotation to the great circle.

4.2.1.1 Representation of seismograms

The synthetic seismograms employed in the inversion are based on simple approximations to the surface wave propagation in smoothly laterally varying media based on the assumption of great-circle propagation and that the receiver lies in the far-field of the source so that the dominant term in the frequency domain is a simple exponential phase term for each mode (see e.g. Kennett 1995). The work of Woodhouse (1974) indicates that for independent mode propagation the phase will be the integral of the phase-speed along the path which can be represented equivalently by a simple averaged phase speed multiplied by the epicentral distance.

In the PWI implementation three different crustal structures can be used: at the source, the propagation path and at the receiver. Care has to be taken that there is not too much contrast between these structures because the 'source' and 'receiver' terms in the seismogram representation are not just local (Kennett 1995). In the CL method different crustal models can be employed for the source and propagation path.

In the later synthetic examples a common upper mantle model is employed for the source, the propagation path and the receiver. This is a smoothed version of the Preliminary Reference Earth Model (PREM) model with no discontinuities in wavespeed.

When the level of heterogeneity is small, it is possible to demonstrate that the condition of averaged phase speed for each mode translates into an equivalent averaged shear wavespeed profile along the path (Debayle & Kennett, 2000a). However models for the shear wave variation in the Australian region include large deviations (8-10%) from the reference models and so the interpretation of the wavespeed profiles obtained from the inversion as path averages is based on extrapolation from the small heterogeneity case.

4.2.1.2 Modal independence

The waveform inversions assume that all the seismic waves are expressed as a summation of surface waves modes and that each mode propagates independently in the Earth. This assumption also needs to be examined. The real Earth contains lateral heterogeneity and the surface waves evolve as they travel along the propagation path. Such effects can be represented theoretically by coupling between the modes of a one-dimensional reference model, and the question arises as to how far such effects need to be included. Kennett & Nolet (1990) have discussed such mode-coupling along the path. Snieder (1986) has shown that scattering of surface waves can also be represented via mode coupling. He also illustrated that the effect of mode coupling on the seismogram became larger if the signal includes higher frequency content. The work of Marquering & Snieder (1995) indicates

that there are advantages in including mode-coupling for the treatment of higher mode arrivals at high frequencies which represent S body waves.

At lower frequencies the interaction of the fundamental and higher modes is weak. Indeed, ray tracing indicates that in the presence of heterogeneity, the paths of the fundamental and higher modes tend to differ from the great circle path in opposite senses. There is a greater likelihood of coupling between the higher modes but this can be controlled by a careful choice of frequency interval (see eg. Kennett, 1995)

4.2.2 Effects of the crustal model

We should bear in mind that our 'path average' crustal structure along the great circle path could have a strong influence on our inversion. For example, when the great circle path between the source and station comes across the ocean-continent boundary, the resulting 1-D crustal model is expected to represent an average between oceanic and continental crustal models. This average structure, however, will be quite different from both oceanic and continental models, particularly when changes of the Moho depth at the boundary are large across the boundary since the average thickness of the oceanic crust is 7 km, while the average thickness of the Australian continental crust is 40 km. The jump of the Moho depth will produce a strong velocity contrast between the vertical profiles on the two sides, so that the reflection and refraction of the seismic waves could occur at the boundary. Such jumps in velocity can cause multipathing effects, which can be misinterpreted as signals propagating along the great-circle path. In consequence, the inclusion of spurious data could influence the result of the waveform inversion by adding unnecessary information on the resulting structures.

4.2.3 Implementation of the PWI method

The Partitioned Waveform Inversion method (PWI) has been applied for the analysis of Rayleigh waves. The seismograms employed are the segments of vertical component records containing fundamental and higher mode Rayleigh waves. The fundamental mode has both lower frequency and lower group velocity and so separates in time from the higher modes representing the superposition of multiply reflected S waves.

4.2.3.1 Separate time window

We choose two time windows based on the group velocities of the different classes of modes. One window is designed to capture the fundamental mode Rayleigh wave and the other to include the higher mode SV waves. The fundamental mode window contains the signals with group velocity in the range 3.4 - 4.2 km/sec, while the higher mode window

covers group velocities of more than 4.0 km/sec. This separation improves the vertical resolution of structure, because the separation allows simultaneous waveform fitting in different frequency bands. Further, while the fundamental modes have relatively shallow penetration the higher modes sample to greater depth and give a different sampling of the structure. In particular, the regular occurrence of deep earthquakes along the convergent plate boundaries around Australia provides data which enhance the resolution of the deeper part of the velocity structure in the region of interest.

4.2.3.2 Frequency range

Two different band-pass filters were applied to the time windows. For the fundamental mode window, we applied a 10-25 mHz filter, while we filtered the higher mode waves in the 10-50 mHz range. Although filtering can have the effect of smearing and overlapping signals of different arrivals, there is a major benefit because the waveforms can be synthesized with fewer modes. In addition, Zielhuis & Nolet (1994) stated that the 25 mHz low-pass filter for the fundamental mode window avoids the influence of scattering on the velocity model. They also described the fact that higher mode signals up to 50 mHz had little scattering effect on the one-dimensional model. These empirical conclusions are supported by the theoretical study of Kennett & Nolet (1990), which showed that the assumption of independent propagation of mode contributions is valid for a model with modest upper mantle heterogeneity for the fundamental mode up to 20 mHz and for the higher modes up to 50 mHz.

4.2.3.3 Forward modeling

Once we have an adequate starting model, we can synthesize multi-mode seismograms. We then compare the synthetic and the filtered seismograms in order to evaluate the starting model and the information on the source. The waveform calculation has to be based on both an adequate starting model and accurate information on focal depth and source mechanism. In their study of Europe using the PWI method, Zielhuis & Nolet (1994), have found, however, that an earthquake in the Mediterranean Sea had three incompatible source mechanisms. They pointed out that the inaccurate focal mechanisms of the Mediterranean earthquake gave rise to difficulty of the waveform fittings. Also Zielhuis & Nolet (1994) indicated that choice of the starting model clearly changed the amplitude and phase of the synthetic seismograms.

4.2.3.4 Waveform matching (envelope mode)

To find the global minimum of the penalty function without ending up a local minimum, we start with a low upper corner frequency in the filtration process. We applied a 10-20

mHz band-pass filter to the fundamental mode wave and the 10-40 mHz filter to the higher mode waves. We then iteratively matched the envelope of the synthetic signal to that of the observed waveform in the two time windows. In other words, we performed group velocity matching for the fundamental mode and higher mode waves, when one of the time windows showed very poor fit to the envelope. We did not use the waves in the next step, namely the phase velocity matching. However, when the envelopes of the synthetic higher modes and the synthetic fundamental modes fit well to those of the observations, we used both higher and fundamental modes in the next step.

4.2.3.5 Waveform matching (waveform mode)

Adding higher frequency signals to the data, we conducted more detailed matching to improve the resolution of the phase velocity information. For the fundamental mode, the upper corner frequency was increased from 20 mHz to 25 mHz in steps. For the higher modes, we raised the upper limit of the frequency window to 50 mHz. When the higher mode fitting is quite poor, we usually move back to the envelope mode matching and then try to fit only fundamental mode waves.

4.2.4 Implementation of Secondary Variable Inversion

The Cara & Lévêque method has been used for the inversion of Rayleigh waves on the vertical component (Lévêque et al., 1991) and for both Rayleigh and Love waves on the vertical and tangential components (Debayle & Lévêque, 1997). The characteristic of the CL method is to introduce 'secondary observables' as a new data set, instead of directly dealing with waveform data themselves. This is because the relation between the secondary observables and the seismic parameters is expected to be less non-linear than that between the waveforms and the seismic parameters.

4.2.4.1 Prior information

The inversion scheme developed by Tarantola & Vallette (1982) is required to set appropriate prior information on the covariance matrices of the secondary observables ($\mathbf{d_0}$) and of the initial model ($\mathbf{m_0}$). Both covariance matrices are represented by the form:

$$C(\mathbf{r},\mathbf{r}') = \sigma(\mathbf{r})\cdot\sigma(\mathbf{r}')\cdot\exp\left\{-\frac{1}{2}\frac{\|\mathbf{r}-\mathbf{r}'\|^2}{L_{cor}^2}\right\}\cdot C_{mn}\ . \tag{4.1}$$

Thus we need to set prior information on the standard deviation (σ), the correlation length (L_{cor}), and the coupling matrix (C_{mn}) for both initial model ($\mathbf{m_0}$) and the secondary observables ($\mathbf{d_0}$).

For our Rayleigh and Love joint inversion, the model ($\mathbf{m_0}$) consists of the SV wavespeed β_v, the anisotropic parameter ξ, the quality factor $logQ_\beta$, and the seismic moment $logM_0$. The standard deviations $\sigma(\mathbf{r})$ have been set to 0.05 for β_v, 0.03 for ξ, 0.3 for $logQ_\beta$, and 0.5 for $logM_0$. We assume there is no prior coupling among the four elements, so that the coupling matrix C_{mn} is a diagonal matrix. The correlation length (L_{cor}) which represents vertical dependence of each element is commonly set to 50 km. The secondary observables ($\mathbf{d_0}$) are comprised of the envelope data (g_p) and the phase data (Φ_p) for mode p. Their standard deviations are set to 5 % for the envelope data and 1% for the phase data. We assume the data covariance matrix is diagonal. Lévêque et al. (1991) point out that the validity of this assumption depends on the contents of the actual signal; however, if the spacing of the central frequencies of the bandpass filters is chosen equal to their bandpass width, this assumption can be justified.

4.2.4.2 Time window and frequency range

The CL method takes rather longer time-windows which contain the major portions of the fundamental and several higher mode Rayleigh and Love waves on the vertical and horizontal components. The time-windows cover group velocities in the range of 7 - 2.2 km/sec.

We then take cross-correlation between the windowed empirical waveform and the windowed single-mode synthetic seismogram for each mode (p) which is calculated from a given source mechanism and wavespeed structures. From the resulting cross-correlogram for each mode, we further construct the empirical secondary observables for each mode: the envelope function g_p and the phase Φ_p.

Similarly, the cross-correlations between the full-mode (5 modes) synthetic seismogram and single-mode synthetic seismograms are taken and produce the two synthetic secondary observables for each mode.

The next step is to find the optimal model parameters ($\mathbf{m}$) which minimise the difference between the synthetic and empirical secondary observables (g_p and Φ_p). These model parameters are expected to produce a good match between the synthetic seismogram and the observed seismogram. To achieve good matches of the synthetic and observed waveforms in a wide range of frequency, several bandpass filters are applied to both types of secondary observables. In our case, the central frequencies of the filters are 0.02 Hz (50s) and 0.01 Hz (100s).

4.2.4.3 Matching of the secondary observables

The inversion procedure starts to match the synthetic envelope to the observed envelope sequentially from the fundamental mode to higher modes with changing the model ($\mathbf{m}$).

One envelope is represented by three samples, so that we try to make the three points on the synthetic envelope closer to those on the observed envelope. After obtaining satisfactory matches of the envelopes, we further attempt to match the phases (Φ_p) of the filtered cross-correlograms for each mode.

This matching procedure for each mode for different frequency ranges is designed to try to extract the maximum information from the secondary observables. In particular, different frequency windows for different modes have different vertical sensitivity kernels, so that this matching procedure can obtain more homogeneous vertical coverage of the model than other approaches.

4.3 Comparison of Waveform Inversions

Both the PWI and CL styles of approach for building a 3-D upper mantle model use a linear inversion based on the interpretation of the 1-D shear wavespeed models along many source-receiver paths as path averages. However, the two approaches differ in the way that they deal with waveforms and their dependence on the velocity structure. As we have discussed above the PWI approach follows Nolet (1990) by dividing vertical component Rayleigh waves records into two different group velocity windows with different frequency filters and applies a non-linear waveform matching to each window as a means of obtaining 1-D structures. On the other hand, the inversion scheme of Cara & Lévêque (1987) does not separate the waveforms into different windows nor directly inverts the Rayleigh wave seismograms into a shear wave speed structure. With the aim of decreasing the strong non-linearity between waveforms and the wave speed profile, the CL method uses secondary observables derived from the cross-correlation of synthetic seismograms for individual modes with filtered observations.

4.3.1 Synthetic tests: method and 'observed' data

In order to understand the impact of upper mantle reference structure and variations in crustal properties on the two styles of inversions we have carried out inversion tests using surface wave trains calculated for known models as the 'observed' data.

The most difficult circumstance for metering mantle structure comes for shallow events for which the fundamental mode dominates the seismograms and there is little excitation of the higher modes and hence limited penetration to depth. We have therefore used a simulation of the data recorded at station CAN for the shallow earthquake in the Kimberly near the town of Derby. The source information

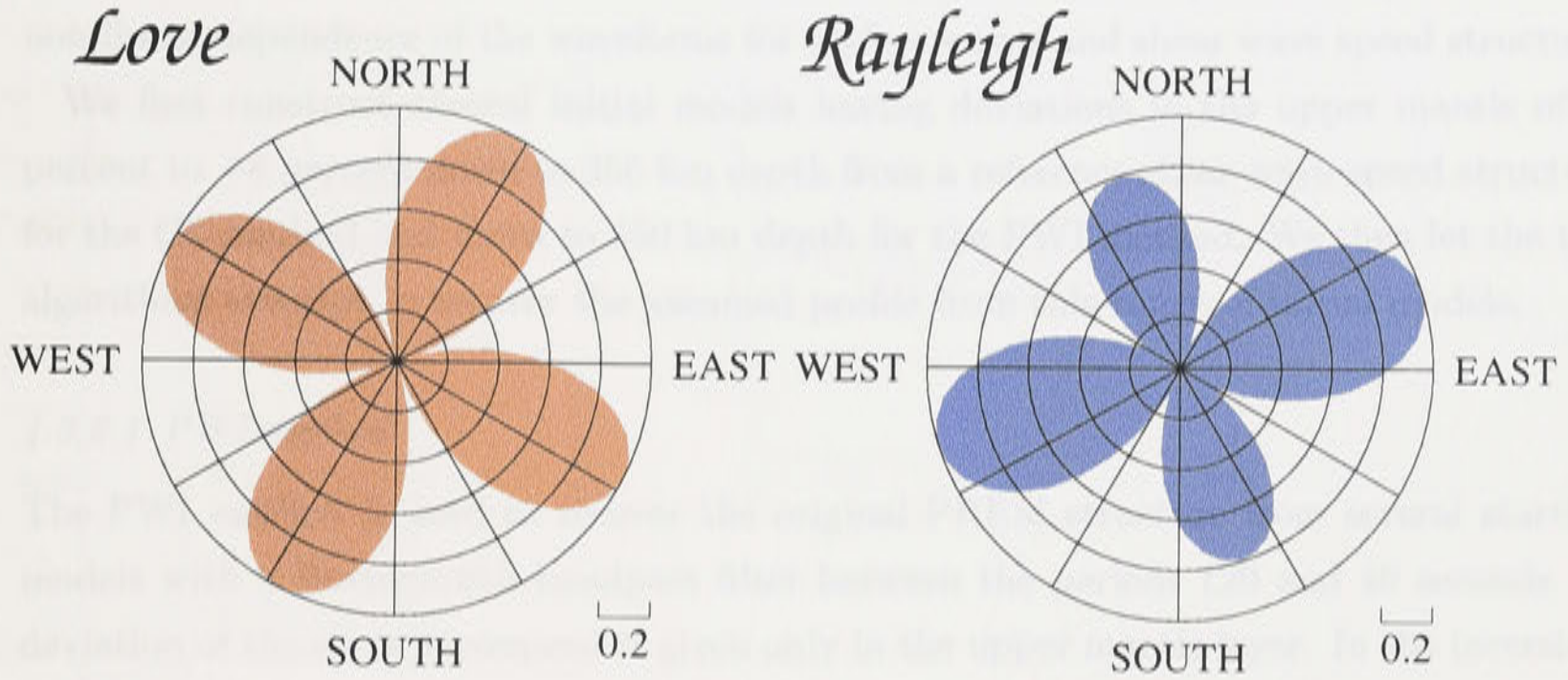

Fig. 4.1. Source mechanism used for synthetic tests on structure recovery, the station CAN lies at azimuth 135.64 degree and is thus moderately close to a Rayleigh wave node.

on the 'Derby' event from the Harvard CMT catalog is in the following table.

Region	Date	Time	Lat.	Lon.	Depth	Mw	mb	Ms
West. Australia	970810	09:20:38	-15.98	124.48	15.0	6.2	5.9	6.0

We use the focal depth of 10 km which comes from the NEIC data catalog, in stead of the centroid depth 15 km for this very shallow event.

Seismograms were synthesized using the smoothed PREM model with the source mechanism for the Derby event placed at a depth of 10 km (figure 4.1). For comparison the same focal mechanism was also used at depths of 100, 200 and 300 km for which the higher modes become increasingly important.

The first set of tests were based on using different starting models for upper mantle structure with the object of retrieving the structure used to create the data. The second set concentrates on the influence that misestimation of crustal structure might make on the velocity model recovered for the upper mantle.

4.3.2 Sensitivity tests for different initial models in the upper mantle

A group of synthetic tests was carried out for each of the CL and PWI methods to determine how sensitive the different approaches are to the starting models used in the waveform inversion procedures. The methods differ in the way that they handle the non-linear dependence of the waveforms for surface waves and shear wave speed structure.

We first construct several initial models having deviations in the upper mantle of -4 percent to +8 percent down to 350 km depth from a reference shear wave speed structure for the CL method and down to 650 km depth for the PWI method. We then let the two algorithms attempt to recover the assumed profile from this range of initial models.

4.3.2.1 PWI method

The PWI method is used to recover the original PREM structure from several starting models with a Butterworth bandpass filter between the periods 120 and 40 seconds. A deviation of the shear wavespeed is given only in the upper mantle layer. In the inversion, both crustal and mantle structures are inverted using one time-window, so that the information on the fundamental Rayleigh waves is mainly extracted. We also attempt to match both fundamental mode and several overtones in two time-windows. However, higher modes are not very well excited by the Derby source mechanism (its focal depth is set to 10 km), so that the two time-window approach fails to recover even 3 % deviation from the smoothed PREM model. Thus, the following recovery tests are all performed using one time-window which including the major portion of overtones and fundamental mode.

We start the first recovery test with the initial model having +3% deviation of the shear wavespeed from the smoothed PREM model (figure 4.2). The final recovered model is in good accordance with the smoothed PREM model between about 80 km and 250 km depths. However, in the layer above about 80 km, we observe significant differences between the recovered model and the smoothed PREM model. Although the starting model has no deviation from the smoothed PREM model in the crust, the inversion algorithm tries to make the crustal wavespeed slower and the wavespeed in the uppermost mantle (down to 80 km) faster. This is probably because there is not enough higher mode energy between the period of 120s to 40s to recover the structure above about 80 km depth. In the layer deeper than about 250 km, the curve of the recovered model gradually converges to the starting model, while decreasing the vertical resolution of both fundamental and higher mode Rayleigh waves in this frequency range.

In the next recovery test, we put +4 % deviation of the shear wavespeed to the initial model (blue line in the figure 4.3a). The recovery appears less significant and only the

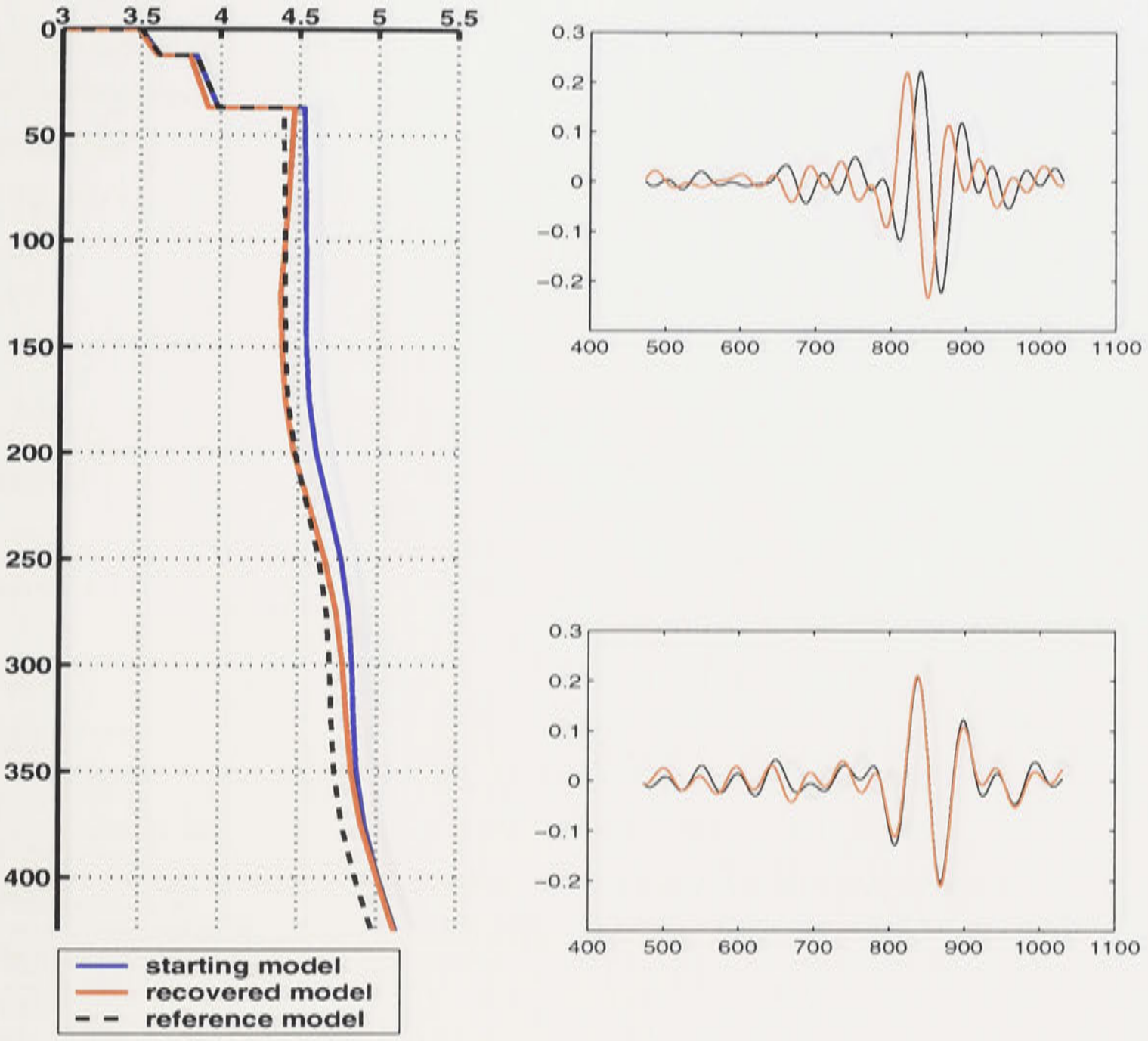

Fig. 4.2. The results of the PWI synthetic recovery test of the vertical component Rayleigh waves. (a) The left plot displays the final recovery of the shear wavespeed model (red line) from the starting model of +3 % deviation (blue line) from a smoothed PREM (dashed black line). The focal depth is 10 km. (b) The upper-right plots show that the 'observed' seismogram (thin black line) synthesized by the smoothed PREM model and the forward seismogram (thin red line) based on the starting model. (C) The lower-right plots indicate the final waveform matches between the observed data and final model. The bandpass filter between the wave period of 40 and 120 seconds is applied to all the signals.

layer between 100 km and 180 km depths is somewhat retrieved. Corresponding to the fluctuations of the recovered profile in the shallow layer, the higher mode waveform matching (figure 4.3c) degrades over the whole time series. However, the major portion of the fundamental Rayleigh waves maintains a good match to the observed seismogram.

When the starting model shifts +6% from the reference model (figure 4.4a), an

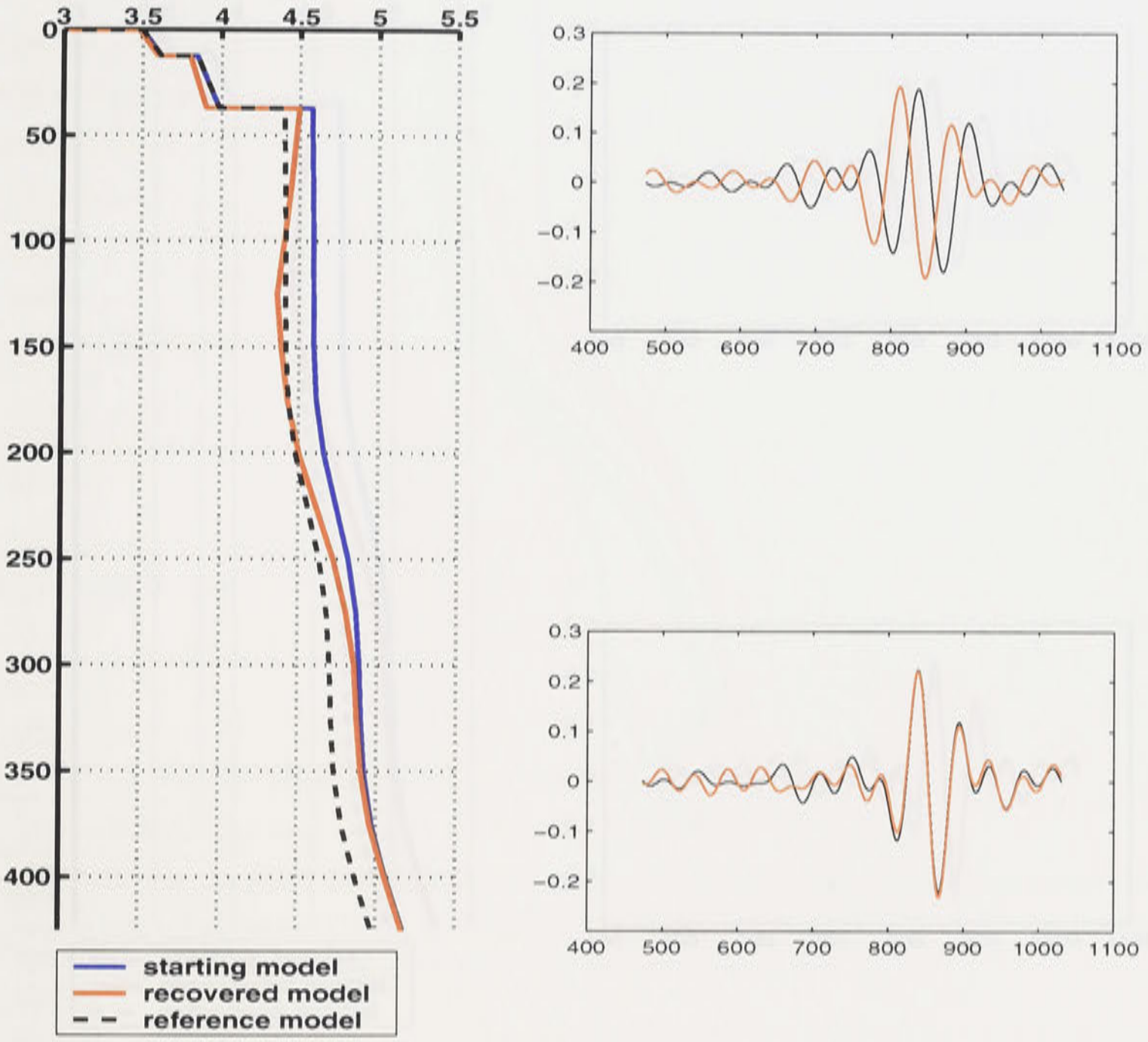

Fig. 4.3. The results of the same test as in figure 4.2. But the deviation is + 4 %.

acceptable level of the recovery is achieved only in the layer between 80 km and 120 km depths. The perturbation of the shear wavespeed in the crust becomes the largest among the synthetic recovery tests. Moreover, the waveform matches of the fundamental mode Rayleigh waves as well as the high modes become poorer and amplitude differences over the whole time series cannot be ignored.

From the above examples (figures 4.2 to 4.4), it is safe to say that the PWI single time-window approach can recover the reference smoothed PREM structure in the layer between 80 km 250 km depths, if the starting model has less than +4% difference from

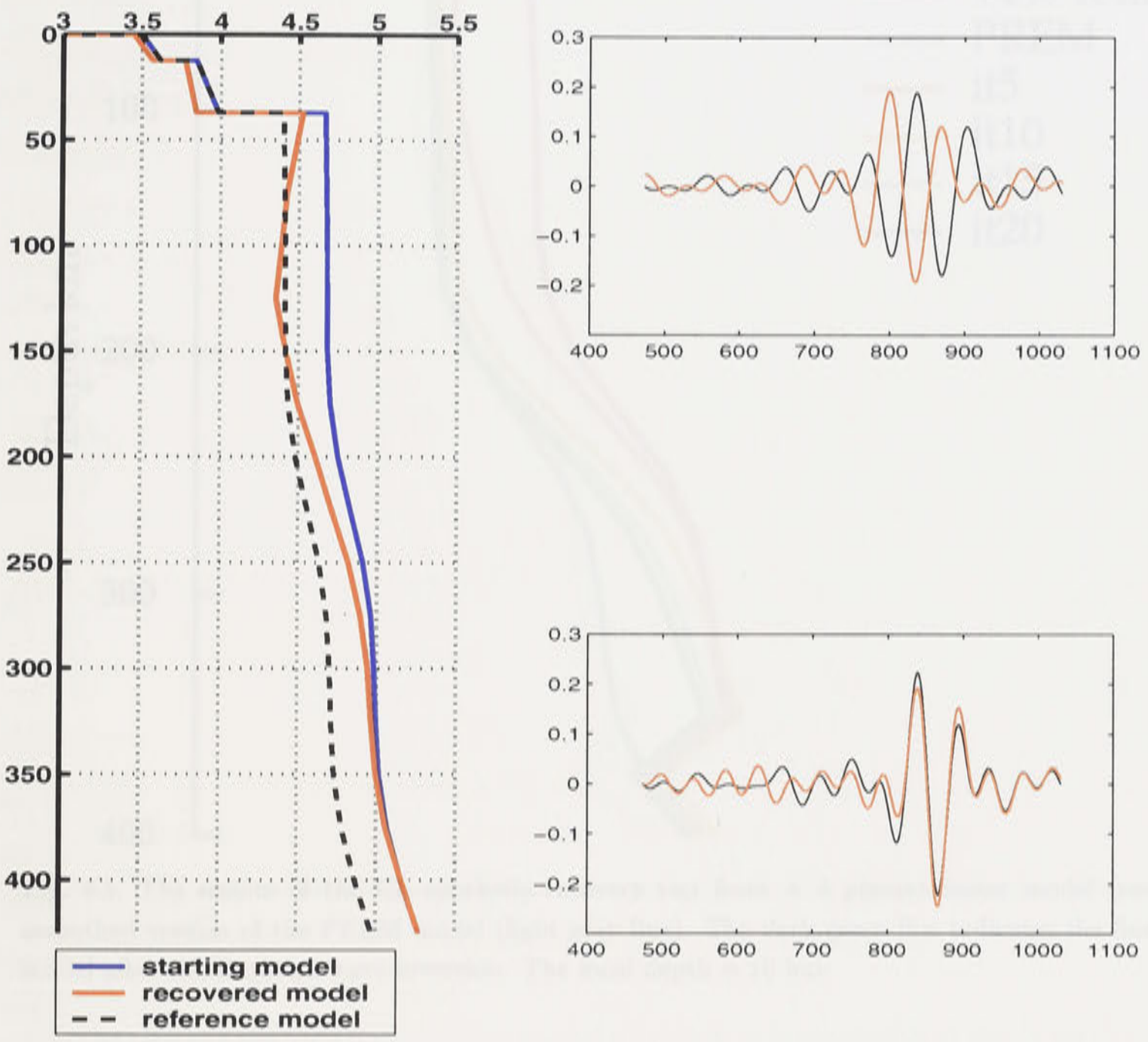

Fig. 4.4. The results of the same test as in figure 4.2. But the deviation is + 6 %.

the smoothed PREM model. However, if the deviation goes beyond 4 % ,the final profiles have acceptable recoveries of the reference model only in a rather limited depth range.

4.3.2.2 CL method

The CL method is expected to be less dependent on the starting model than the PWI method, because the CL method uses the 'secondary observables' and tries to make the relation between the waveform information and the seismic structure weakly non-linear. Thus, we perform more detailed synthetic tests for the CL inversion. In addition to the

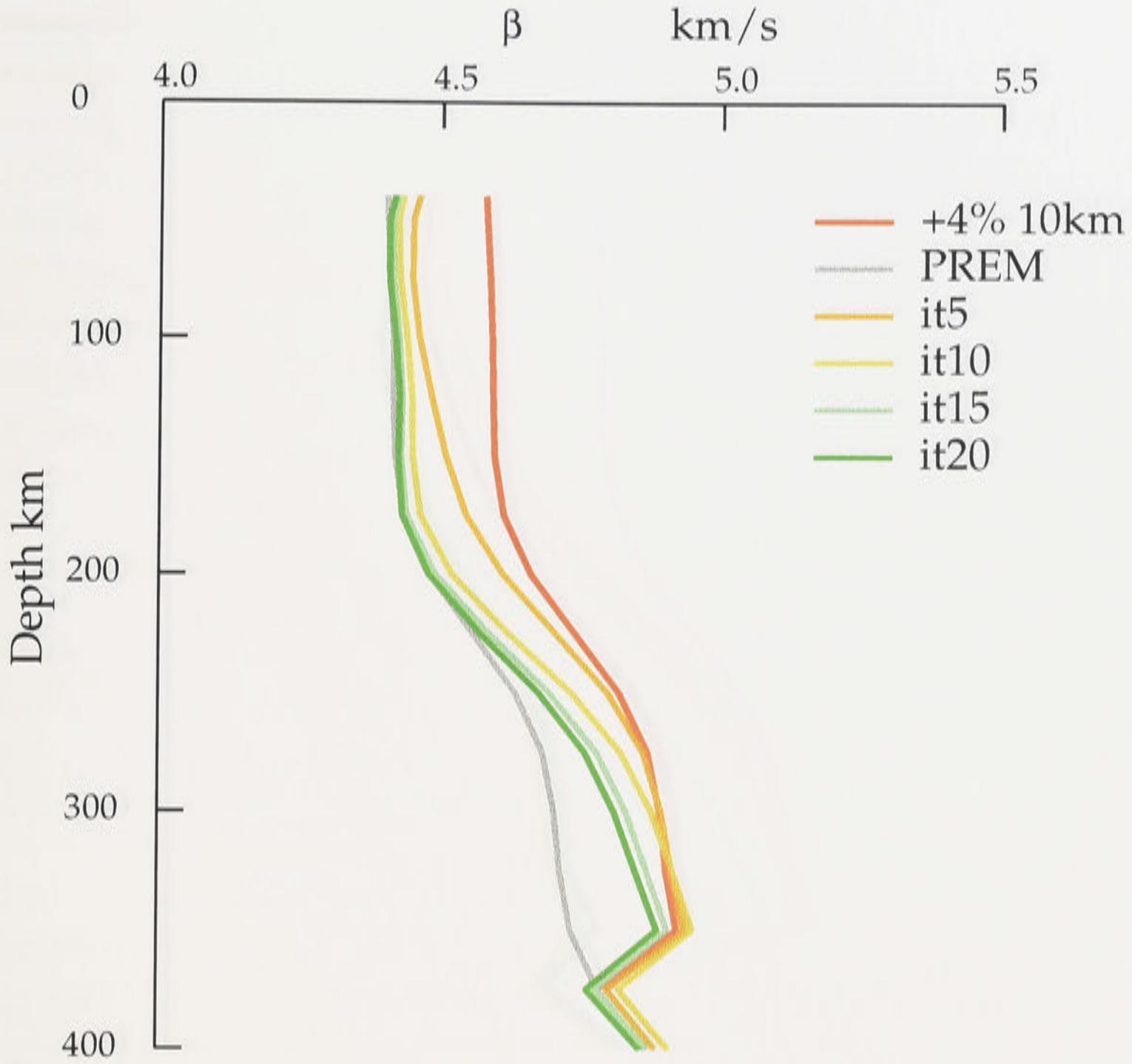

Fig. 4.5. The results of the CL synthetic recovery test from + 4 percent faster model (red line) to a smoothed version of the PREM model (light gray line). The dark green line indicates the final recovered model after the Rayleigh wave inversion. The focal depth is 10 km.

changes of the shear wavespeed structure, different focal depths (10 km to 200 km) are introduced.

The CL method was applied to each of the initial models with a constant of filters at 40s, 70s and 120s with inversion for both the envelope and phase of the modal cross-correlation functions. Inversion was carried out for shear wavespeed in the mantle alone, with fixed crustal structure.

With a deviation of the shear wavespeed in the upper mantle by ± 2% from the smoothed PREM reference model the recovery of the model is quite good to 200 km for a source at 10 km depth, but as the fundamental mode amplitude diminishes, and so little information is available, the wavespeed tends towards the starting model. If the source depth is shifted to

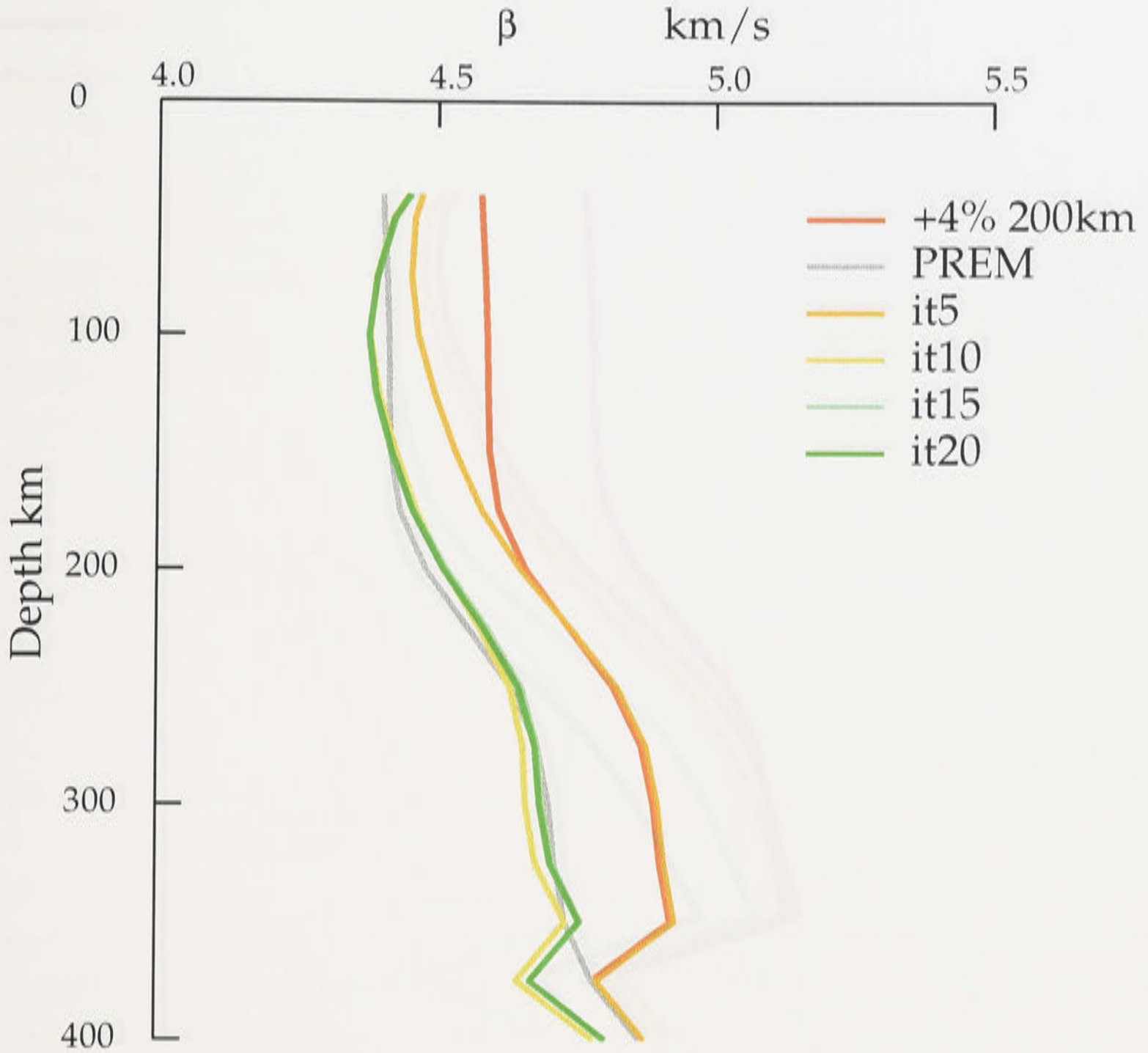

Fig. 4.6. The results of the same synthetic test as in figure 4.5. But the focal depth is 200 km.

100 km the recovery of the starting model at depth is improved and the inversion converges to a model which nearly coincides with the true structure down to 280 km depth.

We might expect that such modest perturbations should be recoverable and in the next group of tests the amplitude of the shifts in the initial models was doubled to ±4%. We illustrate the behaviour for a shift of +4% from the true model but a very similar class of results are obtained with a -4% shift. In each case we are able to recover a significant segment of the true structure with an increased depth range when the source depth is greater and so higher mode information is available.

We consider source depths of 10, 100 and 200 km and show the progress of the inversion by plotting the velocity model at intervals of 5 iterations and the modal correlation functions and model fit for the final model (20 iterations of the linearised inversion). Note that the partial derivatives are not updated during the calculations and these continue to

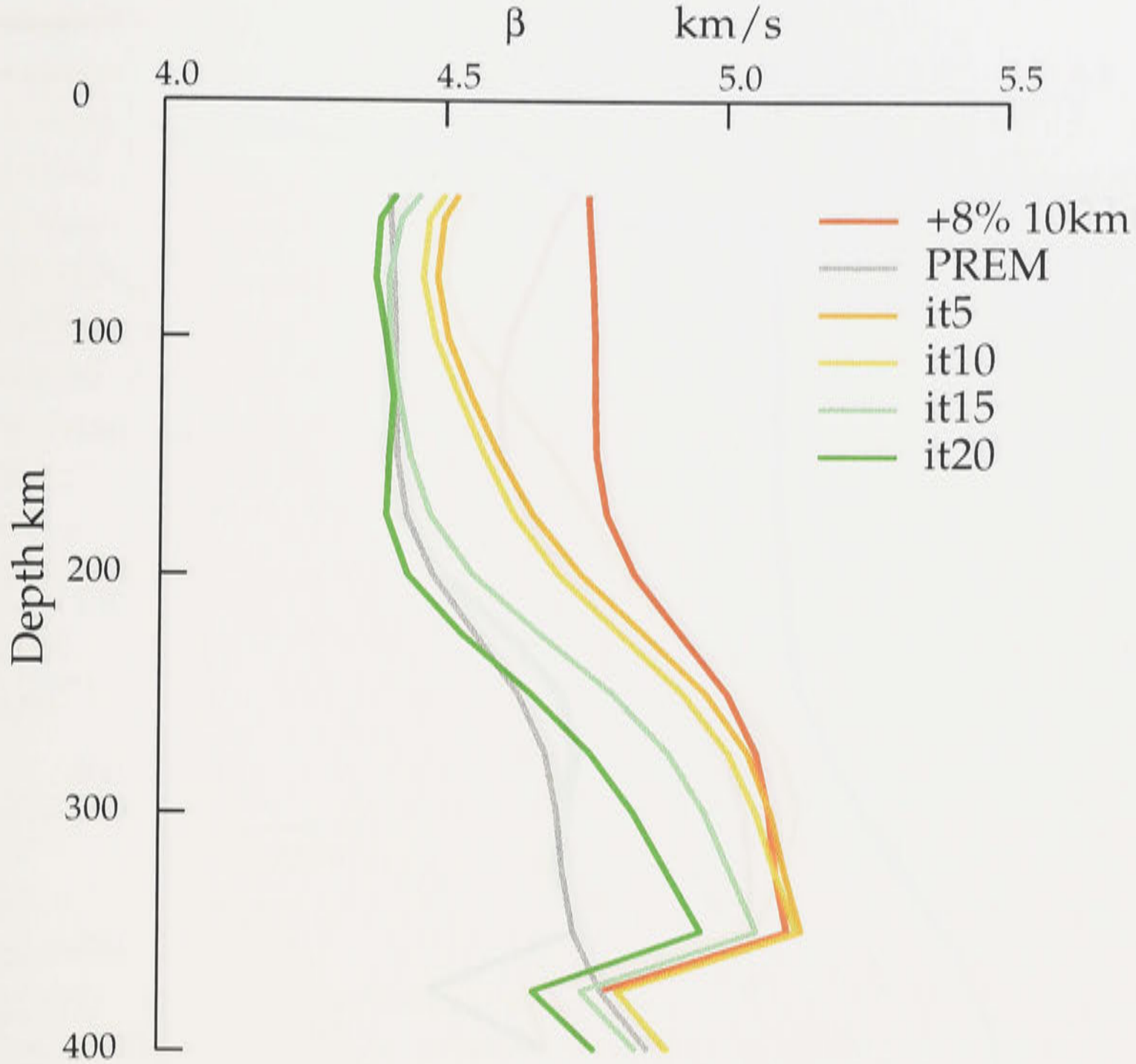

Fig. 4.7. The results of the same synthetic test. But the deviation of the starting model (red line) from the *PREM* model reaches + 8%. The focal depth is 10 km.

be evaluated for the initial model even though the wavespeed model is varying through the iterations.

For the shallowest source at 10 km depth, the uppermost mantle rapidly tends towards the true velocity profile and with progressive iterations extends to greater depth with a good match down to 200 km (figure 4.5).

When the source is moved to 100 km the match of the velocity model is extended to below 250 km as the higher modes begin to contribute to the inversion, but the effects are most marked for a source at 200 km depth for which nearly full recovery of the true profile can be achieved (figure 4.6).

Thus for a deviation as large as 4% the CL method provides a good recovery of the true model in a depth range dictated by the information content of the 'observed' seismogram.

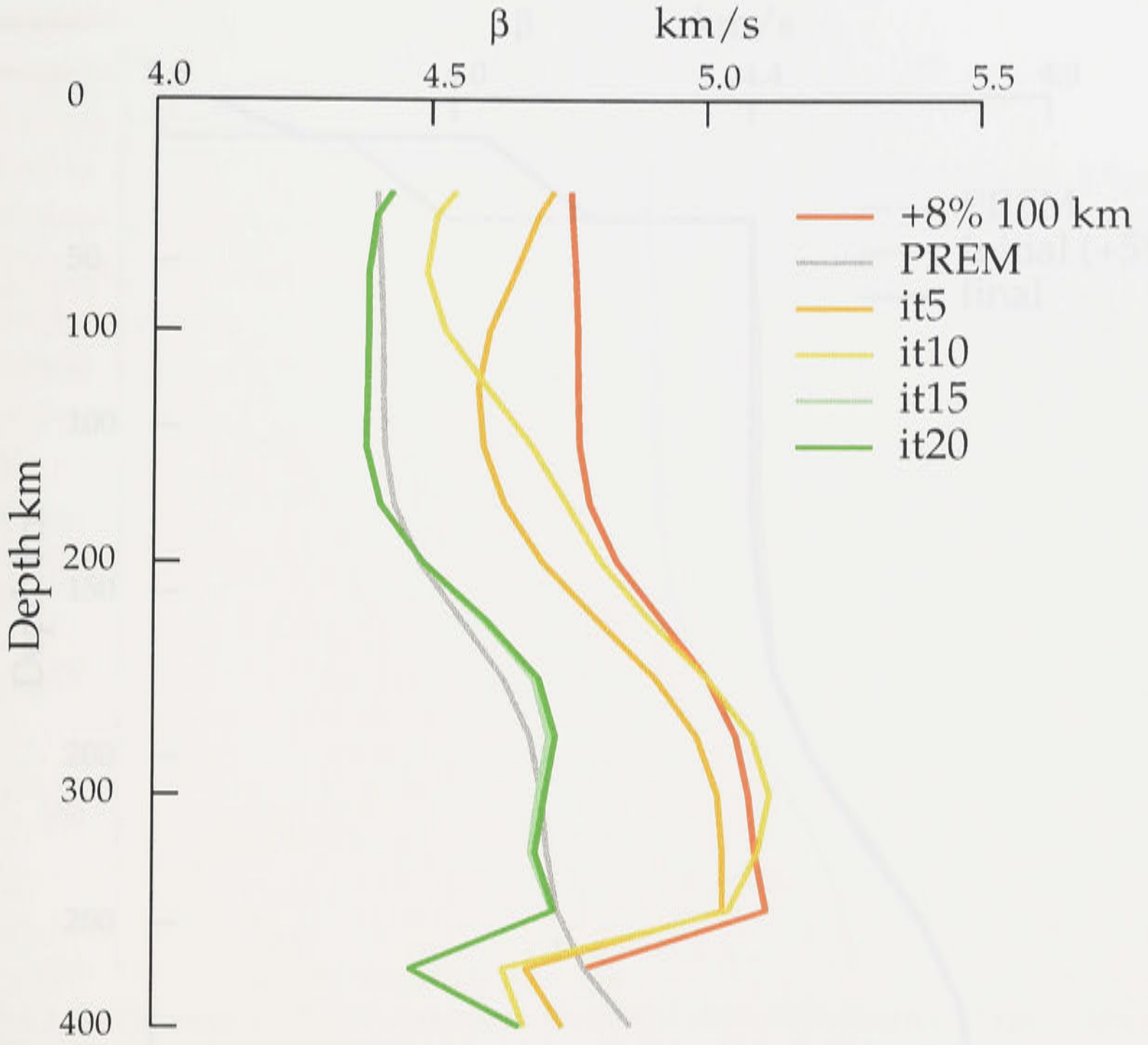

Fig. 4.8. The results of the same synthetic test as in figure 4.7. The focal depth is 100 km.

The aim of the use of the secondary observables is to extend the range of the quasi-linear dependence on the model and clearly ±4% is well within the effective range of convergence.

Even for an 8% shift from the starting model there is both rapid convergence and good recovery of the true shear wavespeed profile for the Rayleigh wave. Figure 4.7 shows the convergence for a source at 10 km depth with a close match to the target; however, the fit to the seismograms is beginning to suffer a little with this large perturbation as we reach the limits of the zone of linearity. A reasonable recovery of the true velocity profile can also be achieved for a source at 100 km depth but small amplitude oscillations become apparent (figure 4.8).

4.3.3 Sensitivity tests for different crustal structures

Although the previous regional tomographic studies of the Australian continent (eg. Debayle & Kennett, 2000a) have tried hard to avoid the effects of mistreatments of the

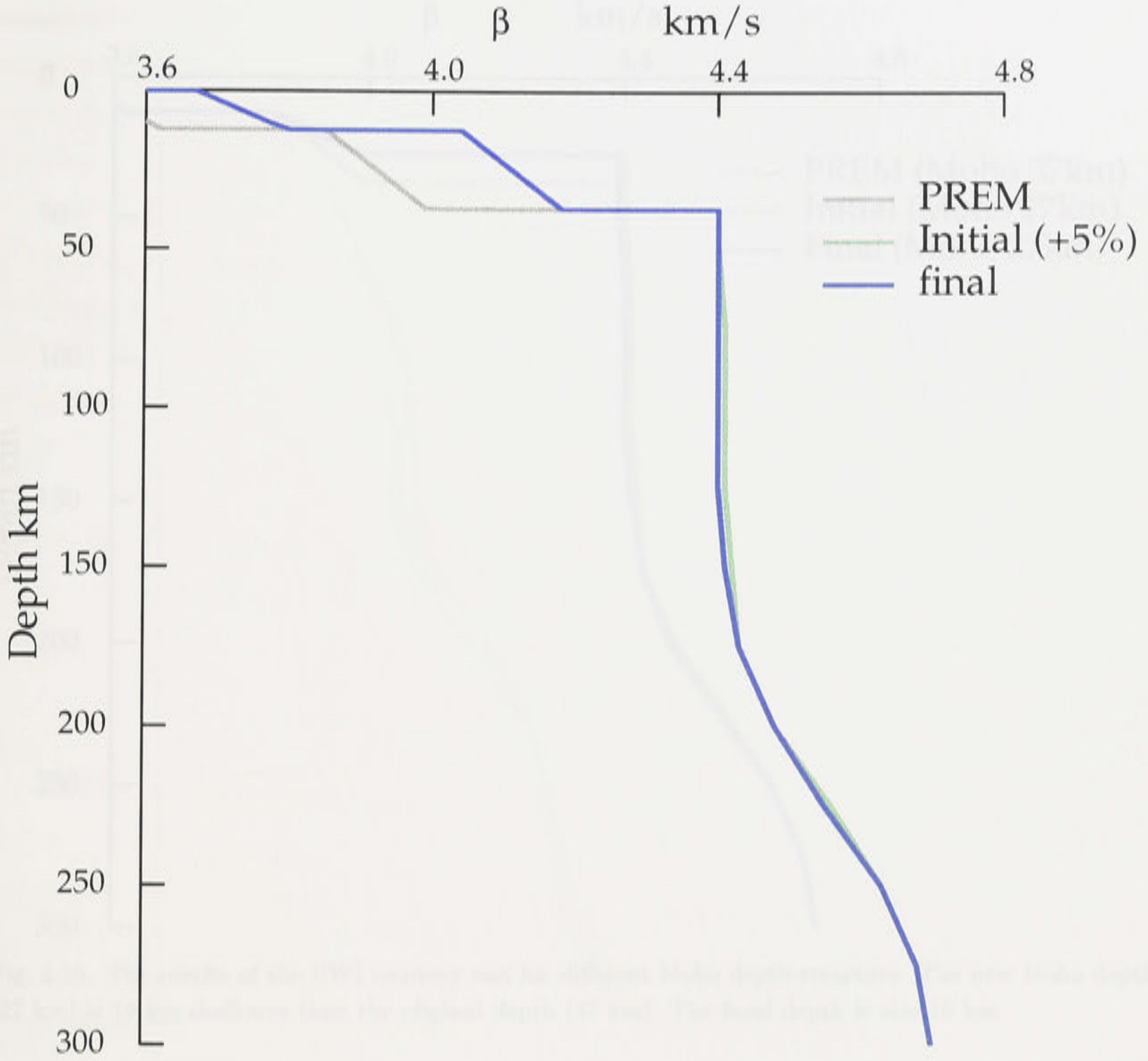

Fig. 4.9. The results of the PWI synthetic recovery test for different crustal structure. In this case, +5 % deviation is given only in the crust. The PWI algorithm inverts shear wavespeed in the layer from the surface to the bottom of the transition zone (675 km). The focal depth is 10 km.

crust with restricting the working frequency range, the travelling distance, and the starting depth of the inversion, very few studies (eg. Lévêque et al., 1991) quantify how much crustal effects could propagate into their inversion results. It is therefore worthwhile isolating the effect of misestimates of the crustal model along the great circle path and delineating the consequent influence on the inversion results.

In the following synthetic recovery tests for different crustal structures, both PWI and CL methods use two different starting models with the working frequency range between 40s to 120s.

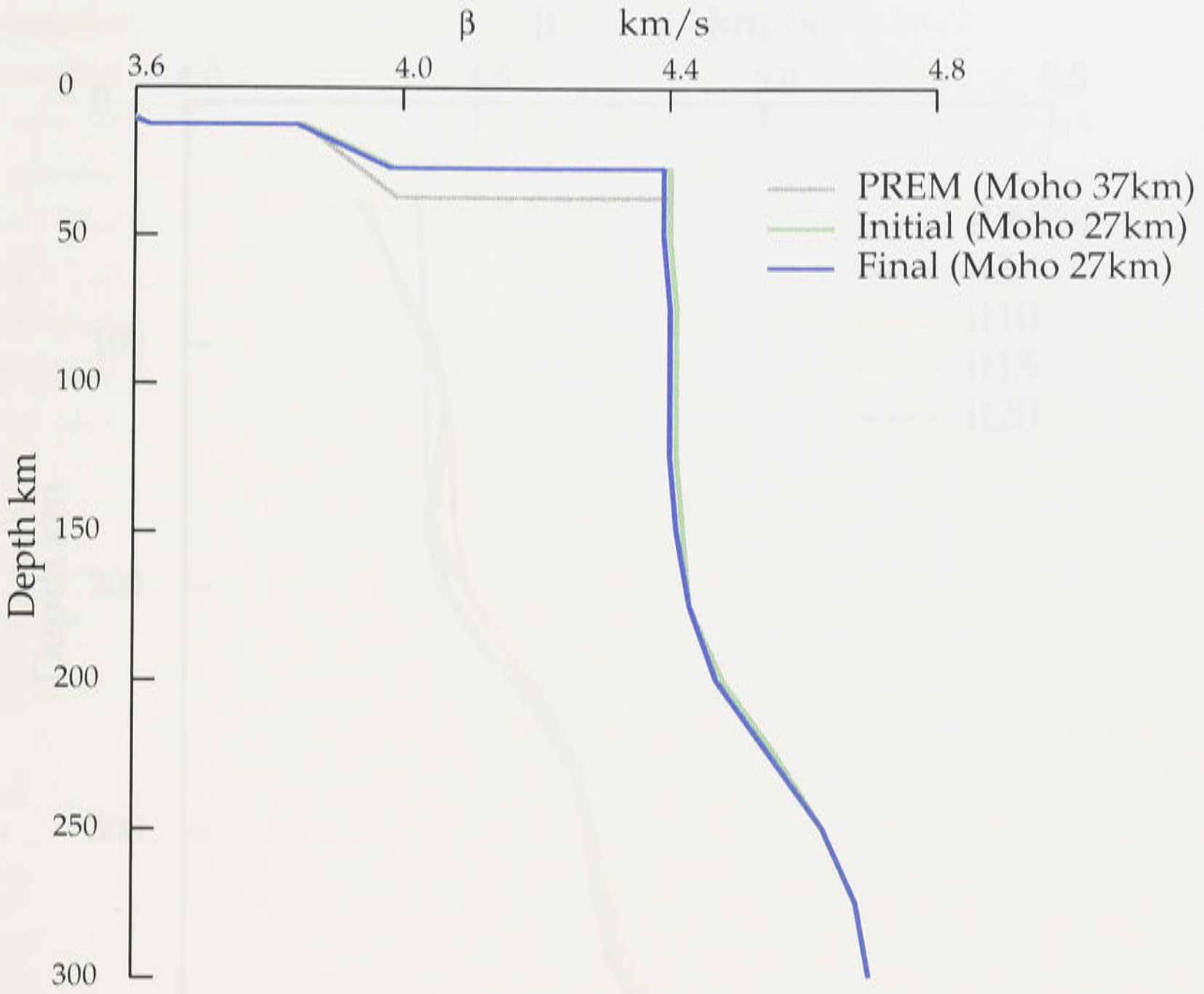

Fig. 4.10. The results of the PWI recovery test for different Moho depth structure. The new Moho depth (27 km) is 10 km shallower than the original depth (37 km). The focal depth is also 10 km.

4.3.3.1 PWI method

We prepare for two different starting models for two PWI synthetic tests. The first starting model allows 5 % deviation of β_v from the smoothed PREM model only in the crust and the other initial model has the 10 km shallower Moho depth (27 km) than the original Moho depth (37 km). Both PWI inversions are conducted in the layer from the surface to the bottom of the transition zone (675 km).

+5% deviation of β_v in the crust : We first allow only the crust layer to change β_v and let the algorithm recover + 5% difference from the smoothed PREM model given in the crust. As a result, about 2 % of the deviation is recovered in the crust, probably because the sensitivity kernels of the modes we use have very small values in the crust for the current working frequency range (0.008 Hz-0.025 Hz), so that the PWI algorithm cannot fully recover the 5 % deviation in the crust.

Next, we allow the layers from the surface down to 300 km depth to adjust β_v for

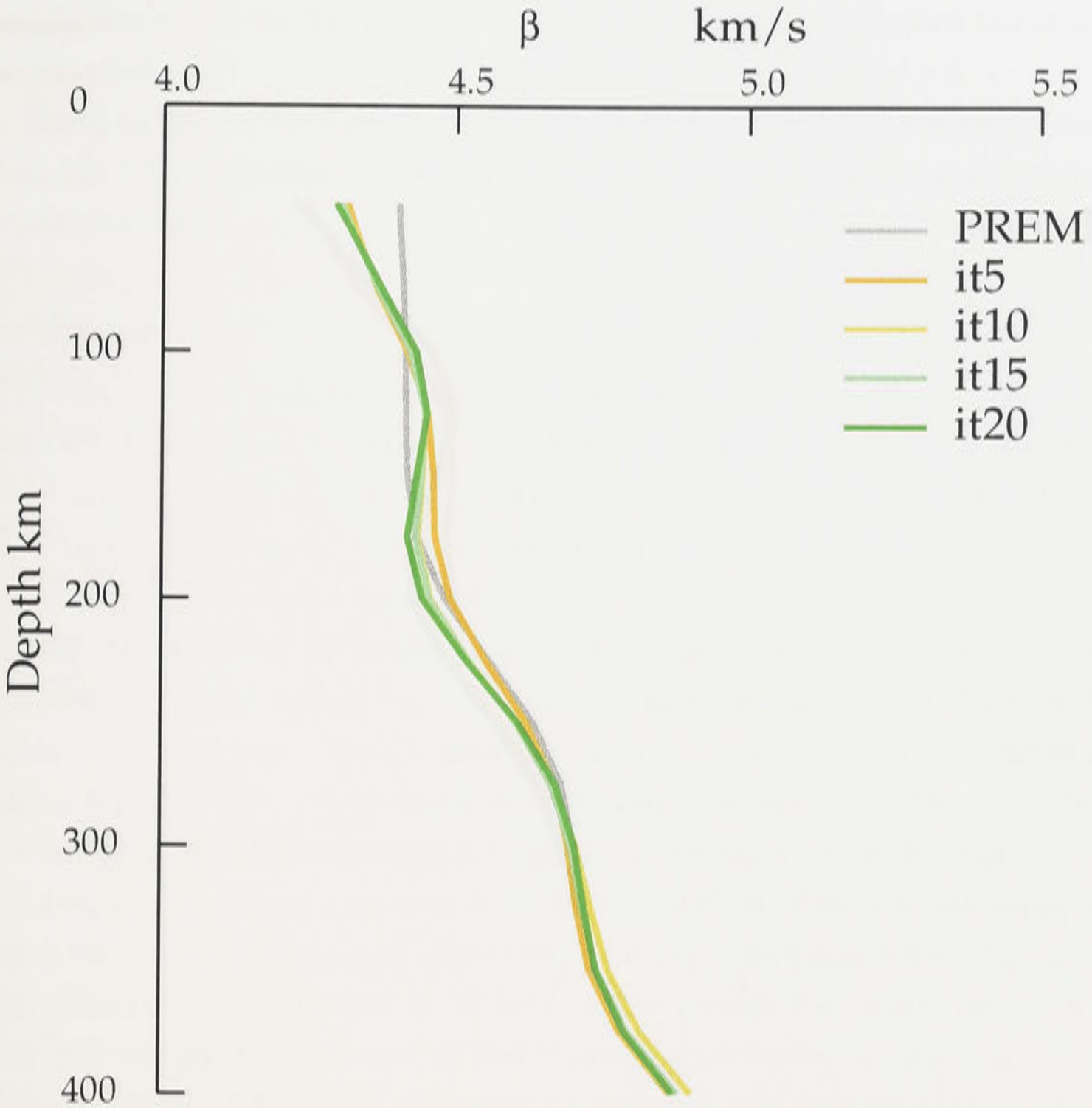

Fig. 4.11. The results of the CL synthetic recovery test for different crustal shear wavespeed (+3 % deviation is given only in the crust). The CL algorithm allows to invert shear wavespeed in the layer from the Moho depth (37 km) to the bottom of the transition zone (675 km). The focal depth is 10 km.

recovering + 5% deviation in the crust. The resulting profiles (figure 4.9) display that only very slight changes of β_v from the initial model (green line) to the final model (blue line) occurring in the layer from 80 km to 180 km depth. Moreover, no β_v recovery is observed in the crust. However,the synthetic seismogram perfectly matches the 'observed' waveform. We repeat the same experiments, changing the shapes of the basis functions which can control the vertical correlation length of β_v implicitly. We have almost the same results as the first experiment. This is probably because the fundamental mode of Rayleigh waves in the frequency range (0.008 Hz-0.025 Hz) has the strongest sensitivity in the layer between 80 km and 180 km depth, so that the PWI algorithm attempts to

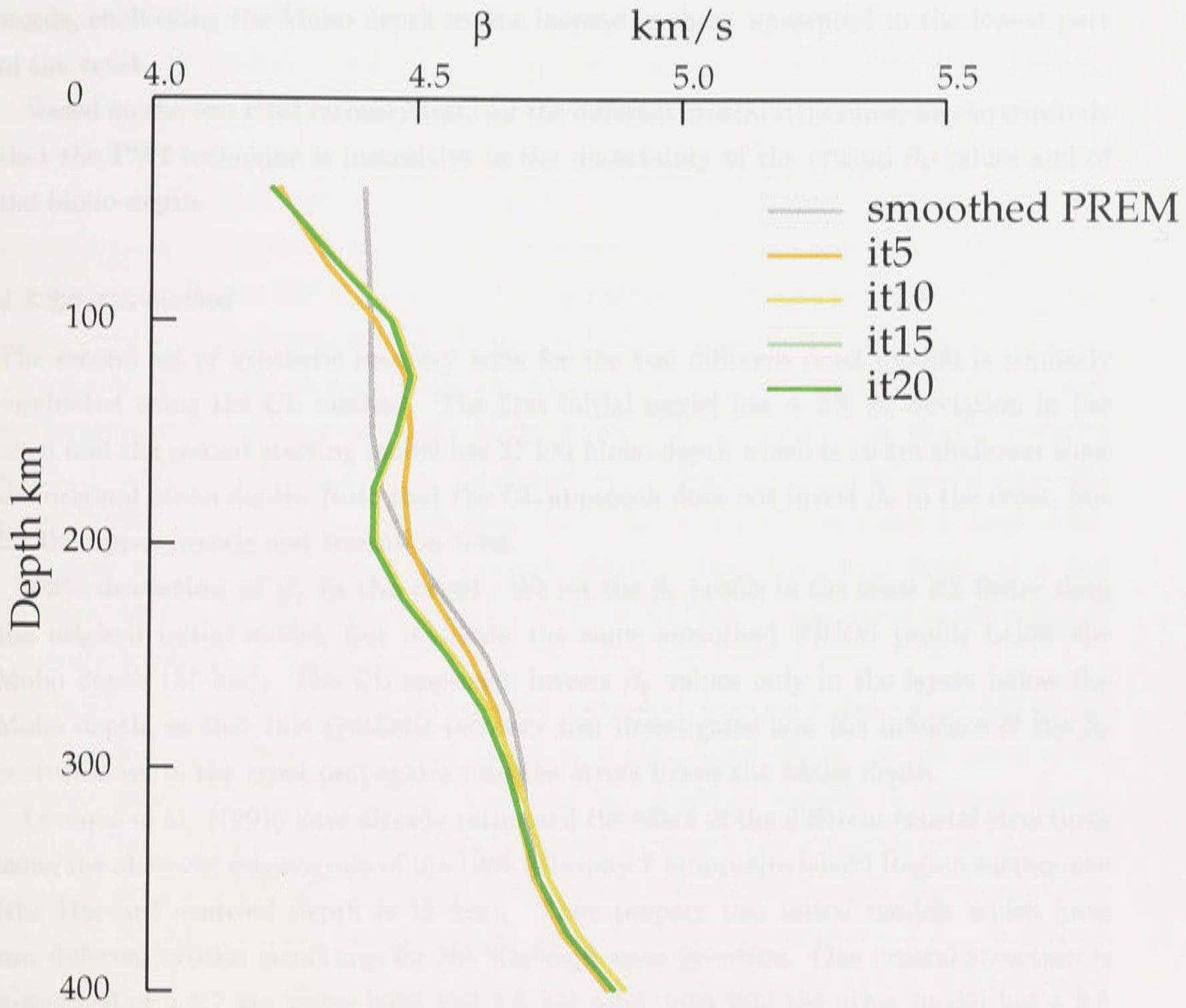

Fig. 4.12. The results of the CL recovery test for different Moho depth structure. A new Moho depth (27 km) is 10 km shallower than the original depth (37 km). The recovered layer is the upper mantle and the transition zone, excluding the crust. The focal depth is also 10 km.

modify the β_v profile in the layer between 80 km and 180 km depth to compensate for the crustal β_v perturbation, rather than changing the crustal structure itself.

10 km shallower Moho depth : We perform the same kind of PWI synthetic recovery test with shallowing the Moho depth from the original depth (37 km) to a new depth (27 km) in the initial model. Figure 4.10 illustrates the result of this test. We allow the layer from the surface to 300 km depth to modify the β_v profile to match the synthetic and observed waveforms. The very slight modification of the β_v curve is observed in the crust and the upper mantle layer. This result is somehow predictable from the previous recovery test, because shallowing the Moho depth is equivalent to inserting a new faster layer, which is about 10 % faster than the original profile, into just above the Moho depth. In other

words, shallowing the Moho depth means increasing shear wavespeed in the lowest part of the crust.

Based on the two PWI recovery tests for the different crustal structures, we can conclude that the PWI technique is insensitive to the uncertainty of the crustal β_v values and of the Moho depth.

4.3.3.2 CL method

The second set of synthetic recovery tests for the two different crust models is similarly conducted using the CL method. The first initial model has + 3% β_v deviation in the crust and the second starting model has 27 km Moho depth which is 10 km shallower than the original Moho depth. Note that the CL approach does not invert β_v in the crust, but for the upper mantle and transition zone.

+3% deviation of β_v in the crust : We set the β_v profile in the crust 3% faster than the original initial model, but maintain the same smoothed PREM profile below the Moho depth (37 km). The CL approach inverts β_v values only in the layers below the Moho depth, so that this synthetic recovery test investigates how the influence of the β_v perturbation in the crust propagates into the layers below the Moho depth.

Lévêque et al. (1991) have already estimated the effect of the different crustal structures using the observed seismogram of the 1987 February 7 Marquaire Island Region earthquake (the Harvard centroid depth is 15 km). They prepare two initial models which have two different crustal structures for the Rayleigh wave inversion. One crustal structure is comprised of a 5.7 km water layer and 6.4 km solid crust and the other model has a 3.5 km water layer and a 4.5 km sedimentary layer overlying a 7 km oceanic crust. Their inversion result shows that the large difference between the two final β_v models starting from the two crustal structures is observed in the upper 150 km depth. Thus, Lévêque et al. (1991) state that great care should be taken in selecting the crustal models when the CL approach is applied to surface waveforms at intermediate periods.

Figure 4.11 illustrates the result of the CL recovery test for + 3% deviation of the β_v profile in the crust. The difference between the smoothed PREM model (gray line) and the final iteration (green line) appears down to about 280 km. Its amplitude is the largest just below the Moho depth and is almost as same as the initial deviation (+ 3%) in the crust. This result is consistent with the previous examination using the thinner oceanic crusts by Lévêque et al. (1991), although the magnitude of the crustal effect is larger and the penetration depth is much deeper (figure 4.11). This is because we set much thicker continental crust (37 km) and put much larger perturbation (+3 %) in the whole crustal layers than the case by Lévêque et al. (1991).

10 km shallower Moho depth : The same kind of CL synthetic recovery test is performed in figure 4.12, but shallowing the Moho depth from 37 km (the original depth) to 27 km. The inverted layer starts from the original Moho depth to the bottom of the transition zone.

The final iteration (green line in figure 4.12) displays that the influence of the misestimation of the Moho depth penetrates deeper (about 330 km depth) than the +3 % deviation case (about 280 km depth). The amplitude marks the maximum value at just below the Moho depth and is roughly equal to 5 % of the β_v value at the depth.

From the above two recovery tests, we can conclude that perturbations of S wavespeed in the crust and misestimation of the Moho depth have large impact on the CL inversion result. In particular, when using an inaccurate Moho depth in an initial model especially for a thicker crustal area, the resulting β_v profile potentially includes a large error. Therefore we suggest that the CL method should include the Moho depth as a new inversion factor (e.g. van der Lee & Nolet, 1997) or add the crustal layers to the region of the inversion.

In addition, we need to point out that the vertical correlation length (L_{cor}) will be the most influential factor of the vertical smearing of the crustal effects. In this series of CL recovery tests, L_{cor} is set to 50 km. However, L_{cor} could be variable in different depths and in different paths. The current CL algorithm requires to fix a L_{cor} value as one of the pieces of prior information, while the PWI method adjusts the vertical correlations with changing the shapes of the basis functions. Furthermore, the magnitude of L_{cor} is difficult to estimate for different depths and paths. So far we have no good means of determining L_{cor}. Thus we have to recognise that the choice of L_{cor} also gives some impact on the CL inversion result.

4.4 Conclusions

The set of tests described in this chapter has been designed to try to elucidate the performance of the different waveform inversion schemes, and to indicate ways in which they can be improved.

As we shall see the CL method can indeed be used over a large range of variation in upper mantle wavespeed, but needs the inclusion of crustal inversion to avoid contamination from shallow structure. In this term the CL approach is very suitable for exploitation of a region such as Australia with strong variation in shear wavespeed structure. The weakness of the approach lies in the strong influence of the fundamental mode whenever this is present. We also point out that, even if the CL approach can recover a large deviation from the starting

model, the CL method has a limitation of recoverable wavespeed deviations, because of accumulated errors of the calculation of the synthetic seismogram.

The Nolet-style waveform inversion component of the PWI approach can give good results when a suitable starting model is available. A good feature is the separation of higher mode and fundamental mode windows with the option of different filtering. However, if the higher modes are given enhanced weighting there is the possibility of biasing models. In addition, an advantage of the PWI method is robustness to the uncertainty of the crustal structures.

The tests show how the two methods respond to different synthetic input data, so that a quantitative assessment of their limitations can be made and appropriate conditions can be found for their application.

5

SURFACE WAVE POLARISATION ANISOTROPY FOR AUSTRALIAN PATHS

5.1 Introduction

The Australian region is bordered by extensive regional seismicity which provides frequent seismic sources to the northern and eastern plate boundaries of the continent, with more infrequent events to the west and on the Australian-Antarctic ridge to the south. The subduction zones running along the Indonesian arc provide events at a wide range of depths while those at the mid-ocean ridges are relatively shallow. Surrounded by those seismic belts, the Australian continent itself remains seismically stable. However, the detailed surveys of its surficial geology suggests that the Australian continent consists of an amalgamation of several tectonic blocks: the Phanerozoic eastern province, the Proterozoic central cratons and the Archean cratons in the western Australia (Plumb 1979 ; Shaw et al., 1995).

Recent regional studies of the surface waveform inversion over the Australian continent (Zielhuis & van der Hilst, 1996; van der Hilst et al., 1998; Debayle 1999; Debayle & Kennett, 2000a) confirm a strong lateral contrast of the shear wavespeed between the eastern younger belt and the western cratons which could reach more than 10 percent at 150 km depth. In addition to the shear wavespeed changes, the vertical cross-sections of their tomographic images display distinct changes of the thickness of the lithosphere at the boundary between the eastern Phanerozoic fold belt and the central Precambrian cratons.

A comprehensive P and S wave study by Kaiho & Kennett (2000) using the *Skippy* broad-band seismograms also reveals this prominent wavespeed contrast between the eastern and western parts of Australia. It also supports the horizontal changes of the thickness of the Australian lithosphere drawn from the surface wave studies. In addition, they suggest that in the western Archean craton there are very fast shear wavespeed

anomalies which could reach around 8 percent faster than the reference model *ak135* (Kennett et al., 1995).

To establish a more accurate model of the seismic wavespeed beneath the Australian continent, we should add information on anisotropic structure to the current images of the strong lateral heterogeneity between eastern and western Australia. In other words, it is likely that the degree of the lateral contrast of the shear wavespeed over the continent could be modified by introducing new information on upper mantle anisotropy, because of the trade off between seismic heterogeneity and anisotropy.

Regional anisotropic structures beneath the Australian continent have been investigated by several studies. Based on the examination of the high quality digital seismograms recorded at Warramunga array in the Norther territory, Tong et al. (1994) present the shear wave splitting of the refracted waves on the radial and tangential components and proclaim the presence of anisotropy in the lithosphere beneath northern Australia. Debayle (1999) and Debayle & Kennett (2000a) use a more comprehensive data set provided by surface waves recorded at several GEOSCOPE and IRIS permanent stations and portable broad-band seismometers from several regional array deployments (e.g. the SKIPPY project) in the Australasian region. They illustrate the SV wavespeed distributions and its azimuthal variations, which they describe as azimuthal anisotropy, in their tomographic images for the whole continent. With the maximum amplitude of the azimuthal anisotropy reaching 3 percent, their SV wavespeed maps maintain the general characteristics of the strong lateral heterogeneity between eastern and western Australia. However, the vertical distributions of azimuthal anisotropy beneath the continent provide a new clue for speculation on the past and current upper mantle deformations. Debayle & Kennett (2000a) find the clear differences of the horizontal patterns of azimuthal anisotropy over the whole continent between an upper layer and a lower layer bounded above at around 150 km depth. They propose a two-layer model of the Australian upper mantle: azimuthal anisotropy in the upper layer due to the frozen effects of past deformation in the lithosphere; that in the lower layer is reflected by the current deformation due to the northward motion of the Australian plate.

In addition to azimuthal anisotropy, another style of anisotropy, polarisation anisotropy or radial anisotropy, has been measured by several studies of broad-band seismograms recorded at Australian stations (Gaherty & Jordan, 1995; Gaherty et al., 1999; Debayle & Kennett 2000b). Polarisation anisotropy arises from differences between the wavespeeds for propagation in the vertical direction and the horizontal direction. In a simple model of transverse isotropy with a vertical symmetry axis, polarisation anisotropy can be parameterised with 5 elastic constants (Love, 1927). In addition to the vertical and

horizontal wavespeeds α_v, α_h and β_v, β_h for P and S waves a further parameter is needed to describe the behaviour in full. The character of the polarisation anisotropy can described by the ratios $\xi = (\beta_h/\beta_v)^2 = N/L$, $\phi = (\alpha_v/\alpha_h)^2 = C/A$ and $\eta = F/(A-2L)$ where A, C, F, L and N are the elastic constants. In the case of isotropy $F = \lambda$, $A = C = \lambda + 2\mu$, and $N = L = \mu$. Generally the most dominant and best resolved parameter ξ has been used for representing polarisation anisotropy in the upper mantle structure (e.g. Nishimura & Forsyth, 1989).

Gaherty & Jordan (1995) and Gaherty et al. (1999) propose a seismic layering model (AU3) for the Australian upper mantle based on ScS reflectivity profiles and observations of wave arrivals on the three components and surface waves propagation in a corridor from New Britain region to south-western Australia. The AU3 model is characterised by high shear wavespeeds throughout the upper 350 km of the mantle, with no low velocity zone(LVZ). In terms of polarisation anisotropy, there is a single layer from Moho depth down to 250 km of the mantle which has positive ξ values (1.053 to 1.081), the layer below this depth (Lehmann discontinuity) is a complete isotropic mantle.

On the other hand, Debayle & Kennett (2000b) use Rayleigh and Love waves for 1584 paths crossing the whole continent and perform the joint Rayleigh-Love waveform inversion based on an automated procedure developed by Debayle (1999). With satisfactory waveform matching for 358 crossing paths, they shed light on the presence and 3-D distribution of polarisation anisotropy in the upper 200 - 250 km of the mantle, in particular, for Precambrian Australia. The resulting pattern of the polarisation anisotropy in depth agrees well with that of the azimuthal anisotropy demonstrated by Debayle & Kennett (2000a), so that Debayle & Kennett (2000b) suggest that the 3-D patterns of both azimuthal and polarisation anisotropy in Australia support the two layered anisotropic model proposed by Debayle & Kennett (2000a). However, because the amplitudes of polarisation anisotropy locally reach an extreme value of 10 percent that is difficult to explain by the current knowledge of mineralogy, Debayle & Kennett (2000b) mention that such large value could be due to the origin of the continental anisotropy or the limited ability to determine its nature with current assumptions.

In consequence, adding new information on anisotropy to the previous SV wavespeed models beneath the continent raises several new questions on the nature of the seismic structure in the Australian upper mantle. The first question is how significant is the polarisation anisotropy in comparison with the vertical and horizontal distributions of the SV wavespeed in the upper mantle? In other words, the issue is whether or not the pattern and amplitude of the polarisation anisotropy is related to those of the SV wavespeed. This is particularly important for establishing an anisotropic model of the Australian

upper mantle, because the polarisation anisotropy model proposed by Debayle & Kennett (2000b) does not have a direct correlation with SV wavespeed and has larger amplitudes in a few regions than might be expected. The second question is what is the vertical and horizontal distribution of the polarisation anisotropy beneath the Australian continent. The two models proposed by Gaherty & Jordan (1995) and Debayle & Kennett (2000b) are clearly different in terms of the vertical distribution of polarisation anisotropy. Gaherty & Jordan (1995) select a north-eastern to south-western corridor crossing Australia which crosses regions with significant lateral variations of the seismic wavespeed. The two layered model proposed by Debayle & Kennett (2000b) could contain the influences of the ocean-continent boundary on the waveforms of surface waves which would not be noted explicitly due to its automated procedure. Thus, both studies potentially project 3-D shear wave heterogeneity along the path into the resulting 1-D polarisation models. In addition to these two questions, we are interested in investigation of the seismic structure in the Archean craton. There is no regional-scale mapping of either the shear wavespeed or the polarisation anisotropy in the upper mantle over the Archean craton in western Australia. We do not know the seismological structure of the upper mantle in one of the oldest cratons on the Earth.

To answer these questions, first we carefully select a limited number of travel paths which are mainly pure continental paths but with broadspan in azimuth, and secondly, manually perform the inversion of Rayleigh and Love waveforms for the paths, rather than using an automated procedure (Debayle, 1999). Moreover, we select the smoothed PREM model and the AU3 model as starting models and conduct the waveform inversion to check whether or not the resulting amplitudes and its vertical pattern of the polarisation anisotropy change significantly. Finally we examine the anisotropic structure in the Archean shield region using the surfacewaves traveling through the region.

5.2 Data

We use surface wave data recorded by the three-component broadband seismometers at the two permanent stations: NWAO (IRIS) at Narrogin placed on the Archean craton in southwestern Australia and CAN (GEOSCOPE) at Canberra on the younger eastern belt in the southeastern part of the continent (figure 5.1).

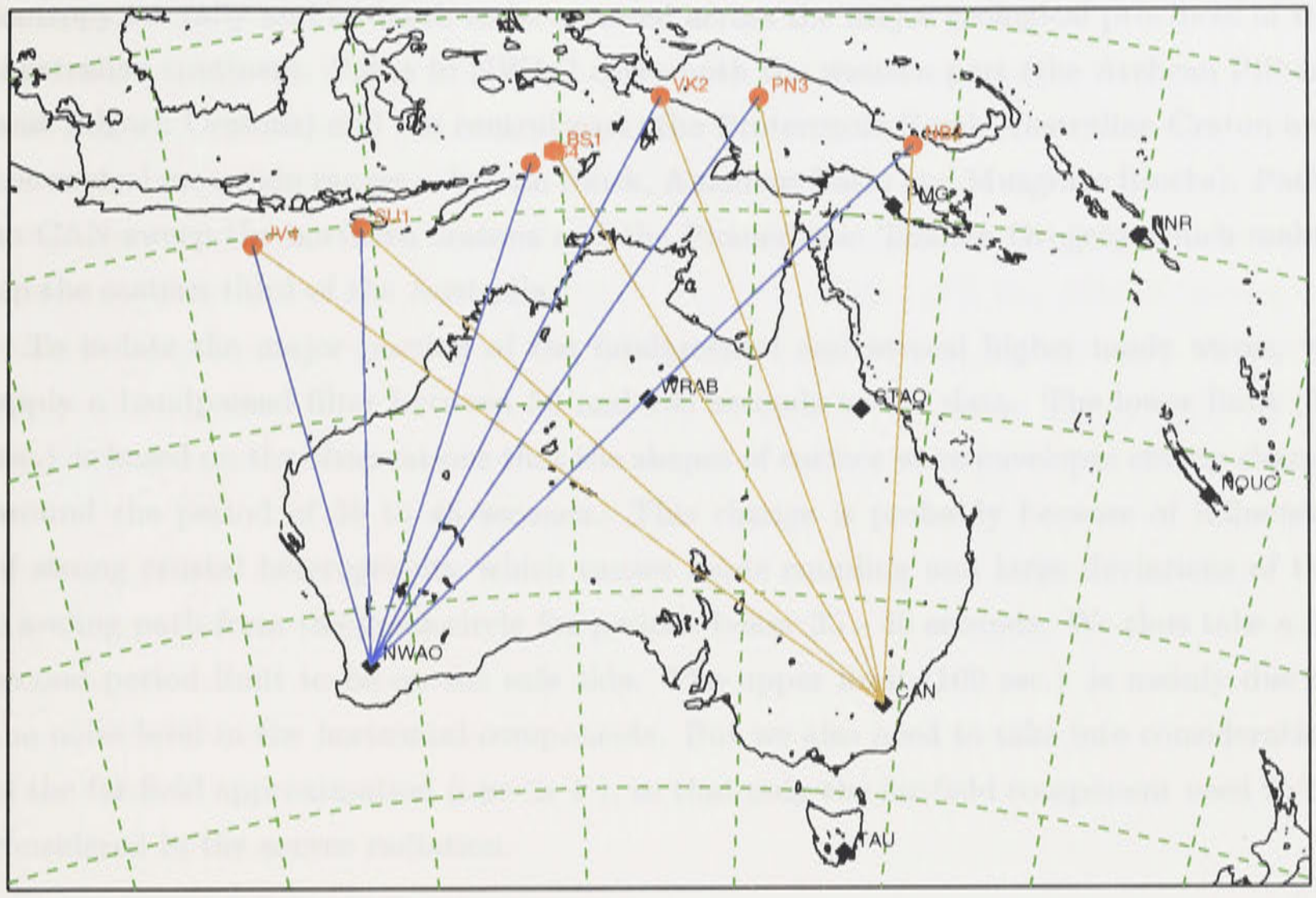

Fig. 5.1. Ray path distributions from 7 events to the permanent stations CAN and NWAO.

Name	Date	Time	Lat.	Lon.	Depth	Mw	mb	Ms
NB2	930929	08:02:01.400	-6.22	147.89	90.2	5.4	5.2	
PN3	960117	10:06:51.600	-4.23	139.98	96.6	6.1	5.6	
VK2	940104	19:32:03.900	-4.27	135.05	20.2	5.9	5.7	6.1
BS1	951225	04:43:36.400	-6.93	129.65	160.7	7.1	6.2	
BS4	941201	06:11:07.000	-7.82	128.25	113.5	5.3	5.3	
SU1	941212	14:53:03.300	-10.21	119.46	41.4	5.5	5.5	5.0
JV4	940615	09:23:01.100	-10.43	113.75	17.0	6.0	5.8	6.1

We selected data with a good signal-to-noise ratio from seven events which occurred along the northern seismic belt from the Island of Java, Indonesia to Papua New Guinea (figure 5.1), with a source depth range between 30 km and 160 km (the above table). These earthquakes have favourable source mechanisms for which the paths to the stations do not lie too close to the nodes of both Love and Rayleigh waves.

This set of selected paths allows the variation in seismic heterogeneity and transverse isotropy laterally and in depth to be assessed across the major geological provinces of the Australian continent. Paths to NWAO cover both the western part (the Archean Pilbara and Yilgarn Cratons) and the central part (the Proterozoic North Australian Craton and the central mountain ranges – Arunta Block, Amadeus Basin and Musgrave Blocks). Paths to CAN sweep the northern cratons and the Phanerozoic Tasman Orogeny which makes up the eastern third of the Australia.

To isolate the major portion of the fundamental and several higher mode waves, we apply a bandpassed filter between 50 and 100 seconds to the data. The lower limit (50 sec.) is based on the observations that the shapes of surface wave envelopes clearly change around the period of 35 to 45 seconds. This change is probably because of influences of strong crustal heterogeneity which causes mode coupling and large deviations of the traveling path from the great-circle for periods below 35 - 40 seconds. We thus take a 50 second period limit to be on the safe side. The upper limit (100 sec.) is mainly due to the noise level in the horizontal components. But we also need to take into consideration of the far-field approximation ($\omega pr \gg 1$), so that only the far-field component need to be considered in the source radiation.

5.3 Starting models

We perform waveform inversions for each path with a crustal structure derived from the 3SMAC model (Nataf & Ricard, 1996) and a common upper mantle starting model based on the PREM model (Dziewonski & Anderson, 1981) with smoothed discontinuities but without the anisotropy present in the top 220 km of the upper mantle. The results of the inversion for individual paths are therefore directly comparable.

The average crustal structure along each path has been extracted from the 3SMAC model in each case. The 3SMAC (3 dimensional Seismological Model *A priori* Constrained) model is designed as a 3-D reference model for various global tomographic inversions. It distributes the four seismic parameters (density, P velocity, S velocity, and quality factor) vertically from the sea surface to the bottom of the upper mantle with 33 layers and horizontally on 2-degree by 2-degree grids over the whole earth surface. The model contains the different class of the seven 'chemical' layers as water-ice, sediments, upper crust , lower crust, olivine, β-spinel, and γ-spinel. At the boundaries between the chemical layers, discontinuities of the four seismic parameters are allowed. The information included in the model is based on the thicknesses of the chemical layers over the globe, the 3-D distribution of geotherm from thermal plate modellings , mineralogy in the upper mantle

derived from pressure-temperature distributions, and laboratory measurements of the four parameters as a function of pressure and temperature.

The crustal structures of 3SMAC model in the Australian region generally agree with other crustal researches. For example, receiver function analyses recently carried out by Shibutani et al. (1996) and Clitheroe et al. (2000) illustrate the crustal structures beneath the *Skippy* stations over the Australian continent. Although some local deviations of the crustal structure derived from the receiver function studies and the 3SMAC model are observed in a few regions, we find a general agreement between both models. However, the models by the receiver function analyses reveal information on the structure of the continent in a narrow region around each station. Moreover, the receiver function analyses include gradual changes of seismic parameters at the crust-mantle boundaries beneath several stations, while 3SMAC model uses sharp discontinuities at the Moho depth. In consequence, it is possible that the 3SMAC is not a good representation in a few regions of the continent. The most significant is too thick a crust in the Pilbara craton of western Australia. However, the influence of local perturbations on the average structure along each path will be small. But, as we saw in chapter 4, there is a potential for error in the crustal model to contaminate the upper mantle structure of the inversion results.

We also use a different starting model (AU3) proposed by Gaherty & Jordan (1995) and Gaherty et al. (1999). The model AU3 has a simple crustal structure and high shear velocities throughout the upper 350 km of the mantle without a low-velocity zone in the isotropically averaged shear velocities. Moreover, AU3 contains polarisation anisotropy in the upper mantle from the Moho depth of 54 km down to the Lehmann discontinuity at the depth of about 250 km.

5.4 Rayleigh and Love waveform inversion

5.4.1 1-D waveform inversion

We aim to construct an anisotropic 1-D model for each path based on exploiting information on the three-component seismograms. For that purpose, a 1-D waveform inversion technique, which is an extension of the first stage of the Cara & Lévêque (1987) method, is applied to process the fundamental Love and Rayleigh wave portions of the surface waves and also several overtones for both the vertical and tangential components. The resulting 1-D path dependent model is expected to represent the upper mantle structure to explain both Love and Rayleigh waves on the tangential and vertical components. We follow the first stage of the method of Debayle & Kennett (2000b) but without their automated procedure and apply this method to the individual seismograms

for selected paths. These manual inspections of anisotropic structures beneath the selected paths can help to find answers to several of the questions raised by Debayle & Kennett (2000b). In particular, it is worthwhile investigating the causes of the large amplitudes of the parameter ξ in eastern Australia which appears in their tomographic maps. These large amplitudes of ξ suggest that the differences between SV and SH wavespeeds exceed what we expect.

5.4.2 Parameterisation of a transversely isotropic medium

The 1-D shear wavespeed models obtained from the waveform inversion allow surface waves in the vertical and horizontal components to propagate at different wavespeeds and therefore possess information on polarisation anisotropy. Furthermore, the 1-D models potentially contain information on azimuthal variations of the shear velocity (Lévêque et al., 1998) through the expected azimuthal dependence for weak anisotropy,

$$\delta\hat{\beta}_v = \delta\beta_v + \left(\frac{G_c}{2\rho\beta_v}\right) \cdot \cos 2\theta + \left(\frac{G_s}{2\rho\beta_v}\right) \cdot \sin 2\theta \ , \tag{5.1}$$

and

$$\delta\hat{\beta}_h = \delta\beta_h - \left(\frac{C_c}{2\rho\beta_v}\right) \cdot \cos 4\theta - \left(\frac{C_s}{2\rho\beta_v}\right) \cdot \sin 4\theta \ , \tag{5.2}$$

where β_v and β_h are shear wavespeeds in the vertical and horizontal components, ρ is density, and θ is an azimuth of the propagation path. G_c, G_s, C_c, and C_s are the constants defined in Montagner & Nataf (1986). However, we perform the anisotropic waveform inversion without corrections for any azimuthal variations. This could oversimplify the real anisotropic structures beneath the ray paths, because the upper mantle structure is expected to have some azimuthal variation resulting from the preferred orientation of anisotropic minerals with their fast axis close to the horizontal direction. When the azimuthal variations of the phase velocity can be estimated prior to the investigation of polarisation anisotropy (Lévêque & Cara, 1985) or the path averaged structure can average out the azimuthal variations of the shear wavespeed (Gaherty & Jordan, 1995), it is still useful to measure polarisation anisotropy without considerations of its azimuthal variations. In such cases, we can introduce a transversely isotropic model with a vertical symmetry axis (TIV) in a set of the 1-D models.

The phase velocities of Rayleigh and Love waves (C_r and C_l) propagating in a flat Earth structure depend on the partial derivatives of the five elastic parameters (A, C, L, N, F) , and density ρ (Takeuchi & Saito, 1972). In a TIV effective medium with no variations in density, the above relations are formulated as

$$\delta C_r = \int_{z=0}^{R} \left[\frac{\partial C_r}{\partial A} \cdot \delta A + \frac{\partial C_r}{\partial C} \cdot \delta C + \frac{\partial C_r}{\partial F} \cdot \delta F + \frac{\partial C_r}{\partial L} \cdot \delta L\right] \cdot dz \ , \tag{5.3}$$

and

$$\delta C_l = \int_{z=0}^{R} \left[\frac{\partial C_l}{\partial L} \cdot \delta L + \frac{\partial C_l}{\partial N} \cdot \delta N \right] \cdot dz \; . \tag{5.4}$$

Note that the two equations derived for a flat Earth structure are still a good approximation to the spherical Earth structure for regional epicentral distances (2000 km - 4000 km) and frequency ranges (0.01 Hz - 0.02 Hz) we use in the waveform inversion

Anderson (1961) proposes another style of expression of transverse isotropy using a different parameter set ($\alpha_h, \alpha_a, \beta_h, \beta_v$, and η). The first four parameters are related to the five elastic parameters(A, C, L, N, and F) with $A = \rho \cdot \alpha_h^2$, $C = \rho \cdot \alpha_v^2$, $L = \rho \cdot \beta_v^2$, and $N = \rho \cdot \beta_h^2$. The last parameter η is introduced as $F = \eta(A - 2L)$. With these relations, the equations 5.3 and 5.4 are transformed in the new parameter set ($\alpha_h, \alpha_a, \beta_h, \beta_v$, and η).

However, surface waves do not carry enough information to resolve all the five parameters. Nishimura & Forsyth (1989) demonstrate that only the the two dominant and best-resolved parameters (β_v and ξ) can be interpreted with reasonable confidence. They used fundamental mode Rayleigh and Love waves and obtain transversely isotropic models beneath the Pacific ocean which are represented by two parameters; the SV velocity $\beta_v = \sqrt{L/\rho}$ and the S wave anisotropic parameter $\xi = N/L = (\beta_h/\beta_v)^2$. Muijzert & Snieder (2000) calculates the partial derivatives of the Love and Rayleigh wave phase velocities with respect to both the Love-style parameter set and the Anderson-style parameter set. He draws the partial derivatives against depth up to the second overtones at different wave periods. His visual examinations of these curves conclude that L and β_v are the best resolved parameters for Rayleigh waves and N, β_v, and β_h are the most prominent parameters for Love waves. These observations including effects of several overtones agree well with the investigations of the fundamental mode surface waves by Nishimura & Forsyth (1989).

In consequence, we assume a TIV medium specified by these two best-resolved parameters β_v and ξ. The Rayleigh and Love joint inversion is conducted to construct a 1-D transversely isotropic model for the upper mantle. From the amplitude behaviour of the seismograms, we also invert for the shear wave quality factor Q_β as parameterised by $\log Q_\beta$ and the scalar seismic moment of the source $\log M_0$. The resulting TIV model has the possibility of reconciling the inconsistent one-dimensional models from separate isotropic inversions of Rayleigh and Love waveforms.

5.5 Results and Discussion

For 12 selected paths crossing the continent (figure 5.1), Rayleigh and Love joint surface waveform inversions are performed with two different starting models; anisotropic smoothed AU3 and 3SMAC crustal correction applied to isotropic smoothed PREM. In addition, separate isotropic waveform inversions of both Rayleigh and Love waves are conducted for all the paths with the same two starting models.

We summarise the both joint and separate inversion results from 7 events (NB2, PN3, VK2, BS1, BS4, SU1, and JV4) to two stations (CAN and NWAO) in four figures (from figure 5.2 to figure 5.5). In addition, the vertical and horizontal distributions of polarisation anisotropy (ratio of β_h to β_v) for all the paths to the two stations are examined from figures 5.2 to 5.5.

All the waveform matches for the initial and final models are illustrated in the figures in Appendix A. We note that oscillations and large variations in wavespeed for β_h below 300 km are indicative of lack of resolution.

5.5.1 Joint inversion

5.5.1.1 station: NWAO

β_v profiles (the upper 6 plots in figure 5.2): When a joint waveform inversion converges, the general pattern of β_v solutions ,particularly above 250 km depth, is similar from the two different starting models: AU3 and *PREM* with 3SMAC crustal correction. Only for the NB2-NWAO path the two β_v profiles (dark and light blue lines) have different vertical wavespeed gradients above 300 km depth. This could be due to different parameterisations of the two starting models in the crust. The crust has three layers in PREM with 3SMAC case, while the AU3 has a one-layer crustal model above the Moho (54 km). For the rest of the five paths, the β_v models starting from AU3 and PREM have profoundly good matches. Moreover, these profiles show the low wavespeed layers which axes are located at around 200 km depth.

β_h profiles (the lower 6 plots in figure 5.2): Joint inversions from the two starting models draw quite different β_h curves from the NWAO data. Only one example (NWAO-VK2) provides a reasonable match between the two β_h profiles starting from PREM and AU3 in the layer above 250 km depth. For the three continental paths (NWAO-BS4, -PN3, and -NB2), the final models from AU3 (light green lines) have relatively small deviations from AU3 (thin dotted lines), while the profiles from PREM (dark green lines) have implausible large fluctuations from the starting model. In the models of the ocean-continent mixed paths (NWAO-JV4 and -SU1), the starting model

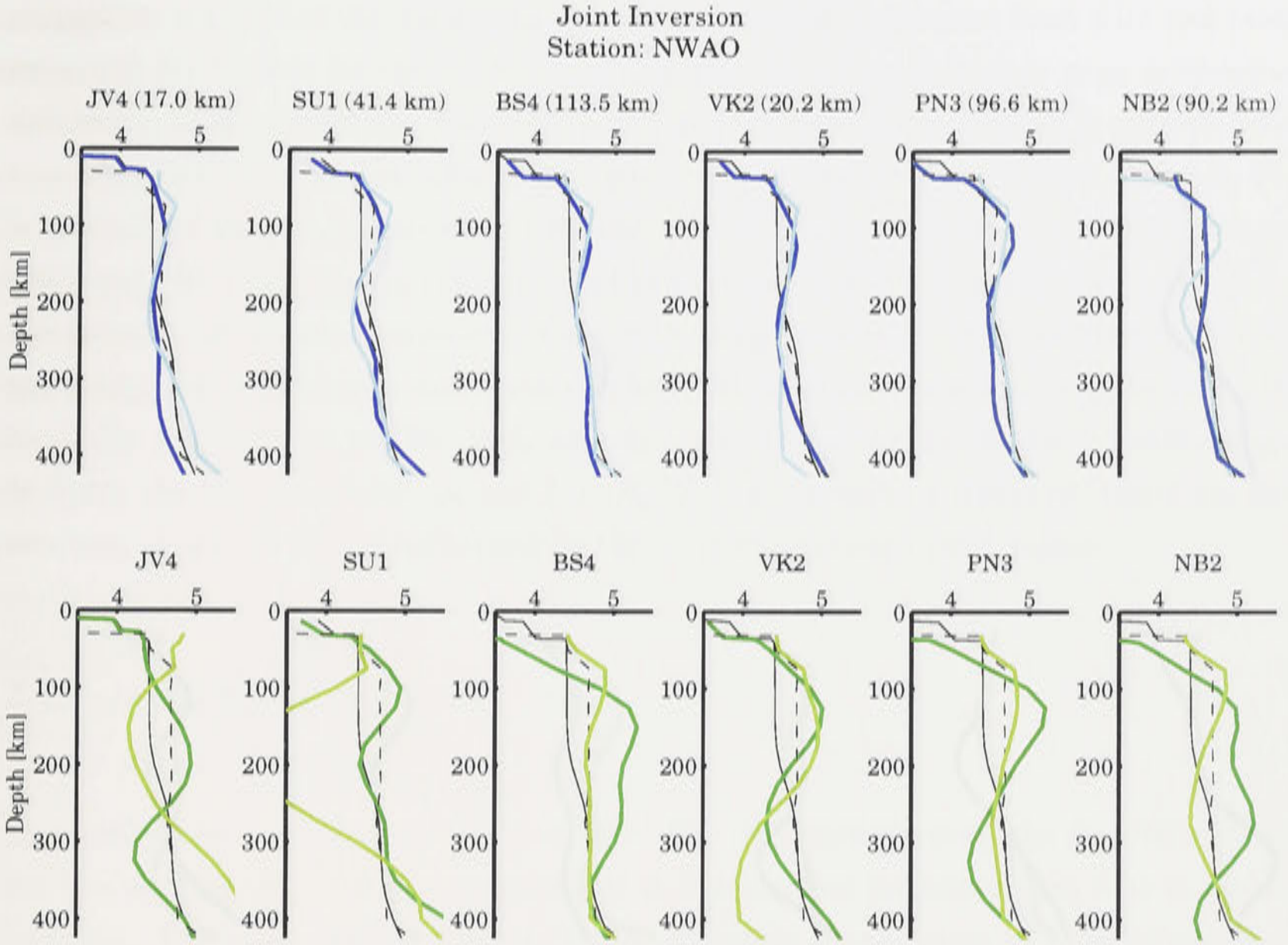

Fig. 5.2. The results of the CL joint inversion of Rayleigh and Love waves for the paths from 6 events to station NWAO. The number after each event name indicates the focal depth of the event. The upper 6 plots display the joint inversion results of β_v, in each plot, the thin black line shows the smoothed PREM model of β_v, and the dashed black line means the smoothed AU3 model of β_v. The dark blue line denotes the final model starting from the smoothed PREM model, while the consequence of the inversion starting from the smoothed AU3 is in light blue line. The lower 6 plots show the joint inversion results of β_h. The thin black line and the dark green line means the starting smoothed PREM model of β_h and its converged model after the 20 iterations. The dashed black line and the light green line depict the smoothed AU3 model and its final iteration of β_h.

AU3 cannot converge to acceptable solutions. In contrast, the profiles from PREM have less significant deviations from the starting model than the AU3 case.

5.5.1.2 station: CAN

β_v profiles (the upper 6 plots in figure 5.3): For the ocean-continental mixed path (CAN-NB2), the difference between the final models of AU3 (light green line) and of PREM (dark green line) is larger than the profiles for the other five paths, mainly because the inversions from PREM-profile have very large fluctuation in the layer even above 300 km. However, the AU3-based model (light green line) beneath the CAN-NB2 path has a good accordance with the previous 3-D studies by the surface waveform inversion

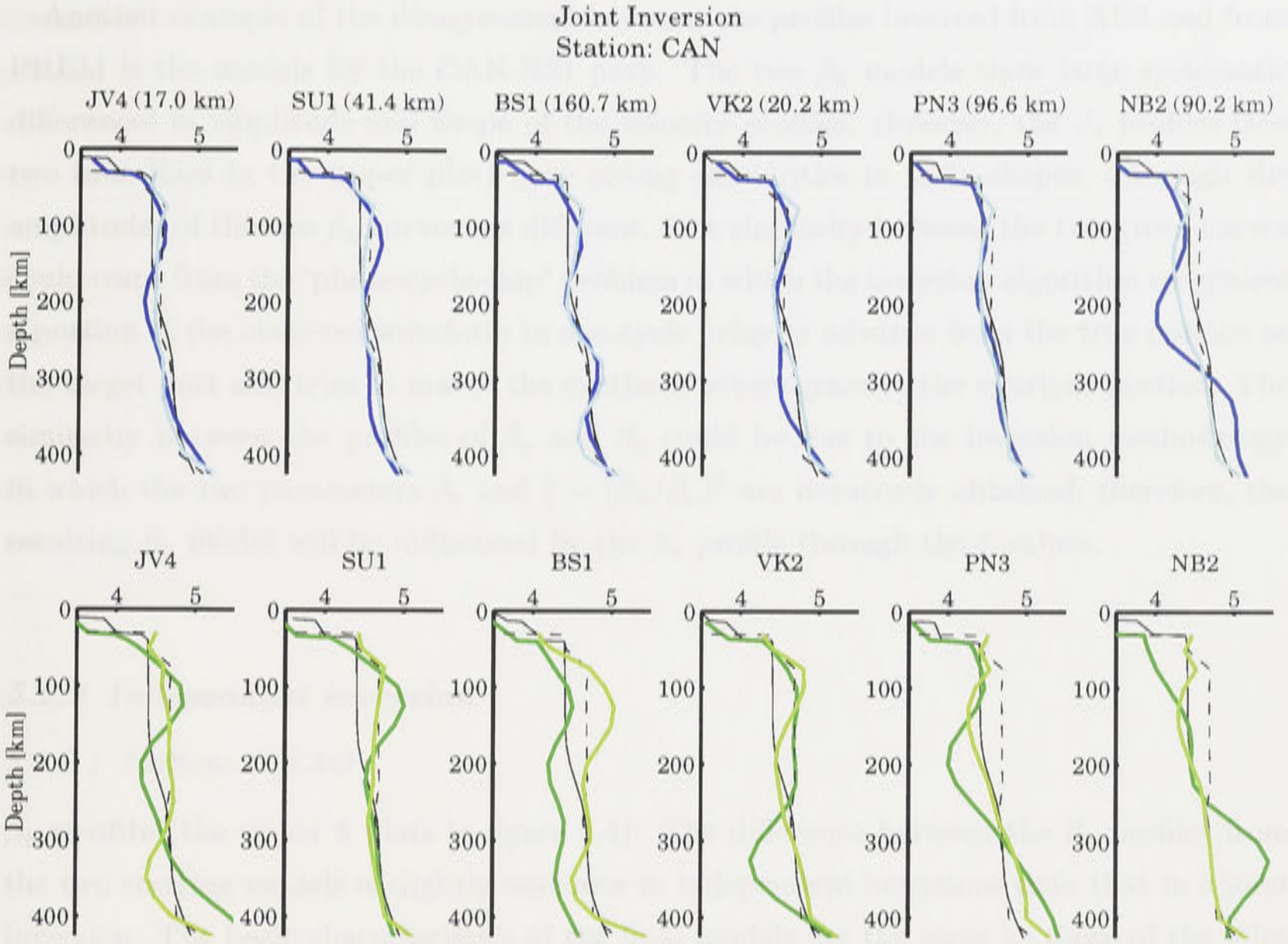

Fig. 5.3. This is the same figure as figure 5.2, but the station is NWAO. We use event BS1, instead of BS4, mainly because the data has a poor signal to noise ratio.

(van der Hilst et al., 1998; Debayle, 1999, Debayle & Kennett, 2000a) which elucidate slower β_v values in the eastern margin of the Australian continent. In the five cases of the continental or almost continental paths, both results from the two starting models are quite good accordance. In particular, the models of CAN-BS1 illustrate that Cara & Lévêque method is quite robust for the perturbation of β_v down to more than 250 km depth, because well excited higher mode waves from event BS1 (focal depth: 160.7 km) well match those of the synthetics in the figures in Appendix A.

β_h profiles (the lower 6 plots in figure 5.3): All the PREM-based β_h models tend to converge to rather unstable solutions except for the path (CAN-SU1). Thus, the discrepancy between the results from the AU3 starting model and that from PREM are large. For the ocean-continent mixed path (CAN-NB2), particularly, the final model (dark green line) displays large fluctuations below 250 km depth. This suggests that, when choice of the starting model is not adequate, it is difficult to match the synthetic seismogram to the higher modes of Love waves. The final convergent models (light green curves) deviate from the initial model AU3 in an acceptable level.

Another example of the disagreement between the profiles inverted from AU3 and from PREM is the models for the CAN-BS1 path. The two β_h models show large systematic differences in amplitude and shape of the velocity profiles. However, the β_v profiles (the two blue lines in the upper plot) have strong similarities in their shapes, although the amplitudes of the two β_v curves are different. The similarity between the two green curves could come from the 'phase-cycle-skip' problem in which the inversion algorithm recognises a portion of the observed waveform in one-cycle delay or advance from the true portion as the target part and tries to match the synthetic seismogram to the spurious portion. The similarity between the profiles of β_v and β_h could be due to the inversion methodology in which the two parameters β_v and $\xi = (\beta_h/\beta_v)^2$ are iteratively obtained; therefore, the resulting β_h model will be influenced by the β_v profile through the ξ values.

5.5.2 Independent inversion

5.5.2.1 Station: NWAO

β_v profile (the upper 6 plots in figure 5.4): The difference between the β_v profiles from the two starting models is slightly narrower in independent inversions than that in a joint inversion. The basic characteristics of the final models are the same as those of the joint inversion cases (the upper 6 plots in figure 5.2). Namely, there are the low wavespeed zones around 200 km depth for the paths (NWAO-JV4, -SU1, and -BS4).

β_h profile (the lower 6 plots in figure 5.4): Except for the path NWAO-VK2, we observe two common characteristics of the relation between the final models starting from PREM and from AU3. First, in the layer above about 100 km depth, the PREM-based final model (dark green line) is slower than that of AU3 model (light green line) . Second, in the layer from about 100 km to 300 km or 400 km depth, the PREM-based profile is faster than the AU3-based model. In particular, the pairs of the two curves for the paths (CAN-NB2, CAN-PN3 and CAN-BS4) resemble each other in shape, probably because their focal depths (NB2: 90.2 km; PN3: 96.6 km; BS4: 113.5 km) are quite close.

The characteristics in the layer above 100 km depth could arise from the fact that Love waves still have strong sensitivity to the structure in the layer, so that the inversion algorithm can less freely change the original wavespeed structure than in the layer below 100 km. Thus, the basic difference between the PREM (thin black line) and AU3 models (thin dashed line) remains within the layer. Below 100 km, the true 1-D model could lie between the PREM and AU3; therefore, the inversion algorithm tries to make the PREM initial model faster and the AU3 starting model slower. In consequence, the PREM final profile becomes too fast and the AU3-based model converges to a slower model than AU3.

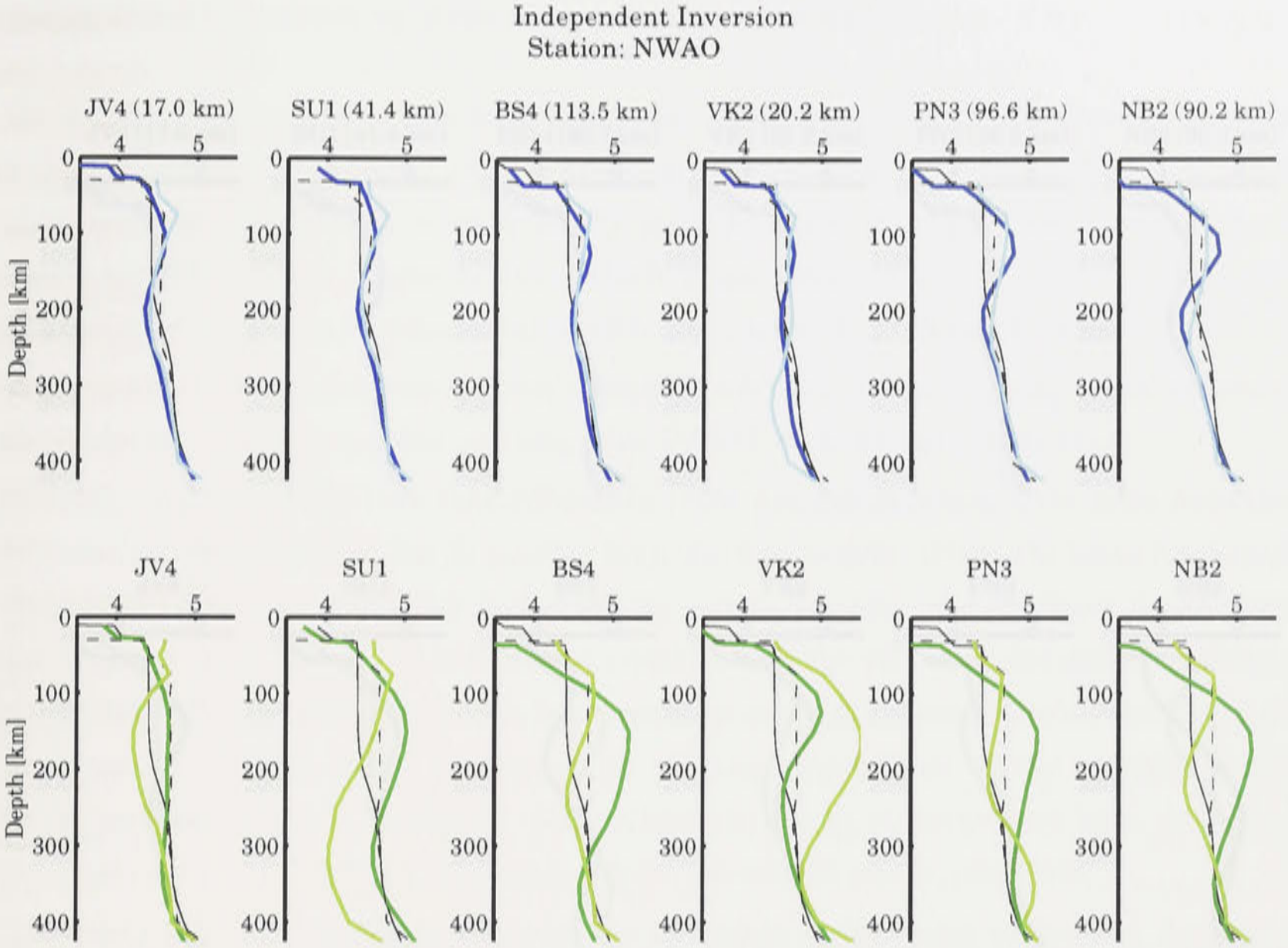

Fig. 5.4. The results of the CL independent inversion of Rayleigh and Love waves for the paths from 6 events to station NWAO. The upper 6 plots display the independent inversion results of β_v. The thin black line shows the smoothed PREM model of β_v,and the dashed black line means the smoothed AU3 model of β_v. The dark blue line denotes the final model starting from the smoothed PREM model, while the consequence of the inversion starting from the smoothed AU3 is in light blue line. The lower 6 plots show the independent inversion results of β_h. The thin black line and the dark green line means the starting smoothed PREM model of β_h and its converged model after the 20 iterations. The dashed black line and the light green line depict the smoothed AU3 model and its final iteration of β_h.

5.5.2.2 Station: CAN

β_v profile (the upper 6 plots in figure 5.5): The two β_h curves are quite similar in shape and amplitude for each path. We also observe the low wavespeed layers which axis is located at around 200 km depth.

β_h profile (the lower 6 plots in figure 5.5): Except for the path CAN-BS1, the other five pairs of the two final models share the same characteristics as we observe in the β_h case in the lower plots in figure 5.4. These are the slower PREM-based models above around 100 km depth and the faster PREM-based profiles in the layer below about 100 km depth. However, the differences between the two final models apparently are smaller than in the lower plots in figure 5.4. This will be firstly because the signal-to-noise ratio

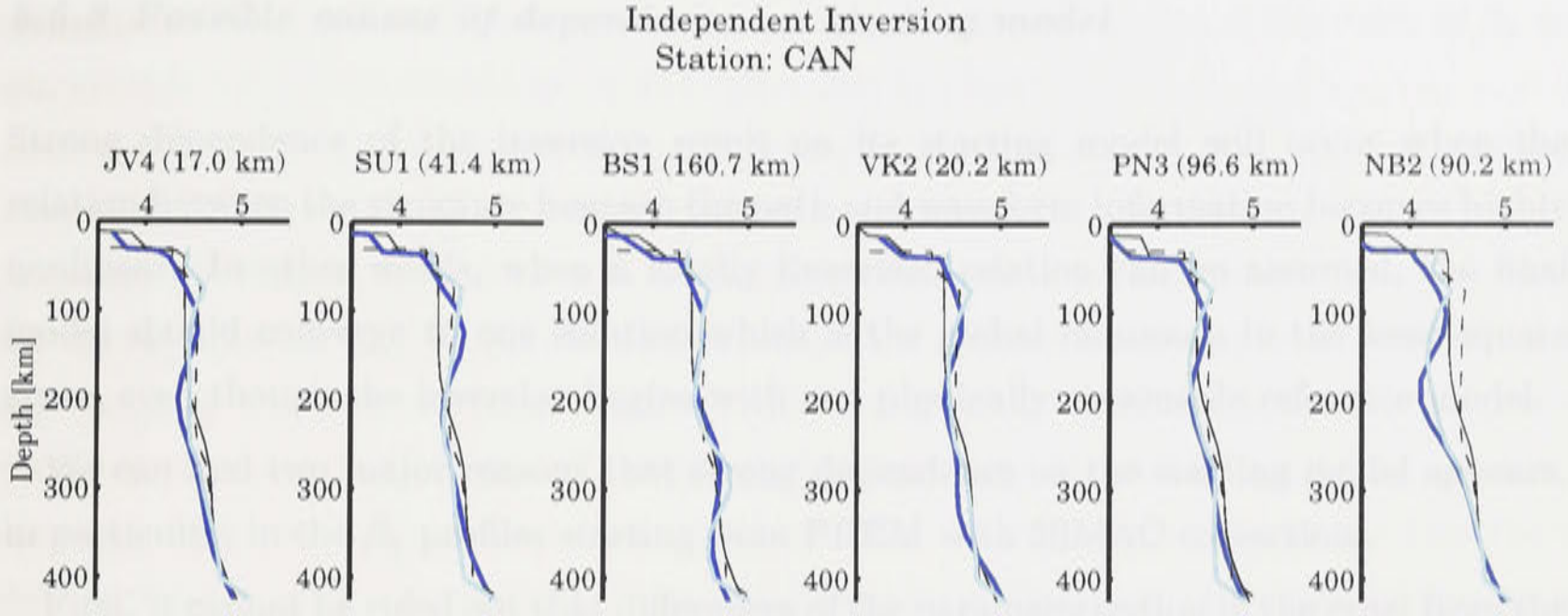

Fig. 5.5. This is the same figure as figure 5.4, but the station is NWAO. We use event BS1, instead of BS4.

in the horizontal component data recorded at CAN is better than that at NWAO. Second, the installation of the horizontal components at NWAO has the larger value (more than five degrees) of instrumental misorientation (Laske & Masters, 1996) than that at CAN. In other words, when we use the horizontal component data recorded at NWAO, we had better correct the data by the misorientation angle.

In summary, the resulting β_v profiles for all the paths from the two different styles of inversions (ie. joint and independent inversions) are quite similar in shape and amplitude even starting from the two different starting models. Thus, it is safe to say that β_v profiles have no significant dependence on their starting models for these paths in both joint and independent inversions. On the other hand, the β_h models have very strong dependence on the starting models. Although the results of the β_h profiles from the independent inversion are better than those from the joint inversion, the final β_h models from both inversions still depend strongly on its starting models.

5.5.3 Possible causes of dependence on starting model

Strong dependence of the inversion result on its starting model will occur when the relation between the structure beneath the path and waveform information becomes highly nonlinear. In other words, when a locally linearised relation can be assumed, the final model should converge to one solution which is the global minimum in the least-square sense, even though the inversion begins with any physically reasonable reference model.

We can find two major reasons that strong dependence on the starting model appears, in particular, in the β_h profiles starting from PREM with 3SMAC corrections.

First, it cannot be ruled out that differences of the parameterisation in the crust from the two models affect those of the β_h profiles from the two models. Given the same frequency range, the Love wave sensitivity kernel has its maximum value at a shallower depth than the Rayleigh wave kernel. It is therefore possible that the effects of the differing crustal parameterisation is magnified in the Love inversion case (β_h) compared with the Rayleigh wave case (β_v). This would tend to cause a strong dependence on the starting model for β_h profiles, because a linearised relation between the β_h structure and Love waveform information breaks down for the depths where the crustal effects penetrate.

Second, the large difference between the β_h values in the crust of western Australia compared with the reference model make it more demanding to obtain any plausible β_h solution, even though convergence can be achieved for lower β_h wavespeeds. If the true wavespeed structure can deviate significantly from the starting model, it is difficult to introduce any linear or weakly non-linear relation within the range of this wavespeed deviation . The β_h profiles in the Australian upper mantle structure have a maximum β_h value about eight percent as fast as the reference model *ak135* (Kaiho & Kennett, 2000). It is not so difficult to expect that some of the average 1-D β_h structures in our paths have comparably faster β_h values than the starting model PREM. In addition, our PREM-based starting model is isotropic, so that the β_h profile is slower than anisotropic PREM and anisotropic AU3 models (both have positive ξ values in the upper mantle); therefore, it could be much slower than the true structure in Australia. This is the reason that the Love inversion based on isotropic PREM is less successful for obtaining plausible β_h solutions than that starting from AU3.

In addition, we would like to mention a possibility that the joint inversion starting from PREM could generate very large polarisation anisotropy in the upper 200 km layer, in particular, as polarisation anisotropy is expressed as the parameter $\xi = (\beta_h/\beta_v)^2$. Some of the β_h models have very high wavespeed bulges above 200 km depth, sometimes down to even 300 km depth, while the β_v profiles keep high wavespeed layers in the similar depth

but smaller amplitudes. Thus, the resulting ξ curve, which is square of the ratio of β_h to β_v, reaches very large amplitude in the upper 200 km layer.

We also have to point out the independence of waveform matches from the two starting models. All the waveform matches between the empirical waveforms and the final synthetics in Appendix A show that the majority of the final models, even the implausible β_h models generate very similar waveforms to the observed seismograms. This means that a phase velocity calculated from an unfeasible model is quite close to that from the true structure, so that there will be the suite of wavespeed models, including the true model, which can explain the empirical waveforms. In other words, from the linearised 1-D waveform inversion such as Cara and Lévêque method, we may not determine a unique structure beneath the path, but may calculate a phase velocity curve that results in synthetic seismograms similar to observed one.

5.5.4 Ocean-continent mixed paths: influence of source

The implicit assumption in the waveform inversion procedure is that the source mechanism can be used directly with the starting model. Normally this assumption works well except for very shallow sources. The long period waves (< 100 sec) used in CMT solutions have limited depth resolution for shallow events because of the influence of the free-surface condition. In consequence, the minimum depth is set at 15 km, and an equivalent point source is derived at this depth. Usually a satisfactory fit to the long-period waveforms can be achieved in this way, but the positions of nodal lines may vary by a few degrees from the directions appropriate to a source at the true depth. For a shallow event, more reliable results can often be obtained by using the moment tensor derived from long-period body waves.

We should also note that CMT solutions are based on the PREM model with corrections for large scale lateral heterogeneity in the upper mantle. If the local deviations in the structure from PREM are large, they will give rise to an additional contribution to the moment tensor and may well contribute to the isotropic component of the source.

For paths with oceanic and continental legs of similar size, the average crustal structure will be significantly different from either the source or the receiver structures. In these circumstances, it may be necessary to adjust the source model, so that there is a satisfactory fit to the synthetic seismograms. The object is to find an equivalent source, so that the source excitation times in the model used for computation match those expected for PREM. The main effect arises from the shape of the eigenfunctions which have more energy close to the surface for oceanic type structures. As a result, it is usually possible to retain the source mechanism but to adjust the depth shallower.

Examples are provided by the paths from events SU1 and JV4 (figure 5.2) to NWAO in western Australia. These are large differences between the synthetics for the starting model and the observations which are evident in the shapes of the cross-correlation envelopes. A much closer match in envelope characters can be achieved by adjusting the source to shallower depth. The best results at NWAO are achieved with an adjustment to 11.4 km from 41.4 km for SU1 and 7 km from 17 km for JV4. However, these changes are not satisfactory for the dominantly continental paths from SU1 and JV4 to CAN. An improvement in envelope fit at CAN can be achieved with a small decrease in source depth.

The need to adjust source parameters for paths containing a large contrast in crustal structures indicates the limitations of the path-averaged concept. As pointed out by Kennett (1995) a more appropriate approach would be to treat the oceanic and continental segments separately with a transfer of the vertical distribution of energy between the modes of the different structures at the transition itself.

5.5.5 Representation of Australian upper mantle structure –choosing the most appropriate starting model for regional tomography

It is difficult to determine one average starting model for the upper mantle structure in Australia from the results of our inversions. The starting models of both AU3 and PREM with 3SMAC corrections could provide the reasonable final models of β_v for the majority of the paths.

In contrast, the final β_h profiles from the two starting models have large variations in their shapes and amplitudes, so that the β_h models depend strongly on the starting models. In other words, the choice of the starting model of the β_h structure is not appropriate for the Australian paths. In the results of the joint inversions for the paths CAN-SU1 and CAN-JV4 (the two lower-left plots in figure 5.3), the starting model AU3 changes very slightly above 300 km depth after the joint inversion. Thus the model AU3 itself represents well the average structure of this particular corridor. For the rest of the paths, the starting model AU3 is required to have some deviations to improve the waveform matches. Except for a few examples (e.g. NWAO-VK2, -SU1, -JV4 and CAN-BS1), such deviations are not extremely large, so that the model AU3 will be a good starting model for some parts of the Australian continent.

The final joint-inversion models of β_h starting from the PREM model with 3SMAC crustal corrections, however, have too large deviation from the starting model for the majority of the paths (dark green lines in the figure 5.3). This is probably because the β_h profile in the PREM is much slower than the true structure in the layer above about

250 km depth. Those deviations become smaller in the independent inversion cases (dark green lines in the figure 5.5). Thus we need to address the question of adequateness of the TIV assumption which makes the β_h model slower.

5.5.5.1 The TIV model can represent the Australian upper mantle structure?

Our inversion results do not support to apply the TIV assumption for recovering the Australian β_h structure for a couple of reasons.

The TIV model is the simplest anisotropic structure which can provide a means of reconciling Rayleigh and Love wave information when these cannot be fit by a common isotropic structure. However, the assumption of cylindrical symmetry about the vertical axis means that there is no allowance for azimuthal variation.

If the structure beneath Australia seems to be weakly anisotropic, then azimuthal variation of the seismic wavespeed would be expected with a bilobate (2θ) dependence for Rayleigh waves and a few lobe (4θ) dependence for Love waves. The azimuthal variation would be expected to be of similar size for the two types of waves. Debayle & Kennett (2000b) attempt to estimate the azimuthal variation for Rayleigh waves, but do not have enough paths to make a comparable representation for Love waves.

As we have already noted that the waveform inversions of surface waves does not provide adequate constraints on all the 5 transversely isotropic parameters. Only 3 have been allowed to vary in the inversion. The separate isotropic inversions are in fact more economical by working with only 2 parameters.

Part of the difficulty of constructing satisfactory β_h models comes from the nature of Love waves. The properties of the fundamental mode Love waves are much closer to that of the higher modes than Rayleigh waves. As a result, the cross-correlation for the Love modes do not have as much discrimination potential as for Rayleigh waves and need to be more tightly constrained to provide comparable control on the velocity model.

We finally comment on the choice of the adequate starting models for Australian paths. The comparison of the final models from the two different starting models indicates that the selection of close starting models to the true model is crucial, in particular, the β_h models. The comparison also represents that only one starting model is not enough to represent whole Australian structure. Thus, we propose that different starting models for corridors covering different tectonic provinces. Although some studies (e.g. Zielhuis & van der Hilst, 1996) use different starting models for source, propagation path and station locations, they change only the crustal structure. We recommend that different upper mantle structures as well as the crustal structures are employed for the linearised 1-D waveform inversion schemes.

5.6 Conclusions

We conduct Rayleigh and Love joint waveform inversion for selected Australian paths with different starting models. Also Rayleigh and Love separate isotropic inversions are performed for the same paths with the same starting models. Both separate and joint inversions generate β_v and ξ profiles for all the paths, from which we try to estimate the horizontal and vertical patterns of polarisation anisotropy in Australia.

Our results supports the following four points: (1) Polarisation anisotropy is present over the whole Australian continent; (2) The variation of the polarisation anisotropy in depth is observed, in particular, in the layer above 200 km depth. The measurement of polarisation anisotropy below 200 km depth has limited resolution, so that it is difficult to quantify the polarisation anisotropy below this depth; (3) The horizontal variation of polarisation anisotropy from path to path could be azimuth dependent. However, it is fairly systematic; (4) The distribution of polarisation anisotropy is not consistent with a simple TIV assumption proposed by Gaherty & Jordan (1995). Crossing paths have different patterns of polarisation anisotropy which is not satisfactorily explained by one simple model. These horizontal and vertical variations could relate to those of azimuthal anisotropy in Rayleigh and Love waves.

We also have to point out some difficulties of the waveform inversion itself. It is often difficult to obtain a comparable level of fit to the waveforms of Rayleigh and Love in both joint and separate inversions. This is due firstly to a larger sensitivity of Love waveform inversion to starting model. In particular, the large deviation of the SH wavespeed profiles in Australia from a starting model enhances the possibility of poor waveform matching in Love waves. Second, the difficulty of a comparable matching is due to that of assuming a simple TIV behaviour for the Australian continent.

When a comparable waveform fit is achieved in the joint inversion, the vertical distribution of polarisation anisotropy is generally similar from different starting models. However, even with a robust approach such as Cara & Lévêque method, it would be still difficult to find a satisfactory SH wavespeed profile for some of paths using a TIV single starting model.

6

CONSTRUCTION OF SUITABLE STARTING MODELS FOR REGIONAL WAVEFORM INVERSION

6.1 Introduction

In chapters 4 and 5, we find two crucial conditions for the two different styles of regional waveform inversions (the PWI and CL methods) applied for Australian paths. The first condition is that starting models for the inversions should be close to the true structures. In other words, we need rather accurate prior information on the structures beneath the paths, when the 1-D linearised waveform inversions are performed. In particular, the PWI method requires less than 4 % deviation from the true model to converge to a solution which has enough resolution in the layer from 80 km to 250 km depth. The second condition is that the Australian continent is not represented by just one simple seismic model. Thus, to characterise the Australian seismic structure, one way is to divide the continent into several corridors (Kaiho & Kennett, 2000) and to put a few possible seismic profiles to each corridor.

However, the previous waveform inversions for the Australian region produced the seismic images of β_v which may have too large deviations from their reference values. The PWI method (van der Hilst et al., 1998) put $\pm$ 5 % wavespeed perturbations from the reference model into the resulting map at 140 km depth (fig 1.3 in chapter 1), because the PWI synthetic test in chapter 4 indicates more than 3 % deviation could not be fully recovered. Debayle (1999) also infers that there are more than $\pm$ 10 % differences from the reference model in the CL inversion result at 150 km depth (figure 1.4 in chapter 1). These large variations of β_v may imply that the initial models are not close enough to the true structures for some of the paths. In addition, both PWI and CL inversions use one single upper mantle model (in particular, below 100 km depth) for the Australian region, although the two methods alter the crustal models for the paths. Moreover, we note the strong lateral contrast of β_v between western and eastern Australia and the

existence of ocean-continent boundaries around the continent. Above all, we suspect that the current two waveform inversion methods may not adequately set their initial models for the Australian continent, which affects the resulting 3-D models for the Australian region.

Thus, it is necessary to find a way to obtain suitable regionalisation of the continent for setting closer initial models for the Australian region. Furthermore, we have to seek an efficient means of determining acceptable initial models independently from the waveform inversion techniques. For the above two purposes, the frequency-time analysis (FTAN) method (Levshin et al., 1972) is a good candidate, mainly because FTAN is a moving-window filtering technique applied to observed waveforms, so that it does not need any synthetic calculation of seismograms; therefore, it is free from the majority of assumptions on structure that the waveform inversions require. As a result, FTAN can independently obtain the group velocity dispersion curve for each path from the empirical signal. From the group dispersion curve, we can determine a structure beneath the path and use it as an initial input model for the inversions.

In this chapter, we first review the basic characteristics of the FTAN technique. Next we investigate how the Australian continent could be regionalised based on the FTAN-based group dispersion curves for the intercontinental paths. Third, to judge the adequateness of the FTAN result, we compare the resulting group dispersion curves from the FTAN filtering and those from the CL joint inversion results for the selected paths. we then show that the FTAN method is an efficient means of constructing acceptable starting models for the regional waveform inversion methods for Australian paths.

6.2 Data and FTAN analysis

To avoid contaminations from rapid changes of the crustal structure at ocean-continent boundaries, we select one of the continental events (the Derby event; chapter 4) and the six permanent broadband seismic stations in Australia (figure 6.1). To compare the oceanic and continental path effects on the FTAN results, we also select three island broadband IRIS stations (COCO, HNR, and PMG). The path from the Derby to COCO is an oceanic path, while the path to PMG is almost a continental path. Moreover, the path to the island station HNR is an ocean-continent mixed path.

Next, we briefly describe weakness and strengths of the FTAN technique. The weakness is that FTAN can extract only the fundamental mode part of Rayleigh and Love waves on the three components. In particular, it is difficult to separate the fundamental part of Love waves from the higher mode signals. On the contrary, one of the strengths is that FTAN extracts the group velocity information from the observed waveform, so that we

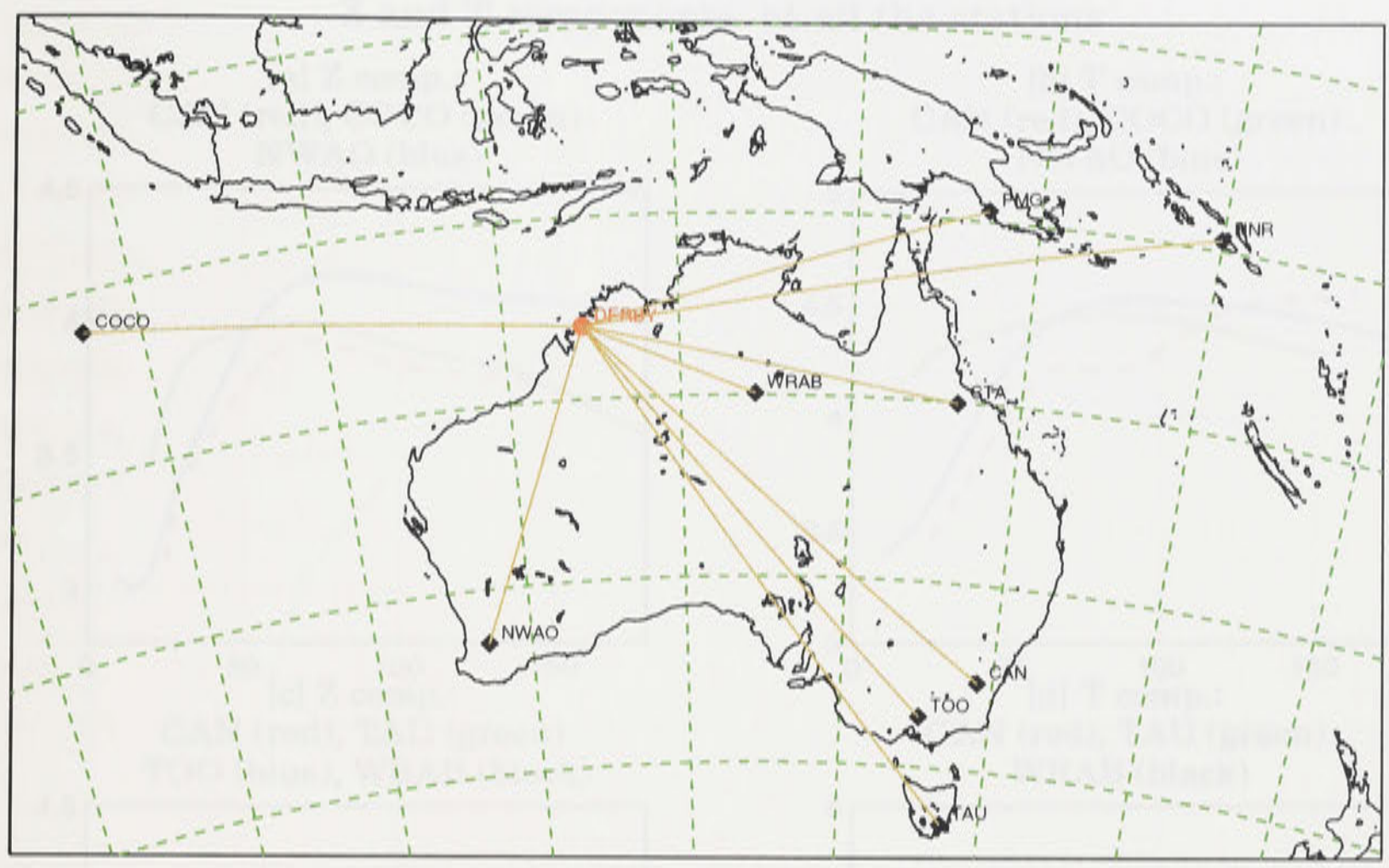

Fig. 6.1. Ray path distribution from the Derby event to IRIS stations (COCO, NWAO, TAU, HNR, and PMG), GEOSCOPE station (CAN) and AGSO stations (TOO and CTA).

need no information on the initial phase at the source. This means FTAN can use the seismograms which do not have information on source mechanisms. The other strength is that group velocity information is weakly related to source mechanism, so that FTAN can avoid on- or near-node problems which reduce the number of usable seismograms for surface waveform inversion. Moreover, the FTAN processing does not need any synthetic calculation of seismograms, so that FTAN is almost free from the assumptions required in the waveform inversion.

6.3 Regionalisation of the Australian continent

We divide the Australian continent into three regions based on the ray path distribution in figure 6.1 and the crustal outcrops and tectonic units (figure 1.1 in chapter 1). The region-1 is a corridor represented by the path from the Derby epicentre to NWAO. This region contains the western Australian cratonic blocks which have an S wavespeed profile more than an 8 % faster than the reference model *ak*135 (Kaiho & Kennett, 2000). The region-2 includes the three paths to TAU, TOO, and CAN. This corridor comes across the old western and central crustal blocks in the first two thirds of the path and the younger eastern belts in the rest of the path, so that the structure of the corridor could be

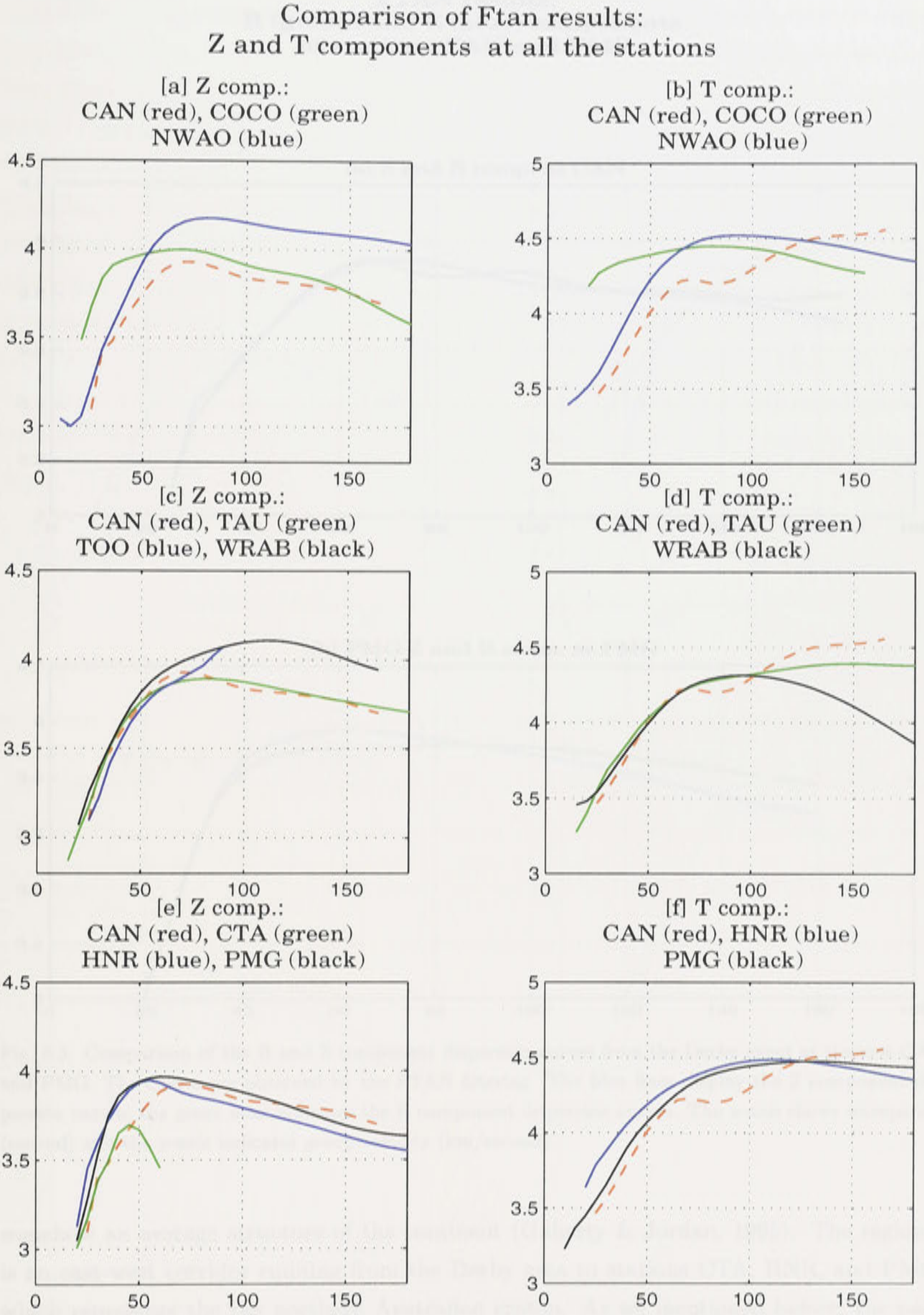

Fig. 6.2. FTAN analyses of the Z and T component data from the Derby event recorded at the nine stations. The x-axis shows waveperiod (second) and the y-axis indicates group velocity (km/second).

FTAN results:
R (green) and Z (blue) components
at stations CAN and PMG

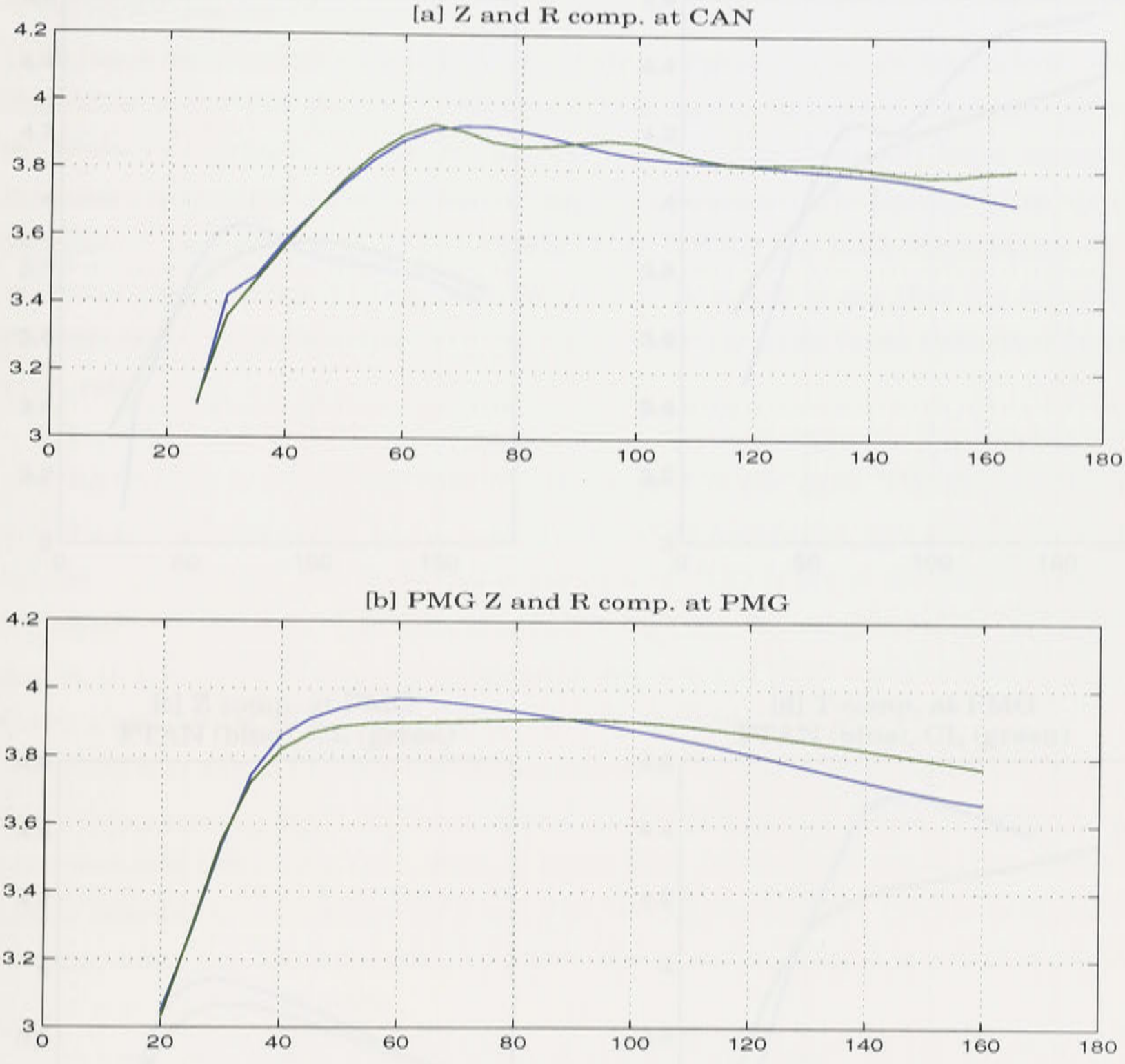

Fig. 6.3. Comparison of the R and Z component dispersion curves from the Derby event at stations CAN and PMG. The curves are obtained by the FTAN filtering. The blue lines display the Z component dispersion curves, the green lines indicates the R component dispersion curves. The x-axis shows waveperiod (second) and the y-axis indicates group velocity (km/second).

somehow an average structure of the continent (Gaherty & Jordan, 1995). The region-3 is an east-west corridor running from the Derby area to stations CTA, HNR, and PMG, which represents the the northern Australian craton. As we mentioned before, the path to PMG is almost continental and the path to HNR has a continental component of about 50 % . More than 60 % of the path to CTA also lies on the northern Australian craton.

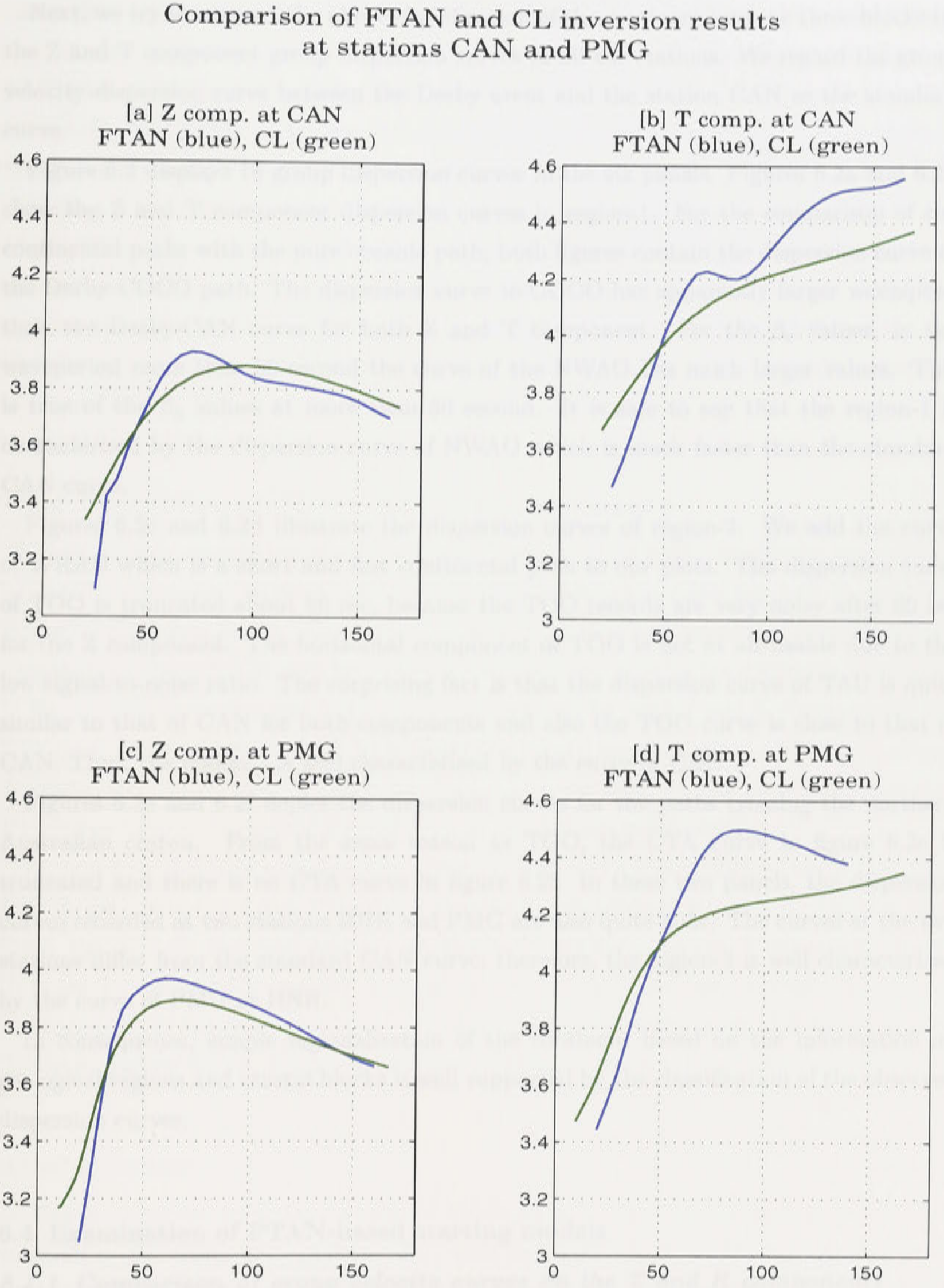

Fig. 6.4. Comparison of the Derby dispersion curves resulting from the FTAN analysis and the Cara and Lévêque method for the Z and T components at stations CAN and PMG. The CL dispersion curves (green lines) are synthesized from the β_v and β_h profiles generated by the Rayleigh and Love joint inversion method (Cara & Lévêque, 1987). The x-axis shows waveperiod (second) and the y-axis indicates group velocity (km/second).

Next, we try to support the above classification of the continent into the three blocks by the Z and T component group dispersion curves at all the stations. We regard the group velocity dispersion curve between the Derby event and the station CAN as the standard curve.

Figure 6.2 displays 16 group dispersion curves in the six panels. Figures 6.2a and 6.2b show the Z and T component dispersion curves in region-1. For the comparison of the continental paths with the pure oceanic path, both figures contain the dispersion curve of the Derby-COCO path. The dispersion curve to COCO has apparently larger wavespeed than the Derby-CAN curve for both Z and T component. For the β_v values, in the waveperiod more than 50 second the curve of the NWAO has much larger values. This is true of the β_h values at more than 60 second. It is safe to say that the region-1 is characterised by the dispersion curve of NWAO which is much faster than the standard CAN curve.

Figures 6.2c and 6.2d illustrate the dispersion curves of region-2. We add the curve of WRAB which is a short and fast continental path to our plots. The dispersion curve of TOO is truncated about 80 sec, because the TOO records are very noisy after 80 sec for the Z component. The horizontal component of TOO is not at all usable due to the low signal-to-noise ratio. The surprising fact is that the dispersion curve of TAU is quite similar to that of CAN for both components and also the TOO curve is close to that of CAN. Thus, the region-2 is well characterised by the curve of CAN.

Figures 6.2e and 6.2f depict the dispersion curves for the paths crossing the northern Australian craton. From the same reason as TOO, the CTA curve in figure 6.2e is truncated and there is no CTA curve in figure 6.2f. In these two panels, the dispersion curves recorded at two stations HNR and PMG are also quite alike. The curves at the two stations differ from the standard CAN curve; therefore, the region-3 is well characterised by the curve of PMG or HNR.

In consequence, simple regionalisation of the continent based on the information on geological regions and crustal blocks is well supported by the classification of the observed dispersion curves.

6.4 Examination of FTAN-based starting models

6.4.1 Comparison of group velocity curves on the Z and R components

Before the examination of the FTAN-based model, we compare the group dispersion curve on the Z component with that on the R component at two stations CAN and PMG. The difference of the two component indicates that adequateness of the setting of the horizontal

component at the stations, because the R component is synthesized from the two horizontal components (N-S and E-W). If there is any misorientation in the horizontal plane or inclination from the horizontal plane, the rotated R component provides unpredictable results. If the R component gives an expected result, the other horizontal component (the tangential component) is expected to be in right setting.

Figures 6.3a and 6.3b show the R and Z component dispersion curves at CAN and PMG. These curves indicate the dispersion of Rayleigh waves in which particle motions are retrograde in the vertical plane, so that if the settings of the seismometers at the two stations are right, the Z and R should be the same. From figures 6.3a and 6.3b, we can say that the settings of the two seismometers have minimum errors, so that we take advantage of the horizontal T component as well as the R component.

6.4.2 Comparison of FTAN and CL inversion results

We have already established an efficient way of constructing initial models for regionalised blocks. It is necessary to check that those initial models are suitable for the 1-D linearised inversion. In other words, we have to examine that the final converged solution by the linearised inversion is not very far from the initial model. Ideally the difference is within 3 % for the PWI inversion and 8 % for the CL inversion for both Z and T components. For that purpose, we compare the FTAN-based observed dispersion curve with the CL-based synthetic dispersion curve. If the difference is small enough , we can justify the idea that FTAN can be a initial model generator for the 1-D linearised inversion.

Figures 6.4a and 6.4c manifest that the FTAN-filtered curve is quite close to that from the CL results at CAN and PMG. The maximum difference is about 3 %. On the other hand, figures 6.4b and 6.4d clarify that the difference between the T component curves from the FTAN and CL methods become very large; the worst case is more than 7%.

Therefore, we can conclude that the FTAN filtering technique is suitable for generating β_v initial models for the 1-D linearised inversion, but not for the β_h initial models.

6.5 Conclusions

In this chapter we investigate a way of obtaining suitable starting models for regional inversions for Australian paths. For that purpose, it is necessary to divide the Australian continent into several seismological blocks and to find an appropriate means of independently determining initial models for the inversions. We try to take full advantage of the FTAN filtering method because of its applicability to the observed data without imposing any prior conditions.

The group velocity dispersion curves derived from FTAN allow regionalisation of the continent into several blocks defined seismologically. We regard the group velocity dispersion curve between the Derby event and the station CAN as the standard curve. Then the blocks are classified by the difference between its own dispersion curve and the standard curve. The first block is characterised by rather faster group velocity curves from 20 to more than 160 seconds, which mainly covers the Archean cratons in the western part of the continent. The second block is the northwestern and southeastern corridor which dispersion curves are represented by the Derby-CAN curve. The third block covers the northern Australian craton for which dispersion curves imply slightly higher β_v values in the waveperiod less than 60 second for the Z component.

The FTAN method can provide an efficient means of determining initial models of β_v for the regional waveform inversion methods. The difference between the group velocity curves from the FTAN analysis and the CL inversion result at the two stations are within 3% from its own value, so that the FTAN-based starting models of β_v are applicable to the current regional surface waveform inversions. In contrast, the resulting tangential-component dispersion curves at CAN and PMG from the FTAN filtering apparently differ from those synthesized by the CL joint inversion results. In the worst case, the perturbation reaches more than 7 %. These deviations are probably due to the existence of polarisation anisotropy and the difficulty of the separation of Love fundamental and higher mode waves. Therefore, the FTAN method could not provides an adequate initial model for the Love waveform inversion for some parts of the Australian continent.

7

SUMMARY AND FUTURE WORK

7.1 Summary

The series of synthetic recovery tests shows that both PWI and CL waveform inversions have different strengths and weaknesses. The PWI approach is quite robust for the perturbations of β_v in the crust and the uncertainty of the Moho depth. Also a good feature is to separate the portion of the fundamental mode Rayleigh waves from the higher modes and to apply different bandpass filters to the two windows. This will enhance the vertical resolution of the final model. In contrast, the PWI method can provide good results only when an adequate initial model is available. In other words, the PWI technique is quite sensitive to the initial model. Moreover, the separation of the two time windows gives biases on the resulting model, when the higher mode window has enhanced weighting.

The CL approach can recover the +8 % deviation from the upper mantle initial model in the synthetic test, so that the CL method can be applied for the region of large β_v wavespeed variations in the upper mantle. On the other hand, perturbations of the crustal β_v values give strong impacts on the resulting β_v profile from the CL inversion. In particular, the effect of the estimation error of Moho depth is significant in its amplitude and penetration depth, when the error is more than 10 km.

To improve the results of the PWI method, it is necessary to find a way of obtaining suitable initial models for the inversion. Also special care should be taken for the use of the higher mode time window in the PWI approach. On the other hand, to avoid contamination from the crustal structure, the CL starting model has to have more accurate crustal structure for each path. The CL approach also needs to invert the β_v profile in the crust and upper mantle, rather than only in the upper mantle.

From the Rayleigh and Love joint and independent inversions for selected Australian paths, we can conclude that the Australian continent has large variations of β_v and β_h

values in both horizontally and vertically. However, the measurements of polarisation anisotropy ($\xi = (\beta_h/\beta_v)^2$) show rather limited resolution below 200 km depth, so that it is difficult to clarify the structures of β_v and β_h below this depth. Furthermore, the presence of azimuthal anisotropy inferred from the observed Rayleigh waves indicates considerable complexity in variations of the β_v throughout the region. Thus, it is safe to say that the Australian seismological structure could not represented by one simple seismological model.

In addition, the comparison of the joint inversion results with those of the independent inversions for Australian paths elucidates the difficulty of obtaining stable β_h models for the paths. This is due partly to a strong sensitivity of Love wave inversion to starting model. Also the assumption of a simple TIV model for the complex Australian structure makes the resulting β_h profiles implausible.

The problem on the waveform inversions for the Australian continent is that we haven't have an efficient means of determining acceptable starting models of shear wavespeed, especially β_h, for the complex Australian seismological structure. We first attempt to divide the continent into three blocks based on the observed group velocity curves which are constructed with the FTAN filtering technique. Each block has one representative seismic profile which is generated from the observed group velocity curve. This classification of the continent simplifies the representative seismic structure of each block; therefore, we can design a closer initial model to the true structure for each block based on the FTAN dispersion curves. The three blocks respectively cover the western cratonic area, the northern craton, and a corridor running from the northwestern part to the southeastern part of Australia. The three blocks are also well classified by the three groups of the FTAN-created dispersion curves.

Second, we examine whether or not the initial model for each block is suitable for the inversion scheme. In other words, we measure the difference between the dispersion curve from the initial model and that from the final profile of the CL inversion. The FTAN-generated group dispersion curve for the Z component is quite close (within 3 % difference) to that synthesized from the CL final β_v profile. Thus, the model of β_v come from the FTAN analysis will be a good candidate of initial models for the CL inversion, because the final model of the CL inversion is not very far from the FTAN-based initial model. However, the β_h profile from the CL inversion constructs a quite different group dispersion curve from that of the FTAN filtering. This means that FTAN could not produce a suitable initial model of β_h for the CL inversion, because the CL Love wave inversion seems to be much more sensitive to the starting models than the CL Rayleigh wave inversion.

In consequence, the FTAN technique plays two important roles for the Australian waveform inversions. The first role is that FTAN helps to regionalise the continent into several seismological blocks which are represented by typical FTAN group dispersion curves. Such a classification of the continent can contribute to the construction of closer starting models for the regional inversion. Second, the FTAN approach can generate a good starting model of β_v for each block. However, the FTAN-generated dispersion curves for the T component at stations CAN and PMG display very poor matches to the final results of the CL inversion, so that the FTAN method is inadequate for constructing β_h starting models for Australian paths.

7.2 Strategy for regional surface waveform inversion

Based on the results of this PhD project, we would like to propose ways of improving the current regional waveform inversion methods. Currently two different styles of regional surface waveform tomography are conducted. The first one is designed to construct a 3-D shear wavespeed model from a suite of individual 1-D profiles for ray paths (e.g. van der Hilst et al., 1998; Debayle & Kennett, 2000a). Each 1-D model comes from 1-D linearised waveform inversions which are extensively discussed in this thesis. The other way is that a final 3-D model is inverted from 2-D group velocity maps at different frequencies, which is referred to as 'surface wave tomography' (Ritzwoller & Levshin, 1998). Thus we separately discuss how we can improve each of the regional-scale inversion methods.

7.2.1 1-D linearised waveform tomography

One of the most important problems on the present regional waveform inversions (e.g. van der Hilst et al., 1998; Debayle & Kennett, 2000a) is how to produce the closest starting model to the true structure for the region of interest, because an inaccurate starting model will enhance the non-linear effect. In comparison with the large variation of the inversion results (e.g. for Australia $\pm$ 10 % β_v variations by the CL method and $\pm$ 5 % by the PWI approach), the tolerated ranges of the β_v variation for both inversion techniques are much smaller. The range for the PWI is about 3% and for the CL method the range is more than 8 % but less than 15 %. This means the current images of the Australian β_v structure could change, if we introduce more appropriate initial models for the continent.

To obtain a better initial model for each path, we propose the use of FTAN filtering results for the following stages. The first stage is to regionalise the inversion area to more seismologically simple blocks based on the classification by the dispersion curves. Second, we choose one of the typical FTAN-based dispersion curves in each block and convert the

curve into the shear wavespeed profile. We then use the converted profile as an initial model for the block.

We also have to avoid accumulation of the linearisation errors in the 1-D linearised inversions. Both PWI and CL inversion methods share the common feature of the mode calculation for Rayleigh waves. They calculate the modes only for the initial model. When the wavespeed structure is perturbed in every iteration of the inversion, the mode file is not renewed and the synthetic seismogram is calculated based on the perturbations from the old mode file. This could make the final 1-D profile inaccurate.

To avoid the above non-linear effects, we propose the following procedure for the 1-D linearised waveform inversions. First, the region of the inversion should be divided into several blocks based on the FTAN dispersion curves. Second, we construct one initial model for each block derived from the typical dispersion curve for the block. Furthermore, we prepare several initial models for the block which may have $\pm$ 6 % wavespeed differences from the original profile. Fourth, we choose the best starting model for the block after the forward calculation. Then the inversion begins with the chosen initial model and continues. For the mode file calculation, it is definitely better to recalculate the mode files at every iteration to minimise non-linear effects. However, this may not be realistic due to the large amount of computation time required.

7.2.2 surface wave tomography

Surface wave tomography has an apparent limitation for improving vertical resolution of current 3-D shear-wave images. A 3-D model is inverted from 2-D group velocity maps at different frequencies. Each 2-D map derives from the FTAN analysis which applies moving filters to the observed waveform to isolate the portion of only the fundamental mode surface waves. In other words, surface waveform tomography can use only information from the fundamental mode surface waves, so that the vertical resolution of the resulting 3-D map is rather limited.

However, if the 1-D linearised waveform inversion (e.g. the PWI method) can be combined with the surface wave tomography, the vertical resolution of the final 3-D model is expected to be much better, because of the use of information on the higher modes. We employ the 1-D linearised waveform inversion as a dispersion predictor for each path, not for constructing a vertically varying 1-D model. In other words, we do not determine one seismologically 'reasonable' 1-D profile for one path from the 1-D linearised inversion, but we just select one of the 1-D profiles, all of which satisfy the reasonable level of observed and synthetic waveform fits. It is not crucial whether or not the selected vertical profile looks plausible, but important that the synthetic seismogram from the selected

model has good agreement with the empirical waveform. This is mainly because we do not have enough prior information on the structure to determine one profile out of the several candidates which match the synthetics to the observed seismogram. We give up constructing a deterministic 1-D model, but extract group velocity information for the path from the empirical waveform. This is a similar approach to the original surface wave tomography, but we use the 1-D linearised waveform inversion as a dispersion curve generator, instead of FTAN. Its advantage is to contain information on the higher mode waves. In addition, we use FTAN as a initial model generator.

The concrete step for obtaining a 3-D model is that we first find a rough regionalisation of the target area based on the suite of FTAN-based dispersion curves. Each block has an initial model which is derived from the representative of typical dispersion curves for the block. Second, the 1-D linearised waveform inversion begins with the initial model and selects one final model for each path which should guarantee the acceptable level of the waveform matches. From the selected profile, the group dispersion curve is generated for the path. Third, 2-D group dispersion maps at different frequencies are constructed by the group of the dispersion curves. Finally, we invert the 2-D dispersion maps into a 3-D shear wavespeed model using the sensitivity kernels of surface waves at each frequency.

8

SUPPLEMENTARY ISSUES

8.1 Introduction

The investigation of the shear wavespeed structures for the selected Australian paths in chapter 5 shows two apparent differences in the inversion results: one is between the independent inversions of Rayleigh and Love waves; the other is between the independent and joint inversions of Rayleigh and Love waves. The two differences appear in the form of different sensitivities to the initial models. In other words, they are related to different constraints on the domains of practical inversion: firstly for the different types of the data, that is to say, Rayleigh and Love waves, and secondly for the different styles of the inversions, namely, independent and joint inversions. Indeed, parts of the differences in the inversions are revealed in a series of comprehensive synthetic recovery tests in chapter 4. However, only Rayleigh waveform data are used in these synthetic tests and only the independent inversion method is applied to the recovery tests. Thus, in this chapter we undertake a further set of synthetic recovery tests of Rayleigh and Love waveform data with both independent and joint inversion techniques.

To explain the two sets of differences, we first conduct more detailed comparisons between the independent Rayleigh and Love waveform inversions than those in chapter 4. A series of new initial models are used for the inversions. Moreover, several control parameters such as focal depths are changed for a series of recovery tests of both Rayleigh and Love waves.

Second, Rayleigh and Love joint recovery tests are introduced with two different sets of β_v and β_h initial models. The comparison of the results of the joint tests and the previous independent tests suggests the adequateness of the assumption of TIV, because only the joint inversion assumes the TIV structure for the paths.

In addition to the above two differences of the CL-style inversions, we also compare the

results of the PWI and CL independent inversions of Rayleigh waves. Combined with the results in chapter 4, this comparison aims at clarifying the difference between the PWI and CL inversions with the same data and same plotting scale.

Finally, we examine an additional source of inversion errors, namely, errors in the synthetic calculations of Rayleigh and Love seismograms. This is crucial because at every iteration of the inversions a synthetic calculation is made and an error can be produced. The errors are accumulated in every iteration, so that the final inversion result can suffer from the influence of the errors in the synthetics due to the use of a fixed set of modes.

8.2 The independent synthetic recovery tests of Rayleigh and Love waves

In chapter 4, we conduct a series of independent synthetic recovery tests of Rayleigh waves to obtain the sensitivity to the initial model. The recovery tests use initial models having several percent deviations from the reference model (a smooth PREM) down to 350 km depth. We consider the behaviour of the resulting wavespeed profiles at intervals of five iterations (i.e. iterations 5, 10, 15, and 20).

However, we now introduce three changes to the independent recovery tests of surface waveform inversions to constrain the domain of practical inversion for Rayleigh and Love waves. Firstly we make independent synthetic recovery tests of both Rayleigh and Love waves, because the results of the independent Rayleigh and Love waveform inversions in chapter 5 suggest that the sensitivity of the Love wave inversion to the initial model is rather different from that of Rayleigh waves. Thus, we try to clarify both Rayleigh and Love sensitivities to the starting models to obtain adequate conditions for both inversions. Secondly, initial model deviations extending deeper (down to 900 km depth) are adopted for the independent recovery tests of Rayleigh and Love waves, in order to illustrate the behaviour of the final recovered profiles below 350 km depth. Thirdly, we examine limitations of the recoverability of the independent Rayleigh and Love inversions, rather than just showing the behaviour of the models after each group of five iterations. In other words, we try to recover the reference model (a smooth PREM) from several starting models, then determine the maximum shift of the initial model at which an acceptable recovery can be achieved.

We construct initial models having shear wavespeed shifts from a smoothed version of the PREM model with offsets of +2 % to +8 % for Love waves and +4 % to +12 % for Rayleigh waves. These deviations extend from the Moho (37 km) to 900 km depth. The simulated earthquake is the 'Derby' event described in chapter 4.3. The corrected focal depth is 10 km and the epicentral distance is 3251.78 km. Following the procedure of Debayle (1999), we take four steps in the CL waveform inversion to obtain a 1-D wavespeed

profile for each path. The first step is a match of the long period envelope of the secondary observables to the 'data' envelope, both are filtered at 100 second. In the second step, we conduct short period and long period envelope matchings of the secondary observable at 50 and 100 seconds. The third step is to introduce phase matching at long period for the secondary observables filtered at 100 second. The fourth step comprises both short and long period envelope matches and also instantaneous phase matches at 50 and 100 seconds. Debayle (1999) states that this procedure of moving from the long period matching to the short period matching is very efficient to avoid phase cycle skips of 2π.

In the following sections, firstly we try to retrieve the smooth PREM from different initial models using the independent CL inversions for Rayleigh waves. The sensitivity of the CL inversion of Rayleigh waves to the initial model will be quantified. Then we take a careful look at changes in the set of recovered models for Rayleigh waves using different values of several control parameters such as focal depths, correlation lengths, standard deviations of the data and of the parameters. Thirdly, independent synthetic recovery tests for Love waves are conducted with using several different initial models and focal depths.

8.2.1 The CL synthetic recovery tests of Rayleigh waves

8.2.1.1 Imposing + 4 % to + 12 % shifts to the starting model

In chapter 4, we have already seen that the CL method can recover the Rayleigh wave structure with an +8 % deviation from the initial model in the upper mantle. The recovery tests, however, suffered from kinks in the recovered models at about 350 km (e.g. figures 4.6 to 4.8) arising from the choice of the initial models. Indeed, the initial models have some percent of deviation in shear wavespeed from the reference model (a smooth PREM) down to 350 km, the deviations were forced to linearly decrease to zero at 400 km depth. This produces artificial effects in the recovery tests conducted with deeper focal depths (figures 4.6 and 4.8).

In this section, we extend the initial model deviations down to the greater depth of 900 km, with + 4 % to + 12 % shifts from a smooth PREM. Through the CL independent inversion of Rayleigh waves, we attempt to recover the smooth PREM model from the four initial models.

Figure 8.1 illustrates one of the four initial models, with +10 % shift from the initial model (a smoothed version of PREM) and the four recovered models. Note that these recovery tests are conducted for mantle structure alone with fixed crustal structure.

In figure 8.1, the recoveries from the four initial models are quite good from the surface

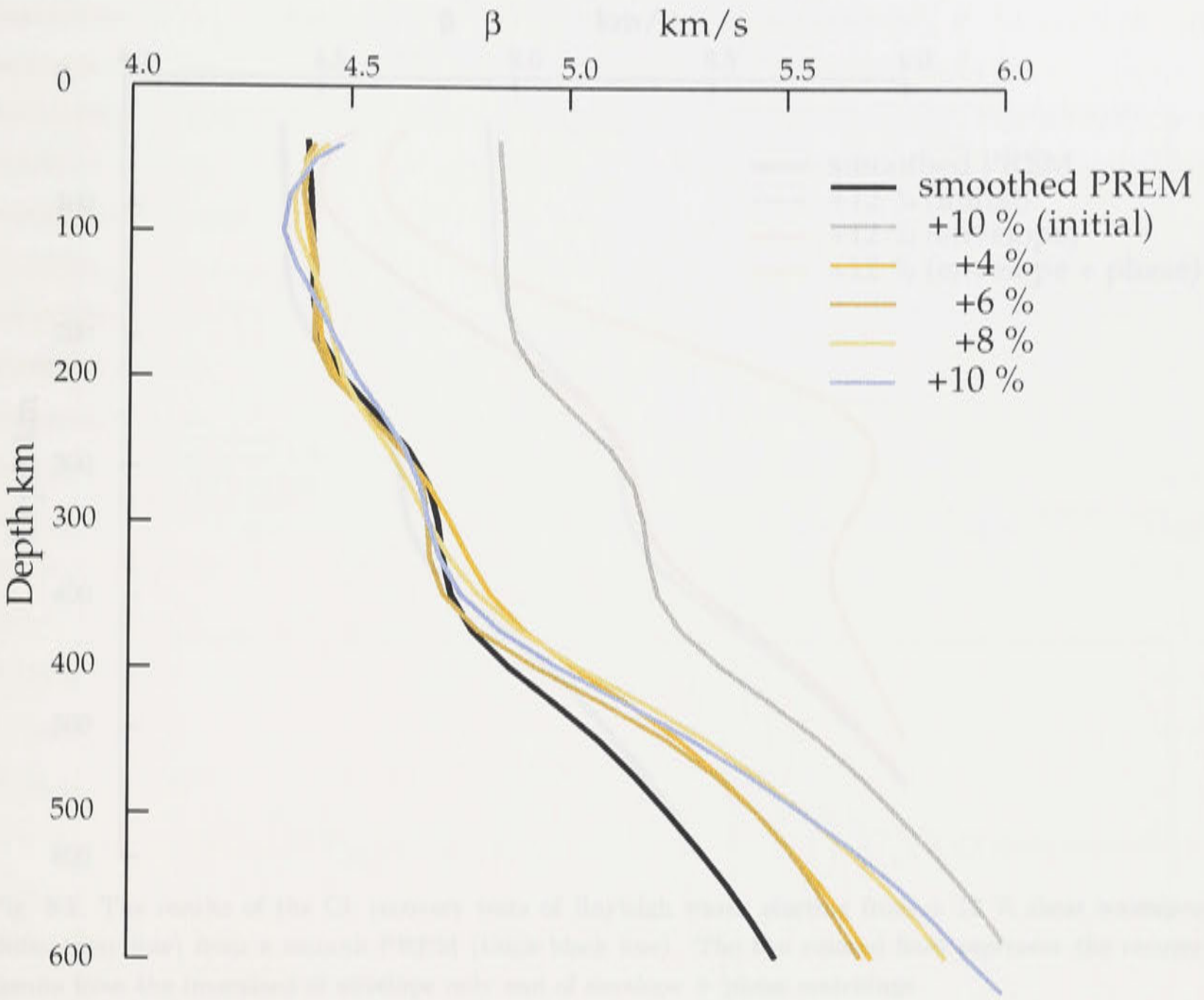

Fig. 8.1. The results of the CL recovery tests of Rayleigh waves from four different starting models (+4, +6, +8, and +10 % faster) to a smooth PREM (the thick black line). The gray line indicates one of the starting models, having the largest 10 % deviation from the reference model. The four colored lines show the final recovery models of the CL inversion starting from the four initial models.

at least down to 300 km. Below about 300 km, the final wavespeed models gradually tend toward the starting model, because the Rayleigh waveform has little information to achieve any resolution below this depth. However, the recovery from the +10 % shifted model has some visible deviations from the smooth PREM above 250 km. This difference could be too large to be acceptable.

For the +12 % recovery test (figure 8.2), we carefully investigate the process of Rayleigh waveform matchings, because the result of this test suggests that a typical 'phase-cycle-skip' problem seems to occur.

In figure 8.2, we see that the model derived from envelope-only matching moves towards the smooth PREM model above 200 km depth. But the CL algorithm still needs to make the curve closer to the reference model, by slowing down the fundamental mode Rayleigh waves in the synthetic seismogram.

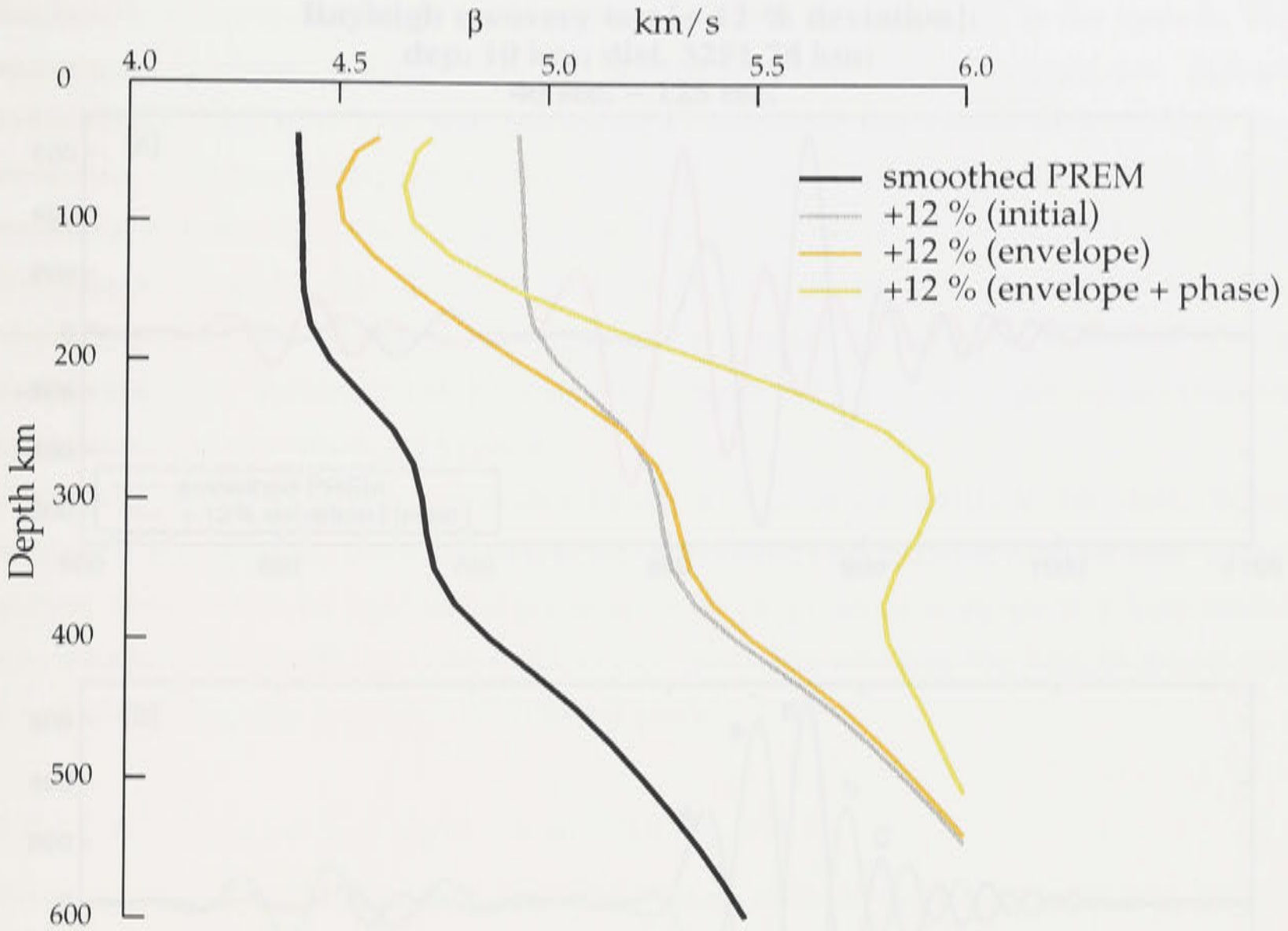

Fig. 8.2. The results of the CL recovery tests of Rayleigh waves starting from + 12 % shear wavespeed shifts (grey line) from a smooth PREM (thick black line). The two colored lines represent the recovery results from the inversions of envelope only and of envelope + phase matchings.

The resulting model from the envelope-phase matchings of the secondary observables has a large bulge in the faster wavespeed area between 150 km and 400 km depths. This is probably due to a 'phase-cycle-skip' phenomenon (figure 8.3). Panel 8.3 [a] shows the result of the forward modeling based on a smooth PREM and on the initial model, having +12 % faster shear wavespeed than the PREM.

In panel 8.3 [b], the CL algorithm slows down the shear wavespeed structure to try to match the synthetic seismogram (green line) to the 'data' seismogram (black line). As a result, the peaks (a and b) of the synthetics seem to shift by π from those (A, B, and C) of the data. To recover the smooth PREM model, the CL algorithm needs to further decrease the shear wavespeed, namely, the peak-a should move toward the peak-B rather than toward the peak-A. Also the peak-b should slide toward the peak-C. However, panel 8.3 [c] reveals that the algorithm chooses to make the synthetic seismogram shift in the faster direction. The peak-a of the synthetics overlaps the peak-A rather than the peak-B and also the peak-b moves to peak-B. This means that after envelope and phase matchings of the secondary observables, the phase of the synthetic seismogram (green line in panel

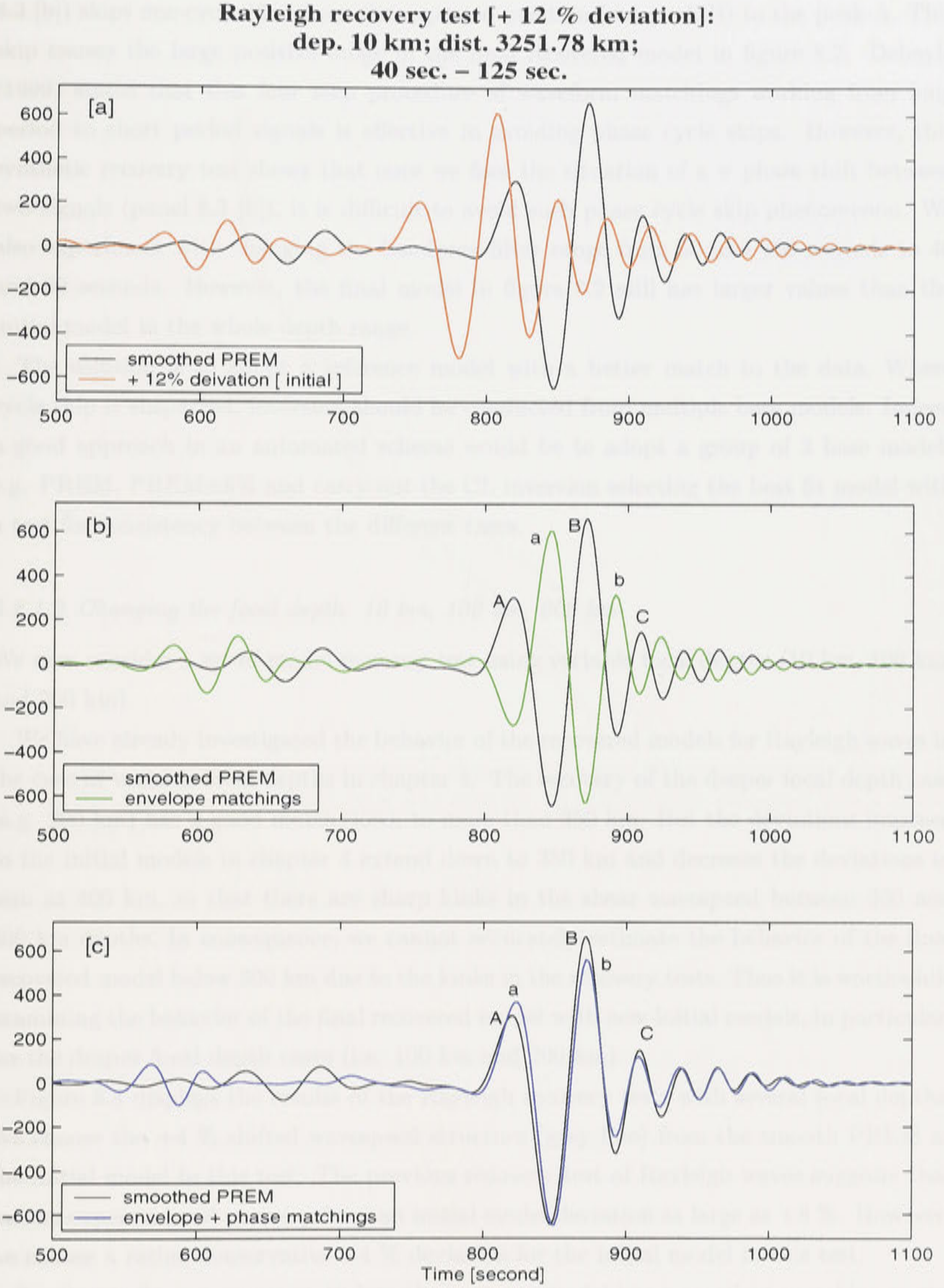

Fig. 8.3. The procedure for matching Rayleigh waveforms. Panel [a] shows forward calculations of the seismogram (red line) based on the starting model (+ 12% shift) and the 'observed' seismogram (black line) based on a smooth PREM. Panel [b] represents the synthetic (green line) and 'observed' seismograms after envelope matchings of the secondary observables filtered at 50 and 100 seconds. Panel [c] displays the inverted (blue line) and 'observed' seismograms resulting from envelope and phase matchings of the secondary observables. The bandpass filter between 40 and 125 seconds is applied to all the signals after the inversion. Detailed explanations are found in the text.

8.3 [b]) skips one-cycle (2π) from the expected position (the peak-B) to the peak-A. This skip causes the large positive bulge in the final recovered model in figure 8.2. Debayle (1999) states that this four step procedure of waveform matchings working from long period to short period signals is effective in avoiding phase cycle skips. However, this synthetic recovery test shows that once we face the situation of a π phase shift between two signals (panel 8.3 [b]), it is difficult to avoid such phase cycle skip phenomenon. We also experiment with changing the bandpass filter range from 50 and 100 seconds to 40 and 80 seconds. However, the final model in figure 8.2 still has larger values than the initial model in the whole depth range.

The solution is to adopt a reference model with a better match to the data. Where cycle skip is suspected, inversion should be conducted from multiple base models. Indeed a good approach in an automated scheme would be to adopt a group of 3 base models e.g. PREM, PREM±6% and carry out the CL inversion selecting the best fit model with a test for consistency between the different cases.

8.2.1.2 Changing the focal depth: 10 km, 100 km, 200 km

We now consider a set of model recovery test using variable focal depths (10 km, 100 km, and 200 km).

We have already investigated the behavior of the recovered models for Rayleigh waves in the case of variable focal depths in chapter 4. The recovery of the deeper focal depth case (e.g. 200 km) has a good match down to more than 350 km. But the deviations imposed to the initial models in chapter 4 extend down to 350 km and decrease the deviations to zero at 400 km, so that there are sharp kinks in the shear wavespeed between 350 and 400 km depths. In consequence, we cannot accurately estimate the behavior of the final recovered model below 300 km due to the kinks in the recovery tests. Thus it is worthwhile examining the behavior of the final recovered model with new initial models, in particular, for the deeper focal depth cases (i.e. 100 km and 200 km).

Figure 8.4 displays the results of the Rayleigh recovery tests with several focal depths. We choose the +4 % shifted wavespeed structure (grey line) from the smooth PREM as the initial model in this test. The previous recovery test of Rayleigh waves suggests that we can expect a good recovery from an initial model deviation as large as +8 %. However, we choose a rather conservative +4 % deviation for the initial model in this test.

For the shallowest source at 10 km, the recovery model has a excellent matching to the smooth PREM down to 280 km. The recovered curve gradually tends toward the initial model below 280 km, then at about 500 km the difference between the recovered and initial models diminishes. When the source is moved to 100 km, the match of the shear

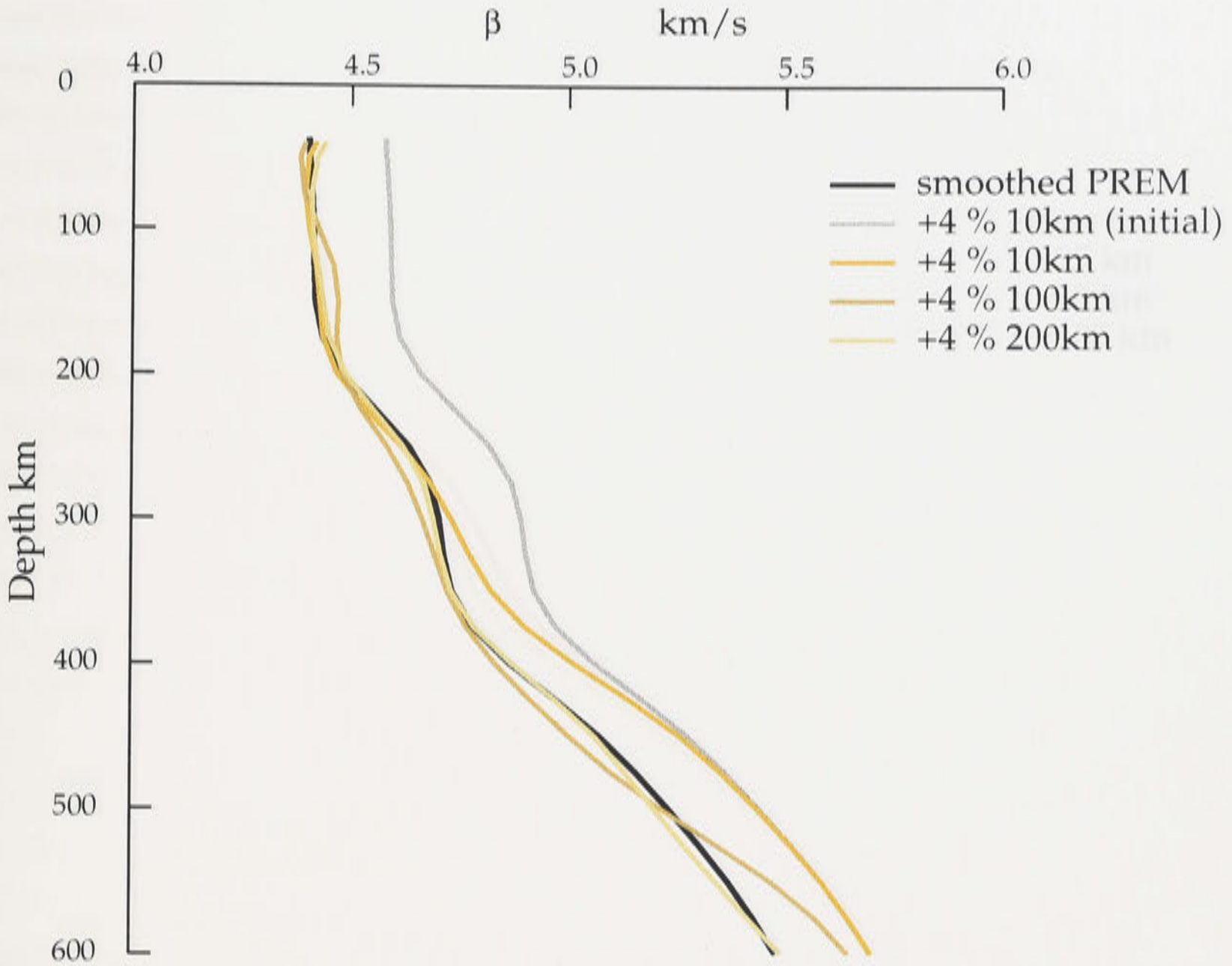

Fig. 8.4. The results of the CL recovery tests of Rayleigh waves with different focal depths (10 km, 100 km, and 200 km). The initial model (light grey line) has +4 % faster shear wavespeed than a smooth PREM (black line).

wavespeed model is extended to more than 400 km. However, we observe small amplitudes oscillations in the whole depth range in figure 8.4. For the deepest source at 200 km, nearly full recovery of the smoothed PREM wavespeed structure can be achieved down to more than 600 km depth. The good recoveries in the deeper source cases suggest that the CL method can effectively recover information of the higher modes which are well excited by deep focus earthquakes.

As noted by Yoshizawa & Kennett (2001) the phase dispersion associated with recovered models is more robust than the models themselves. The small oscillations have little effect because dispersion relies on integrated properties of the models.

8.2.1.3 Changing other control parameters

In addition to the properties of the source there are a number of other control parameters for the inversion. In the CL inversion technique, prior information such as correlation lengths (L_{cor}), the standard deviation of the data (σ_{d_0}), and the standard deviation of the

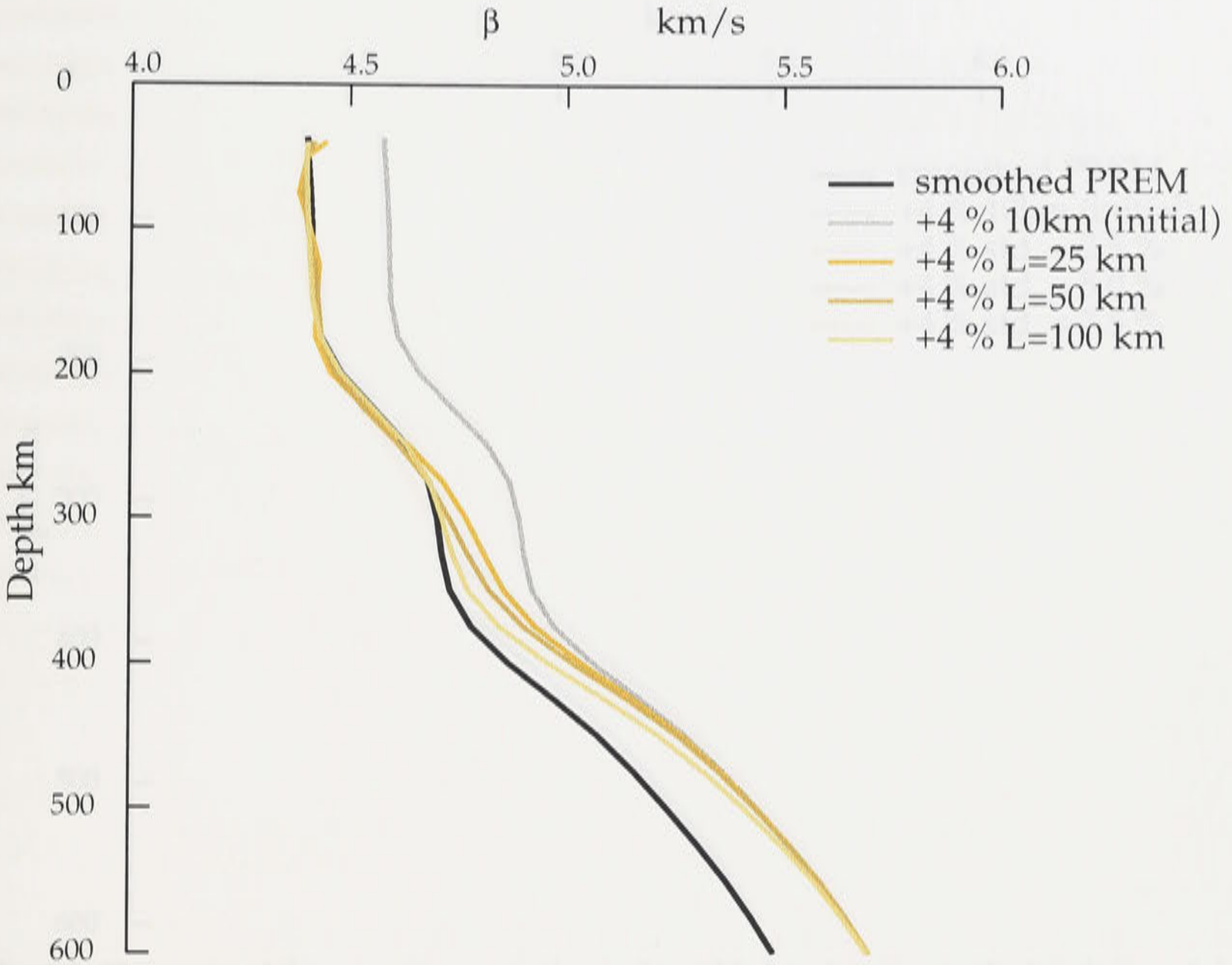

Fig. 8.5. The results of the same recovery tests as in figure 8.4, but changing correlation lengths (L_{cor} = 25 km, 50 km, and 100 km). The focal depth is fixed at 10 km.

initial model (σ_{p_0}) could influence the results. The relation between these parameters are specified by two equations:

$$C^{ij}_{d_0 d_0}(x_i, x_j) \;=\; \sigma_{d_0}(x_i) \cdot \sigma_{d_0}(x_j) \cdot \delta_{ij} \;, \tag{8.1}$$

where the prior standard deviation $\sigma_{d_0}(\mathbf{x})$ denotes the uncertainty of the date measurement at a depth x, when all the errors are independent and are within the order of σ_{d_0}.

$$C_{p_0 p_0}(\mathbf{x}, \mathbf{x}') \;=\; \sigma_{p_0}(\mathbf{x}) \cdot \sigma_{p_0}(\mathbf{x}') \cdot \exp\left\{ -\frac{1}{2} \frac{\|\mathbf{x} - \mathbf{x}'\|^2}{L^2_{cor}} \right\} \;. \tag{8.2}$$

The second equation describes the imposition of prior information on the vertical varying initial model p_0 with using a scale factor σ and a scale length L. The standard deviation σ_{p_0} is the uncertainty of the initial model p_0 at a point x which controls the amplitude of the perturbation, while L_{cor} is the correlation length between the two neighbouring points $(\mathbf{x}, \mathbf{x}')$ which decides the vertical smoothness of the model. This prior Gaussian function therefore makes the prior model smoothed in amplitude and vertical extension.

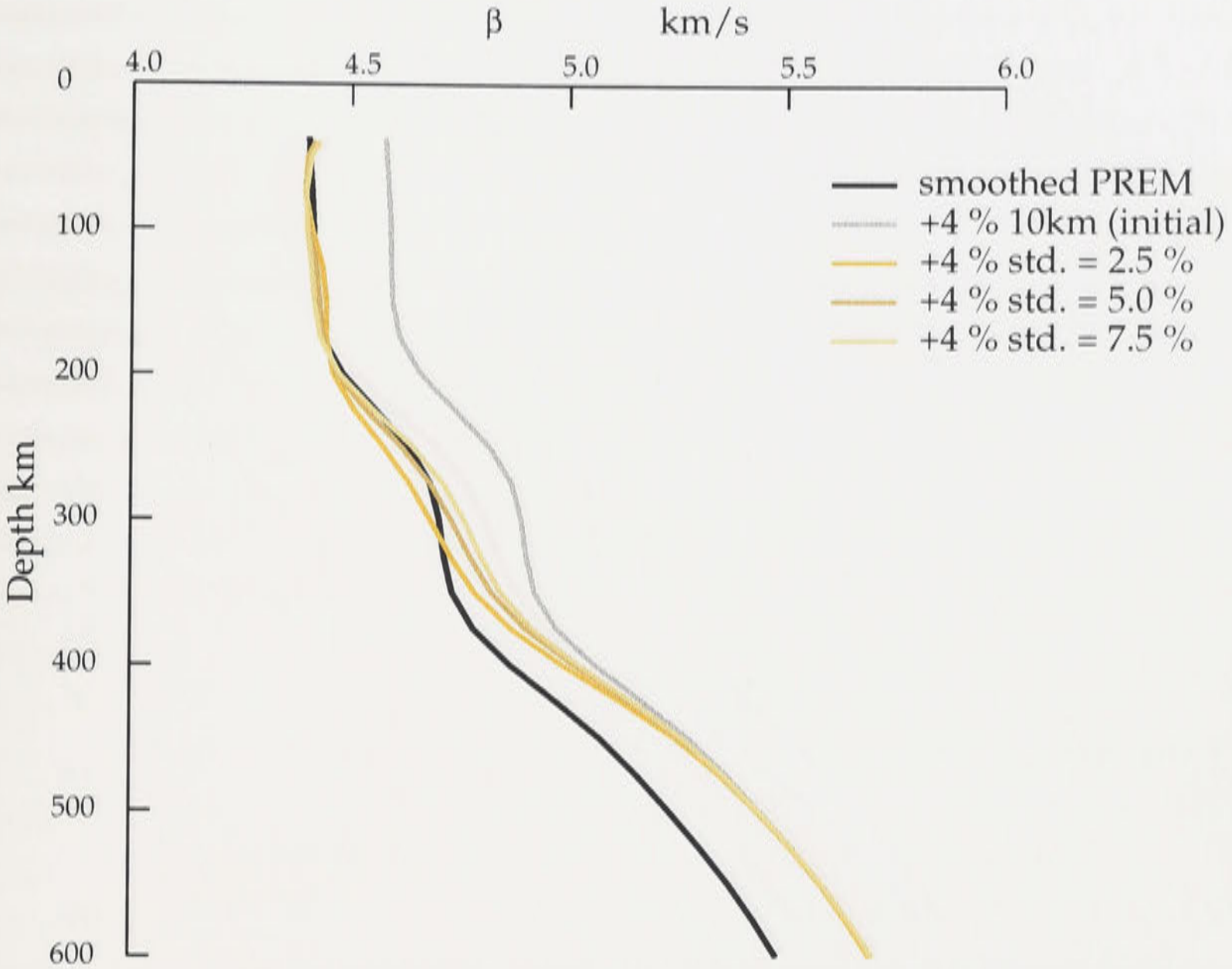

Fig. 8.6. The results of the same recovery tests as in figure 8.5, but changing standard deviations of the data (σ_{d_0} = 2.5 %, 5.0 %, and 7.5 %). The focal depth is 10 km.

Correlation length: 25 km, 50 km and 100 km (figure 8.5): The correlation length (L_{cor}) is one of the possible candidates to control results of the synthetic recovery tests. Lévêque et. al (1991) proposed L_{cor} is 50 km for the shear wavespeed structure, so that we set three choices for this particular test, namely, 50 km and two neighbouring values of 25 km and 100 km. Figure 8.5 reveals that all the three recovered models from +4 % shifted structure have no significant differences above about 270 km. Below 270 km depth, although the curve of the L_{cor} = 25 km has slightly faster values, all the three models are quite close and are absorbed into the initial model (grey line).

The standard deviations of the data: 2.5 %, 5.0 %, 7.5 % (figure 8.6): The recoveries having the three σ_{d_0} values from +4 % shift model have a good match to the smooth PREM model down to 250 km. The three curves are also quite close each other down to 200 km. Below 200 km depth, the curve with σ_{d_0} = 2.5 % has slightly smaller β_v values from the other two curves. Below about 400 km depth, all the three curves draw almost the same curves and tend towards the initial model.

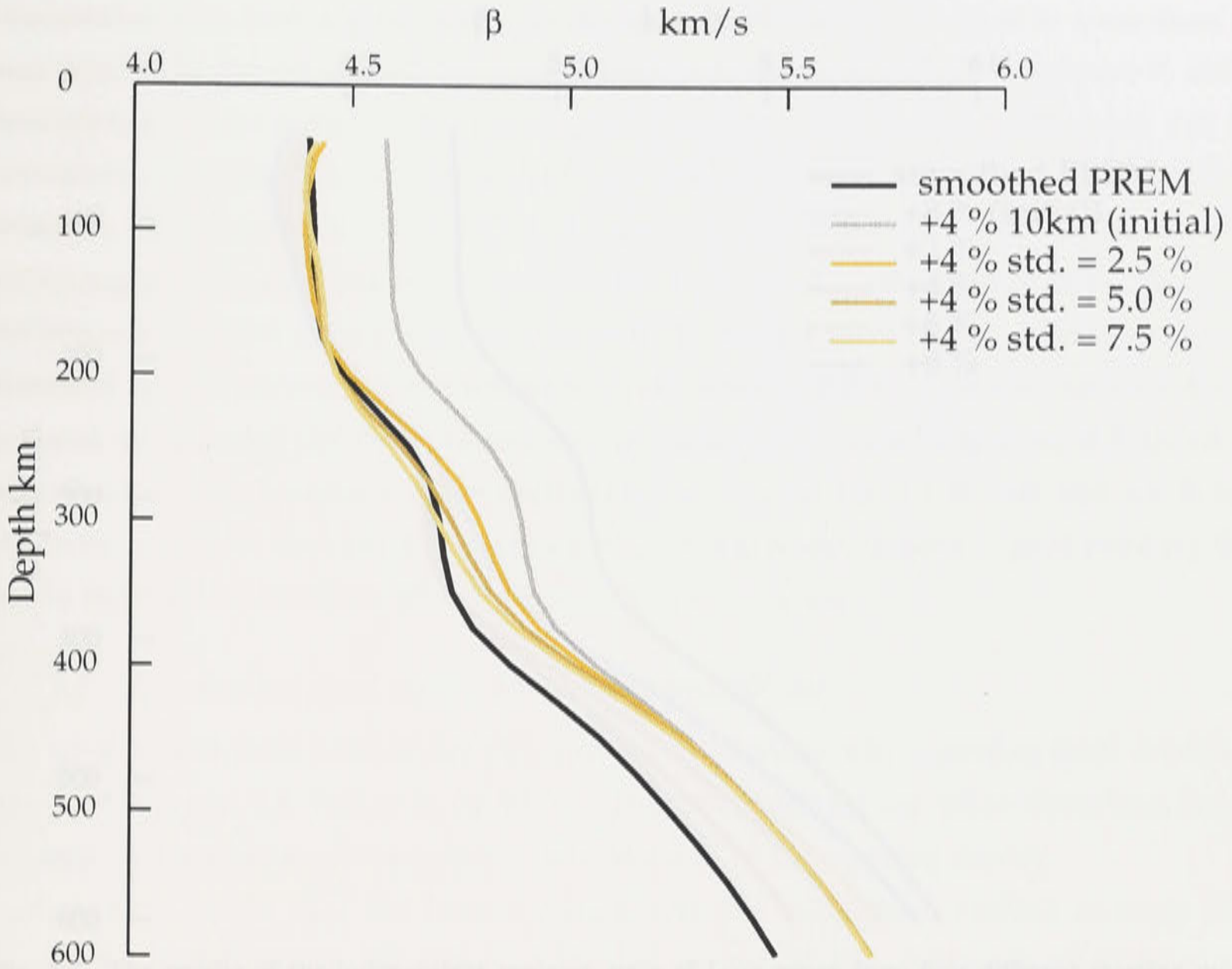

Fig. 8.7. The results of the same recovery tests as in figure 8.5, but changing standard deviations of the parameters (σ_{p_0} = 2.5 %, 5.0 %, and 7.5 %). The focal depth is 10 km.

The standard deviations of the initial model: 2.5 %, 5.0 %, 7.5 % (figure 8.7): Changing the values of σ_{p_0} between 2.5 % and 7.5 % also gives no significant impact on the recovery results of Rayleigh waveform inversion. All the recoveries are reasonably good to the depth of 300 km. The small difference between the three curves appears in the layer between 200 km and 400 km depths. Below 400 km depth, there is no significant difference among the three models and all the three curves move to the initial model.

The fundamental problem with regard to these control parameters is how to choose a suitable set of values. The previous studies of the surface waveform inversion using the CL technique (e.g. Lévêque et. al, 1991) do not show why the choice of parameters values, L_{cor} = 50 km, σ_{d_0} = 5.0 %, and σ_{p_0} = 5.0 %, was made. However, the synthetic tests clarify that those values of the three parameters are reasonable to recover the smooth PREM. Also some deviations of the three parameters from the originally proposed values provide acceptable levels of recovery.

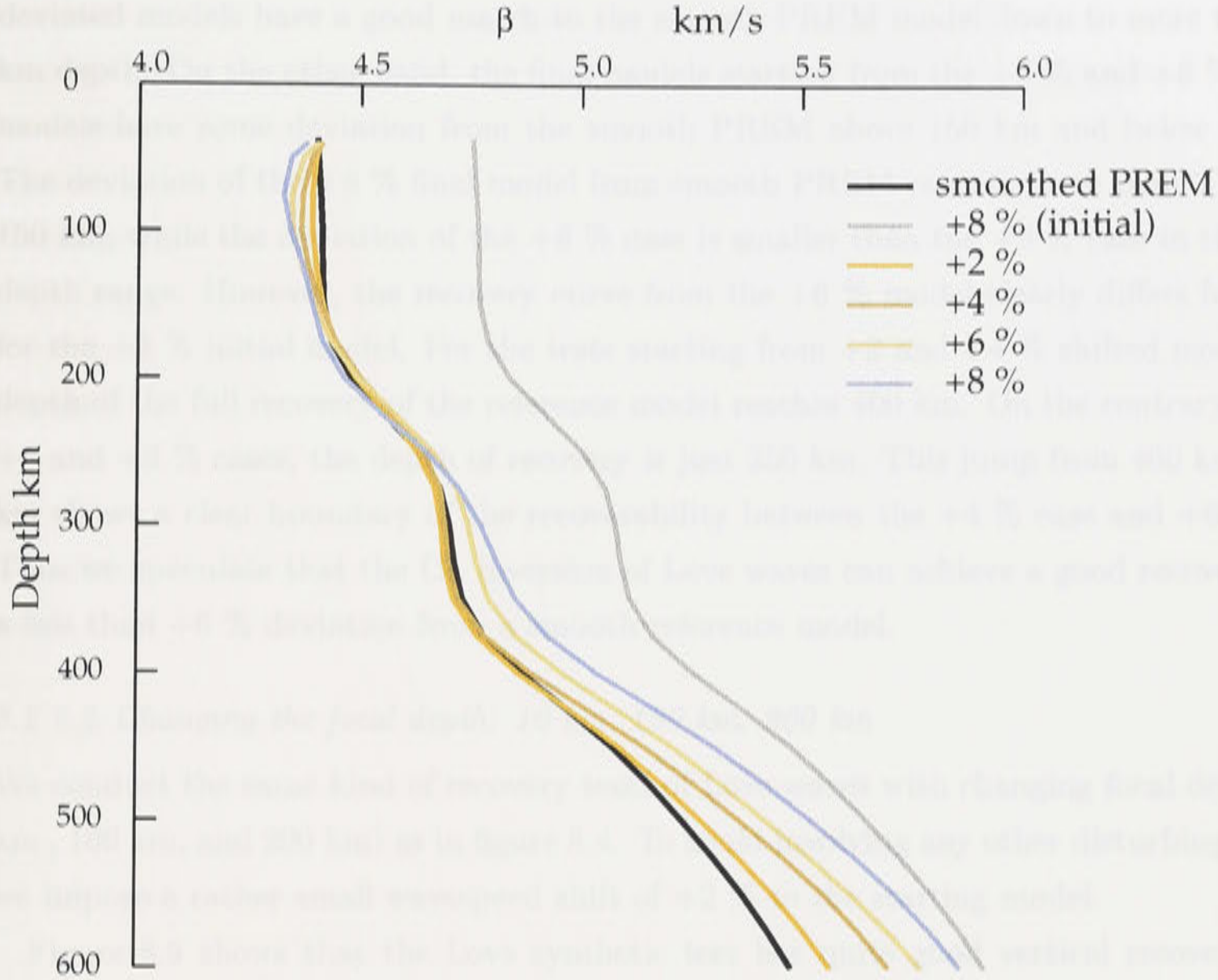

Fig. 8.8. The results of the independent recovery tests of Love waves from four different starting models having +2, +4, +6, and +8 % faster β_h wavespeeds than the smooth PREM (the thick black line). The gray line indicates one of the starting models, having the largest 8 % deviation from the smooth PREM. The four colored lines show the final recovery models of the CL inversion starting from the four initial models.

8.2.2 The CL synthetic recovery tests of Love waves

In chapter 5, we suggest that Love wave inversion should be more sensitive to the initial model than the Rayleigh wave inversion. However, we have not yet quantified to what degree the Love inversion is sensitive to the initial model. We therefore conduct an independent synthetic recovery test of Love waves using different initial models. In addition, the other type of the Love recovery test is conducted with different focal depths (10 km, 100 km, and 200 km), because the focal depth should be the most influential control parameter to the recovery result.

8.2.2.1 Imposing + 2 % to + 8 % shifts to the starting model

We construct four starting models having +2, +4, +6, and +8 % faster β_h wavespeeds than the smooth PREM and attempt to recover the smooth PREM model from these initial models. We again simulate the 'Derby' event with focal depth fixed at 10 km.

Figure 8.8 shows that the two recovered models starting from the +2 % and +4 %

deviated models have a good match to the smooth PREM model down to more than 400 km depth. On the other hand, the final models starting from the +6 % and +8 % shifted models have some deviation from the smooth PREM above 150 km and below 250 km. The deviation of the +8 % final model from smooth PREM reaches more than 2 % above 150 km, while the deviation of the +6 % case is smaller than the +8 % case in the whole depth range. However, the recovery curve from the +6 % model clearly differs from that for the +4 % initial model. For the tests starting from +2 and +4 % shifted models, the depth of the full recovery of the reference model reaches 400 km. On the contrary, for the +6 and +8 % cases, the depth of recovery is just 250 km. This jump from 400 km to 250 km shows a clear boundary of the recoverability between the +4 % case and +6 % case. Thus we speculate that the CL inversion of Love waves can achieve a good recovery from a less than +6 % deviation from a smooth reference model.

8.2.2.2 Changing the focal depth: 10 km, 100 km, 200 km

We conduct the same kind of recovery tests of Love waves with changing focal depths (10 km , 100 km, and 200 km) as in figure 8.4. To avoid involving any other disturbing factors, we impose a rather small wavespeed shift of +2 % to the starting model.

Figure 8.9 shows that the Love synthetic test has quite good vertical recovery down to 450 km, even though the source is located at just 10 km. Although small amplitude oscillation are observed in the recovery cases of 100 km and 200 km focal depths, the recovery from a +2 % shift are quite good down to more than 500 km depth.

8.3 The CL Rayleigh-Love joint recovery tests

The set of independent synthetic recovery tests for Rayleigh and Love waves suggests that we can recover the smooth PREM model from a +10 % shift in starting model for Rayleigh waves and from offsets of less than +6 % for Love wavespeed structure. In other words, the Rayleigh independent inversion is not very sensitive to the initial model having +10 % deviation from a smooth reference model. The Love independent inversion also are insensitive to the difference of the initial models, when the initial models deviate by less than +6 % from a smooth reference model.

In chapter 5, we conclude that the joint inversion results are less stable than those of the independent inversion. In particular, some of the Love final models of the joint inversion are far from plausible. A interesting question arises whether or not the same recovery can be achieved for the Rayleigh and Love joint inversion as for the independent cases. This is particularly important for judging the limitations of Rayleigh-Love joint inversion, that is, the adequateness of the assumption of a TIV medium (Transverse Isotropy with

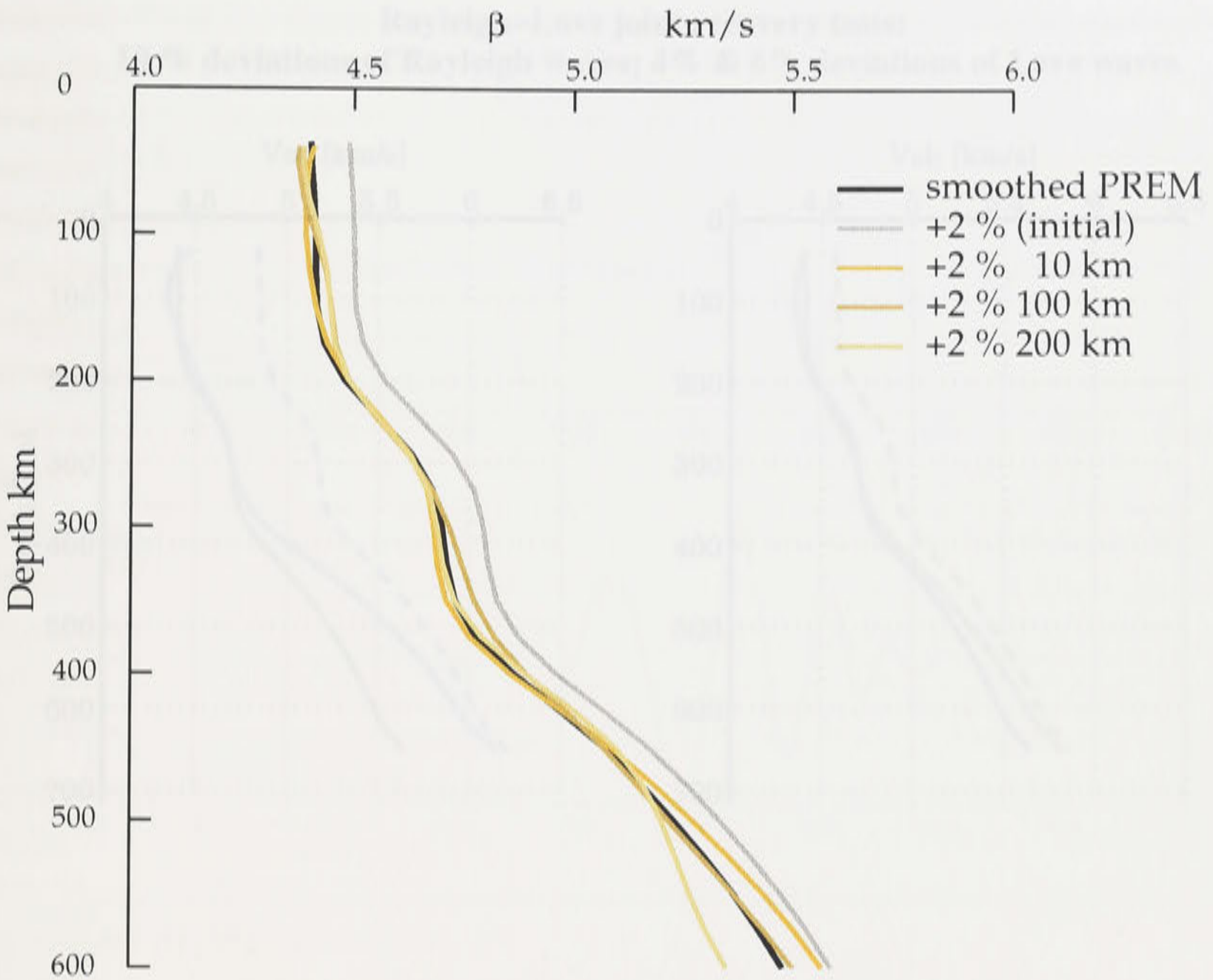

Fig. 8.9. The results of the CL recovery tests of Love waves from the + 4 % faster initial model (light grey line) to a smooth PREM (black line). The three colored lines indicate the final recoveries of the inversion with different focal depths (10 km, 100 km, and 200 km).

a Vertical axis), because the joint inversion relates β_v to β_h through the inversion of β_v and ξ $(= [\beta_h/\beta_v]^2)$. In the following joint inversion tests, we would like to investigate the sensitivities of the Rayleigh and Love joint results to the initial models and stability of the final model of the joint inversion.

We conduct two different Rayleigh-Love joint inversion tests. In the first test, the Rayleigh initial model deviates by +10 % from the smooth PREM and the Love initial model shifts by + 4 % from the PREM (the dashed lines in the upper two panels in figure 8.10). For the second test, we use the same Rayleigh initial model, but the Love initial model has a larger deviation imposed of +6 % from the smooth PREM (the dashed lines in the lower two panels in figure 8.10).

The upper two panels in figure 8.10 demonstrate the results of the first joint recovery test. The Rayleigh recovery model (thick blue line) shows a very good recovery to the reference model from the top of the mantle down to about 350 km depth, whilst the Love

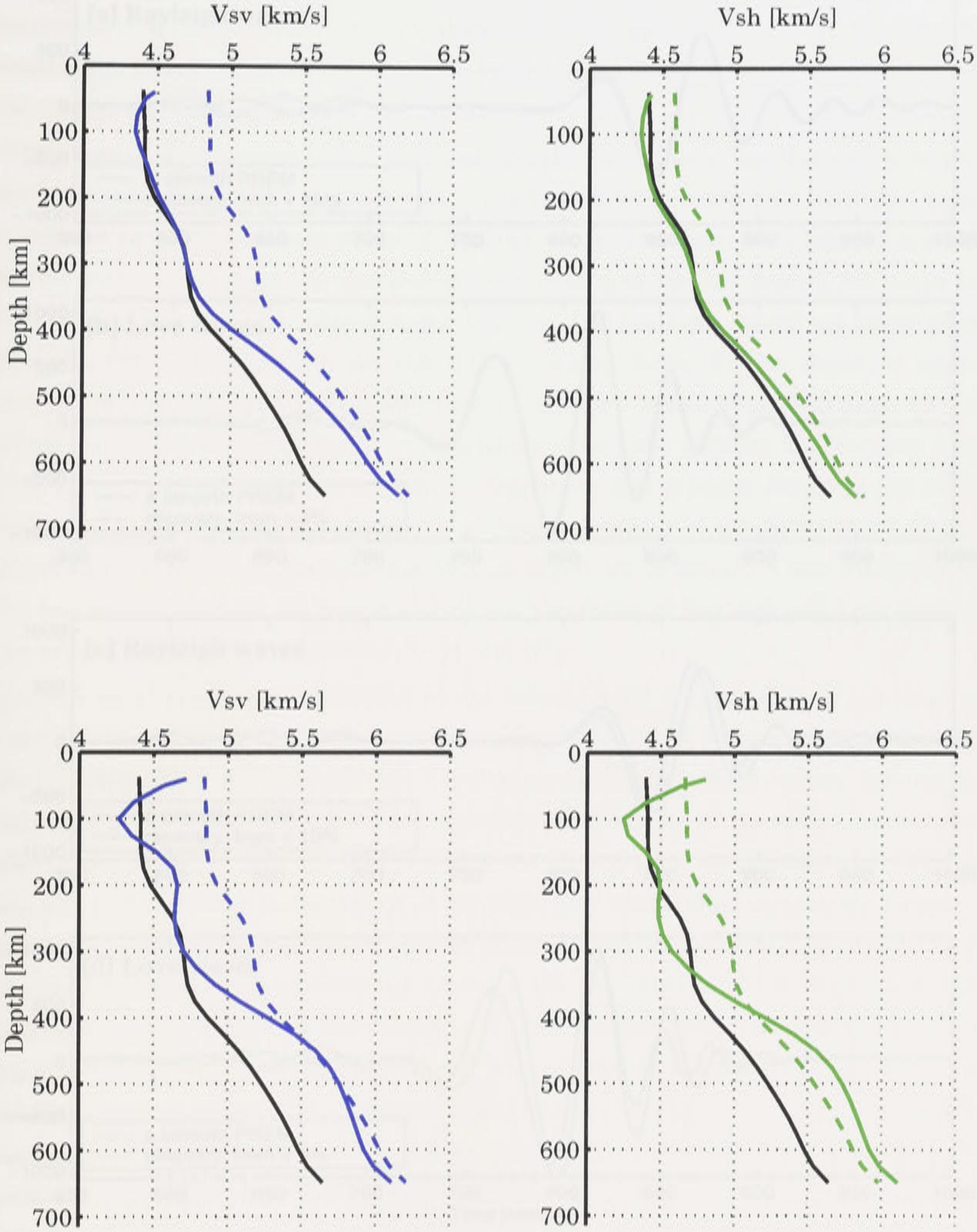

Fig. 8.10. The results of two synthetic recovery tests of the Rayleigh-Love joint inversion. The upper two panels show the result of the first test: The β_v structure (thick blue line) recovered from the initial model of Rayleigh waves (dashed blue line) having +10 % shifts from a smooth PREM (thick black line), while the β_h model (thick green line) is recovered from the initial model of Love waves (dashed green line) with +4 % offset from a smooth PREM. The second set of the joint recovery test is illustrated in the lower two panels: The same starting model of Rayleigh waves (+10 % shift) is used as the first test; however, + 6 % shift is imposed to the initial model of Love waves (the lower right panel).

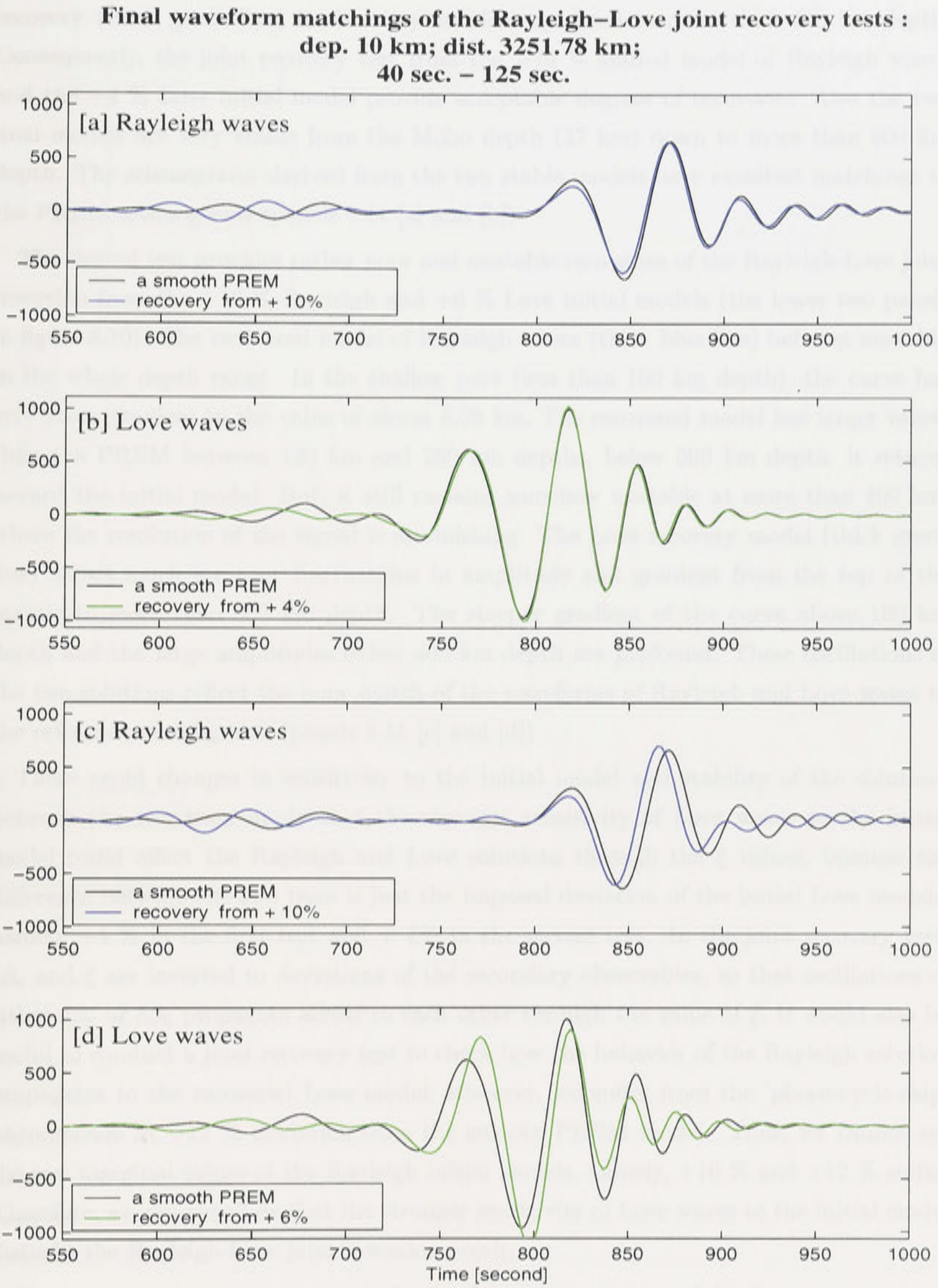

Fig. 8.11. Recovered and reference seismograms of Rayleigh and Love waves derived from the final models in figure 8.10. Panels [a] and [b] show the resulting seismograms from the first joint recovery test (the upper two panels in figure 8.10). Panels [c] and [d] represent the seismograms synthesized from the final models of the second test (the lower two panels in figure 8.10). The black lines indicate reference seismograms of Rayleigh and Love waves based on a smooth PREM. The bandpass filter between 40 to 125 seconds is applied to all the signals.

recovery (thick green line) is also very satisfactory down to more than 400 km depth. Consequently, the joint recovery test from the +10 % shifted model of Rayleigh waves and the +4 % Love initial model provide acceptable degrees of recoveries. Also the two final models are very stable from the Moho depth (37 km) down to more than 600 km depth. The seismograms derived from the two stable models have excellent matchings to the PREM seismograms (panels 8.11 [a] and [b])

The second test provides rather poor and unstable recoveries of the Rayleigh-Love joint inversion from the +10 % Rayleigh and +6 % Love initial models (the lower two panels in figure 8.10). The recovered model of Rayleigh waves (thick blue line) behaves unstably in the whole depth range. In the shallow part (less than 100 km depth), the curve has very steep gradient to the value of about 4.25 km. The recovered model has larger values than the PREM between 120 km and 250 km depths, below 300 km depth, it returns toward the initial model. But, it still remains somehow unstable at more than 400 km, where the resolution of the signal is diminishing. The Love recovery model (thick green line) shows much stronger fluctuations in amplitude and gradient from the top of the mantle to more than 600 km depth. The steeper gradient of the curve above 100 km depth and the large amplitudes below 400 km depth are profound. These oscillations of the two solutions reflect the poor match of the waveforms of Rayleigh and Love waves to the reference seismograms (panels 8.11 [c] and [d])

These rapid changes in sensitivity to the initial model and stability of the solutions between the two tests imply that the stronger sensitivity of Love waves to the initial model could affect the Rayleigh and Love solutions through the ξ values, because the difference between the two tests is just the imposed deviation of the initial Love models, namely +4 % in the first test and + 6% in the second test. In the joint recovery test, $\delta\beta_v$ and ξ are inverted to deviations of the secondary observables, so that oscillations of either $\delta\beta_v$ or $\delta\beta_h$ propagate across to each other through the value of ξ. It would also be useful to conduct a joint recovery test to check how the behavior of the Rayleigh solution propagates to the recovered Love model. However, we suffer from the 'phase-cycle-skip' phenomenon at +12 % deviation from the smooth PREM model. Thus, we cannot set the two marginal values of the Rayleigh initial models, namely, +10 % and +12 % shifts. Therefore, we can conclude that the stronger sensitivity of Love waves to the initial model disturbs the Rayleigh-Love joint inversion result.

Moreover, the joint recovery tests imply that we may lose useful information on both Rayleigh and Love waveforms in the joint inversion, because the joint inversion is less able to achieve a good waveform match in the marginal domain of the shear wavespeed shifts (i.e. the β_v deviation is more than +10 % and the β_h is as large as +6 %) than

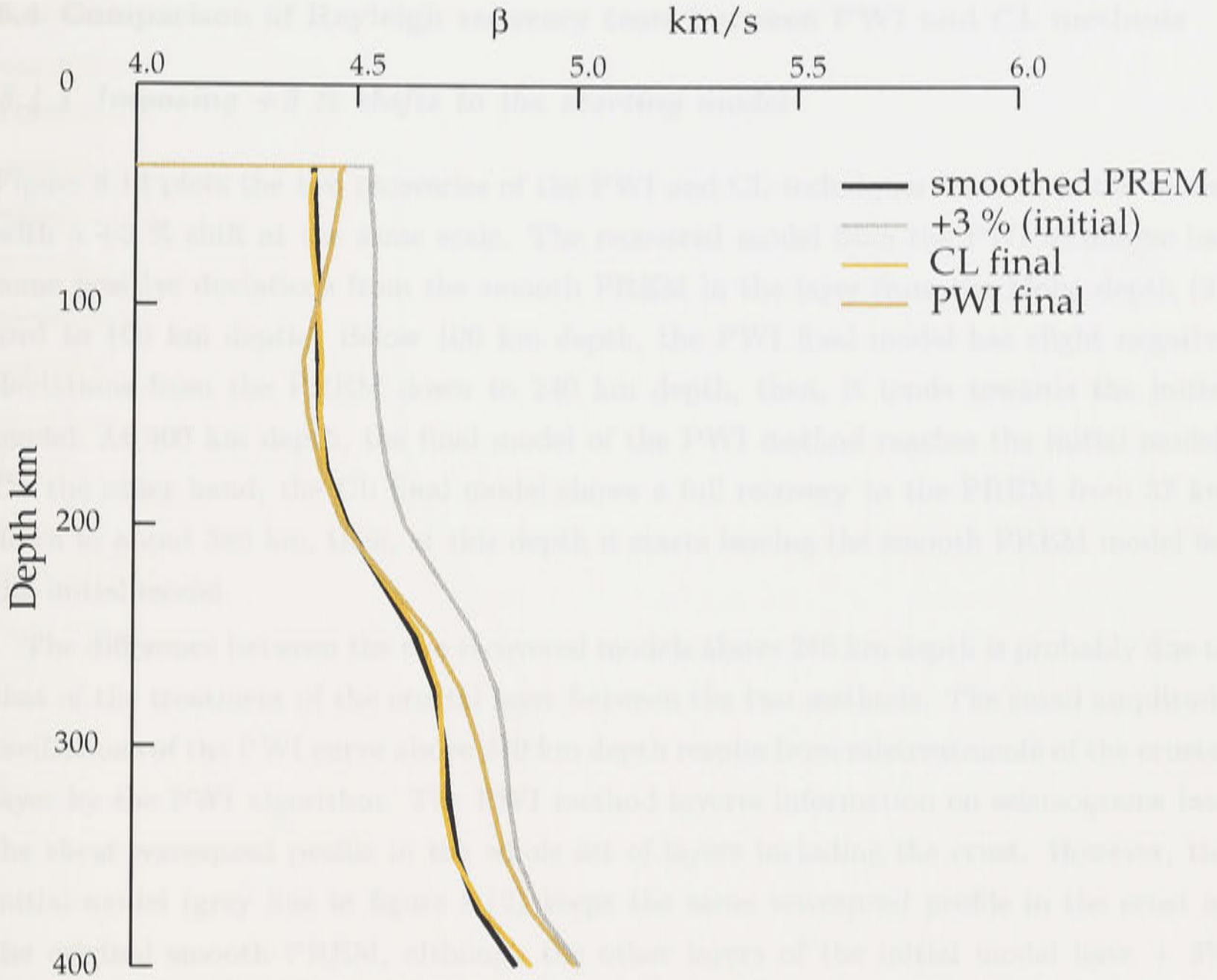

Fig. 8.12. Comparison of CL and PWI recovered models of Rayleigh waves. The initial model (light gray line) is shifted by + 3 % from a smooth PREM (black line). The PWI method inverts the wavespeed structure between the top of the crust and the bottom of the transition zone, while the CL technique excludes the crustal layer for the inversion.

the independent inversion case. In particular, an automated inversion procedure (e.g. Debayle, 1999) does not use the waveform data, if the difference between the final inverted and observed waveforms is beyond an preconditioned threshold. On the other hand, the independent waveform inversion has more chance to take advantage of the waveform data. Even if the distance between the initial model and the truce structure comes close to the marginal values (+10 % for Rayleigh waves and +6 % for Love waves), the CL independent inversion provides better waveform matches between synthetic and observed seismograms. Consequently, the independent inversion can salvage more waveform data than the joint inversion technique in the marginal domain of the shear wavespeed structure.

8.4 Comparison of Rayleigh recovery tests between PWI and CL methods

8.4.1 Imposing +3 % shifts to the starting model

Figure 8.12 plots the two recoveries of the PWI and CL techniques from an initial model with a +3 % shift at the same scale. The recovered model from the PWI technique has some positive deviations from the smooth PREM in the layer from the Moho depth (37 km) to 100 km depth. Below 100 km depth, the PWI final model has slight negative deviations from the PREM down to 240 km depth, then, it tends towards the initial model. At 400 km depth, the final model of the PWI method reaches the initial model. On the other hand, the CL final model shows a full recovery to the PREM from 37 km down to about 380 km, then, at this depth it starts leaving the smooth PREM model for the initial model.

The difference between the two recovered models above 240 km depth is probably due to that of the treatment of the crustal layer between the two methods. The small amplitude oscillations of the PWI curve above 240 km depth results from mistreatments of the crustal layer by the PWI algorithm. The PWI method inverts information on seismograms into the shear wavespeed profile in the whole set of layers including the crust. However, the initial model (grey line in figure 8.12) keeps the same wavespeed profile in the crust as the original smooth PREM, although the other layers of the initial model have + 3% deviation from the PREM. Therefore it is quite possible that the PWI algorithm tries to compensate the +3 % deviation in the upper mantle to some wavespeed changes in the crustal wavespeed profile. In other words, the deviation in the upper mantle could propagate upwards to the crust in the final model.

The depths at which the final recovered models leave the smooth PREM model for the initial model are 240 km for the PWI method and 380 km for the CL method. This difference is due to that of the frequency ranges that the two methods use. In the PWI synthetic test, we impose a Butterworth bandpass filter between 40 to 125 seconds to the signal and then perform the PWI inversion of the filtered waveforms. On the other hand, the CL technique inverts information on the secondary observable Gaussian-filtered at the center time period of 50 and 100 seconds. The Gaussian-filtered signals at 50 and 100 s include a broader frequency band than the Butterworth-filtered signal at 40 to 125 seconds. Therefore the CL technique can extract more information on the shear wavespeed in the deeper part than the PWI method. In other words, the CL method can achieve the deeper wavespeed recovery in this synthetic test. For deeper sources where the higher modes are better excited the PWI method should be able to recover the true model to greater depth.

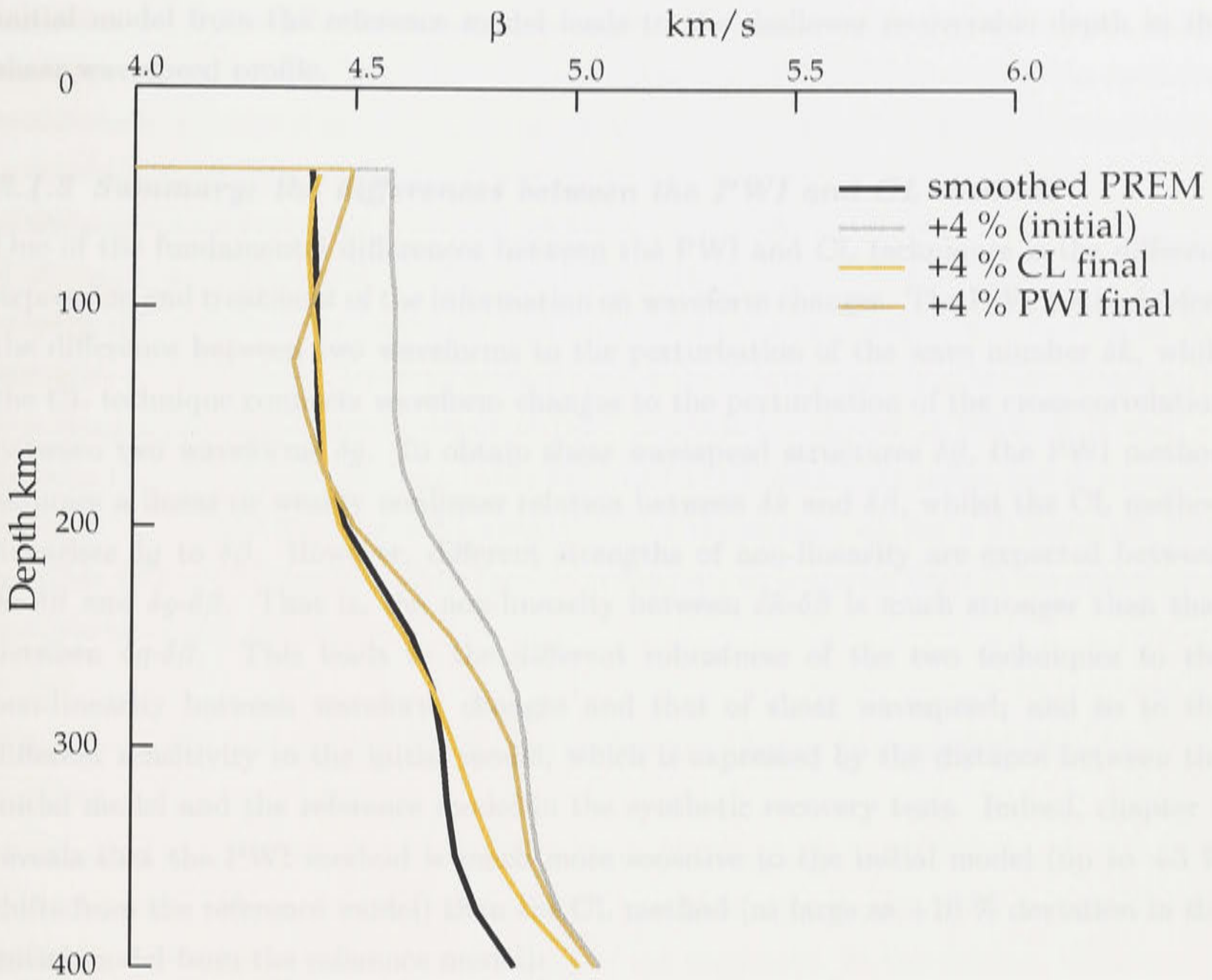

Fig. 8.13. The same comparison in figure 8.12, but + 4 % deviation from a smooth PREM is imposed to the initial model (light gray line).

8.4.2 Imposing +4 % shifts to the starting model

Figure 8.13 illustrates the results of the PWI and CL recovery tests from the +4 % shifted initial model. The recovered model of the PWI method has much larger oscillations between the Moho depth and 180 km depth than the +3 % case in figure 8.12. Below the depth of 180 km, the PWI final model already starts running out of vertical resolution. This depth is also much shallower than the previous case (240 km). On the other hand, the CL method can provide a full recovery in a significant portion of the wavespeed profile from the initial model. However, the perfect match to the PREM model extends to the shallower depth of 280 km rather 380 km depth for the +3 % case.

As we stated in chapter 4, the PWI's poorer recovery from the +4 % initial model demonstrates that the result of the PWI inversion is sensitive to the +4 % shifted starting model. In other words, when the starting model of the PWI inversion is offset by +4 % from the true structure, the final result of the PWI inversion would not necessarily converge to the true profile. For the CL recovery test we conclude that the larger deviation of the

initial model from the reference model leads to the shallower recoverable depth in the shear wavespeed profile.

8.4.3 Summary: the differences between the PWI and CL methods

One of the fundamental differences between the PWI and CL techniques is the different expression and treatment of the information on waveform changes. The PWI method refers the difference between two waveforms to the perturbation of the wave number δk, while the CL technique connects waveform changes to the perturbation of the cross-correlation between two waveforms δg. To obtain shear wavespeed structures $\delta\beta$, the PWI method assumes a linear or weakly nonlinear relation between δk and $\delta\beta$, whilst the CL method linearises δg to $\delta\beta$. However, different strengths of non-linearity are expected between δk-$\delta\beta$ and δg-$\delta\beta$. That is, the non-linearity between δk-$\delta\beta$ is much stronger than that between δg-$\delta\beta$. This leads to the different robustness of the two techniques to the non-linearity between waveform changes and that of shear wavespeed; and so to the different sensitivity to the initial model, which is expressed by the distance between the initial model and the reference model in the synthetic recovery tests. Indeed, chapter 4 reveals that the PWI method is much more sensitive to the initial model (up to +3 % shifts from the reference model) than the CL method (as large as +10 % deviation in the initial model from the reference model).

The other basic difference is the different treatment of the crustal layer in the inversion process. The PWI method inverts waveform information into the wavespeed structure from the top of the crust to the bottom of the transition layer. On the other hand, the CL technique excludes the crustal layer and starts the inversion layer from the top of the upper mantle to the bottom of the lower mantle. In chapter 4, a series of the synthetic recovery tests illustrates that the inaccurate estimation of the crustal structure (i.e. Moho depth and shear wavespeed) in a smoothed PREM model gives rise to the different effects on the upper mantle shear wavespeed structures between the PWI and CL results. The PWI method has little impact on the resulting upper mantle shear wavespeed from the inaccurate estimation of the crust, firstly because the deviation in the crust is mainly absorbed into the crustal structure itself and secondly because the waveforms having the working frequency range (the wave period between 40 and 120 seconds) is not very sensitive to the crustal misestimation. On the other hand, the CL method excludes the crustal layer into the inversion, so that the deviation in the crust structure has to be compensated by the shallow part of the upper mantle structure. Debayle & Kennett (2000a) indicate that a 10 km change of the Moho depth causes changes of the shear wavespeed β_h, propagating into at least 100 km depth.

In chapter 4, the CL technique transfers the misestimation in the crust down to the upper mantle structure. This chapter reveals that the PWI inversion makes the deviation of the shear wavespeed in the upper mantle propagate upward to the crustal structure.

In addition to the upward and downward propagations of the errors in the shallow part of the crust-mantle structure, the recoverability of the $\delta\beta_v$ structure in more than 200 km depth is compared between the PWI and CL methods. The figures 8.12 and 8.13 show a notable differences of the recovered profiles between the two methods in more than 200 km depth. In particular, the maximum depth of the full recovery is different between the two techniques. The recovery depth of the CL method is deeper in both +3 % and +4 % cases than the CL method, probably because the CL technique makes use of a broader range of frequencies than the PWI method. The PWI method applies a Butterworth filter between 40 and 120 seconds, while the CL technique use Gaussian filter to the center wave periods of 50 and 100 seconds.

8.5 The error estimation of the perturbation theory in synthesizing seismograms

We have emphasised the differences of the data (i.e. Rayleigh and Love waves) and of the inversion method (i.e. independent and joint inversions and also the PWI method and CL method) for elucidating the characteristics of the inversions. In this section, the common feature of all the inversions is focused on, that is, the method of synthesizing seismograms in the inversion, because the synthetic calculation of seismograms is suspected to be a possible source of the inversion error under a strongly non-linear condition. Indeed, all the inversions use the same formalism of synthesizing seismograms based on the perturbation theory of δk in terms of $\delta\beta$. We therefore would like to investigate a relation between the synthetic error and the strength of the non-linearity between δk and $\delta\beta$.

The sensitivity arguments to the initial model in the previous sections have revealed that the deviation of as large as +10 % from the reference model provides a good recovery in the Rayleigh synthetic tests, whilst the Love wave recovery tests allow less than +6 % shift from the reference model for practical inversion. This is probably because the relations between the perturbation of waveform information (e.g. wave number δk) and of shear wavespeed ($\delta\beta$) can be linear or weakly non-linear within the ranges of up to +10 % for Rayleigh waves and for less than +6 % for Love waves.

A new concern on the accuracy of the synthetic seismogram in the inversion arises because the synthetic calculation also assumes a linear or weakly non-linear relation between δk and $\delta\beta$. Errors of the synthetic calculation is expected to be an acceptable level if the shift of the initial model is within the same range of the linear relation

as the sensitivity cases. It is, however, worthwhile quantifying the errors of the synthetic seismograms, firstly because non-linear effects on the inversion process have been underestimated in some of the previous regional waveform inversion studies, secondly because the inversion algorithm repeats the synthetic calculation of waveforms at every iteration, so that the error of the synthetics can accumulate in the inverted wavespeed profile at every iteration; consequently the accumulated errors of the synthetic calculation can affect the shear wavespeed structure determined from the inversion.

In this section, we quantify the errors of the synthetic calculations of both Rayleigh and Love waveforms, changing the degree of the non linearity between the phase perturbation and that of the shear wavespeed. Furthermore, we discuss any difference between the synthetic errors of Rayleigh waves and of Love waves.

There are two styles of the synthetic calculations of Rayleigh and Love waves in the regional scale waveform inversion. The first style of the seismogram (S^{new}) is synthesized at every iteration from a summation of the modes for an iteratively updated wavespeed profile. At each iteration, the inversion algorithm should recalculate the modes for a new wavespeed profile and sum up all the renewed modes, so that the aim is to minimize possible errors in the synthetics, but at considerable computational cost. On the other hand, the second style of the seismogram (S^{per}) firstly sums up the non-updated modes for the initial wavespeed model. S^{per} is then updated by adding a new up-dated perturbation δk to the phase term in each iteration. The magnitude of δk derives from the first-order perturbation theory of δk in terms of the iteratively updated shear wavespeed $\delta\beta$. In other words, S^{per} is required to assume a linear or weakly non-linear relation between δk and $\delta\beta$ for its update. However, S^{per} needs only one mode calculation for the initial model at the very first stage of the synthetic calculation, so that it has a much lower cost for the mode computation. Consequently, in the domain of a linear or weakly non-linear relation between δk and $\delta\beta$, the regional waveform inversion schemes (e.g. PWI and CL methods) use the synthetic calculation of S^{per}, rather than S^{new} which is updating all the modes at each iteration.

The seismogram of $S^{new}(\omega)$ in the frequency domain is expressed as

$$\begin{aligned} S^{new}(\omega) &= \sum_{n=0}^{\infty} A_n^{new}(\omega) \exp[ik_n^{new}(\omega)\Delta] \\ &= \sum_{n=0}^{\infty} \mathcal{S}_n^{new}(\omega) \ , \end{aligned} \tag{8.3}$$

where

n : mode number

ω : angular frequency

Δ : epicentral distance

A : excitation coefficient

k : wave number

The equation (3.11) in chapter 3 shows synthetic seismograms $S^{per}(\omega)$ in the frequency domain being expressed as a summation of the modes (n) for the reference model ($S_n^0(\omega)$) and its perturbation ($\delta S_n(\omega)$). Note that this seismogram is based on the first-order perturbation theory of δk in terms of $\delta\beta$:

$$\begin{aligned} S^{per}(\omega) &= \sum_{n=0}^{\infty} A_n^0(\omega)\exp[i(k_n^0(\omega)+\delta k_n(\omega))\Delta] \\ &= \sum_{n=0}^{\infty}\{A_n^0(\omega)\exp[i(k_n^0(\omega)\Delta] + A_n^0(\omega)\exp[i\delta k_n(\omega)\Delta]\} \\ &= \sum_{n=0}^{\infty}\{\mathcal{S}_n^0(\omega)+\delta\mathcal{S}_n(\omega)\} \\ &= S^0(\omega)+\delta S(\omega)\ , \end{aligned} \tag{8.4}$$

where

0 : laterally homogeneous reference model

δk : perturbations of wave number from the reference model

This equation (8.4) is applicable to synthesizing seismograms based on a new 1-D depth varying wavespeed structure, only when the structure is within a certain range from the reference model. Under the condition that we can use the first-order approximation between $\delta k_n(\omega)$ and $\delta\beta(\mathbf{r})$ (equation 3.14)

$$\delta k_n(\omega)\Delta = \int_0^a \left[\frac{\partial k_n(\omega)}{\partial\beta(r)}\right] \int_P \delta\beta(\mathbf{r})\, d\Delta dr \tag{8.5}$$

where

a : radius of the Earth

P : integration along the path.

Applying Inverse Fourier Transform to the signals ($S^{per}(\omega)$ and $S^{new}(\omega)$) in the frequency domain, we obtain the corresponding seismograms $S^{per}(t)$ and $S^{new}(t)$ in the time domain.

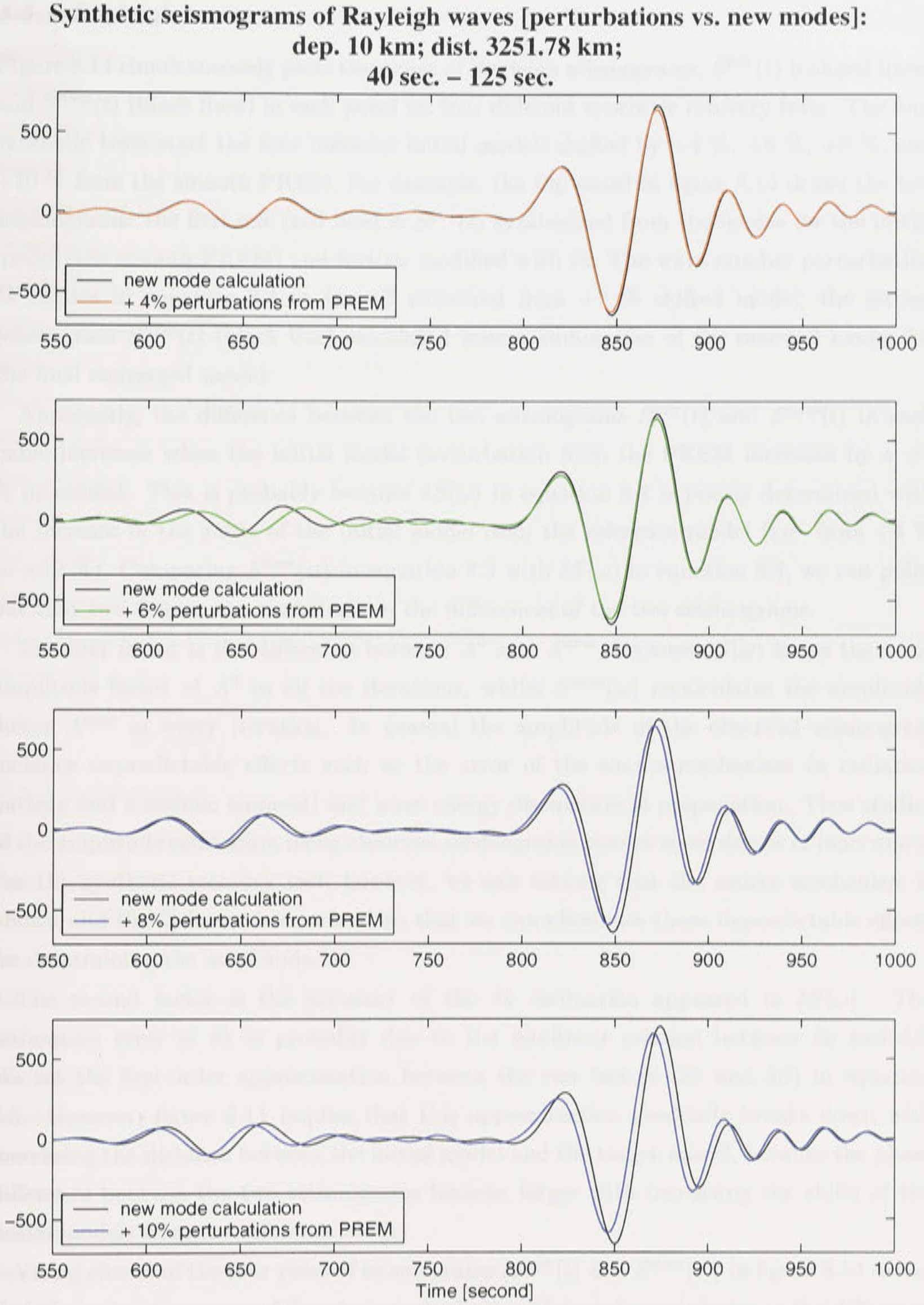

Fig. 8.14. Synthetic seismograms of Rayleigh waves (black lines: $S^{new}(t)$) are derived from renewed modes for the final models in the inversion (thick colored lines in figure 8.1). The colored four seismograms $S^{per}(t)$ are synthesized from the modes for the four initial models and modified with wave number perturbations δk. The bandpass filter between 40 to 125 seconds is applied to the signals.

8.5.1 Rayleigh waves

Figure 8.14 simultaneously plots two types of Rayleigh seismograms, $S^{per}(t)$ (colored lines) and $S^{new}(t)$ (black lines) in each panel for four different synthetic recovery tests. The four synthetic tests start the four different initial models shifted by +4 %, +6 %, +8 %, and +10 % from the smooth PREM. For example, the top panel in figure 8.14 draws the two seismograms: the first one (red line) is $S^{per}(t)$ synthesized from the modes for the initial model (the smooth PREM) and further modified with δk. The wave number perturbation δk relates in equation 8.4 to the $\delta\beta$ recovered from +2 % shifted model; the second seismogram $S^{new}(t)$ (black line) calculated from a summation of the renewed modes for the final converged model.

Apparently, the difference between the two seismograms $S^{per}(t)$ and $S^{new}(t)$ in each panel increases when the initial model perturbation from the PREM increases by a +2 % increment. This is probably because $\delta S(\omega)$ in equation 8.4 is poorly determined with the increase of the shifts of the initial model from the reference model (i.e. from +4 % to +10 %). Comparing $S^{new}(\omega)$ in equation 8.3 with $\delta S(\omega)$ in equation 8.4, we can point out that two factors can contribute to the differences of the two seismograms.

The first factor is the difference between A^0 and A^{new}, because $\delta S(\omega)$ keeps the same amplitude factor of A^0 in all the iterations, whilst $S^{new}(\omega)$ recalculates the amplitude factor A^{new} at every iteration. In general the amplitude of the observed seismogram includes unpredictable effects such as the error of the source mechanism (a radiation pattern and a seismic moment) and wave energy dissipation in propagation. Thus studies of the amplitude estimation using observed seismograms involve some degree of inaccuracy. For the synthetic recovery test, however, we can assume that the source mechanism is known and the Q factor is constant, so that we can eliminate those unpredictable effects for determining the amplitude.

The second factor is the accuracy of the δk estimation appeared in $\delta S(\omega)$. The estimation error of δk is probably due to the nonlinear relation between δk and $\delta\beta$. We set the first-order approximation between the two factors (δk and $\delta\beta$) in equation 8.5. However, figure 8.14 implies that this approximation gradually breaks down with increasing the distance between the initial model and the target model, because the phase difference between the two seismograms become larger with increasing the shifts of the initial models from the reference model.

Visual checks of the four pairs of seismograms ($S^{per}(t)$ and $S^{new}(t)$) in figure 8.14 reveal that the estimation error of the phase perturbation δk mainly contributes to the difference of the two seismograms in each pair. But, the changing nature of the phase superpositions lead to variations in the net amplitude, so that the difference of the amplitude factors

(A^0 and A^{new}) also provides some contribution to the difference of the two Rayleigh seismograms.

Using the CL style waveform inversion, we project the differences of the two seismograms ($S^{per}(t)$ and $S^{new}(t)$) in figure 8.14 onto the β_v-depth plane for the four different cases (figure 8.15). The CL algorithm tries to match the seismogram $S^{new}(t)$ (black line in figure 8.14) to the 'observed' seismogram $S^{per}(t)$ (colored line in figure 8.14) to obtain the closest profile (colored line in figure 8.15) corresponding to the seismogram $S^{per}(t)$. The initial model of this inversion is set to the final model obtained in the Rayleigh recovery tests (figure 8.1). For example, the initial model (black line) in the lower left panel in figure 8.15 is exactly the same as the +10 % final model in figure 8.1.

In the upper two panels in figure 8.15, almost no difference is observed between the two types of β_v profiles. Whilst on the other hand, the lower two panels demonstrate that the deviation between the two β_v models becomes apparent with increasing the distance between the initial and reference models. In the +10 % shifted case (the lower right panel), the maximum difference between two lines reaches about 1.5 % of the original wavespeed profile at 280 km depth. This value of 1.5 % may be large enough to be significant, because we compare the 2 % different cases to determine the sensitivity of the waveform inversion to the initial model.

8.5.2 Love waves

For the Love wave case, there are much more notable differences between two styles of Love synthetic seismograms $S^{per}(t)$ and $S^{new}(t)$: one is synthesized from the summation of the renewed modes for the final β_h model; the other Love seismogram is calculated from the summation of the modes for the initial β_h model but further modified with δk corresponding to $\delta\beta_h$ in equation 8.5.

Figure 8.16 illustrates that the comparison of the two types of the Love synthetics in each panel with the four different starting models. The shifts of the initial model from the reference model are from +2 % to +8 % by a +2 % increment. When the initial model deviates by less than 6 % from the reference model, the synthesis of Love waves in the recovery test has acceptably small errors. The difference between the two types of the seismograms becomes significant when the shift of the initial model reaches +6 % (the third panel). For the Love wave case, the difference between $S^{per}(t)$ and $S^{new}(t)$ results mainly from the estimation error of δk rather than the amplitude difference between A^0 and A^{new}. In particular, the results in the lowest panel in figure 8.16 assure us that the difference δk is more significant than that of the amplitude.

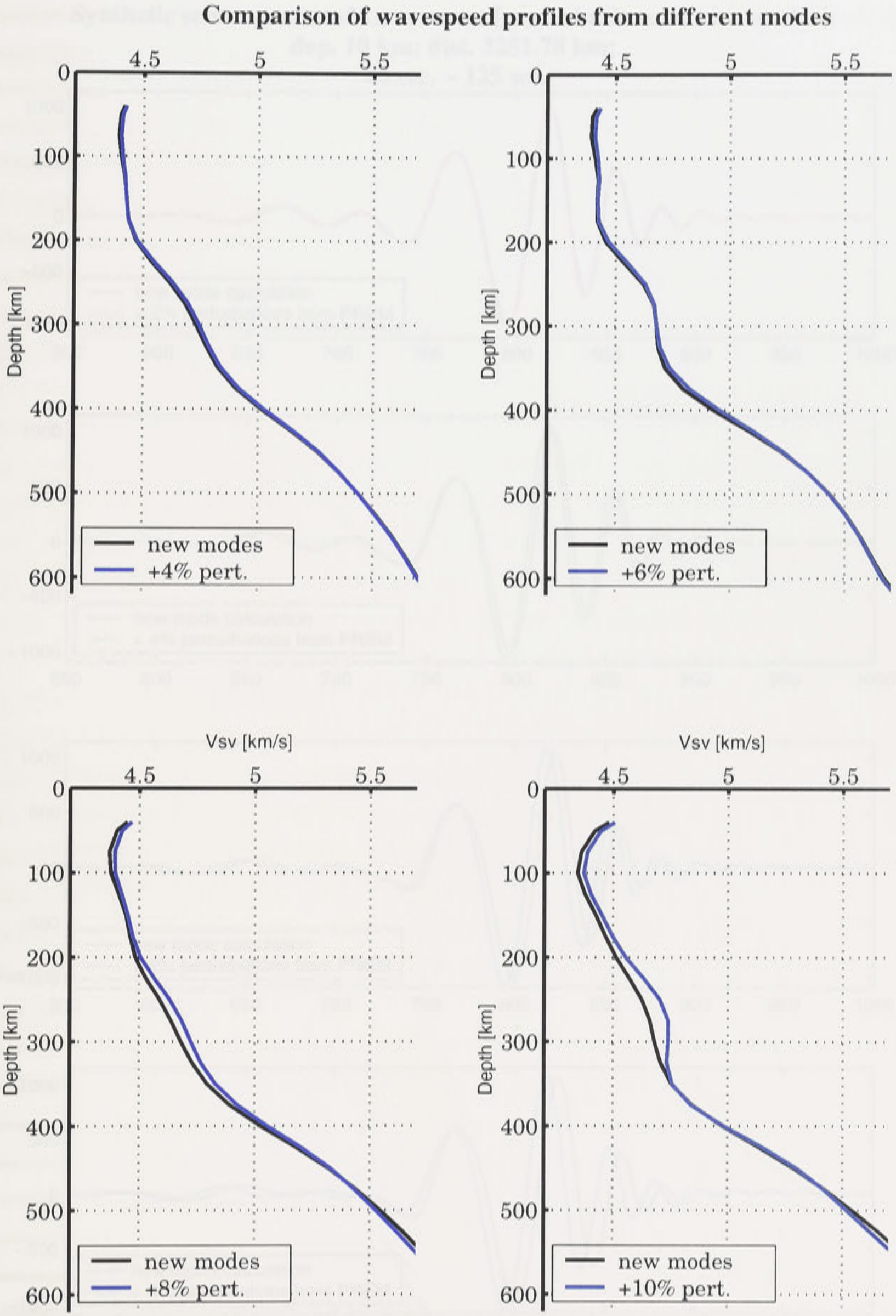

Fig. 8.15. Comparison of the two types of β_v profiles inverted from Rayleigh seismograms ($S^{per}(t)$ and $S^{new}(t)$) in figure 8.14: The first type of β_v profiles (black lines) is derived from seismograms $S^{new}(t)$. The blue lines represents the second type of β_v profiles inverted from seismograms $S^{per}(t)$.

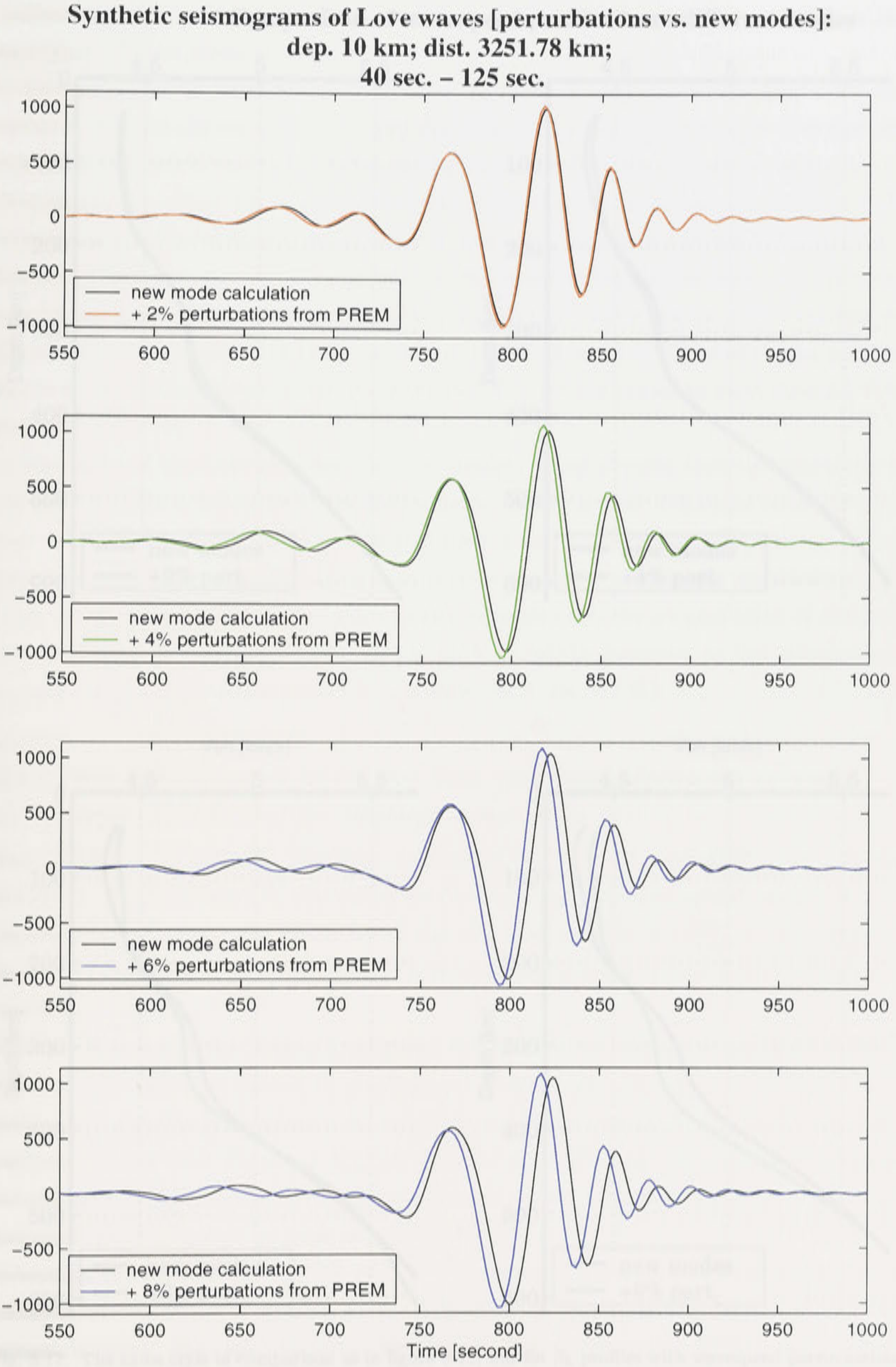

Fig. 8.16. The same comparison of synthetic seismograms ($S^{per}(t)$ and $S^{new}(t)$) as in figure 8.14, but each panel shows the comparison of synthetic Love waves.

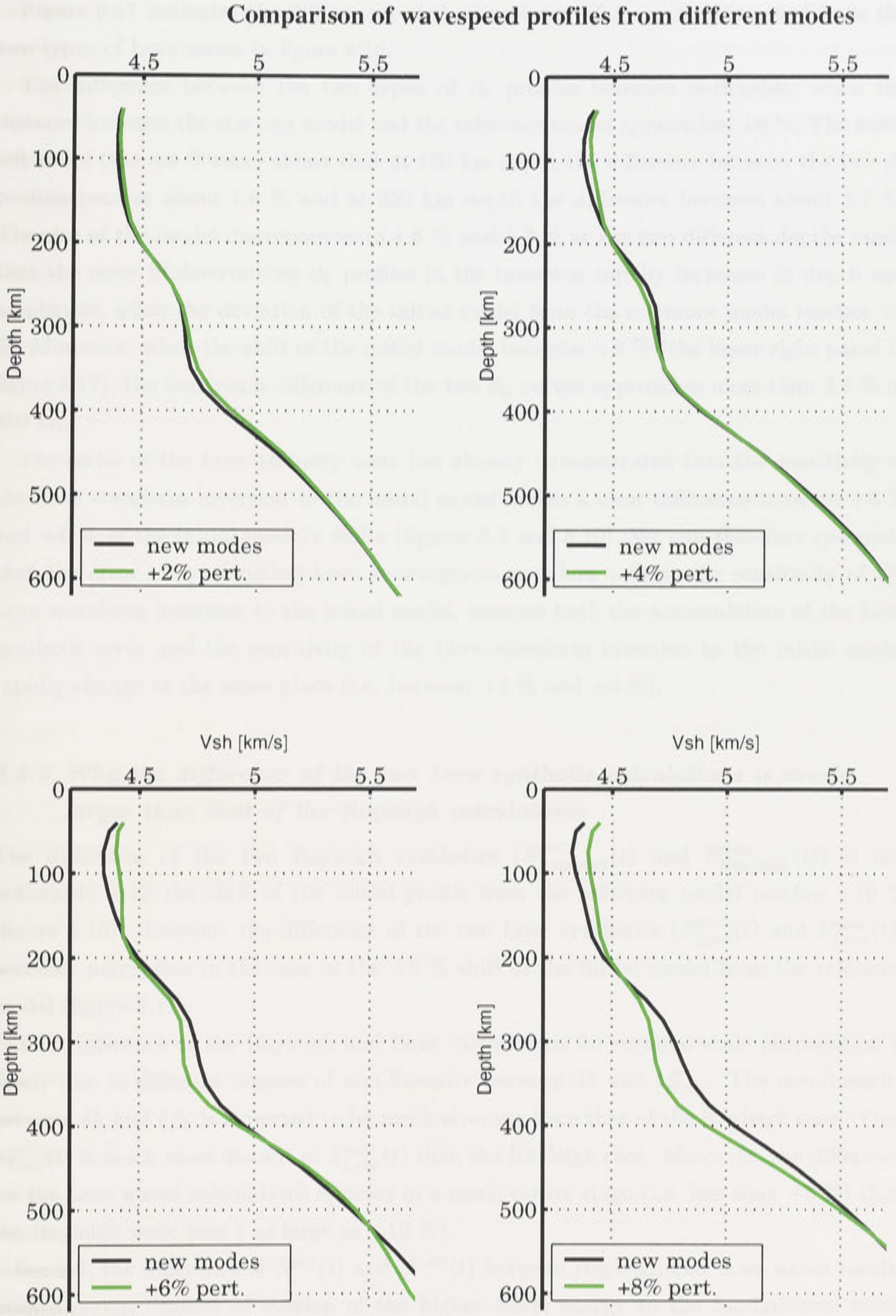

Fig. 8.17. The same style of comparison as in figure 8.15, but for β_h profiles with wavespeed perturbations of +2 %, +4 %, +6 %, and +8 %.

Figure 8.17 indicates the differences of the two types of β_h profiles inverted from the two types of Love waves in figure 8.16.

The difference between the two types of β_h profiles becomes noticeable, when the distance between the starting model and the reference model approaches +6 %. The lower left panel (the +6 % case) shows that at 100 km depth the difference between the two β_h profiles reaches about 1.6 % and at 350 km depth the difference becomes about 1.7 %. The size of the model discrepancies of 1.6 % and 1.7 % at the two different depths imply that the error in determining β_h profiles in the inversion rapidly increases in depth and amplitude, when the deviation of the initial model from the reference model reaches +6 %. Moreover, when the shift of the initial model becomes +8 % (the lower right panel in figure 8.17), the maximum difference of the two β_h curves approaches more than 2.5 % at 350 km.

The series of the Love recovery tests has already demonstrated that the sensitivity of the Love waveform inversion to the initial model makes a clear difference between +4 % and +6 % of the initial model's shifts (figures 8.8 and 8.10). We can therefore speculate that the error in synthesizing Love seismograms somehow reflects the sensitivity of the Love waveform inversion to the initial model, because both the accumulation of the Love synthetic error and the sensitivity of the Love waveform inversion to the initial model rapidly change at the same place (i.e. between +4 % and +6 %).

8.5.3 Why the difference of the two Love synthetic calculations is much larger than that of the Rayleigh calculations

The difference of the two Rayleigh synthetics ($S^{per}_{Rayleigh}(t)$ and $S^{new}_{Rayleigh}(t)$) is not noticeable until the shift of the initial profile from the reference model reaches +10 % (figure 8.15). However, the difference of the two Love synthetics ($S^{per}_{Love}(t)$ and $S^{new}_{Love}(t)$) becomes perceptive in the case of the +6 % shift of the initial model from the reference model (figure 8.17).

This difference of the Rayleigh and Love calculations for regional scale propagation is firstly due to different degrees of non-linearity between δk and $\delta\beta_{v,h}$. The non-linearity between δk and $\delta\beta_h$ is expected to be much stronger than that of the Rayleigh case. Thus $S^{per}_{Love}(t)$ is much more distant to $S^{new}_{Love}(t)$ than the Rayleigh case. Moreover, the difference for the Love waves calculations appears in a much earlier stage (i.e. less than +6 %) than the Rayleigh wave case (as large as +10 %).

Second, the difference of $S^{per}(t)$ and $S^{new}(t)$ between Rayleigh and Love waves results from different degrees of overlap of the higher mode energy to the fundamental mode energy between Rayleigh and Love waveforms. The difference of $S^{per}(t)$ and $S^{new}(t)$,

or the calculation error, comprises a summation of the errors of all the modes. If the fundamental mode overlaps the overtones, the errors of the fundamental mode calculation are also overlapped by those of the higher modes. Thus we see a summation of the errors from both fundamental and higher modes within a particular time window for the inversion. For Rayleigh waves bandpass-filtered between wave periods of 40 and 125 seconds, the major portion of the fundamental mode is well separated by that of the overtones, because, in a regional scale propagation, the group wavespeed of the main portion of the fundamental mode is much slower than that of the higher modes. Thus the synthetic errors of the Rayleigh fundamental mode and the overtones appear in separate time windows. Consequently, a summation of the Rayleigh synthetic errors from all the modes spreads along the time axis and looks less significant in amplitude. On the contrary, the major portion of the Love overtone energy comes much closer to that of the Love fundamental mode than the Rayleigh wave case, so that a summation of the Love synthetic errors from all the modes is concentrated on and around the Love fundamental mode.In consequence, we observe that a large amplitude of the synthetic errors from all the Love modes in a rather narrow time window.

This error condensation of the Love waves is particularly important for deeper events which generate more Love overtone energy, because the inversion algorithm cannot distinguish the synthetic error of the fundamental mode from that of the overtones. Therefore it is quite difficult to correctly invert the errors into the vertical shear wavespeed profile beneath the path.

The comparisons of $S^{per}(t)$ and $S^{new}(t)$ for Rayleigh and Love synthetics quantify the difference between $S^{per}(t)$ and $S^{new}(t)$ in terms of the four shifted initial models. We, however, note that the magnitude of the difference could be underestimated by two conditions we have set in the synthetic calculations for $S^{per}(t)$ and $S^{new}(t)$. The first condition is that a number of the modes for the synthetics is set up to five (i.e. the fundamental mode and the four overtones). Accumulation of the error of the synthesizing Rayleigh and Love waves depends on a number of the modes used in the synthetic process. The more modes you use in the synthetic calculation, the more errors are accumulated at each iteration in the synthetic seismograms. For example, the CL inversion uses the fundamental mode and four overtones for the synthetic seismogram, whilst the PWI method usually sums up more than ten modes for the Rayleigh wave calculation. Thus, the difference between $S^{per}(t)$ and $S^{new}(t)$ in the actual inversion could be more than that of the five-mode synthetic tests.

The second condition is that the magnitude of the higher mode energy is not well developed in a series of the synthetic tests, because the simulated 'Derby' event has a focal

depth of 10 km. Because of the low excitation of higher modes we may underestimate the errors compared with the situation with deeper events.

8.5.4 Comment on accumulation of the errors of the inversion

There are two ways that errors in the synthetics can propagate in the inversion: First, as a newly generated synthetic error at every iteration; Second, the accumulated errors in the inverted wavespeed profile from the previous iterations. At the first iteration in the inversion, the synthetic calculation of a seismogram generates some error, mainly because non-linearity is expected between δk and $\delta\beta$, then the inversion program transfers the errors of the synthetics into the inverted wavespeed profile through the waveform matching. At the next iteration, the algorithm synthesizes a new seismogram based on the error-containing profile. The calculation of a seismogram itself produces new errors at every iteration, so that the resulting profile contains new errors from the synthetics at this iteration and carried-over errors from the previous iteration. In other words, the more iteration the inversion makes, the more errors the inversion result contains. Therefore, we conclude that the number of iterations in the inversion can control the accuracy of the inversion result through the mechanism of the error accumulation.

It is desirable that the results of any inversions are therefore checked by carrying out a full calculation of the synthetics for the proposed model using the S^{new} style of seismogram calculated with fresh modes.

References

Anderson, D.L., 1961 Elastic wave propagation Layered Anisotropy Media, *J. Geophys. Res.*, **66**, 2953–2963.

Anderson, D.L., BenMenahem, A., & Archambeau, C.B., 1965. Attenuation of seismic energy in the upper mantle, *J. Geophys. Res.*, **70**, 1441–1448.

Bowman, J.R.,& Kennett, B.L.N., 1990. An investigation of the upper mantle beneath northwestern Australia using a hybrid seismic array, *Geophys. J. Int.* **101**, 411–424.

Cara, M., 1979. Lateral variation of S velocity in the upper mantle from higher Rayleigh modes, *Geophys. J. R. Astr. Soc.*, **57**, 649–670.

Cara, M., & Lévêque, J. J., 1987 Waveform inversion using secondary observables, *Geophys. Res. Lett.*, **14**, 1046–1049.

Clitheroe, G., Gudmundsson, O.,& Kennett,B.L.N., 2000. The crustal thickness of Australia *J. Geophys. Res.*, **105**, 13697–13713.

Cummins, P., Takeuchi, N., & Geller, R., 1996. Computation of complete synthetic seismograms using Direct Solution Method, submitted to *Geophys. J. Int.*

Collins, C. D. N., 1991. The nature of the crust-mantle boundary under Australia from seismic evidence, *Geol. Soc. Austral. Spec. Publ.*, **17**, 67–80.

Das, T., & Nolet, G., 1995. Crustal thickness estimation using high frequency Rayleigh waves, *Geophys. Res. Lett.*, **22**, 539–542.

Debayle, E. 1999. Sv-wave azimuthal anisotropy in the Australian upper-mantle: preliminary results from automated Rayleigh waveform inversion. *Geophys. J. Int.*, **137**,747–754.

Debayle, E. & Lévêque, 1997. Upper mantle heterogeneities in the Indian Ocean form waveform inversion, *Geophys. Res. Lett.*, **24**,245–248.

Debayle, E. & Kennett, B. L. N., 2000a. The Australian continental upper mantle: Structure and deformation inferred from surface waves, *J. Geophys. Res.*, **105**,25423 – 25450.

Debayle, E. & Kennett, B. L. N., 2000b. Anisotropy in the Australian upper mantle from Love and Rayleigh waveform inversion, *Earth Planet Sci. Lett*, **184**, 339 – 351.

Denham, D., 1991. Shear wave crustal models for the Australian Continent, in *The Australian Lithosphere*, **17**, 23–44. ed. Drummond, B.J., Geol. Soc. Aust., Spec. Publ.

Dey, S.C., Kennett, B.L.N.,Bowmann, J.R., & Goody, A., 1993. Variations in upper mantle structure under northern Australia *Geophys. J. Int.*, **114**, 304–310.

Drummond, B. J., Muirhead, K.J., Wellman, P., & Wright, C., 1989. A teleseismic travel-time residual map of the Australian continent, *BMR Journal of Australian Geology and Geophysics* **11**, 101-105.

Durek, J. J., Ritzwoller, M. H., & Woodhouse, J. H., 1993. Constraining upper mantle anelasticity using surface wave amplitude anomalies, *Geophys. J. Int.*, **114**, 249–272.

Dziewonski, A. M., 1984. Mapping the lower mantle, *J. Geophys. Res.*, **89**, 5929–5952.

Dziewonski, A. M., Bloch, S.,& Landisman, M., 1969. A technique for the analysis of transient seismic signals, *Bull. Seism. Soc. Am.*, **59**, 427–444.

Dziewonski, A. M., Mills, J.,& Bloch, S., 1972. Residual dispersion measurement: a new method of surface wave analysis, *Bull. Seism. Soc. Am.*, **62**, 129–139.

Dziewonski, A. M., & Anderson, D. L., 1981. Preliminary reference earth model, *Phys. Earth. Planet. Int.*, **25**, 297–356.

Dziewonski, A. M., & Steim, J. M., 1982. Dispersion and attenuation of mantle waves from waveform inversion, *Geophys. R. Astr. Soc.*, **70**, 503–527.

Ewing, W.M., Jardetsky, W.S., & Press, F., 1957. *Elastic Waves in Layered Media*, McGraw-Hill, New York, 1957.

Fukao, Y., Obayashi, M., Inoue, H., & Nenbai, M., 1992. Subducting slabs stagnant in the mantle transition zone, *J. Geophys. Res.*, **97**, 4809–4822.

Gaherty, J.B. & Jordan, T.H., 1995. Lehmann discontinuity as the base of anisotropic layer beneath continents, *Science* **268**, 1468–1471.

Gaherty, J.B., Kato, M., & Jordan, T.H., 1999. Seismological structure of the upper mantle: a regional comparison of seismic layering, *Phys. Earth. Planet. Int.*, **110**, 21–41.

Geller, R. J., & Takeuchi, N., 1995. A new method for computing highly accurate DSM synthetic seismograms, *Geophys. J. Int.*, **123**, 449–470.

Gudmundsson, O., Kennett, B.L.N., & Goody, A., 1994. Broadband observations of upper mantle seismic phases in northern Australia and the attenuation structure in the upper mantle., *Phys. Earth. Planet. Int.*, **84**, 207–226.

Hager, B. H., & Clayton, R. W., 1989. Constraints on the structure of mantle convection using seismic observations, flow models, and the geoid, in *Mantle Convection*, ed. W. R. Peltier, Gordon and Breach, New York.

Hales, A.L., Muirhead, K.J., & Rynn, J.M.W., 1980a. A compressional velocity distribution for the upper mantle, *Tectonophysics* **63**, 309–348.

Hara, T., Tsuboi, S., & Geller, R. J., 1993. Laterally heterogeneous upper mantle S-wave velocity structure obtained by iterative linearized waveform inversion, *Geophys. J. Int.*, **115**, 667–698.

Herrin, E., & Goforth, T., 1977. Phase matched filters: application to the study of Rayleigh waves, *Bull. Seism. Soc. Am.*, **67**, 1259–1269.

Inoue, H., Fukao, Y., Tanabe, K., & Ogata, Y., 1990. Whole mantle P-wave travel time tomography, *Phys. Earth. Planet. Int.*, **59**, 294–328.

Kaiho, Y. & Kennett, B. L. N., 2000. Three-dimensional seismic structure beneath the Australian region from refracted wave observations, *Geophys. J. Int.*, **142**, 651–668.

Kennett, B. L. N., 1983., *Seismic Wave Propagation in Stratified Media*, Cambridge University press.

Kennett, B. L. N., 1984. Guided wave propagation in laterally varying media –I. Theoretical development, *Geophys. J. R. Astr. Soc.*, **79**, 235–255.

Kennett, B. L. N., 1995. Approximations for surface-wave propagation in laterally varying media, *Geophys. J. Int.*, **122**, 470–478.

Kennett, B. L. N., 1998. Guided wave propagation in three dimensional structure, *Geophys. J. Int.*, **133**, 159–174.

Kennett, B. L. N., & Nolet, G., 1990. The interaction of the *S*-wavefield with upper mantle heterogeneity, *Geophys. J. Int.*, **101**, 751–762.

Kennett, B. L. N., & Engdahl, E. R., 1991. Traveltimes for global earthquake location and phase

identification, *Geophys. J. Int.*, **105**, 429–465.

Kennett, B. L. N., Gudmundsson,O., & Tong,C., 1994. The upper mantle S and P velocity structure beneath northern Australia form broadband observation, *Phys. Earth. Planet. Int.*, **86**, 85–98.

Kennett, B. L. N., Engdahl, E. R., & Buland, R., 1995. Constraints on seismic velocities in the Earth from traveltimes, *Geophys. J. Int.*, **122**, 108–124.

Knopoff, L., 1972. Observation and inversion of surface wave dispersion, *Geophys. J.R.Astr.Soc.*, **133**, 159–174.

Knopoff, L., 1983. The thickness of the lithosphere from dispersion of surface waves, *Geophys. J.R.Astr.Soc.*, **133**, 159–174.

Laske, G., 1995. Global observation of off-great-circle propagation of long-period surface waves, *Geophys. J. Int.*, **123**, 245–259.

Laske, G., & Masters, G., 1996. Constraints on global phase velocity maps from long-period polarization data, *J. Geophys. Res.*, **101**, 16059–16075.

Leven, J.H.,1985. The application of synthetic seismograms in the interpretation of the upper mantle P-wave velocity structure in northern Australia *Phys. Earth. Planet. Int.*, **38**, 9–27.

Lévêque, J. J & Cara, M., 1985. Inversion of multi mode surface wave data: evidence for sub-lithospheric anisotropy *Geophys. J.R. Astr. Soc.*, **83**, 753–773.

Lévêque, J. J., Cara, M., & Rouland, D., 1991. Waveform inversion of surface wave data: test of a new tool for systematic investigation of upper mantle structures, *Geophys. J. Int.*, **104**, 565–581.

Lévêque, J. J., Debayle, E., & Mauopin, V., 1998. Anisotropy in the Indian ocean upper mantle form Rayleigh- and Love- inversion, *Geophys. J. Int.*, **133**, 529–540.

Levshin, A.L., Pisarenko, V.F., & Pogrebinsky, G.A., 1972. On a frequency-time analysis of oscillation, *Ann. Geophys.*, **28**, 211-218.

Levshin, A.L., Ratinikova, L., & Berger, J., 1992. Peculiarities of surface wave propagation across central Eurasia, *Bull. Seism. Soc. Am.*, **82**, 2464–2493.

Li, X.-D., & Tanimoto, T., 1993. Waveforms of long-period body waves in a slightly aspherical Earth model, *Geophys. J. Int.*, **112**, 92–102.

Li, X.-D., & Romanowicz, B., 1995. Comparison of global waveform inversions with and without considering cross-branch model coupling, *Geophys. J. Int.*, **121**, 695–709.

Love, A.E.H., 1927. *A Treatise on the Mathematical Theory of Elasticity*, Cambridge University Press, Cambridge.

Marquering, H., & Snieder, R., 1995. Shear-wave mode coupling for efficient forward modelling and inversion of body-wave phases, *Geophys. J. Int.*, **120**, 186–208.

Marquering, H., & Snieder, R., 1996. Shear-wave velocity structure beneath Europe, the northeastern Atlantic and western Asia from waveform inversions including surface-wave mode coupling, *Geophys. J. Int.*, **127**, 283–304.

Marquering, H., Snieder, R., & Nolet, G., 1996. Waveform inversions and the significance of surface wave mode coupling, *Geophys. J. Int.*, **124**, 258–278.

Montagner J.P., 1986. Regional three-dimensional structures using long-period surface waves, *Ann. Geophys.*, **4**, 283–294.

Montagner J.P., & Nataf, H.C., 1986. A simple method for inverting the azimuthal anisotropy of surface waves, , *J. Geophys. Res.*, **91**, 511–520.

Muirhead, K. J. & Drummond, B.J., 1991. The seismic structure of the lithosphere under Australia and its implications for continental plate tectonics, in *The Australian Lithosphere*, **17**, 23–44. ed. Drummond, B.J., Geol. Soc. Aust., Spec. Publ.

Muyzert, E. & Snieder, R, 2000. An alternative parameterisation for surface waves in a transverse isotropic media, *Phys. Earth. Planet. Int.*, **118**, 125–133.

Nataf, H.C., & Ricard, Y., 1996. 3SMAC: An a prior tomographic model of the upper mantle based on geophysical modeling, *Phys. Earth. Planet. Int.*, **95**, 101–122.

Nataf, H.C., Nakanishi,I., & Anderson, D.L., 1986. Measurements of mantle wave velocity and inversion form lateral heterogeneities and anisotropy *J. Geophys. Res.*, **91**, 7261–7307.

Nishimura, C.E., & Forsyth, D.E., 1989. The anisotropic structure of the upper mantle in the Pacific, *Geophys. J.R. Astr. Soc.*, **96**, 203–229.

Nolet, G., 1987. Waveform Tomography, in *Seismic Tomography*, pp 301–322, ed. Nolet, G., Reidel Publishing Company, Dordrecht.

Nolet, G., 1990. Partitioned waveform inversion and two-dimensional structure under the Network of Autonomously Recording Seismographs, *J. Geophys. Res.*, **95**, 8499–8512.

Nolet, G., 1993. Imaging the upper mantle with partitioned nonlinear waveform inversion, in *Seismic Tomography*, pp 8499–8512, eds. Iryer, H. M. & Hirahara, K., Chapman and Hall, London.

Nolet, G., van Trier, J., & Huisman, R., 1986. A formalism for nonlinear inversion of seismic surface waves, *Geophys. Res. Lett.*, **13**, 26–29.

Paige, C. C., & Saundars, M. A., 1982. LSQR: an algorithm for sparse linear equations and sparse least square, *ACM Trans. Math. Soft.*, **8**, 43–71 and 195–209.

Plumb, K.A., 1979. The tectonic evolution of Australia, *Earth Sci. Rev.*, **14**, 205–249

Press, W. H., Flannery, B. P., Teukolsky, S. A., & Vetterling, W. T., 1986. *Numerical Recipes: the Art of Scientific Computing*, Cambridge University Press, Cambridge.

Ritzwoller, M.H., & Levshin, A.L., 1998. Eurasian surface wave tomography: Group velocities *J. Geophys. Res.*, **103**, 4839–4878

Romanowicz, B., 1995. A global tomographic model of shear attenuation in the upper mantle, *J. Geophys. Res.*, **100**, 12375–12394.

Shaw,R.D., Wellman, P., Gunn, P., Whitaker, A., Tarlowski, C., & Morse, M., 1995. Australian crustal elements map: A geophysical model for the tectonic framework of the continent, *Aust. Geol. Surv. Org. Res. Newslett.*, **23**, 1–3.

Shibutani, T., Sambridge, M., & Kennett, B. L. N., 1996. Genetic Algorithm inversion for receiver functions with application to crust and uppermost mantle structure beneath eastern Australia, *Geophys. Res. Lett.*, **23**, 1829–1832.

Simpson, D.W. 1973. P wave velocity structure in the upper mantle in the Australian region, *PhD thesis, Australian National University*, 212p.

Snieder, R., 1986. 3-D linearized scattering of surface waves and a formalism for surface wave holography, *Geophys. R. Astr. Soc.*, **84**, 581–605.

Snieder, R., 1993. Global inversions using normal modes and long-period surface waves, in *Seismic Tomography: Theory and Practice*, edited by H.M. Iryer & Hirahara, K., 23–63, Chapman and Hall, New York.

Snieder, R., Beckers, J., & Neele, F., 1991. The effect of small-scale structure on normal mode frequencies and global inversions, *J. Geophys. Res.*, **96**, 501–515.

Su, W.-J., & Dziewonski, A. M., 1991. Predominance of long wavelength heterogeneity in the mantle, *Nature*, **352**, 121–126.

Su, W.-J., Woodward, R. L., & Dziewonski, A. M., 1994. Degree 12 model of shear velocity heterogeneity in the mantle, *J. Geophys. Res.*, **99**, 6945–6980.

Takeuchi, H., & Saito, M., 1972, Seismic surface waves, in *Methods in Computational Physics*, Vol. 11, pp. 217–295, ed. Bolt, B. A., Academic Press, New York.

Tanimoto, T., 1990. Long-wavelength S-wave velocity structure throughout the mantle, *Geophys. J. Int.*, **100**, 327–336.

Tanimoto, T., & Anderson, D. L., 1984. Mapping convection in the mantle, *Geophys. Res. Lett.*, **11**,

287–290.

Tarantola, A., & Vallette, B., 1982. Generalized nonlinear inverse problems solved using the least square criterion, *Rev. Geophys. Space Phys.*, **20**, 219–232.

Tong,C., Gudmundsson,O., & Kennett, B. L. N., 1994. Shear wave splitting in refracted waves returned from the upper mantle transition zone beneath northern Australia *J. Geophys. Res.*, **99**, 15783–15797.

Trampert, J., & Woodhouse, J. H., 1995. Global phase maps of Love and Rayleigh waves between 40 and 150 seconds, *Geophys. J. Int.*, **122**, 675–690.

Um, J., Dahlen, F. A., & Park, J, 1992. Normal mode multiplet coupling along a dispersion branch, *Geophys. J. Int.*, **106**, 11–35.

van der Hilst, R. D., Kennett, B. L. N., Christie, D., & Grand, J., 1994. SKIPPY: Mobile broad-band arrays to study the seismic structure of the lithosphere and mantle beneath Australia, *EOS Trans. Am. Geophys. Un.*, v. 75, p. 177 & 180, 181.

van der Hilst, R. D., Kennett, B. L. N., & Shibutani T., 1998. Upper-mantle structure beneath Australia from portable array deployment, in *Structure and Evolution of the Australian Continent, Geodyn. ser.*, v. 26, 39–57, edited by J. Braun et al., AGU Washington D.C.

van der Lee, S., & Nolet, G., 1997. Upper mantle S velocity structure of North America, *J. Geophys. Res.*, **102**, 22815–22838.

Vidale, J. E., 1986. Complex polarization analysis of particle motion *Bull. Seism. Soc. Am.*, **76**, 1393–1405.

Widiyantoro, S., & van der Hilst, R. D., 1996. Structure and evolution of lithospheric slab beneath the Sunda arc, Indonesia, *Science*, **271**, 1566–1570.

Woodhouse, J. H., 1974. Surface waves in a laterally varying layered structure, *Geophys. J.R.Astr.Soc.*, **37**, 461–490.

Woodhouse, J. H., & Dziewonski, A. M., 1984. Mapping the upper mantle: Three-dimensional modeling of Earth structure by inversion of seismic waveform, *J. Geophys. Res.*, **89**, 5953–5986.

Woodhouse, J. H., & Wong, Y. K., 1986. Amplitude, phase, path anomalies of mantle waves, *Geophys. R. Astr. Soc.*, **87**, 753–774.

Woodward, R. L., & Masters, G., 1991. Global upper mantle structure from long-period differential travel times, *J. Geophys. Res.*, **96**, 6351–6378.

Yoshizawa, K., & Kennett,B.L.N., 2001. Nonlinear waveform inversion for surface waves with a neighbourhood algorithm - Application to multi-mode dispersion measurements, submitted to *Geophys. J. Int.*,.

Zhang, Y.-S., Tanimoto, T., 1993. High-resolution global upper mantle structure and plate tectonics, *J. Geophys. Res.*, **98**, 9793–9823.

Zhao, H., Ursin, B., & Amundsen, L., 1994. Frequency-wavenumber elastic inversion of marine seismic data, *Geophysics*, **59**, 1868–1881.

Zielhuis, A., 1993, S-wave velocity below Europe from delaytime and waveform inversion, *Ph.D thesis*, University of Utrecht, The Netherlands.

Zielhuis, A., & Nolet, G., 1994. Shear-wave velocity variations in the upper mantle beneath central Europe, *Geophys. J. Int.*, **117**, 695–715.

Zielhuis, A., & van der Hilst, R. D., 1996. Mantle structure beneath the eastern Australian region from partitioned waveform inversion, *Geophys. J. Int.*, **127**, 1-16.

Appendix A

Appendix A includes all the waveform matches in Chapter 5. Each page has three pairs of the vertical (Z) and tangential (T) component matchings from three events. The top title of each page describes the station name. The thick black lines indicate observed seismograms and thin red lines depict forward modelings and thin blue lines shows the final models of the inversion. Each legend has component and event names, also the name of the initial model is in the parentheses (AU3 or a smoothed PREM).

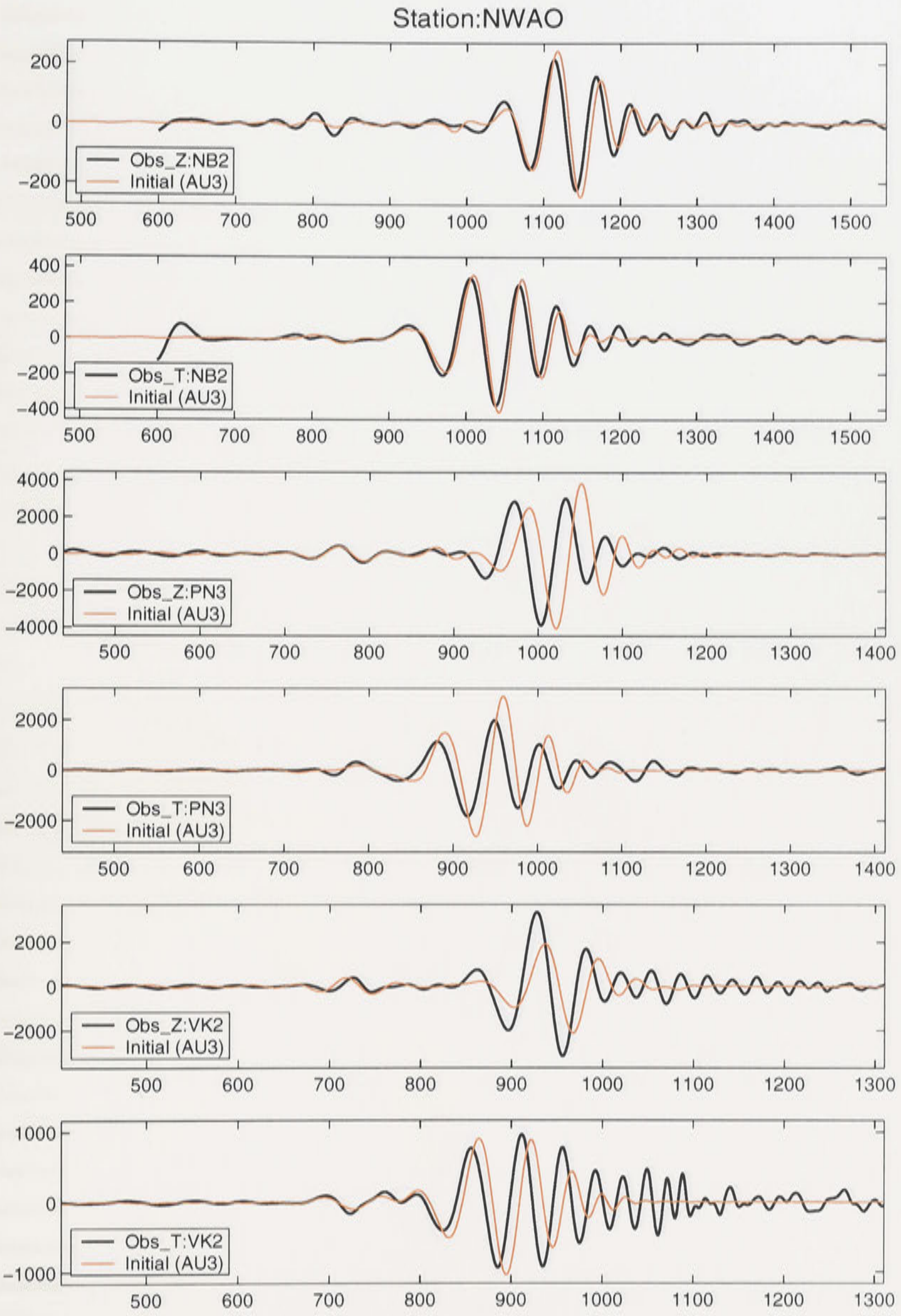

Fig. A0.18. The forward modelings of the Rayleigh and Love joint inversions. The observed station is NWAO and the events are NB2, PN3, and VK2. The starting model is AU3.

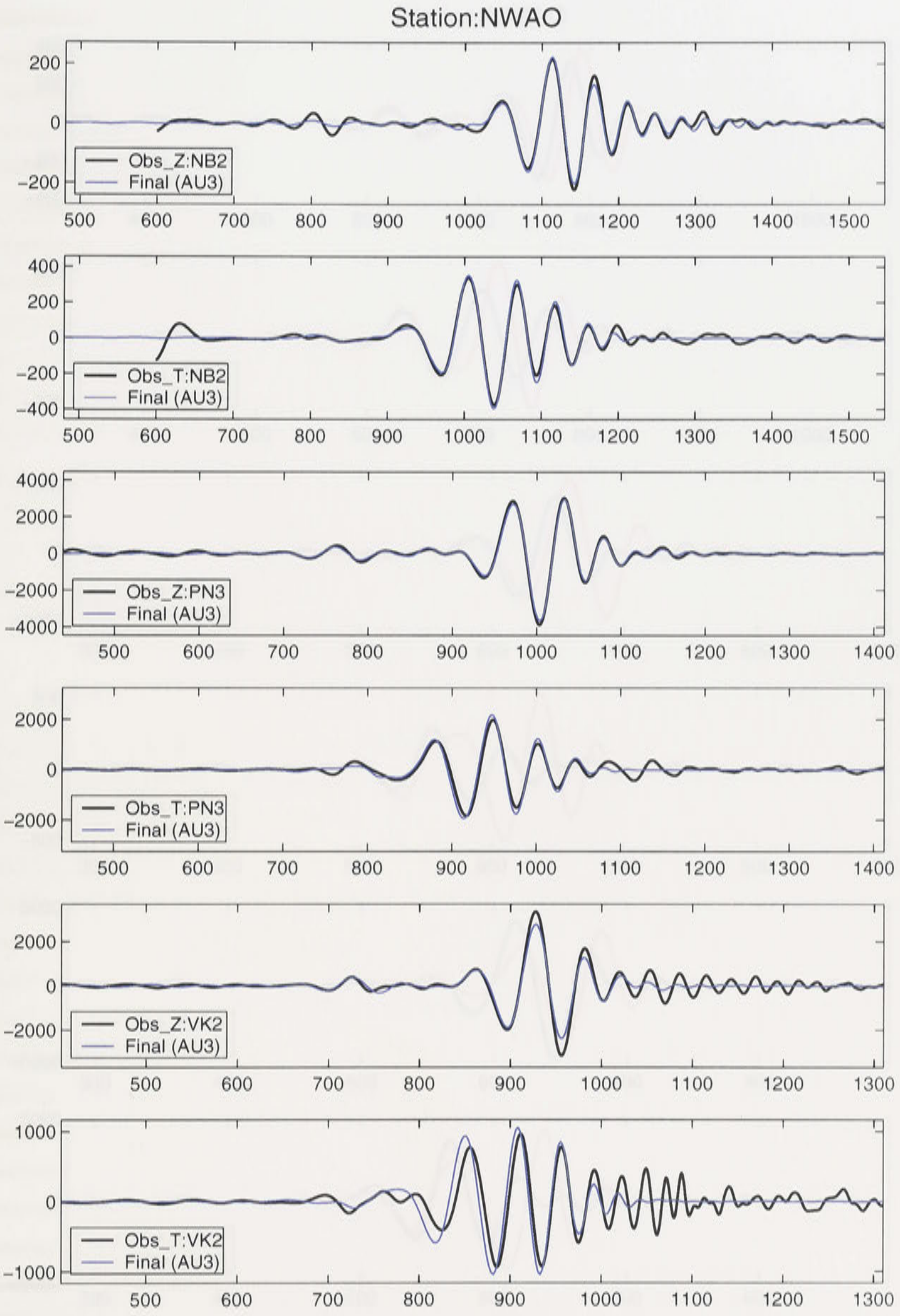

Fig. A0.19. The final results of the Rayleigh and Love joint inversions. The observed station is NWAO and the events are NB2, PN3, and VK2. The starting model is AU3.

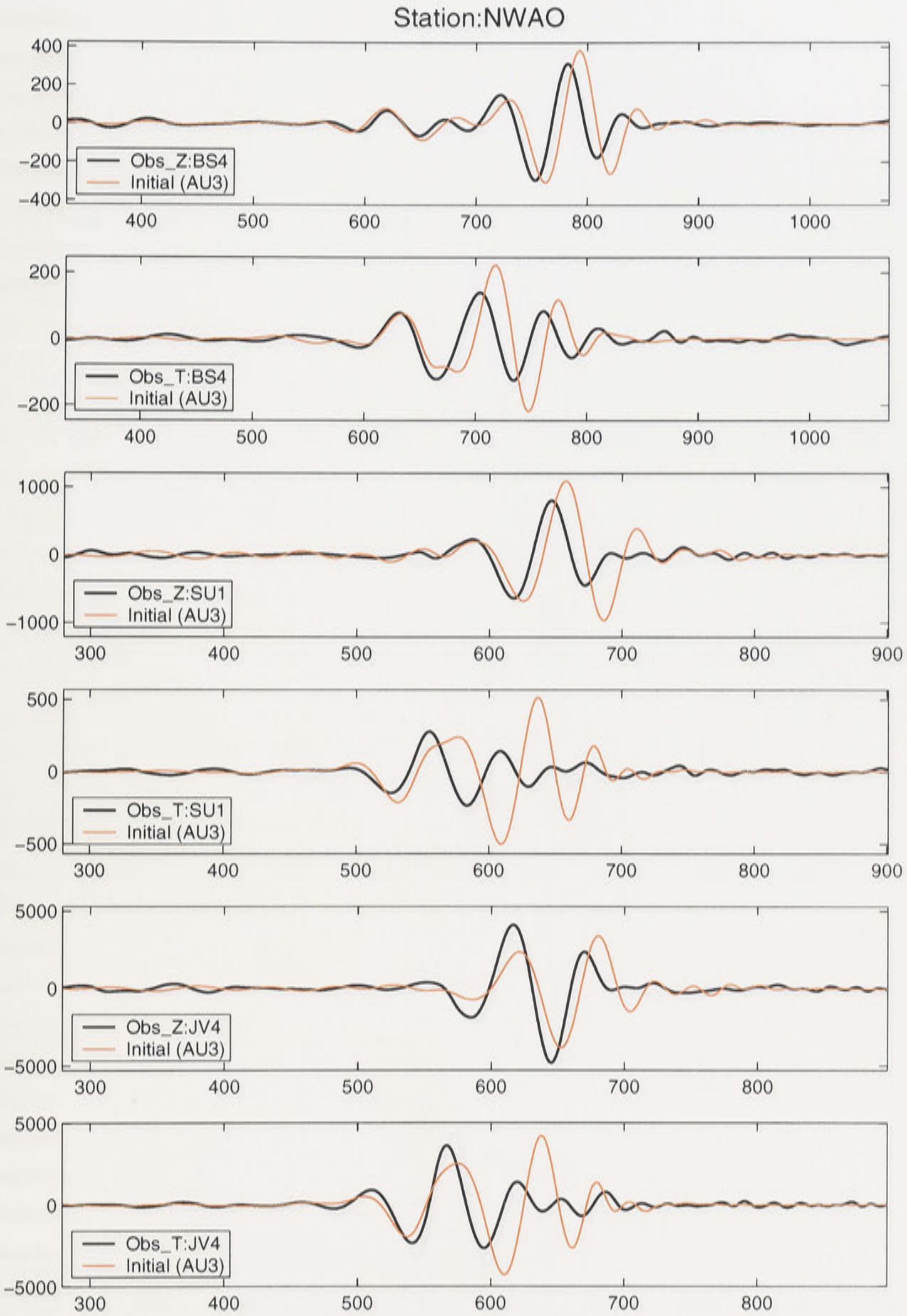

Fig. A0.20. The forward modelings of the Rayleigh and Love joint inversions. The observed station is NWAO and the events are BS4, SU1, and JV4. The starting model is AU3.

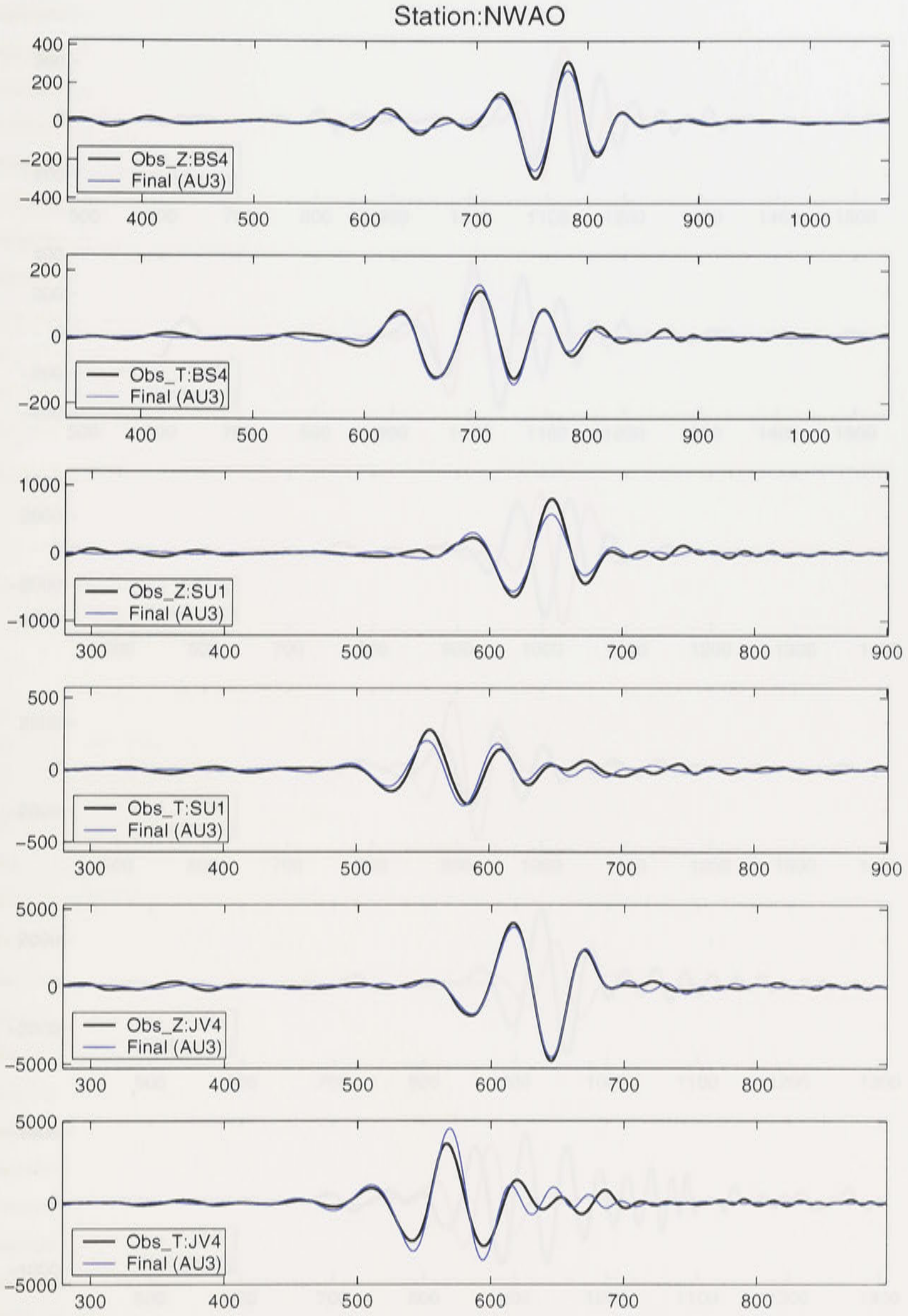

Fig. A0.21. The final results of the Rayleigh and Love joint inversions. The observed station is NWAO and the events are BS4, SU1, and JV4. The starting model is AU3.

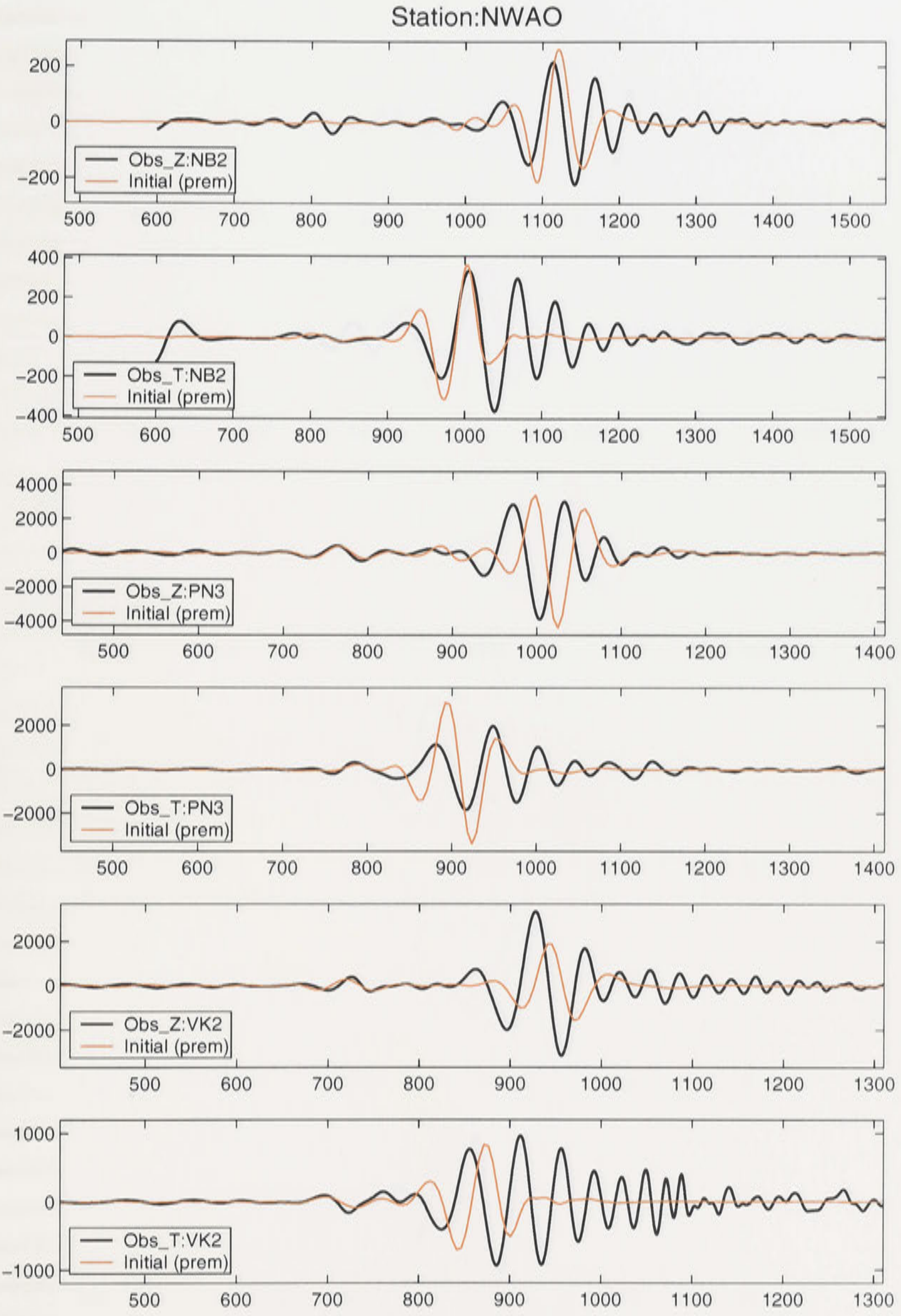

Fig. A0.22. The forward modelings of the Rayleigh and Love joint inversions. The observed station is NWAO and the events are NB2, PN3, and VK2. The starting model is a smoothed PREM.

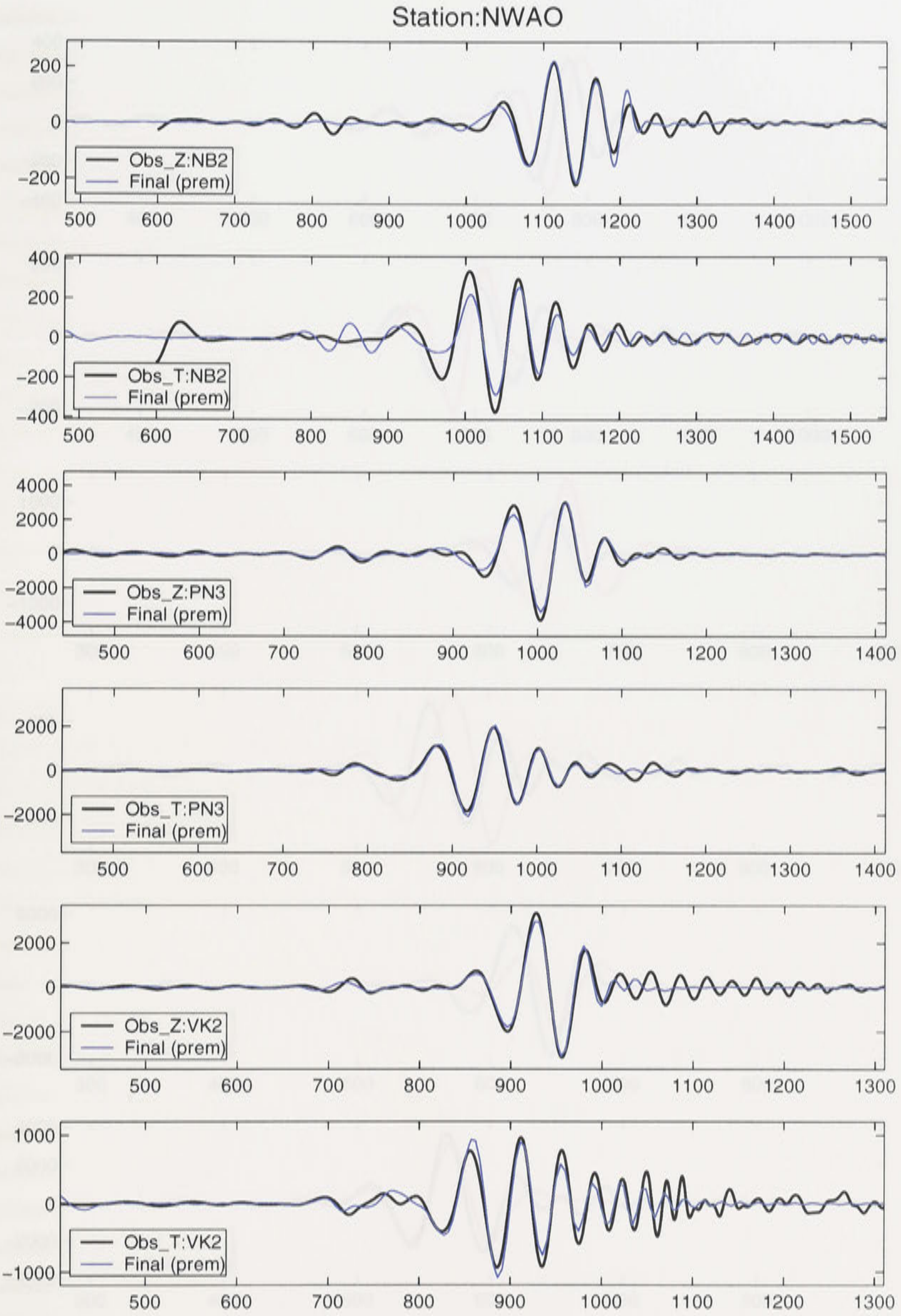

Fig. A0.23. The final results of the Rayleigh and Love joint inversions. The observed station is NWAO and the events are NB2, PN3, and VK2. The starting model is a smoothed PREM.

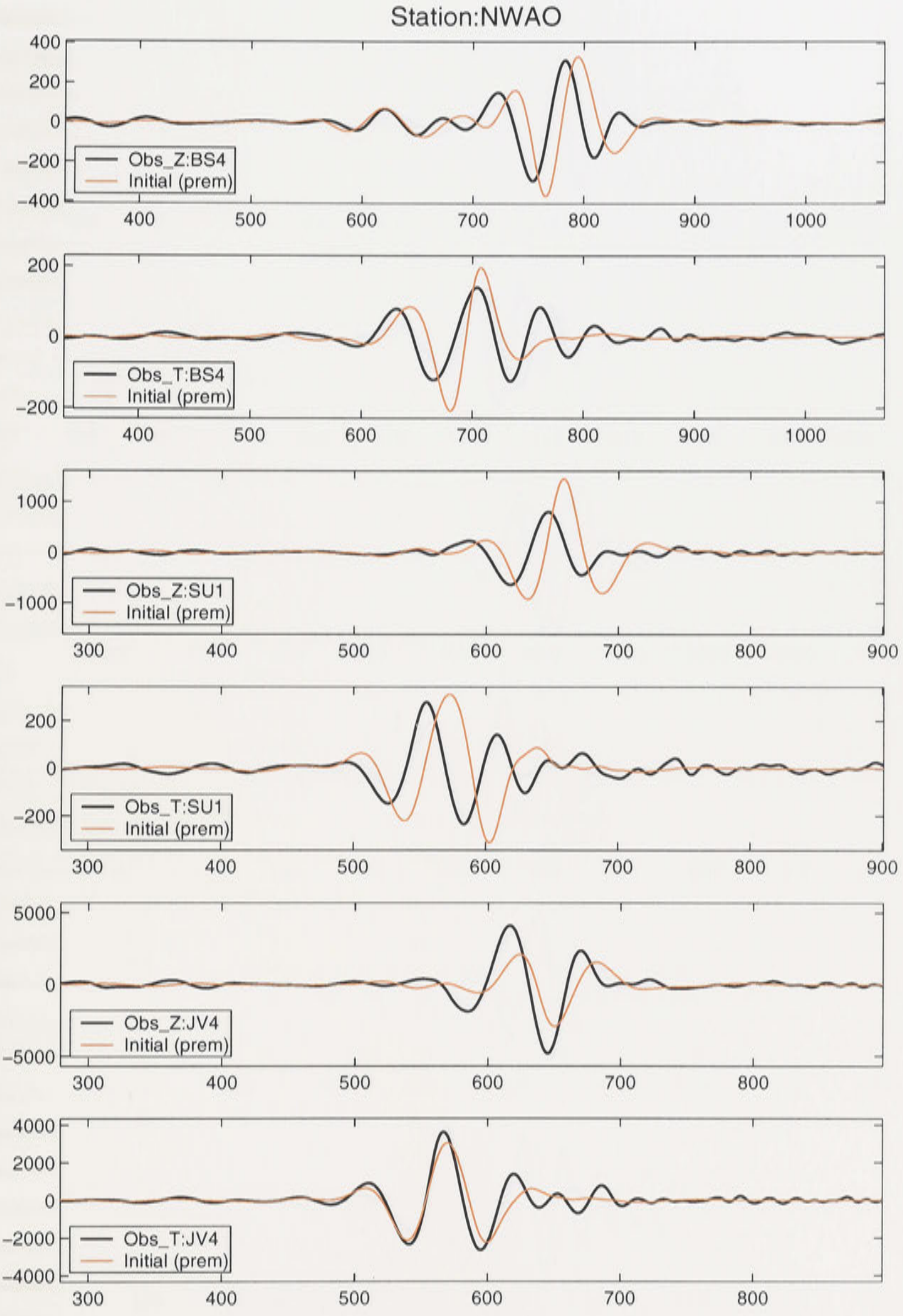

Fig. A0.24. The forward modelings of the Rayleigh and Love joint inversions. The observed station is NWAO and the events are BS4, SU1, and JV4. The starting model is a smoothed PREM.

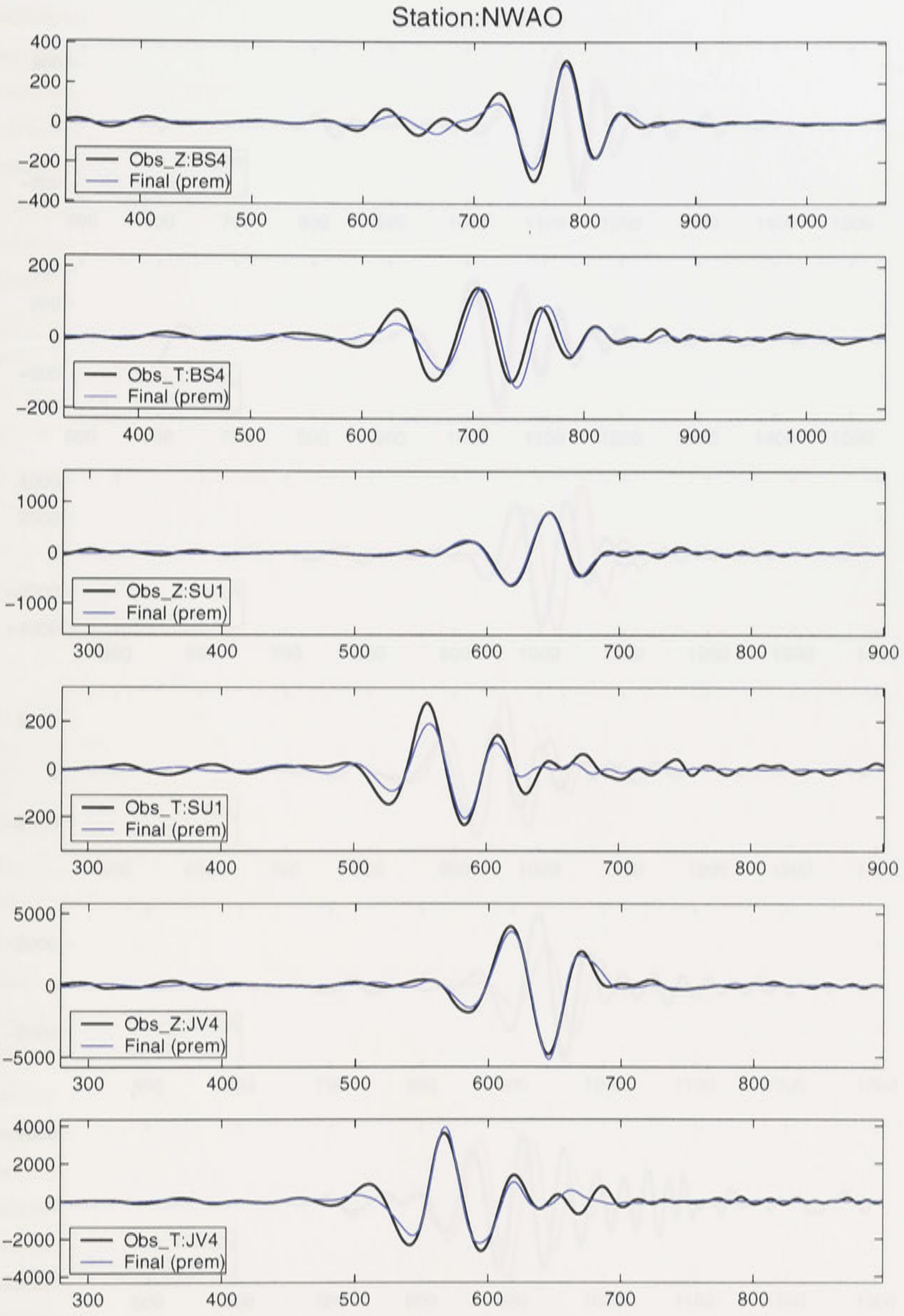

Fig. A0.25. The final results of the Rayleigh and Love joint inversions. The observed station is NWAO and the events are BS4, SU1, and JV4. The starting model is a smoothed PREM.

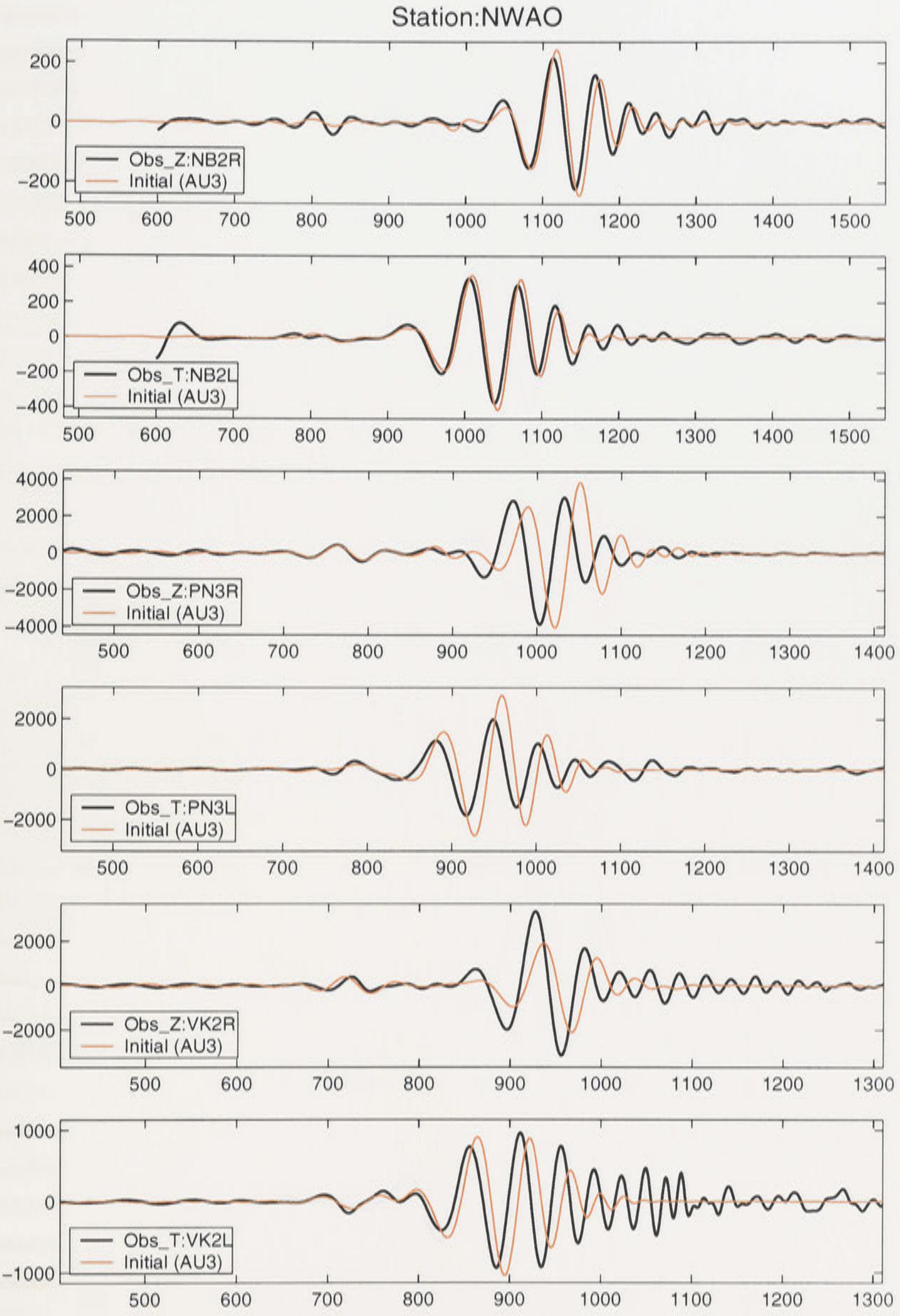

Fig. A0.26. The forward modelings of the Rayleigh and Love independent inversions. The observed station is NWAO and the events are NB2, PN3, and VK2. The starting model is AU3.

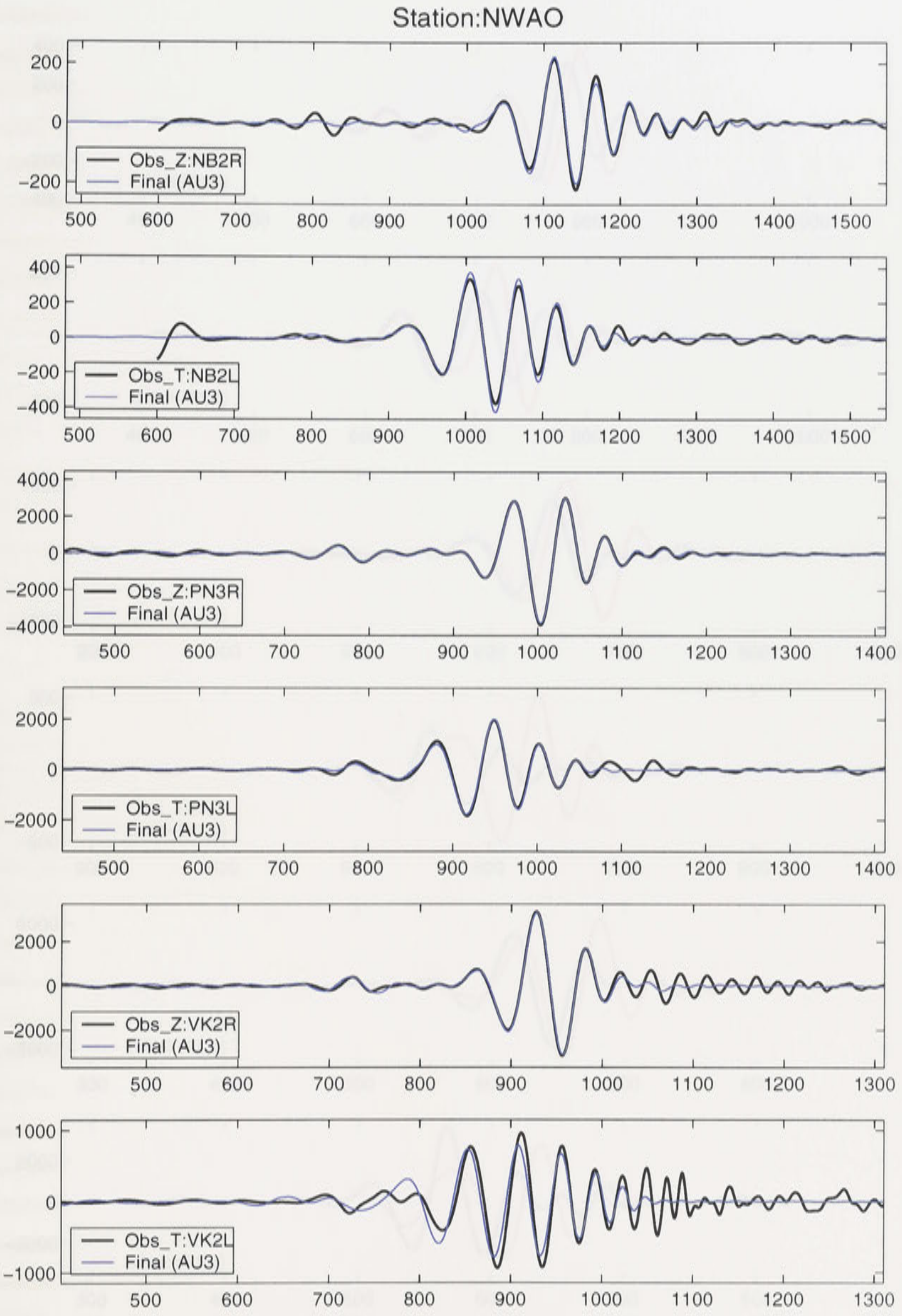

Fig. A0.27. The final results of the Rayleigh and Love independent inversions. The observed station is NWAO and the events are NB2, PN3, and VK2. The starting model is AU3.

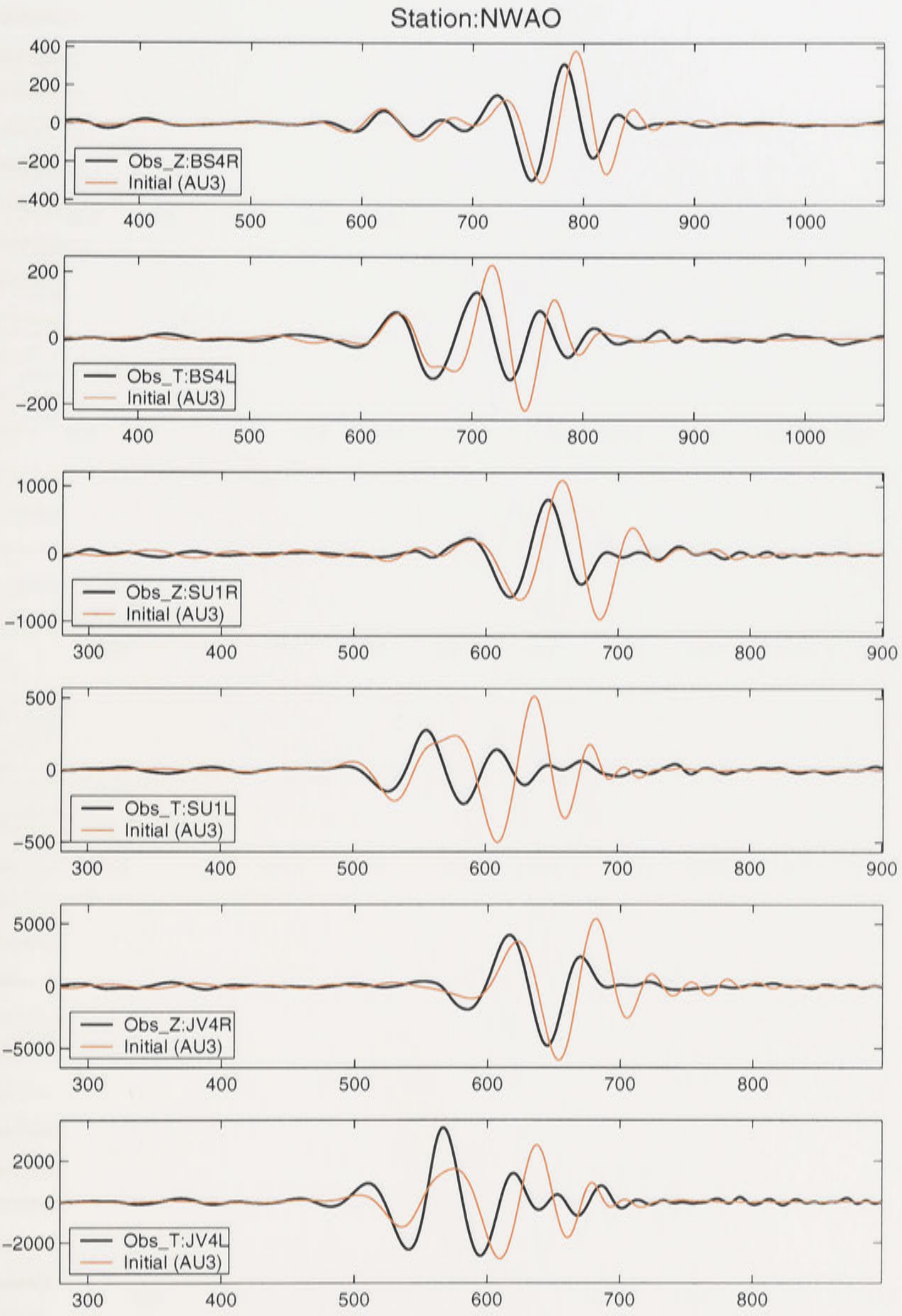

Fig. A0.28. The forward modelings of the Rayleigh and Love independent inversions. The observed station is NWAO and the events are BS4, SU1, and JV4. The starting model is AU3.

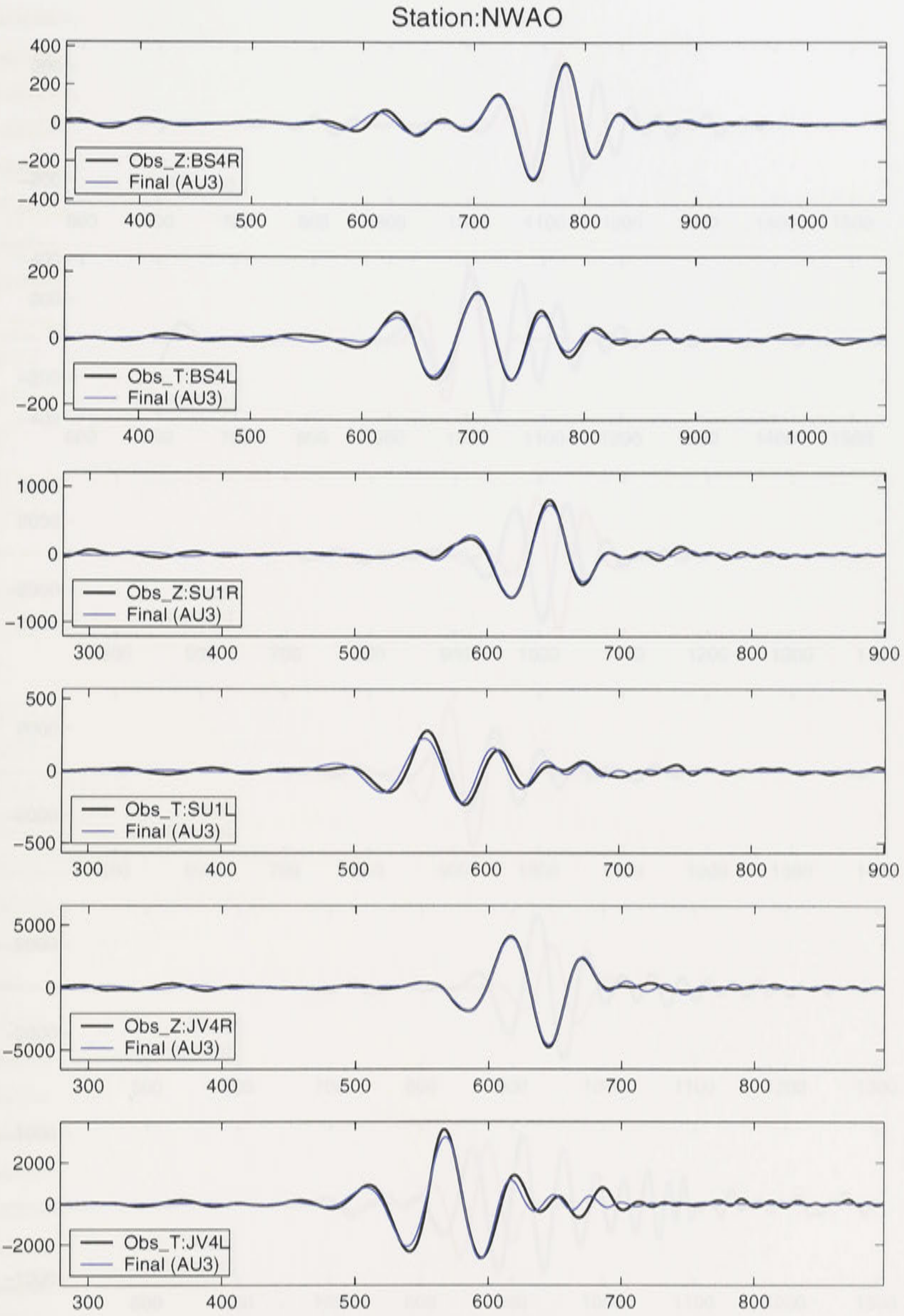

Fig. A0.29. The final results of the Rayleigh and Love independent inversions. The observed station is NWAO and the events are BS4, SU1, and JV4. The starting model is AU3.

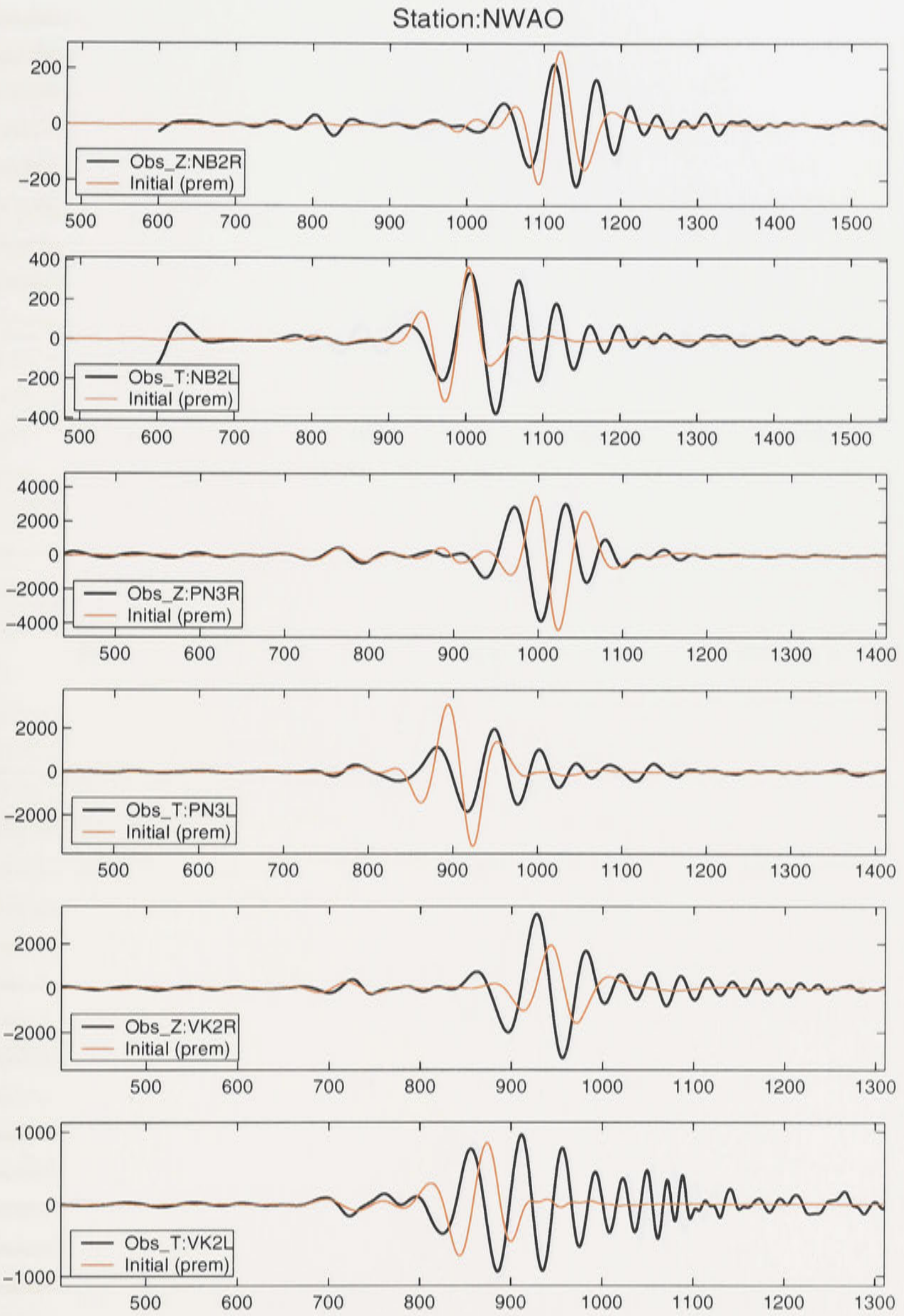

Fig. A0.30. The forward modelings of the Rayleigh and Love independent inversions. The observed station is NWAO and the events are NB2, PN3, and VK2. The starting model is a smoothed PREM.

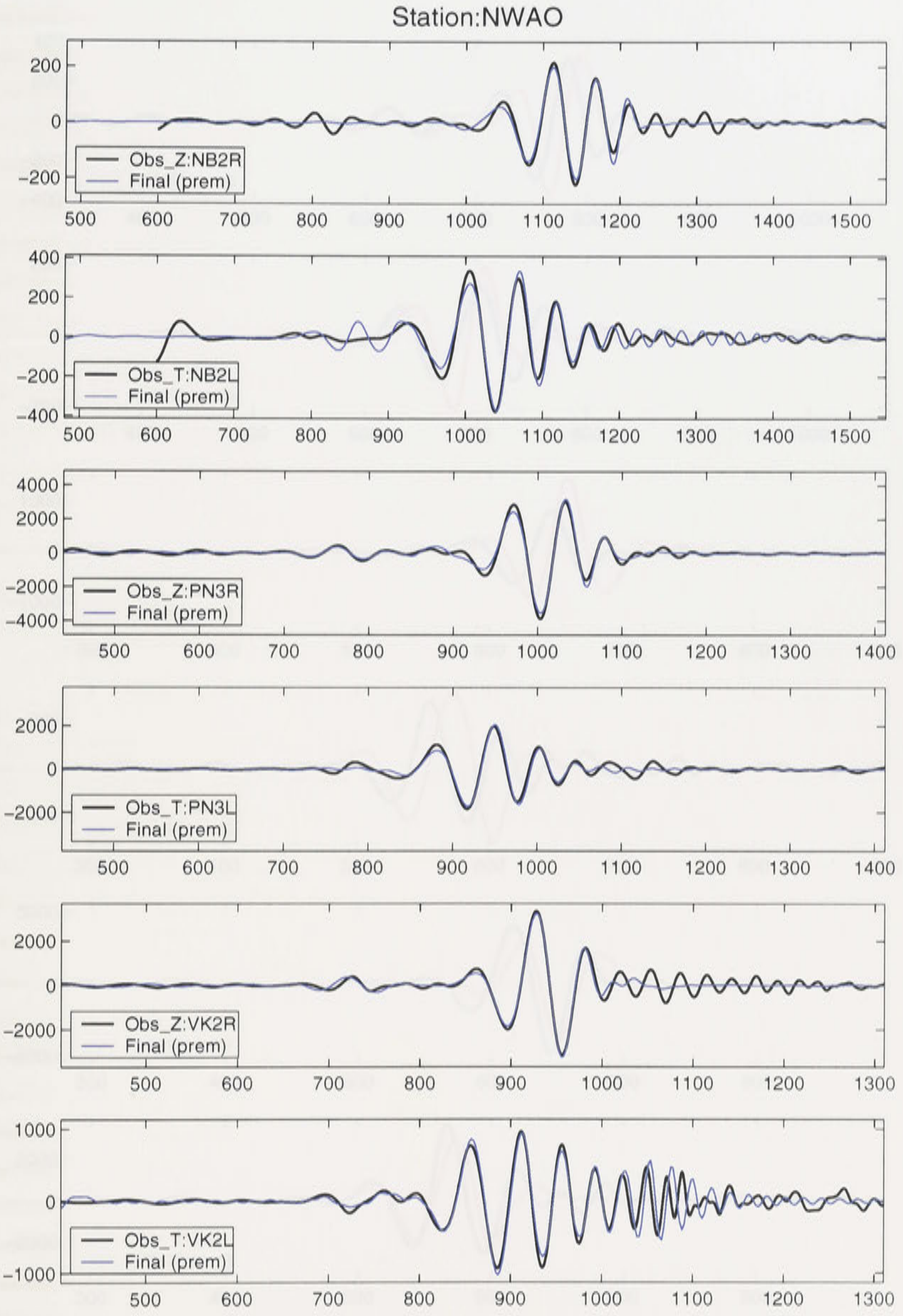

Fig. A0.31. The final results of the Rayleigh and Love independent inversions. The observed station is NWAO and the events are NB2, PN3, and VK2. The starting model is a smoothed PREM

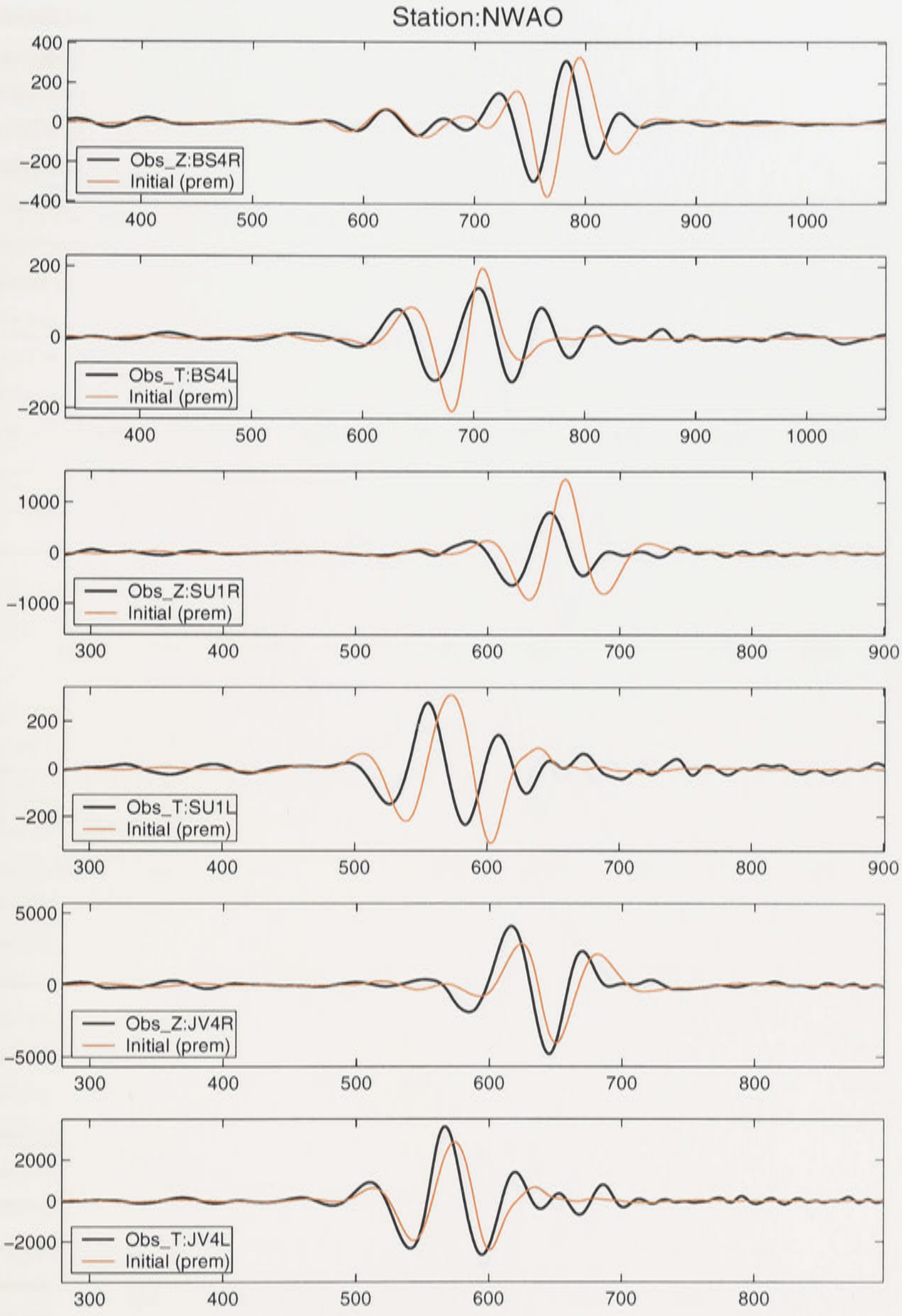

Fig. A0.32. The forward modelings of the Rayleigh and Love independent inversions. The observed station is NWAO and the events are BS4, SU1, and JV4. The starting model is a smoothed PREM.

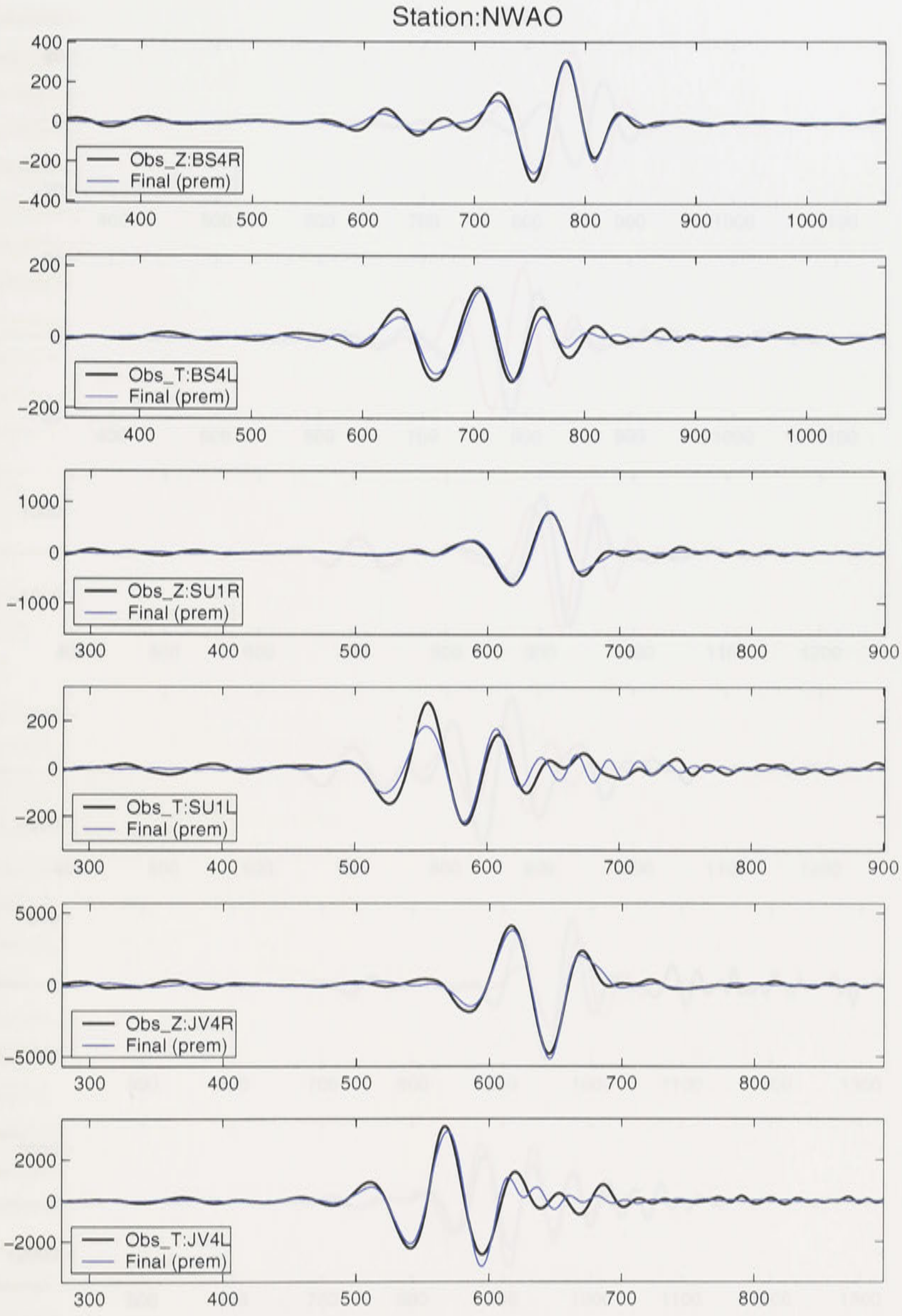

Fig. A0.33. The final results of the Rayleigh and Love independent inversions. The observed station is NWAO and the events are BS4, SU1, and JV4. The starting model is a smoothed PREM.

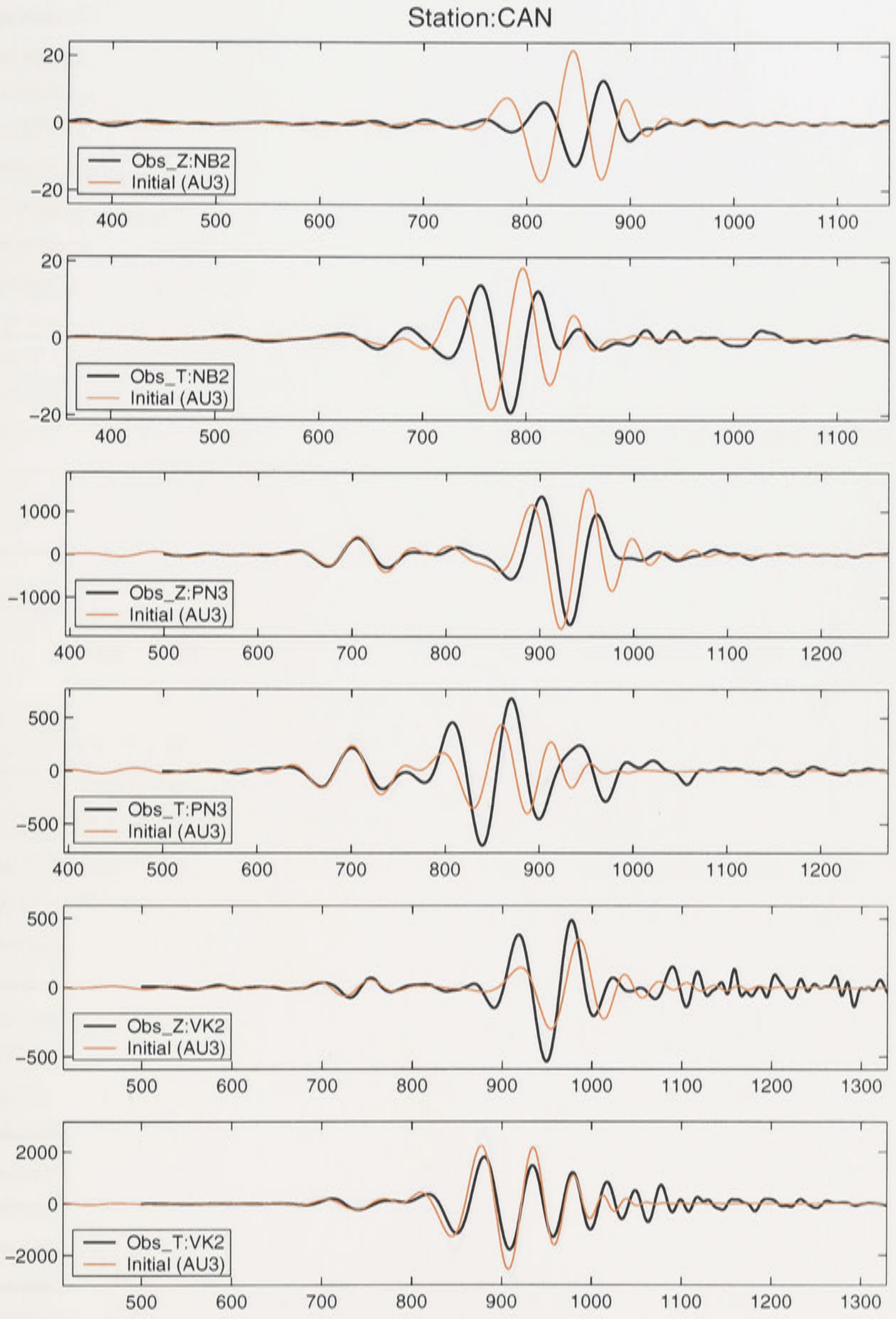

Fig. A0.34. The forward modelings of the Rayleigh and Love joint inversions. The observed station is CAN and the events are NB2, PN3, and VK2. The starting model is AU3.

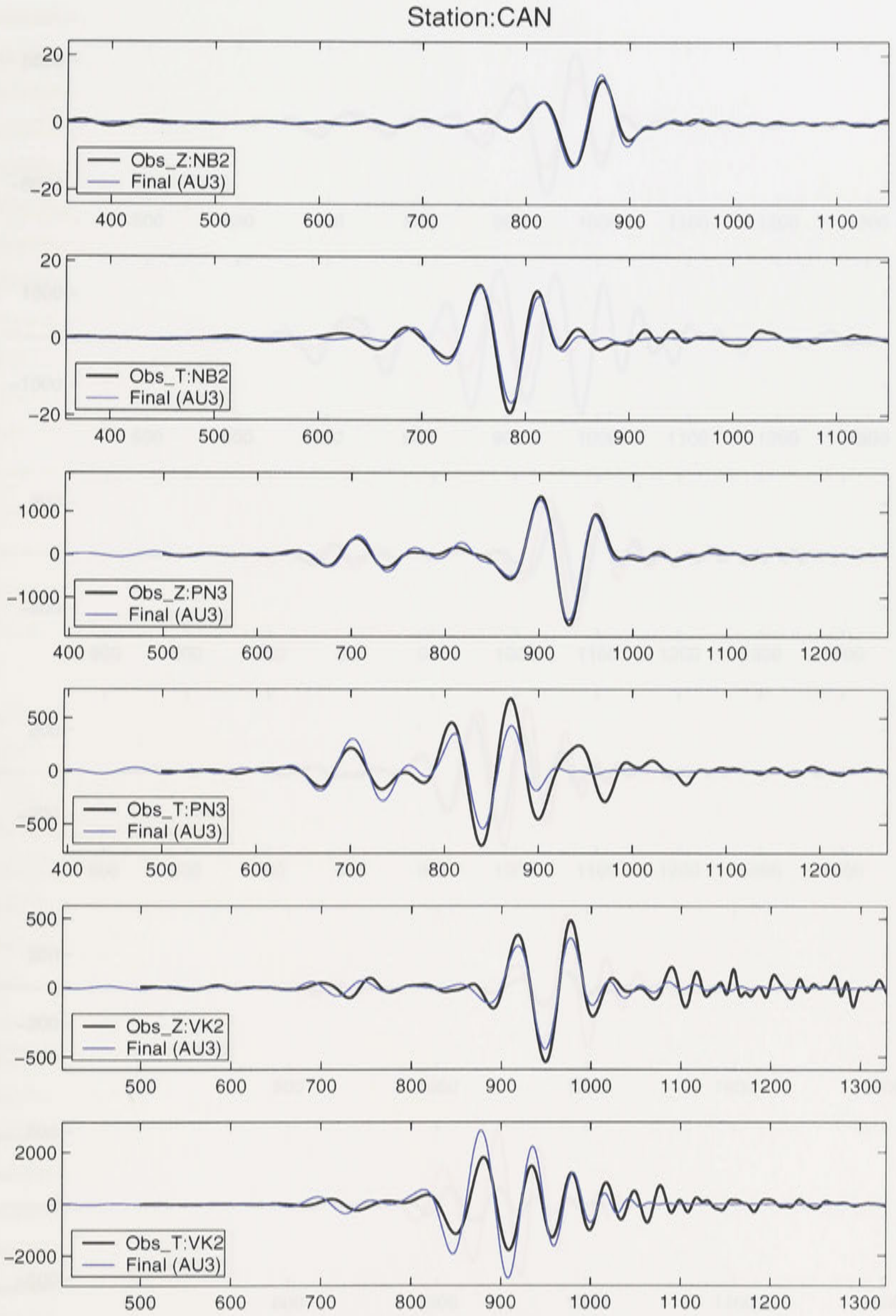

Fig. A0.35. The final results of the Rayleigh and Love joint inversions. The observed station is CAN and the events are NB2, PN3, and VK2. The starting model is AU3.

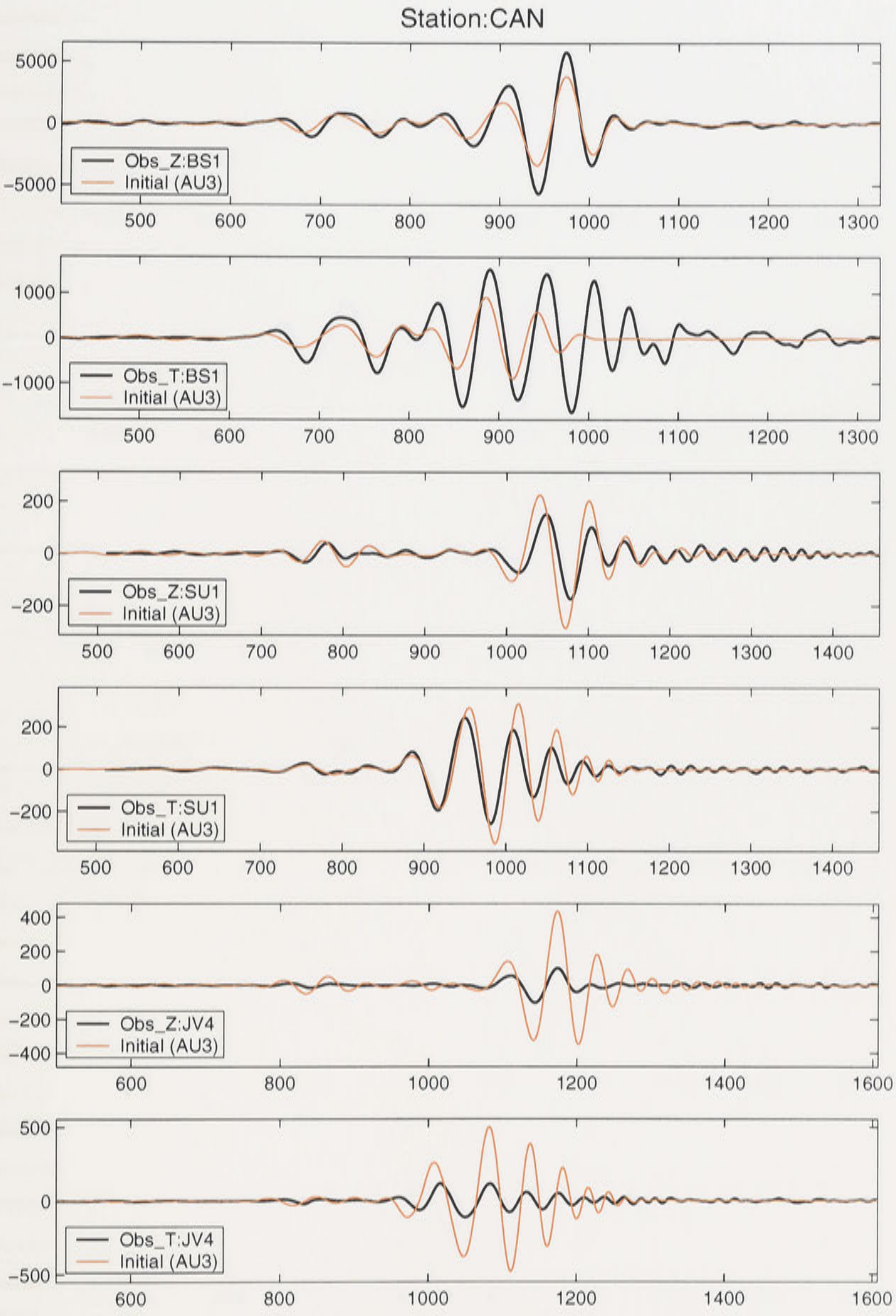

Fig. A0.36. The forward modelings of the Rayleigh and Love joint inversions. The observed station is CAN and the events are BS1, SU1, and JV4. The starting model is AU3.

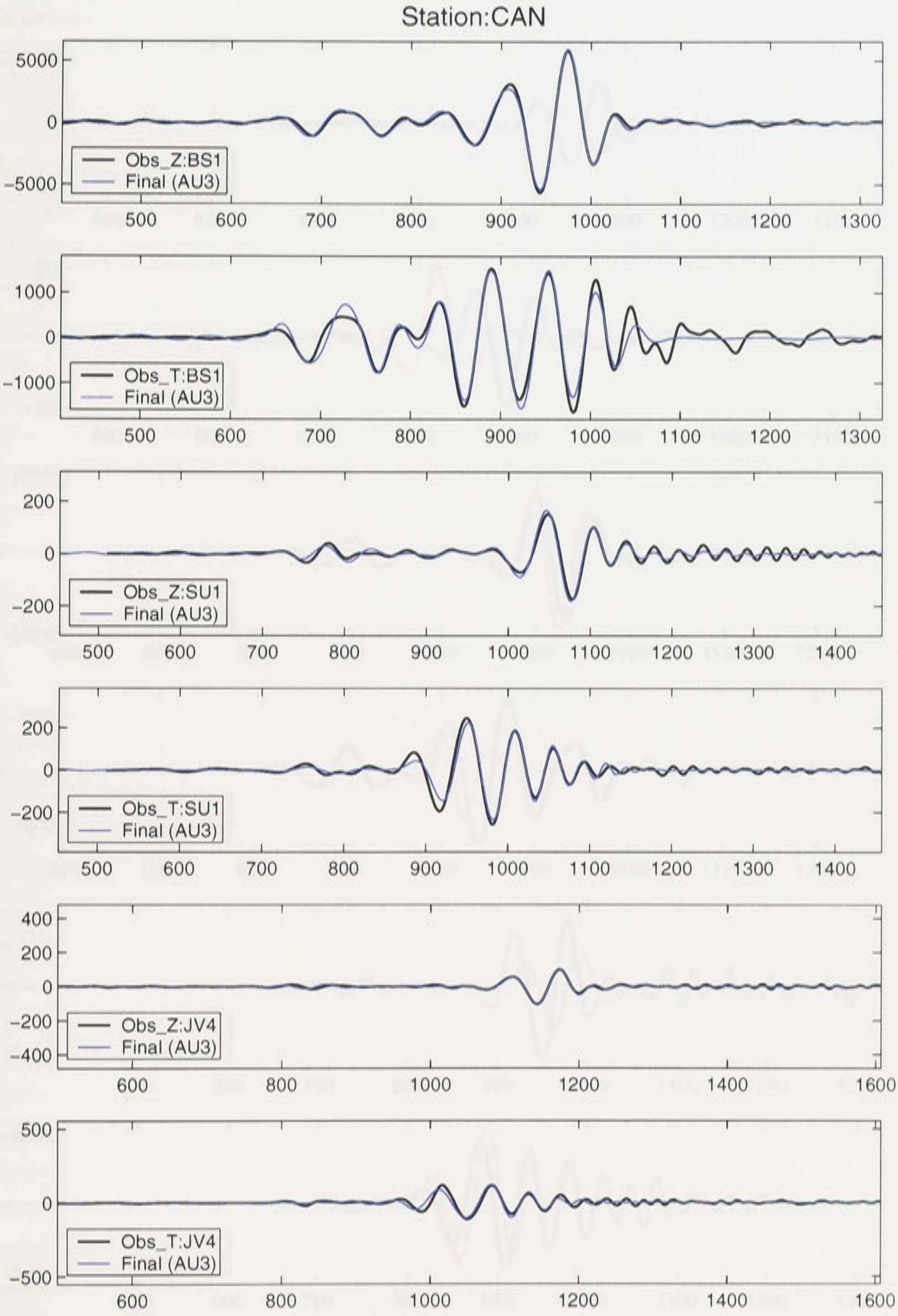

Fig. A0.37. The final results of the Rayleigh and Love joint inversions. The observed station is CAN and the events are BS1, SU1, and JV4. The starting model is AU3.

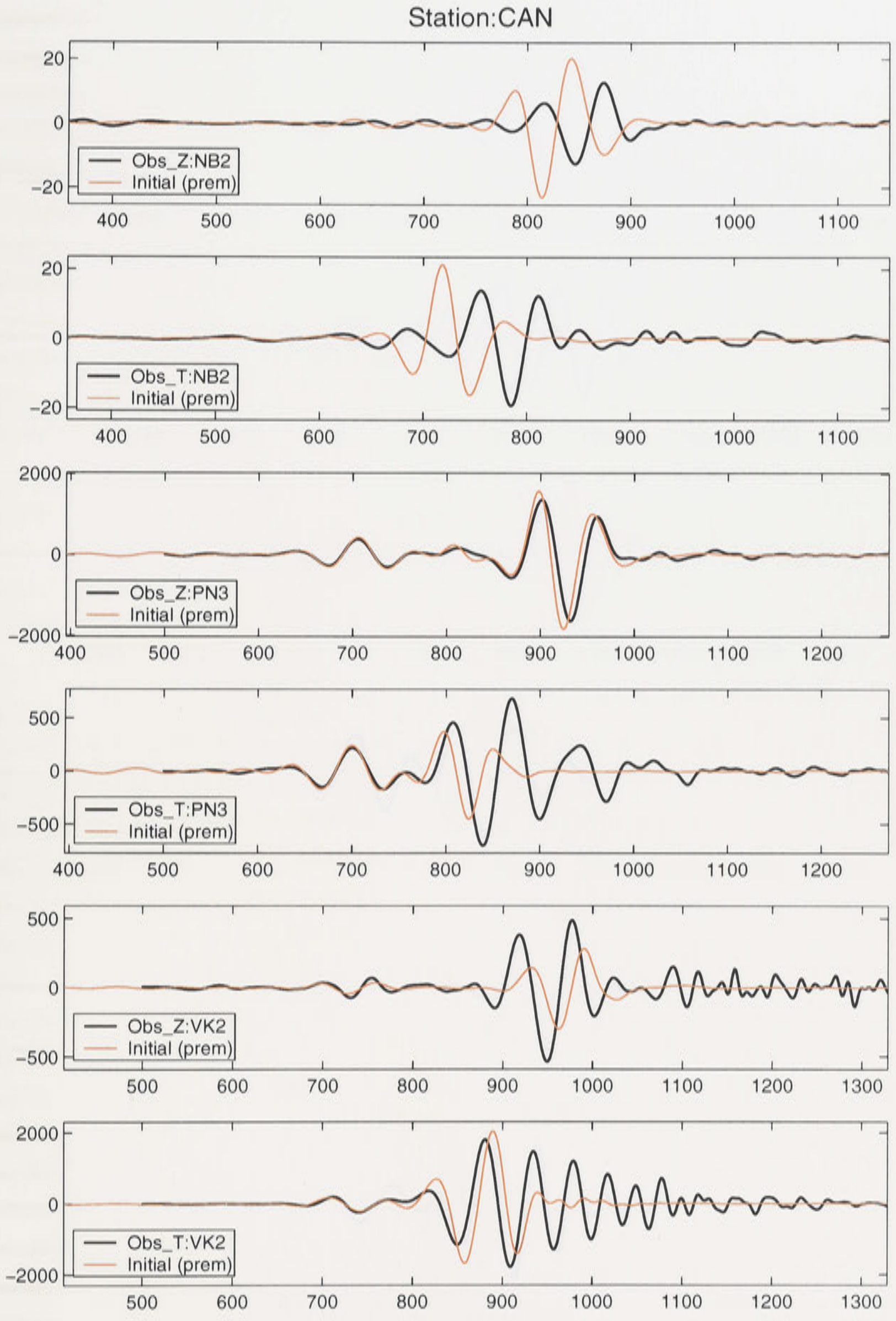

Fig. A0.38. The forward modelings of the Rayleigh and Love joint inversions. The observed station is CAN and the events are NB2, PN3, and VK2. The starting model is a smoothed PREM.

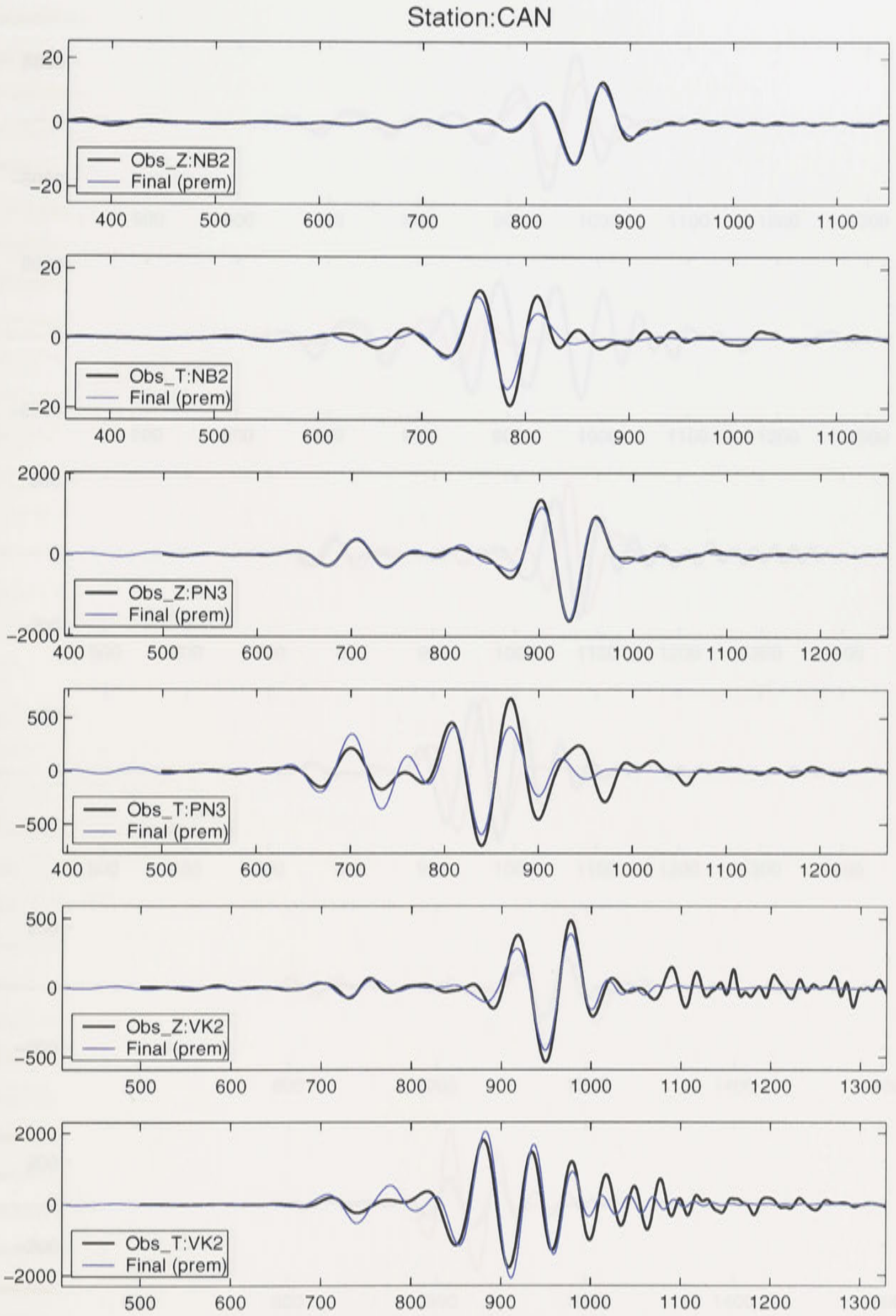

Fig. A0.39. The final results of the Rayleigh and Love joint inversions. The observed station is CAN and the events are NB2, PN3, and VK2. The starting model is a smoothed PREM.

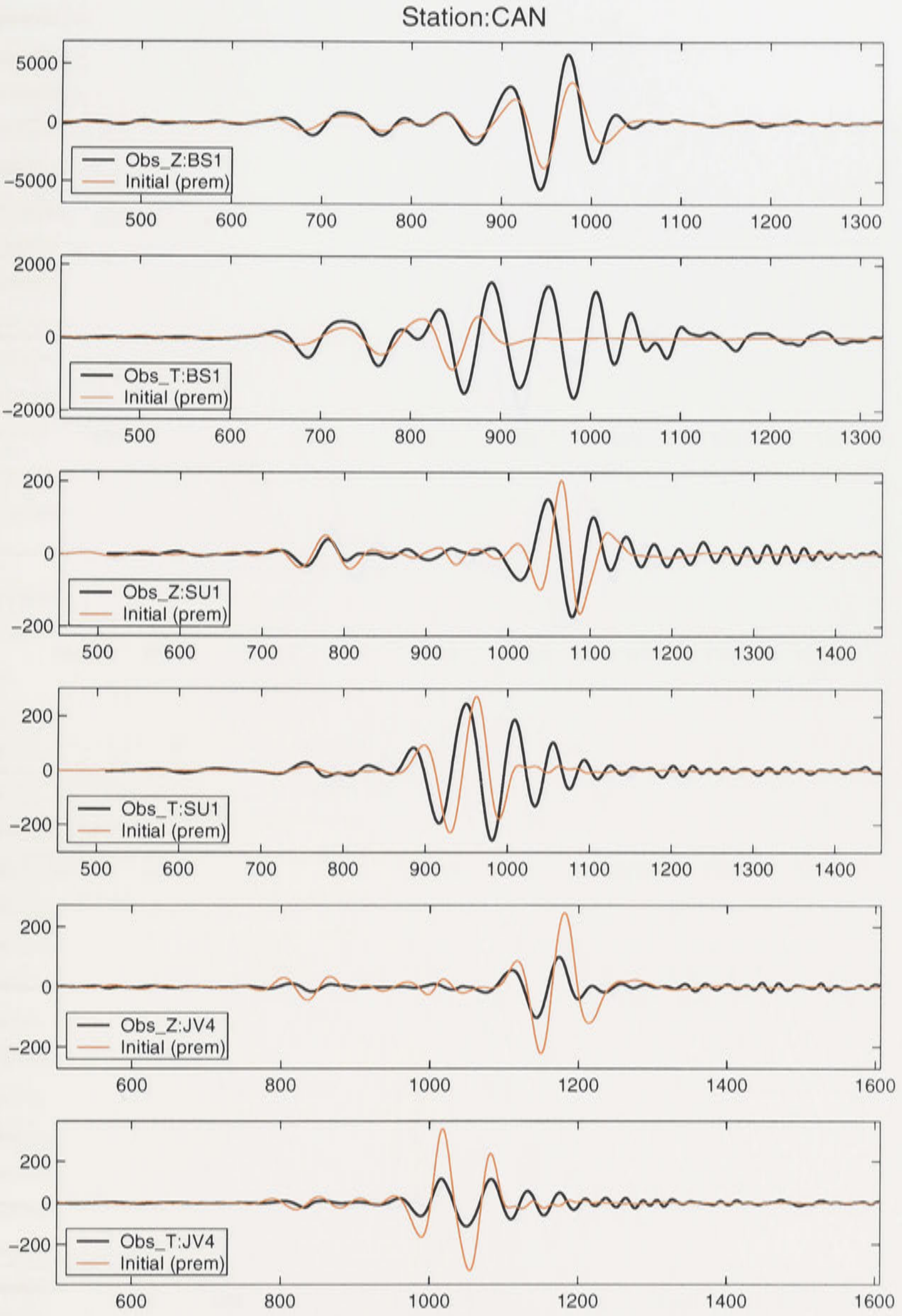

Fig. A0.40. The forward modelings of the Rayleigh and Love joint inversions. The observed station is CAN and the events are BS1, SU1, and JV4. The starting model is a smoothed PREM.

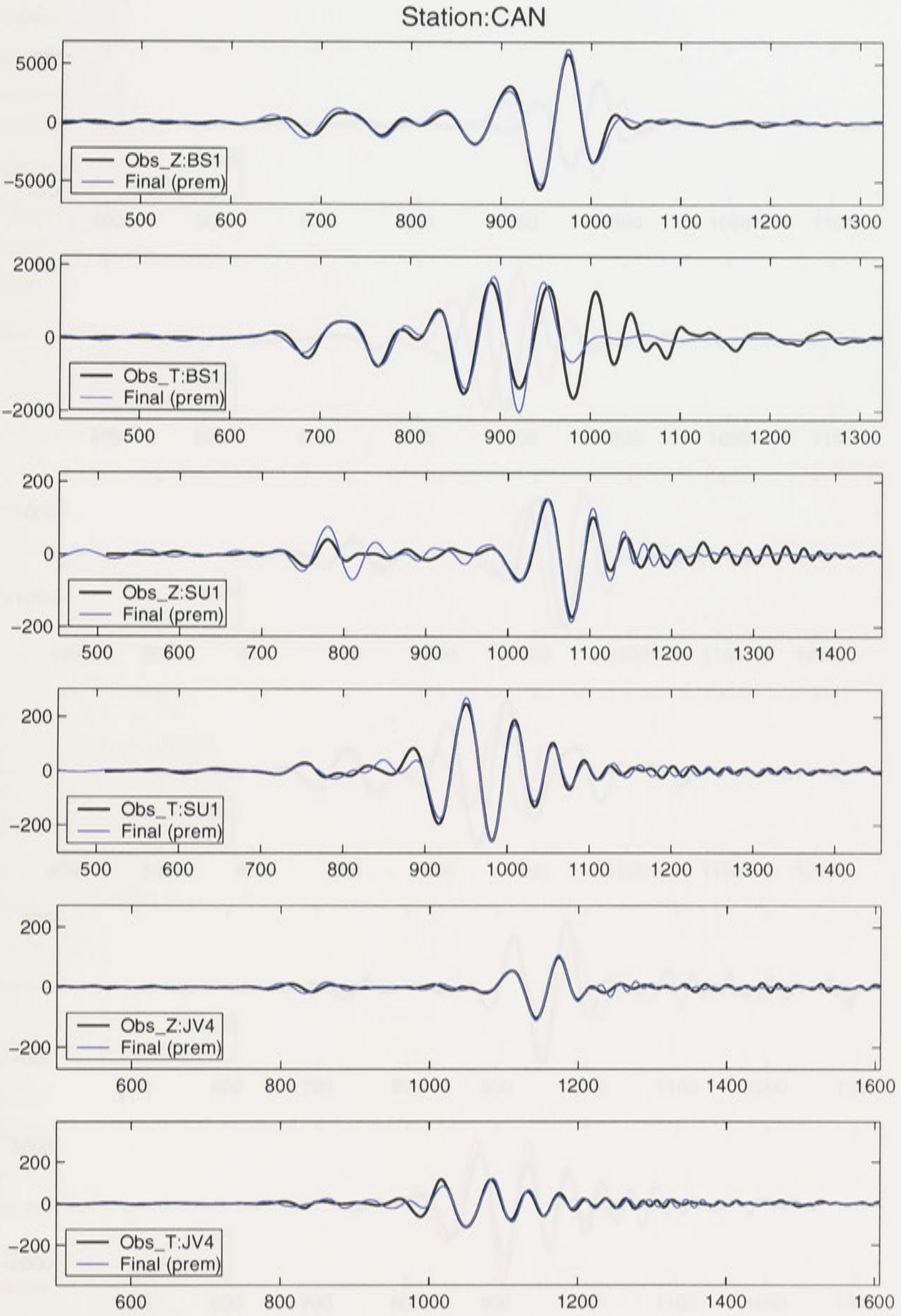

Fig. A0.41. The final results of the Rayleigh and Love joint inversions. The observed station is NWAO and the events are BS1, SU1, and JV4. The starting model is a smoothed PREM.

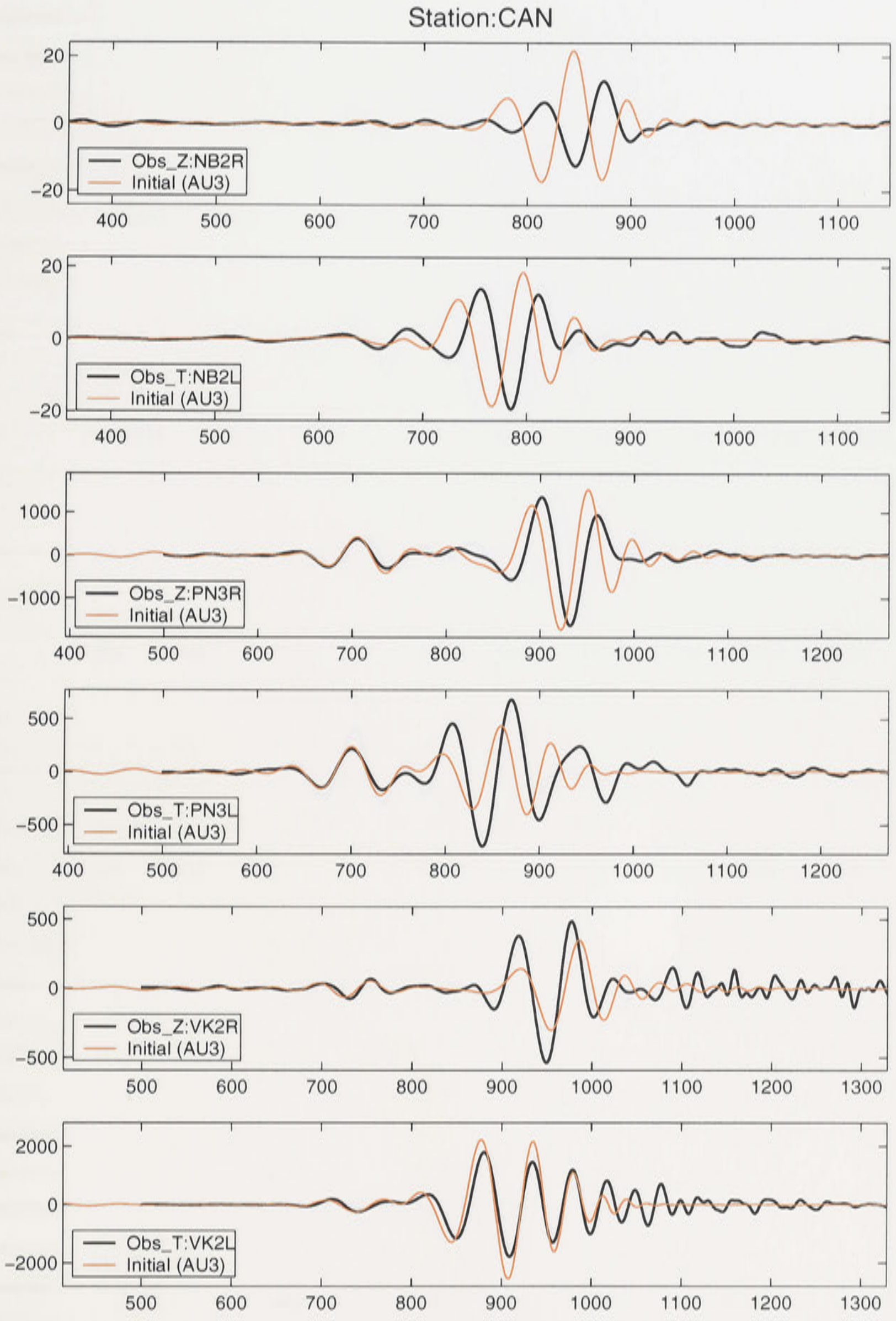

Fig. A0.42. The forward modelings of the Rayleigh and Love independent inversions. The observed station is CAN and the events are NB2, PN3, and VK2. The starting model is AU3.

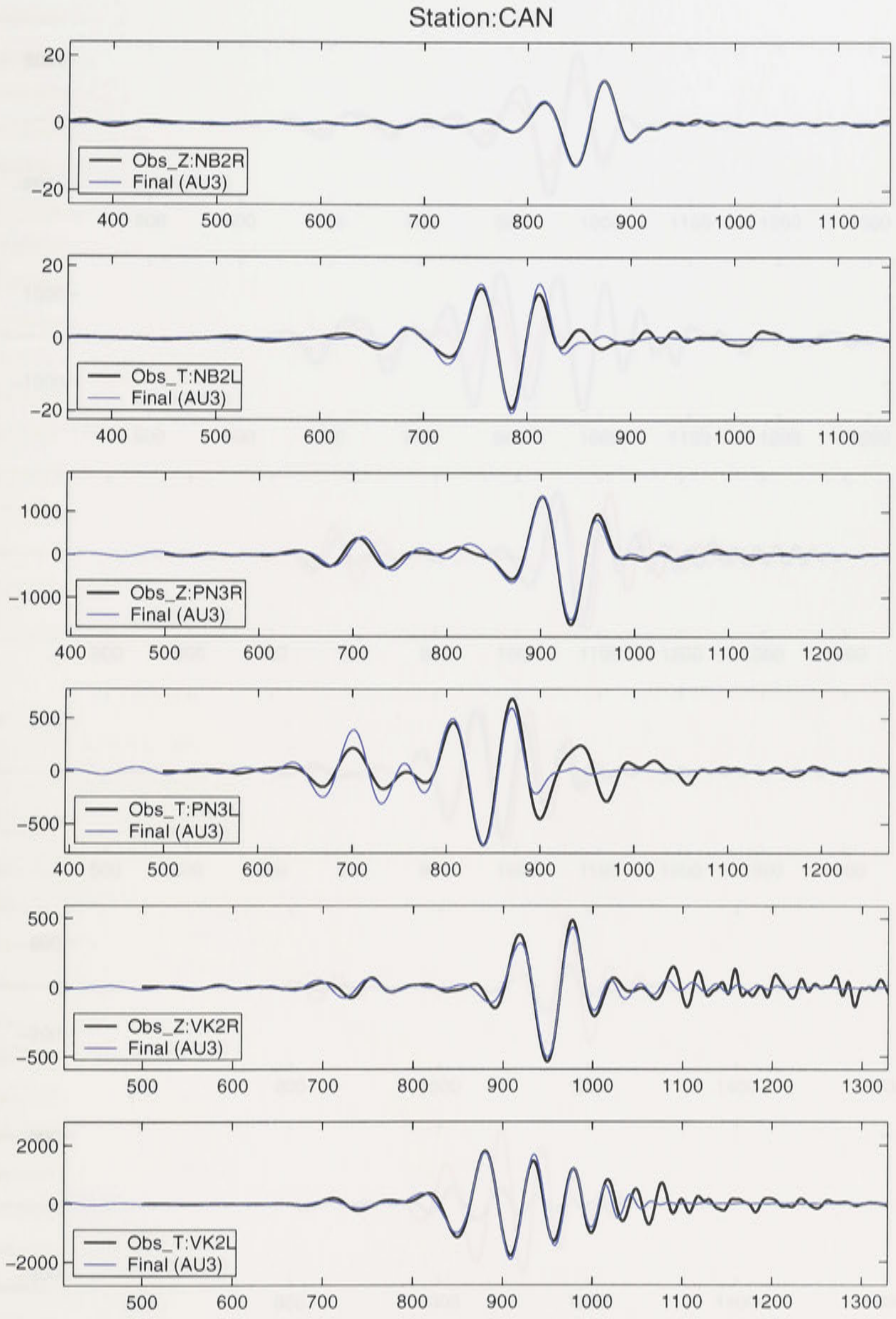

Fig. A0.43. The final results of the Rayleigh and Love independent inversions. The observed station is CAN and the events are NB2, PN3, and VK2. The starting model is AU3.

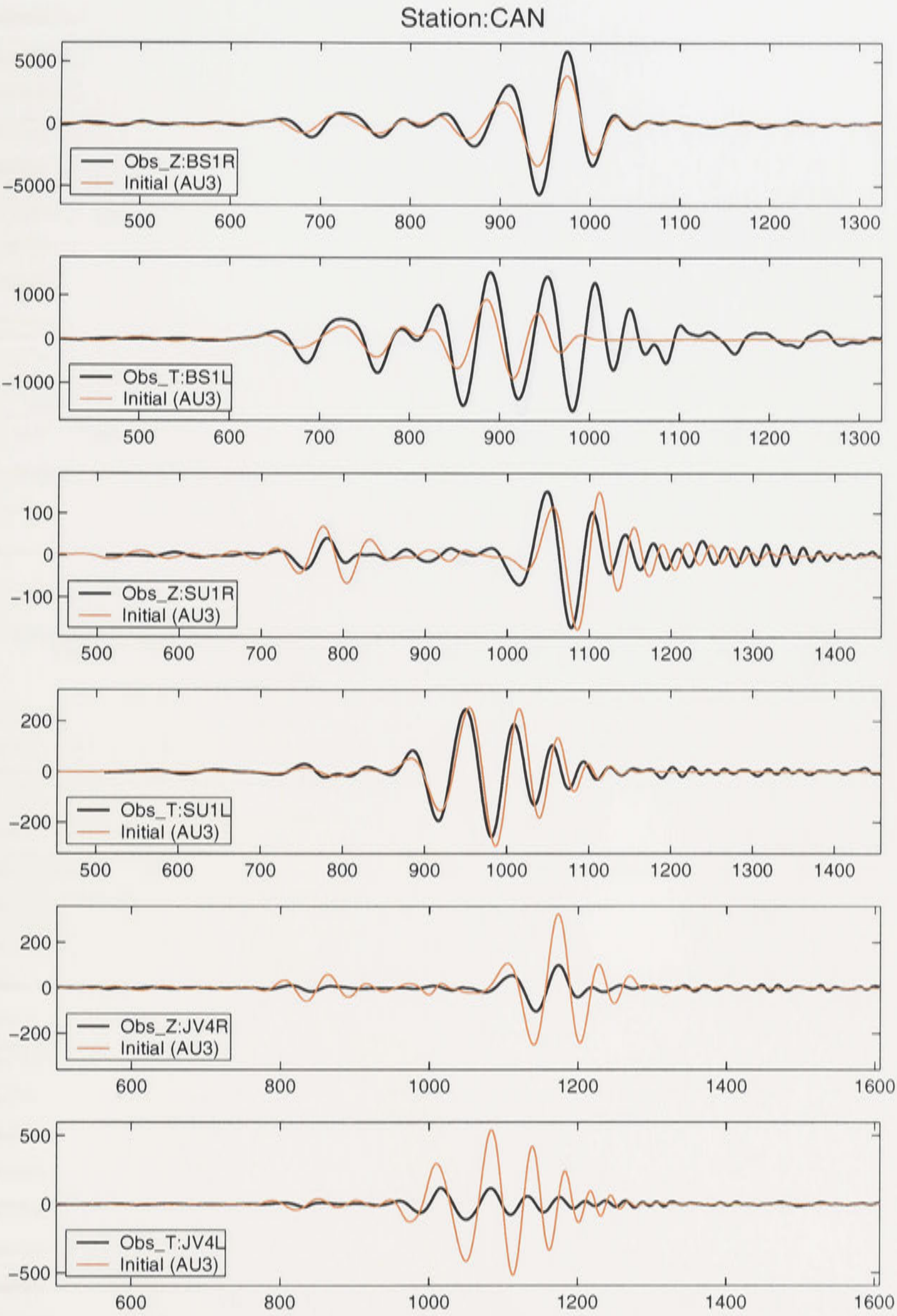

Fig. A0.44. The forward modelings of the Rayleigh and Love independent inversions. The observed station is CAN and the events are BS1, SU1, and JV4. The starting model is AU3.

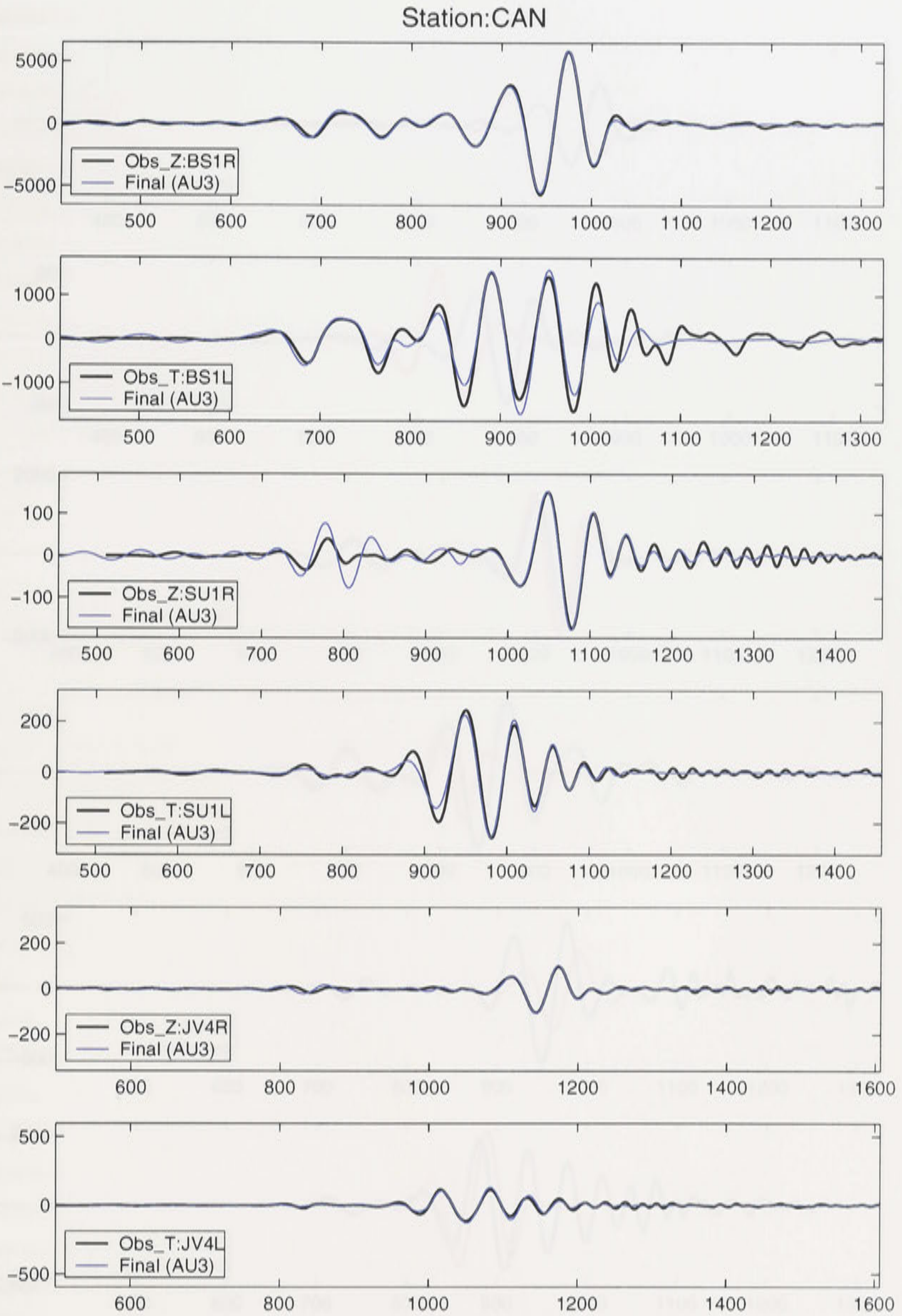

Fig. A0.45. The final results of the Rayleigh and Love independent inversions. The observed station is CAN and the events are BS1, SU1, and JV4. The starting model is AU3.

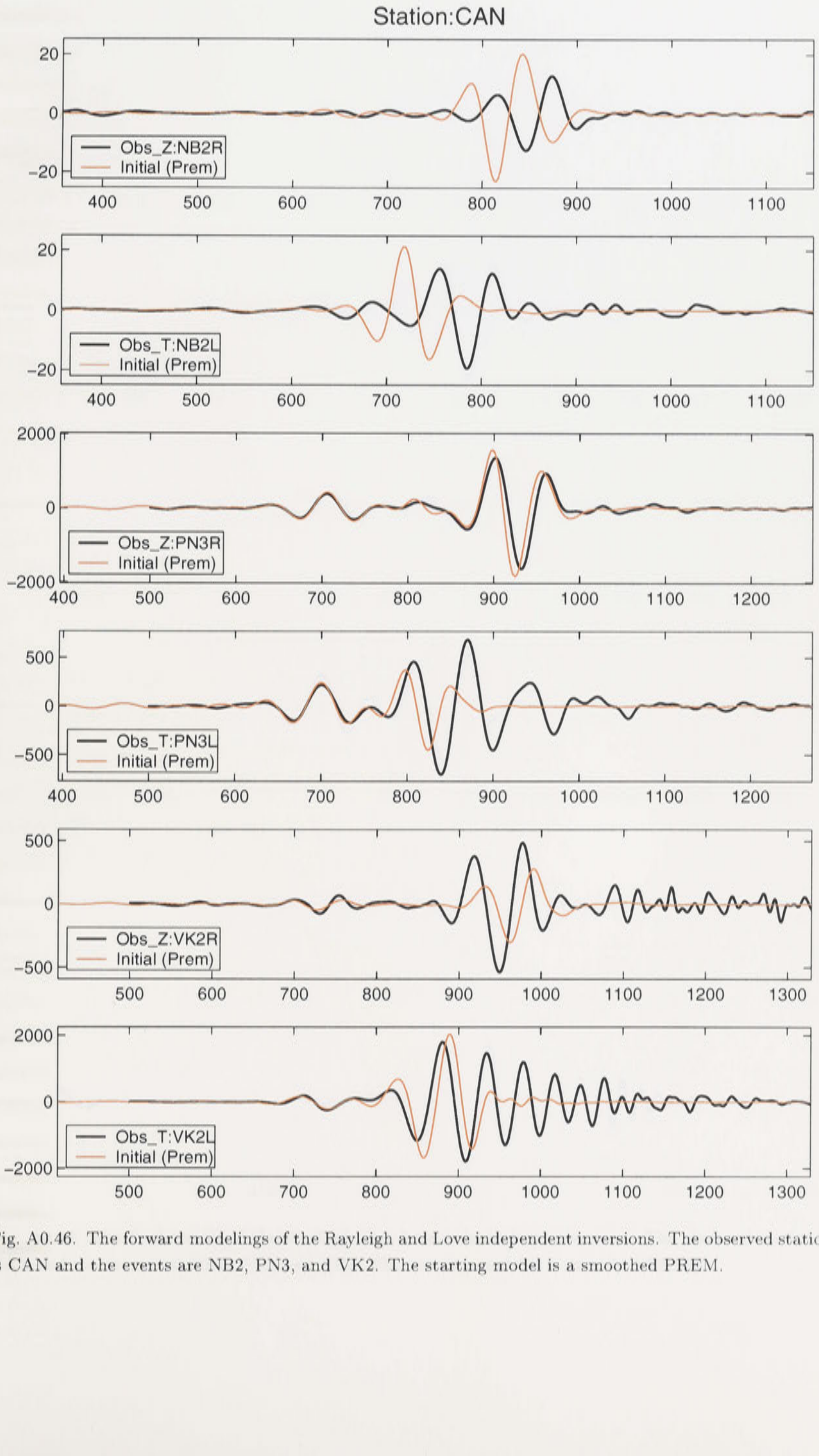

Fig. A0.46. The forward modelings of the Rayleigh and Love independent inversions. The observed station is CAN and the events are NB2, PN3, and VK2. The starting model is a smoothed PREM.

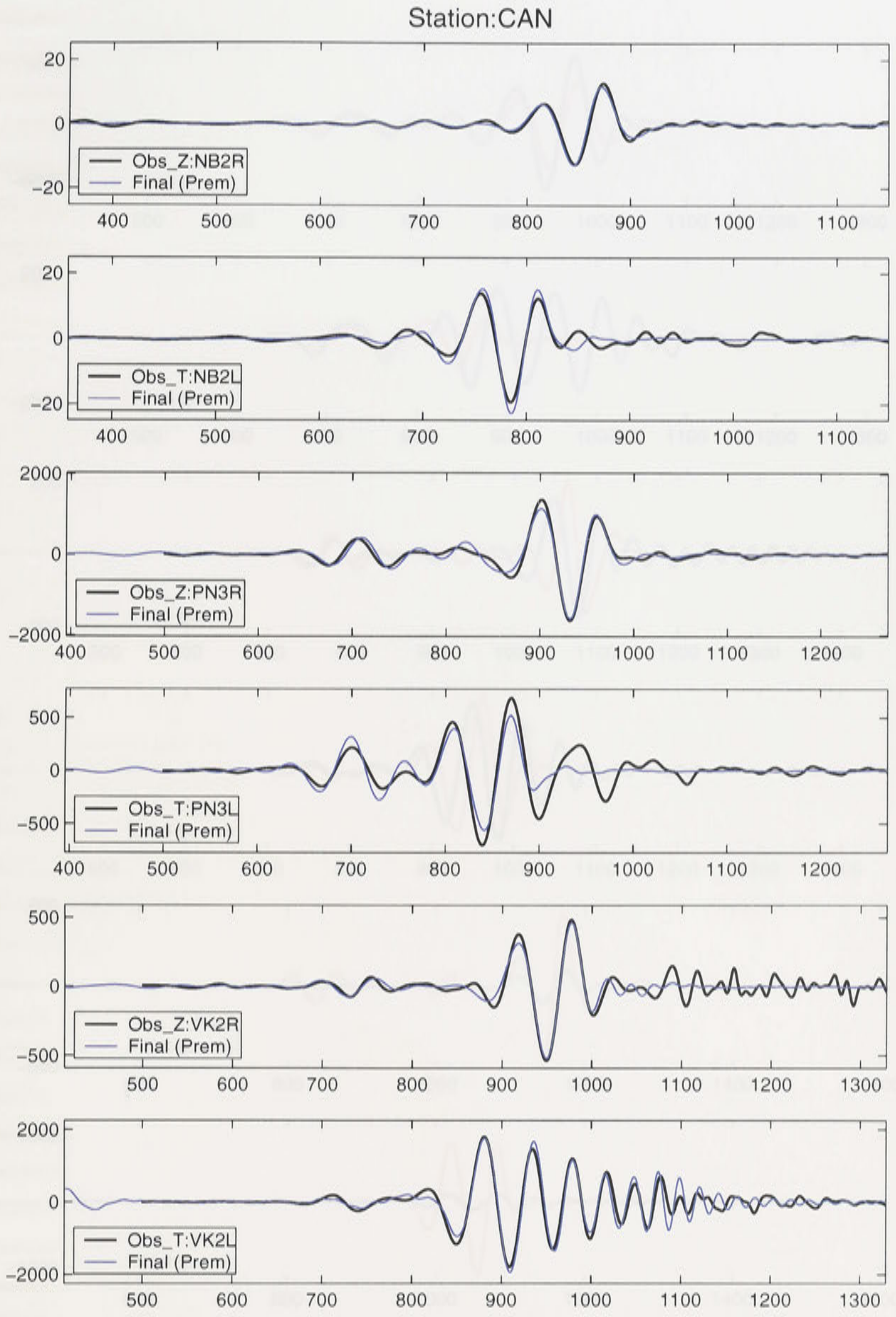

Fig. A0.47. The final results of the Rayleigh and Love independent inversions. The observed station is CAN and the events are NB2, PN3, and VK2. The starting model is a smoothed PREM

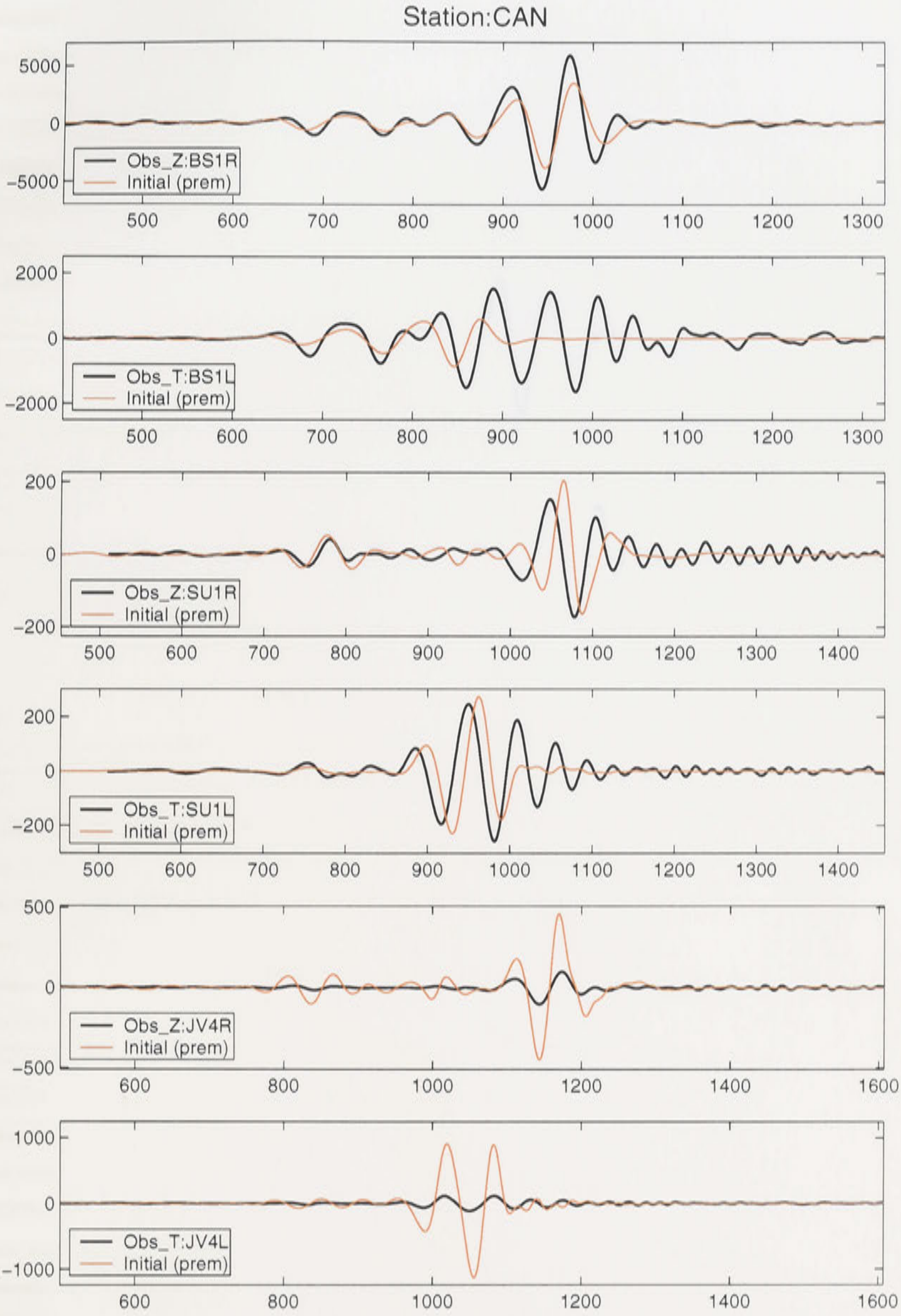

Fig. A0.48. The forward modelings of the Rayleigh and Love independent inversions. The observed station is CAN and the events are BS1, SU1, and JV4. The starting model is a smoothed PREM.

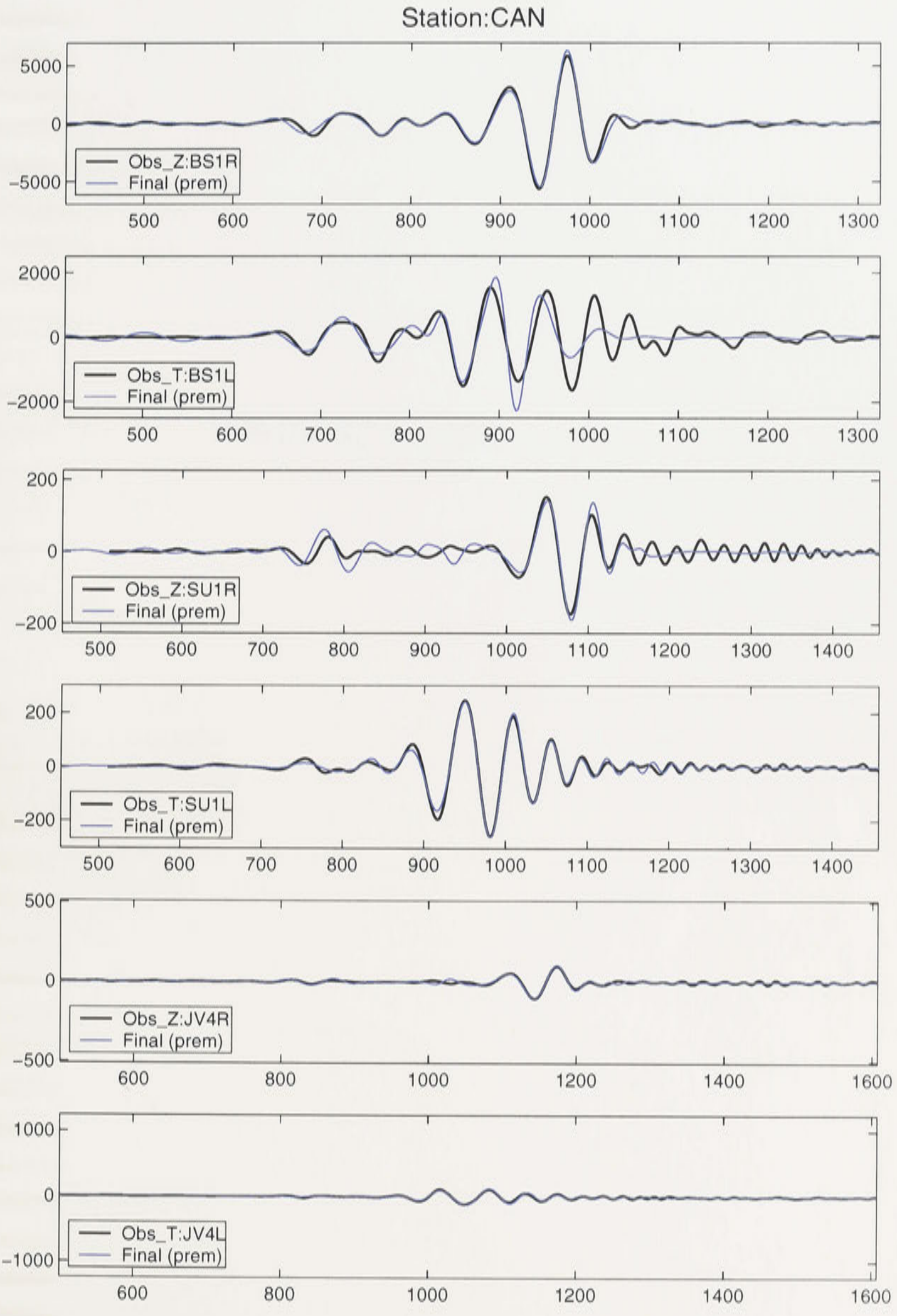

Fig. A0.49. The final results of the Rayleigh and Love independent inversions. The observed station is CAN and the events are BS1, SU1, and JV4. The starting model is a smoothed PREM.